The carbon speciation in the Earth's interior as function of pressure, temperature and oxygen fugacity

Dissertation

Fakultät für Biologie, Chemie und Geowissenschaften
Universität Bayreuth

Vincenzo Stagno
(Diplom-Geologe)
aus Palermo (Italien)

Bayreuth, 2011

Die vorliegende Arbeit wurde von Oktober 2007 bis Februar 2011 am Bayerischen Geoinstitut, Universität Bayreuth unter Leitung von Dr. D.J. Frost and Prof. D.C. Rubie angefertigt.

Datum der Einreichung der Dissertation: 17 Februar, 2011

Datum des wissenschaftlichen Kolloquiums: 30 Mai, 2011

Prüfungssausschuß:

Prof. J. Senker, Universität Bayreuth (Vorsitzender)

Prof. D.C. Rubie, Universität Bayreuth (Erster Gutachter)

Prof. A. Woodland, Universität Frankfurt am Main (Zweiter Gutachter)

Prof. L. Dubrovinsky, Universität Bayreuth

Prof. L. Zöller, Universität Bayreuth

Contents

Abstract

The redox state of the Earth's interior will influence the speciation of volatile elements both in the mantle and in mantle derived magmas. Carbon is one of the principal elements to be affected in this way because under reducing conditions it forms graphite or diamond, and under oxidizing conditions carbonate (or CO_2-bearing) minerals and melts. The cycling and residence time of carbon in the mantle can be strongly effected by the oxygen fugacity because reduced phases such as diamond and graphite are immobile and likely to remain within the mantle and potentially within subducting slabs, while at more oxidizing conditions CO_2-rich fluids or melts can migrate and escape from the interior. The carbon cycle in the Earth may therefore depend on the redox state of mantle rocks. Conversely, an influx of CO_2-rich fluids or melts may act to oxidize the mantle as an additional aspect of metasomatism.

In the first part of this study experiments were performed to measure the oxygen fugacity at which carbon (graphite or diamond) oxidises to carbonate minerals or melts within mantle peridotite assemblages between 2.5 and 11 GPa at 1100-1600 °C. The experiments were performed up to temperatures where carbonate melts evolve towards more silicate-rich compositions. The dilution of the carbonate melt component was found to lower the relative fo_2, expanding the melt stability field with respect to reduced carbon. The results allow the fo_2 of the diamond formation process to be determined both as a function of pressure, temperature and melt CO_2 concentration. These results also have implications for the onset of melting within up welling mantle material. Several studies have indicated that the mantle may become more reduced with depth. This means that the oxidation of elemental carbon (graphite or diamond) may occur in up welling rocks where the oxidized product is a carbonate bearing magma. When the experimental data are compared with current estimates for the fo_2 of mantle rocks the implication is that peridotitic mantle will remain in the diamond stability field up to at least 100-150 km depth. Only at depths shallower than 150 km would Fe^{3+} in mantle silicates react with graphite to produce carbonate rich melts in a redox melting process. Redox melting should limit the depth interval over which carbonate-rich melts can form beneath ridges.

Further experiments were performed to determine the fo_2 at which diamond oxidises to carbonate in the transition zone and lower mantle. Experiments at 45 GPa were performed using the MADONNA D-DIA (1500 tons) apparatus with sintered diamond anvils installed at the Geodynamics Research Centre, Ehime University in Japan. The measured oxygen fugacity was found to be approximately 3

log units above the iron-wüstite oxygen buffer (ΔIW+3). As the oxygen fugacity of the transition zone and lower mantle is most likely at or below the IW buffer this confines the stability of solid carbonate to the upper mantle or to unusually oxidized regions of the deeper mantle. The oxygen fugacity at which magnesite and diamond coexist showed a slight decrease with pressure, however, implying the possibility that magnesite may become the stable host for carbon at the very base of the lower mantle.

The oxygen fugacity at which mantle xenoliths equilibrated can be determined using oxy-thermobarometry equilibria. For garnet-peridotite rocks the only calibrated and tested oxy-barometer employs the equilibrium,

$$\underset{\text{Garnet}}{2Fe_3Fe_2^{3+}Si_3O_{12}} = \underset{\text{Olivine}}{4Fe_2SiO_4} + \underset{\text{Orthopyroxene}}{2FeSiO_3} + O_2$$

In the final section of this thesis $Fe^{3+}/\Sigma Fe$ ratios of garnets produced in a peridotite assemblage in equilibrium with carbon and carbonate melts were measured between 3 and 7 GPa. The oxygen fugacity in these experiments was also constrained, which allowed a test of this widely used oxy-barometer to be made at pressures much higher than previously performed. The results indicate that the pressure dependence of this oxy-barometer may be in error and a preliminary recalibration implies that cratonic lithosphere may not be as reduced as previously considered.

Zusammenfassung

Der Redoxzustand im Inneren der Erde beeinflusst das Auftreten unterschiedlicher chemischer Spezies der volatilen Elemente sowohl im Erdmantel als auch in Magmen, die sich im Erdmantel bilden. Kohlenstoff ist eines der wichtigsten Elemente, das auf diese Art beeinflusst wird, da es unter reduzierenden Bedingungen Graphit oder Diamant bildet, unter oxidierenden Bedingungen dagegen Karbonat- (oder CO_2 enthaltende) Minerale oder Schmelzen. Der Kreislauf und die Verweildauer von Kohlenstoff im Erdmantel kann durch die Sauerstofffugazität stark beeinflusst werden, da reduzierte Phasen wie Diamant oder Graphit relativ immobil sind, so dass sie wahrscheinlich im Mantel und auch möglicherweise in subduzierten Platten verbleiben, während unter mehr oxidierenden Bedingungen CO_2-reiche Fluide oder Schmelzen migrieren und so aus dem Erdinneren entweichen können. Der Kohlenstoffkreislauf in der Erde kann daher vom Redoxzustand der Mantelgesteine abhängen. Umgekehrt kann eine Zufuhr von CO_2-reichen Fluiden oder Schmelzen den Mantel metasomatisch oxidieren.

Im ersten Teil dieser Arbeit wurden Experimente durchgeführt, um die Sauerstofffugazität zu bestimmen, bei der Kohlenstoff (Diamant oder Graphit) in Mantelperidotit-Zusammensetzungen bei 2.5 bis 11 GPa und 1100 bis 1600 °C zu Karbonat-Mineralen oder -Schmelzen oxidiert wird. Die Experimente wurden bis zu den Temperaturen durchgeführt, bei denen die Karbonatschmelzen sich zu mehr silikatischer Zusammensetzung hin entwickeln.

Die Verdünnung der Karbonatschmelzenkomponente führt zu einer Erniedrigung der relativen fo_2, und erweitert dabei das Stabilitätsfeld der Schmelze im Verhältnis zum reduzierten Kohlenstoff. Die Resultate erlauben, die fo_2 der Diamantbildung als Funktion von Druck, Temperatur und CO_2-Konzentration in der Schmelze zu bestimmen. Diese Resultate haben auch Konsequenzen für das Einsetzen der Schmelzbildung in aufsteigendem Mantelmaterial. Eine Reihe von vorhergehenden Untersuchungen hat ergeben, dass im Erdmantel mit grösserer Tiefe mehr reduzierte Bedingungen herrschen. Das bedeutet, dass die Oxidierung von elementarem Kohlenstoff (Graphit oder Diamant) in aufsteigendem Mantelmaterial eintritt, wobei das Produkt der Oxidierung dann eine karbonathaltige Schmelze ist. Beim Vergleich der experimentellen Daten dieser Arbeit mit den gegenwärtigen Schätzungen der fo_2 von Mantelgesteinen ergibt sich, dass sich der peridotitische Mantel ab mindestens 100 bis 150 km Tiefe im Diamantstabilitätsfeld befindet. Nur in Tiefen geringer als 150 km würde das Fe^{3+} in Mantelsilikaten mit Graphit reagieren, um in einem Redox-Schmelzprozess karbonatreiche

Schmelzen zu produzieren. Redox-Schmelzbildung sollte auch das Tiefenintervall begrenzen, in dem sich karbonatreiche Schmelzen unter mittelozeanischen Rücken bilden können.

Weitere Experimente wurden durchgeführt, um die fO_2 zu bestimmen, bei der Diamant in der Übergangszone und dem unteren Erdmantel zu Karbonat oxidiert. Experimente bei 45 GPa wurden an der mit gesintertem Diamantstempeln ausgerüsteten MADONNA D-DIA (1500 Tonnen) Presse durchgeführt, die im Geodynamics Research Center der Universität Ehime (Japan) installiert ist. Die in diesen Experimenten bestimmte Sauerstofffugazität lag ungefähr drei logarithmische Einheiten über der des Eisen-Wüstit-Puffers (ΔIW+3). Da die Sauerstofffugazität der Übergangszone und des unteren Mantels sehr wahrscheinlich im Bereich des IW Puffer liegt, begrenzt dies den Stabilitätsbereich von festen Karbonaten auf den oberen Mantel oder ungewöhnlich hoch oxidierte Bereiche des tieferen Mantels. Die Sauerstofffugazität, bei der Magnesit und Diamant koexistieren, zeigt dagegen eine geringfügige Erniedrigung mit ansteigem Druck, was die Möglichkeit offen lässt, dass Magnesit das stabile Wirtsmineral für Kohlenstoff an der Basis des unteren Erdmantels sein könnte.

Die Sauerstofffugazität, bei der Mantelxenolithe equilibriert sind, kann durch Oxythermobarometrie bestimmt werden. Für Granat-Peridotite lautet die einzige kalibrierte und getestete oxybarometrische Gleichgewichtsreaktion:

$$\underset{\text{Granat}}{2Fe_3Fe_2^{3+}Si_3O_{12}} = \underset{\text{Olivin}}{4Fe_2SiO_4} + \underset{\text{Orthopyroxen}}{2FeSiO_3} + O_2$$

Im letzten Teil dieser Arbeit wurden $Fe^{3+}/\Sigma Fe$ Verhältnisse von Granaten gemessen, die bei 3 bis 7 GPa in einer peridotitischen Zusammensetzung im Gleichgewicht mit Kohlenstoff und karbonatischen Schmelzen gebildet wurden. Diese Experimente wurden unter kontrollierter Sauerstofffugazität durchgeführt, so dass dieses oft genutzte Oxybarometer auch bei höheren Drücken als bisher getestet werden konnte. Die Resultate zeigen, dass die bisher ermittelte Druckabhängigkeit dieses Oxybarometers vermutlich nicht korrekt ist und eine vorläufige Rekalibrierung deutet an, dass die kratonische Lithosphäre nicht so stark reduziert ist wie bisher angenommen.

1. Introduction

1.1 Carbon in the Earth's mantle

The abundance of carbon in the Earth's mantle is of the order of hundreds of parts per million (ppm) by weight and it is, therefore, rightly considered as a trace element. However, its ability to flux melting and vary the form in which it exists makes it of particular interest. In fact, carbon takes part in different geological processes in the form of solid carbonate (magnesite or dolomite), elemental carbon (graphite and diamond) and within liquid phases such as melts (carbonatite and kimberlite) or fluid components (methane, carbon monoxide and dioxide). The formation of diamonds is a major field of research that stimulated some of the very first high pressure experiments (Bundy, 1963b; Kennedy and Kennedy, 1976; Akaishi et al., 1990; Arima et al., 1993;) and the debate over a mantle origin for carbonatitic magmas has continued for many years. The cycling of carbon between the interior and the surface makes the mantle an important carbon reservoir and the mechanisms through which this cycle occurs are relevant to the surface concentrations of the green house gases CO_2 and CH_4 throughout Earth's history.

As mentioned above carbon is found in different forms and forms different accessory phases in rocks from the Earth's interior. In these phases carbon is generally a major component, which arises from the fact that carbon has a negligible solubility in mantle silicates (Shcheka et al., 2006) and is therefore forced to form separate carbon-rich phases. Native carbon in mantle-derived rocks (eclogites and peridotites) occurs both as graphite and diamond. Graphite has been observed in a wide variety of rocks in different geologic environments such as in basalts (Pineau et al., 1987; Barrenechea et al., 1997), andesites (Strens, 1965), peridotites (Luque et al., 1992), mantle xenoliths (Mathez, 1987; Deines, 2002), and mafic rocks in layered intrusions (Hollister, 1980; Ballhaus and Stumpfl, 1985; Ripley and

Taib, 1989). The presence of graphite in these mantle-derived rocks is controversial and may be explained by different processes, such as: a) transformation from an original diamond-bearing assemblage to graphite due to a re-emplacement at lower pressures observed, for example, in garnet-pyroxenite layers from Beni Bousera, Morocco (Pearson et al., 1989); b) exsolution from a carbon-bearing magma at reducing conditions as observed in ultramafic xenoliths from the Algerian Sahara (Kornprobst et al., 1987); c) relict of metasomatic processes in peridotites from Jagersfontein (South Africa) showing multiple graphite flakes of vein-like form (Field and Haggerty, 1990). Finally, for some graphite occurrences carbon is considered to have been assimilated from carbonaceous country rocks during magma ascent or emplacement (Ripley and Taib, 1989; Barrenechea et al., 1997; Luque et al., 1998).

In contrast, most diamond occurrences are restricted to specific rock types, mainly kimberlites, in cratonic areas (Boyd and Gurney, 1986), regions of the continental crust that have remained stable for at least 2.5 Ga and are underlain by thick lithospheric mantle extending to depth of over 200 km. Rocks considered as a host for diamonds have been identified on the base of inclusions in natural diamonds and are represented by eclogites, peridotites and websterites (Meyer, 1987; Gurney, 1989; Stachel and Harris, 2008). The majority of diamonds from these assemblages show a primary mantle origin with a characteristic $\delta^{13}C$ ($^{13}C/^{12}C$ ratio) isotopic signature of about –5 ±1 ‰ relative to the Pee Dee Belemnite international standard. However, isotopic heterogeneity has been observed for eclogitic-type diamonds, where organic carbon is also assumed to have been incorporated into the mantle via subduction of crustal rocks as also shown by $\delta^{13}C$ of –38 ‰ (Deines, 1980; Cartigny, 2005).

Although rarely found in nature, carbon might be also stored as silicon carbide (Leung et al., 1990; Jacob et al., 2004; Mathez et al., 1995) or as an alloying element in metals as suggested by recent high-pressure experimental work on Fe-C systems (Dasgupta and Hirschmann, 2010 and references therein).

The stability of any of these phases in the mantle is strictly dependent on the initial ratio of metallic iron and elemental carbon available and, therefore, mostly linked to restricted chemical conditions of the interior.

Carbon occurs also in the mantle in its oxidized form, e.g. either solid or molten carbonate or CO_2 fluid. Carbonate minerals are usually solid solutions between calcite ($CaCO_3$), magnesite ($MgCO_3$) and siderite ($FeCO_3$) end members strictly related to temperature, pressure and bulk composition. A Ca, Mg-rich phase (dolomite) is stable below 4 GPa (~120 km) in peridotite assemblages (Falloon and Green, 1989; 1990), while a Ca-rich solid phase is shown experimentally to be stable in eclogitic assemblages (Hammouda, 2003; Yaxley and Brey, 2004). An increase in pressure stabilizes the magnesite component with respect to dolomite down to lower mantle conditions (Brey et al., 2008; Ghosh et al., 2009; Litasov and Ohtani, 2009b).

The presence of solid carbonate within mantle silicates affects the melting relations and near-solidus liquids of carbonated peridotite or eclogites which has important implications for the origin of CO_2-rich magmas, such as carbonatites (Bose, 1884; Le Bas, 1981) and kimberlites (Mitchell, 1986). Each of these magmas forms at different pressures and temperatures in the upper mantle and is related to different degrees of partial melting (Gudfinnsson and Presnall, 2005). Carbonatites have been found in several localities with a diverse geological settings related either to intraplate continental rifts or compressive systems such as subduction zones (Wooley, 1989; D'Orazio et al., 2007), although an origin in the mantle for these liquids is not unequivocal. In general, melting studies have shown that carbonatites can originate by: 1) direct partial melting of a metasomatized mantle source (Wyllie and Huang, 1975; Wallace and Green, 1988); liquid immiscibility of carbonated silicate melts (Koster van Groos and Wyllie, 1963); crystal fractionation of carbonated alkali silicate melt (Veksler et al., 1998).

Primary carbonatitic liquids have been also observed to be a metasomatic agent interacting with mantle silicates in peridotite xenoliths from Spitsbergen in Norway (Ionov et al., 1993).

Kimberlitic magmas are also important carriers of carbon that form usually at depths below 150 km as a result of partial melting of mantle peridotite (Mitchell, 1986). Their emplacement on the surface is associated with explosive eruptions during which fragments of unmelted mantle (xenoliths and xenocrysts) sampled during the magma ascent are expelled through the continental crust with the consequent formation of a vertical structure called kimberlitic pipe. Crystallized kimberlitic magmas, kimberlites, are mainly found in cratonic areas in South Africa, Canada and Russia with an age spanning from late Precambrian to the Cretaceous. Diamonds found in kimberlites make these rocks of particular interest for exploration and mining.

Carbonatites and kimberlites are, therefore, important melts by which carbon can flux out the Earth's interior with implications for its residence time over the geological timescale.

Further, the Earth's interior also contains carbon in form of free fluid phase as shown by studies on inclusions in mantle xenoliths (Roedder, 1984; Schrauder and Navon, 1993) and analyses of volcanic gases at the surface (Moore, 1979). Experimental studies and observations on natural inclusions show that the speciation of carbon is well described by the C-O-H system with CO_2 component being the stable phase at shallower conditions, while methane shows the opposite behavior (Zhang and Duan, 2009).

Evidence of C-bearing fluids in the upper mantle comes also from observation of resorption features in diamond crystals recovered from kimberlites and experimentally demonstrated to be a consequence of the interaction with CO_2-saturated fluids (Fedortchouk et al., 2007), which in turn would affect diamond survival during the emplacement of kimberlitic rocks.

Carbon in the Earth's mantle is in exchange with the Earth's surface. At subduction zones carbon in the form of subducted sediments or altered oceanic crust is transported into the mantle. Some is recycled to the surface on a short time scale as a result of island arc processes, but some carbon likely persists in subduction zones and is transported into the deep mantle. Similarly at mid ocean ridges or oceanic islands basaltic magmas bring carbon mainly in the form of CO_2 to the surface. Some of this carbon may be recycled but some may be primordial i.e. present in the mantle since accretion. To understand the cycling of carbon through the mantle requires information on the mobility and solubility of carbon within mantle rocks and magmas, which requires an appreciation of the forms in which carbon is stable at different conditions within the Earth. As carbon can change effective oxidation state, a full appreciation of its behavior must consider changes in state due to differences in the prevailing oxygen fugacity. First it is important, however, to review how much carbon is likely to be in the mantle, and the mechanisms by which it may be cycled through the mantle.

1.2 Estimates of carbon abundance in the Earth' s mantle and the global carbon content

Although termed as an atmophile element in Goldschmidt's classification, the abundance of carbon as CO_2 in the atmosphere (~380 ppm) likely represents only a small amount of the total carbon stored in the Earth. An estimate of the mantle carbon content in terms of global budget is provided by Javoy et al. (1982) who reported the amount of carbon in the mantle ($5x10^{23}$g) to be three times greater than the total carbon of the remaining terrestrial reservoirs, e.g. atmosphere, biosphere and hydrosphere.

Estimates of the carbon content in the mantle are possible by using different approaches, such as:

- relative element ratios between data from undifferentiated chondrites and the Earth;
- analyses of the carbon content dissolved in mid ocean ridge basalt;
- composition of fluid and melt inclusions in natural minerals;

- estimate of the CO_2 degassing from seismic and volcanic areas.

Cosmochemical data have provided information on the Earth's bulk carbon abundance based on the relative depletion of carbon between 61 chondrites and our planet, as well as an estimate using the ratio of elements with similar volatile behaviour (Otting and Zahringer, 1967). Terrestrial carbon abundance of the order of $6.6x10^{23}$ g was derived from the $C/^{36}Ar$ and $C/^{3}He$ (Marty and Jambon, 1987) ratio of chondrites in conjunction with the amount of rare gases in the Earth's atmosphere.

Direct estimates of carbon abundances in mantle reservoirs comes from measurements of dissolved CO_2 in basaltic glasses and melt inclusions (e.g., Dixon, 1997; Bureau et al., 1998), including trapped gas bubbles in basalts (Aubaud et al., 2005), and by using CO_2/incompatible element ratios, e.g. CO_2/He (Trull et al., 1993; Zhang and Zindler, 1993; Marty and Tolstikhin, 1998; Shaw et al., 2003), CO_2/Nb (Saal et al., 2002; Cartigny et al., 2008; Shaw et al., 2010), CO_2/Ar (Tingle, 1998; Cartigny et al., 2001) and CO_2/Cl (Saal et al., 2002). Values for the depleted MORB source mantle range between 20 and 185 ppm of carbon depending to some degree on the partial melt model assumed for the basalt formation. However, uncertainties have to be taken into account for these estimates that derived from melting processes at different degrees and degassing at different rates affecting the real volatile content of the analysed samples. OIBs (basalts erupted from oceanic islands, e.g. Hawaii) and E-MORBs are thought to be possibly representative of the carbon content in undepleted sources and with source concentrations estimated to range between 300 and 1300 ppm (Dixon et al., 1997; Pineau et al., 2004; Aubaud et al., 2005).

The CO_2 degassing from active volcanoes reflects the carbon content of magmatic bodies trapped in the shallower portion of the crust, i.e. concentrated within magma chambers due to crystallization. When the degassing CO_2 concentrations are correlated with noble gases like He, for example, important information about the mantle origin and the mass transport of carbon from the interior of the

Earth to the atmosphere can be obtained. Data are available for many representative currently active volcanoes like Etna (Sicily) with CO_2 emissions of about 13 ±3 Tg yr^{-1} (Allard et al., 2001), while the CO_2 estimated from Kilauea (Hawaii) is about one order of magnitude less (Gerlach and Graeber, 1985). These estimates help us to understand the different fate of volatiles when related to different geological and volcanic settings as well as the immediate response of volcanic edifices to the carbon cycle inside the Earth. In contrast with the CO_2 degassing from volcanic areas, a diffusive (also called non-volcanic or cold) degassing is also observed in regions that are seismically active (Chiodini et al., 2008). Analyses of gaseous samples showed also a mantle origin of the carbon (Minissale, 2004) with estimates ranging between 4 and 30 Tg yr^{-1} in Italy for example (Frezzotti et al., 2009) and, therefore, may affect the estimate of carbon in the mantle and the global carbon cycle.

A complete knowledge of the deep carbon cycle in the Earth's interior would be improved if carbon contents of samples from the transition zone and lower mantle could be obtained. Unfortunately, no samples are available at such conditions and the only minerals that are known to have been formed at depths >200 km are inclusions in natural diamonds. These inclusions, however, are unlikely to be sufficiently representative to give an indication of the carbon content of the deep mantle or to infer that it is any different from either the depleted or enriched MORB sources.

Cosmochemical and geophysical evidences indicate that elements lighter than iron and nickel must be present in the Earth's core. Carbon is often cited as a potential light element that may explain the seismic properties of the core (Poirier, 1994; Hillgren et al., 2000). If carbon were the light element in the core then it would represent the largest terrestrial carbon reservoir.

Along with the outgassing of carbon described above, subduction processes bring carbon down in to the mantle in the form of carbonate within the alterated oceanic crust, carbonate-bearing sediments or biogenic carbon (Sano and Williams, 1996; references therein). Subduction of carbon may have

contributed to maintaining or buffering the atmospheric carbon concentration through geological timescale. Ingassing of carbon by subduction is unlikely to be a steady state process, however, due to the different solubility behavior when hydrous fluids of different chemistry and the relationship with other volatiles are also taken into account, i.e. influences of Cl and S on carbon (Wallace, 2005). However, there is evidence from inclusions in diamonds (Brenker et al., 2007) that carbonate can be subducted into the transition zone and the lower mantle. Many studies have investigated the solidus of carbonate assemblages representative of subducted rocks at those pressures and temperatures recorded from metamorphic rocks, e.g. eclogites, with implications for the origin of CO_2-rich liquids (Dasgupta et al., 2004; Litasov and Ohtani, 2009).

1.3 The stability of carbonate minerals and melts and the solubility of CO_2 in natural magmas

The solubility of carbon in magmas is governed by pressure, temperature and melt composition. Although carbon speciation in a geological context should be described within the C-O-H system, only CO_2 dissolving as CO_3^{2-} has a measurable effect on the physical properties of magmas such as electrical conductivity, viscosity and density, while the solubility of CO and CH_4 species appears negligible (Mysen and Richet, 2005). Noteworthy, the solubility of the carbonate component in basaltic melts was observed to be two times lower than water, $1.8x10^{-8}$ compared to $1.8x10^{-6}$ mol g^{-1} bar^{-1} (Hamilton et al., 1964; Stolper and Holloway, 1988; Pan et al., 1991) with a quasi-ideal behavior described by the Henry's law, where the concentration of a species dissolved in the melt is considered proportional to its activity in the vapor.

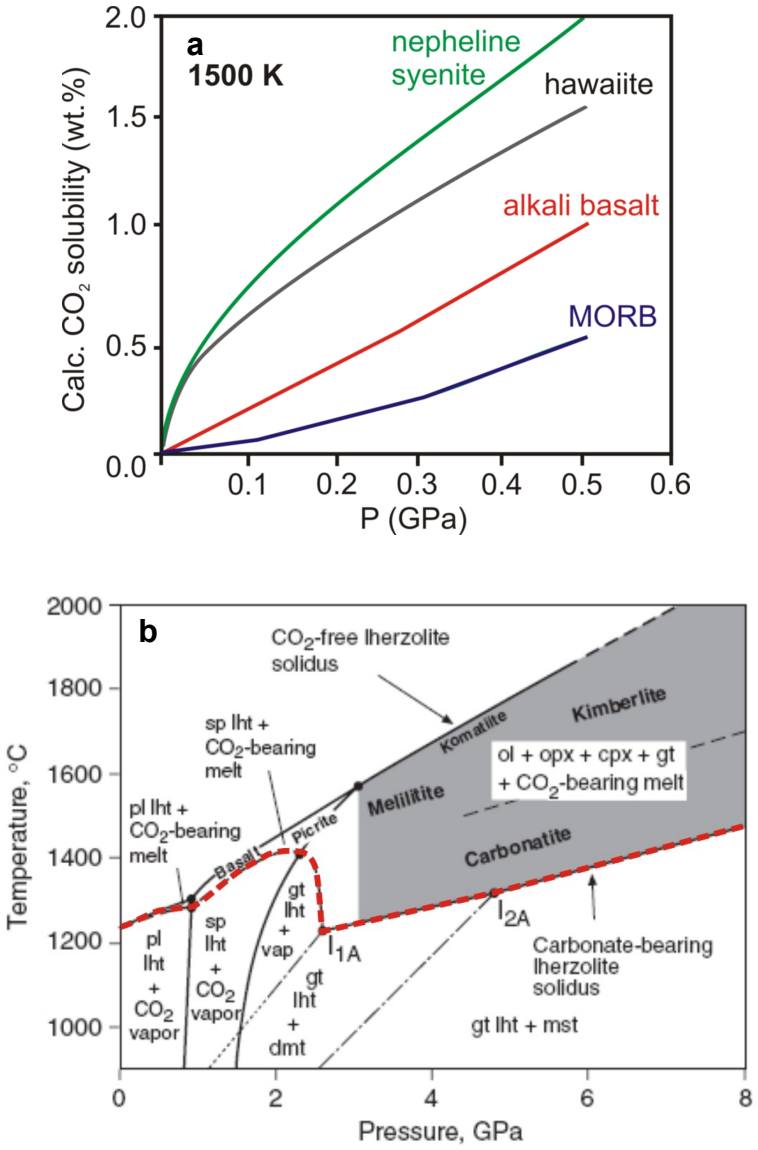

Figura 1.1 a) Shown is the calculated CO_2 solubility in silicate liquid with different composition at 1500 K as function of pressure using the model by Papale (1999). b) Red dashed line indicates the solidus of a carbonated peridotite in the Ca-Mg-Al-Si + CO_2 system by Gudfinnsson and Presnall (2005). Notes: ol, olivine; opx, orthopyroxene; cpx, clinopyroxene; gt, garnet; dmt, dolomite; mst, magnesite; pl, plagioclase; sp, spinel; vap, CO_2 vapor; lht, lherzolite.

Figure 1.1a shows the effect of pressure on the CO_2 solubility in different magmas the compositions of which are described by the olivine-diopside-quartz (-anorthite) basaltic system (Yoder and Tilley, 1962). The increasing melt CO_2 content with pressure correlates also positively with the level of SiO_2 undersaturation of magmas, implying that carbon dissolves as CO_3^{2-} tetrahedral coordinated with respect to more SiO_2-rich magmas in which it dissolves as molecular CO_2. The mechanism of carbon

solubility has been extensively studied using infrared spectroscopy on synthetic and natural glasses and can be easily summarized by the following equilibrium,

$$CO_{2\ molecular} + O^{2-}_{react} = CO_3^{2-} \qquad (1.1)$$

with O^{2-}_{react} indicating the reactive oxygen species in the silicate structure, which decreases with the degree of polymerization (Fine and Stolper, 1985) and increases in the presence of dissolved alkalis (network modifiers). As the solubility of CO_2 in basaltic magmas decreases with decreasing pressure CO_2 saturation can occur during magma ascent causing CO_2 to degas. This promotes vesciculation and fragmentation of the ascending magmas, which has important implications for the eruptive style at the surface. It likely explains why CO_2 is a dominant fluid inclusion in olivine phenocrysts and mantle xenoliths.

At the conditions of mantle partial melting to produce MORB, magma CO_2 solubility is sufficiently high and the bulk CO_2 concentration low enough for liquids to be CO_2 undersaturated. However, as shown in figure 1.1b in the pressure range 1-2 GPa where MORB melts are considered to originate carbonate minerals are unstable below the solidus and CO_2 fluid would be expected to be the host phase for carbon. Above approximately 2.5 GPa, however, carbonate minerals and melts are stabilized within peridotitic assemblages and a strong downward bend in the solidus occurs as carbonate melts become stable. Below the solidus at these pressures dolomite is the main carbon host in CO_2-bearing peridotite assemblages. Numerous studies have been performed to understand decarbonation and the onset of melting in CO_2-bearing mantle systems. References and a more accurate description are provided in Chapter 3. Figure 1.1b shows the effect of carbon as carbonate on the solidus of a peridotite in the simplified Ca-Mg-Al-Si (termed "CMAS") plus CO_2 system as a function of pressure and temperature as reviewed by Gudfinnsson and Presnall (2005). The CMAS system has been often

employed for studies on phase equilibria and origin of mantle melts since it represents the simplest system with analog phases to all the minerals in equilibrium with melt. The red dashed line highlights the solidus curve drawn from the plagioclase-, to the spinel- and garnet-bearing carbonated lherzolite (olivine+orthopyroxene+clinopyroxene assemblage) along which a CO_2-bearing liquid coexists with mantle minerals. The diagram shows also the solidus of plagioclase, spinel and garnet lherzolite in the CMAS system under CO_2-free conditions (black line; Gudfinnsson and Presnall, 1996).

The points on the CO_2-bearing solidus curve I1A and I2A are invariant points determined by Dalton and Presnall (1998a) and Presnall et al. (2002) and mark the transitions from CO_2 vapor-bearing to dolomite-bearing lherzolite at about 2.6 GPa and from dolomite-bearing to magnesite-bearing garnet lherzolite at 4.8 GPa, respectively. Along with the stability of carbonate, either liquid or solid, the diagram shows the dramatic effect of CO_2 in lowering the melting point of a peridotite at dry mantle conditions in typical silicate assemblages. When compared to the solidus of a dry KLB 1 peridotite (Herzberg and Zhang, 1996), the difference is about 300 °C at 3 GPa in agreement with the solidus in the CMAS system explored by Gudfinnsson and Presnall (1996).

At depths where spinel and plagioclase are stable the effect of CO_2 is less remarkable and most of the carbonate component would exsolve as molecular CO_2 at these conditions. Nevertheless, magmas generated in the oceanic mantle are known to form in the presence of spinel with the result that carbonatitic or kimberlitic liquids rarely occur. However, geochemical (Salters and Hart, 1989) and seismic observations demonstrated the occurrence of deeper melting processes in the garnet-bearing lherzolite stability field that might result in small amounts of CO_2-rich (carbonate) liquids. The strong partitioning of incompatible trace elements into these small degree melts may scavenge trace elements from deeper fertile rocks and, therefore, may influence the trace element signature in erupted MORB. During decompressive melting the melt fraction will increase as pressure decreases consistent with an

increase of the SiO_2 content of the liquid. In turn, the CO_2 (carbonate) in the melt will decrease as a consequence of dilution causing a carbonate-silicate melt (CO_2 content ~20-25 wt. %) evolution at approximately 3 GPa. Figure 2b shows also the stability field for carbonatitic liquid in equilibrium with a lherzolitic assemblage in a pressure range between 3 and 8 GPa. These are liquids with less than 10 wt. % of SiO_2 and high Ca and Mg content. Kimberlitic melts are generated at higher temperatures than carbonatites with greater melt fractions as observed in a simplified CMAS+CO_2 system (Dalton and Presnall, 1998; Gudfinnsson and Presnall, 2005). With increasing pressure the kimberlitic composition varies from IB-type at ~5 GPa to I-A type kimberlites at 10 GPa (Smith et al., 1985), while the primitivity of the magma is still recognizable by the MgO/CaO ratio being close to the unity.

Due to the important role in terms of CO_2 storage in the Earth's interior, Dasgupta and Hirschmann (2006) recently argued that carbonate melts would be formed in up welling magnesite-bearing peridotite at 300 km. This is show in figure 1.2a and 1.2b where the solidi of typical mantle assemblages are plotted as function of pressure and temperature. A more realistic scenario is proposed by plotting the two possible thermal profiles relative to an adiabat applicable beneath mid ocean ridges and a "hot" adiabat that refers to hotspot-like environments (figure 1.2a). Several lines of geophysical evidence support the presence of melts at depths between 200 and 300 km beneath ridges based on seismic anisotropy (Gu et al., 2005; Dunn et al., 2001; Evans et al., 1999) and electrical conductivity measurements near ridge axes (Gaillard et al., 2008).

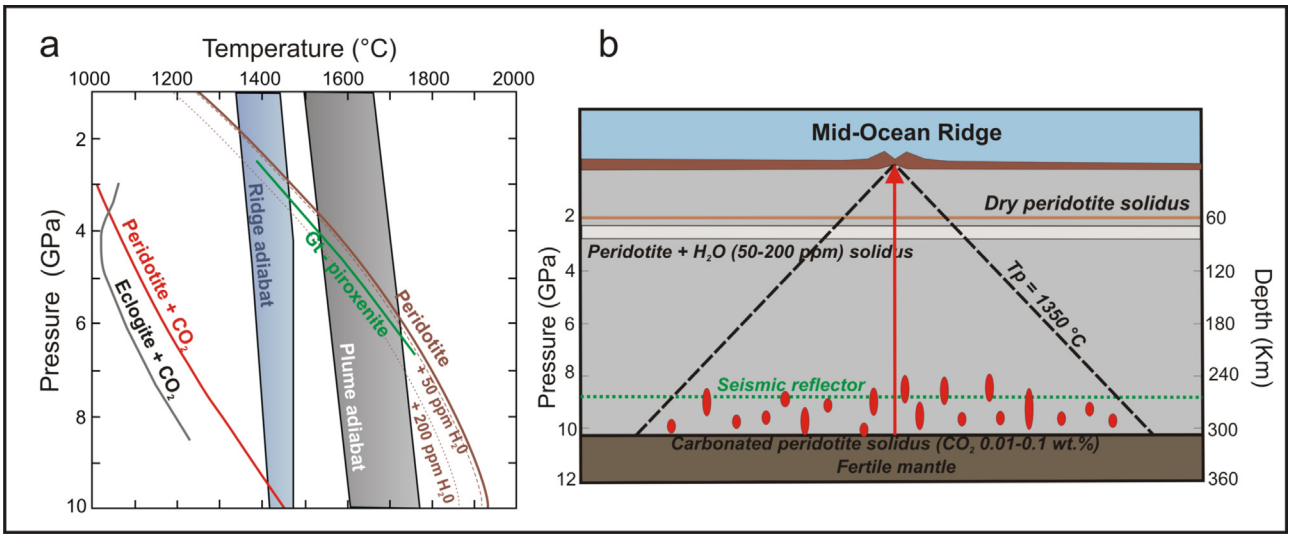

Figura 1.2 a) From Dasgupta et al., 2007 modified. Pressure-temperature diagram showing the locations of mantle solidi with the intersection between oceanic geotherms (blue area) and carbonated mantle peridotite solidus (Dasgupta and Hirschmann, 2006-red line), carbonated eclogite solidus (Dasgupta et al., 2004 -grey line), solidus of volatile-free and H_2O-bearing peridotite (Hirschmann, 2000 - brown line), and the solidus of garnet pyroxenite (Kogiso et al., 2003 - green line). Small degree carbonate melts could form in up welling mantle at pressures of 10 GPa or approximately 300 km as the carbonated peridotite solidus is crossed. References like in a). b) Shown are the depths of solidi of different assemblages (dry, H_2O-bearing and CO_2-bearing peridotite) along a 1350 ºC potential temperature (Tp) geotherm. The green dotted line indicates the location of seismic anomalies reported by Gu et al. (2005) beneath the East Pacific Rise.

If this is the case, a deep initial phase of carbonate melting beneath mid ocean ridges would imply large scale scavenging of carbon from the mantle, with implications for the above discussed transport of incompatible elements. However, a more precise approach would require the knowledge of the redox conditions in the upper mantle in order to clarify whereas carbonatitic liquids are stable with respect to graphite or diamond.

The stability of a carbonated peridotite has been also investigated at temperatures and pressures of the transition zone and lower mantle. Results showed that CO_2 can lower the melting temperature of a peridotite assemblage by ~500 °C at 20 GPa (Litasov and Ohtani, 2009) although, melting temperatures may be further reduced by the presence of additional elements, such as alkalis (Na and K) as discussed by Ghosh et al., (2009).

To date, the stability of solid carbonate has been investigated at pressures to ~115 GPa corresponding almost to the core-mantle boundary. Several experiments were performed in diamond

anvil cell with the aim of determining possible decarbonation reactions (Kraft et al., 1991; Biellmann et al., 1992 and 1993; Issiki et al., 2004). All the results reported no decarbonation reactions, which excludes the possibility that magnesite, aragonite or calcite may break down producing a free fluid phase at mantle temperature conditions. However, a phase transition was observed for magnesite at pressures compatible with the base of the lower mantle (~115 GPa), called magnesite II (Issiki et al., 2004) with an orthorhombic symmetry, with the important implication for solid carbonate being a possible source of carbon in the deep Earth's interior. But, again, no hypothesis has been suggested that takes into account the effect of oxygen fugacity on carbonate stability in the deep mantle even though conditions might be reduced enough in the lower mantle to allow the precipitation of metallic phases (Frost et al., 2004).

1.4 Oxygen fugacity in the Earth's interior

Oxygen fugacity, or partial pressure of oxygen (Eugster, 1957), is a thermodynamic variable used to indicate the chemical potential of oxygen in reactions where both reagents and products contain the same element(s) but with different oxidation states. These reactions are termed "redox reactions" and are described by a univariant curve in fO_2-temperature diagrams. At a given temperature, above this curve the oxidized phase of an assemblage will be stable whereas, below the reduced phases will be stable.

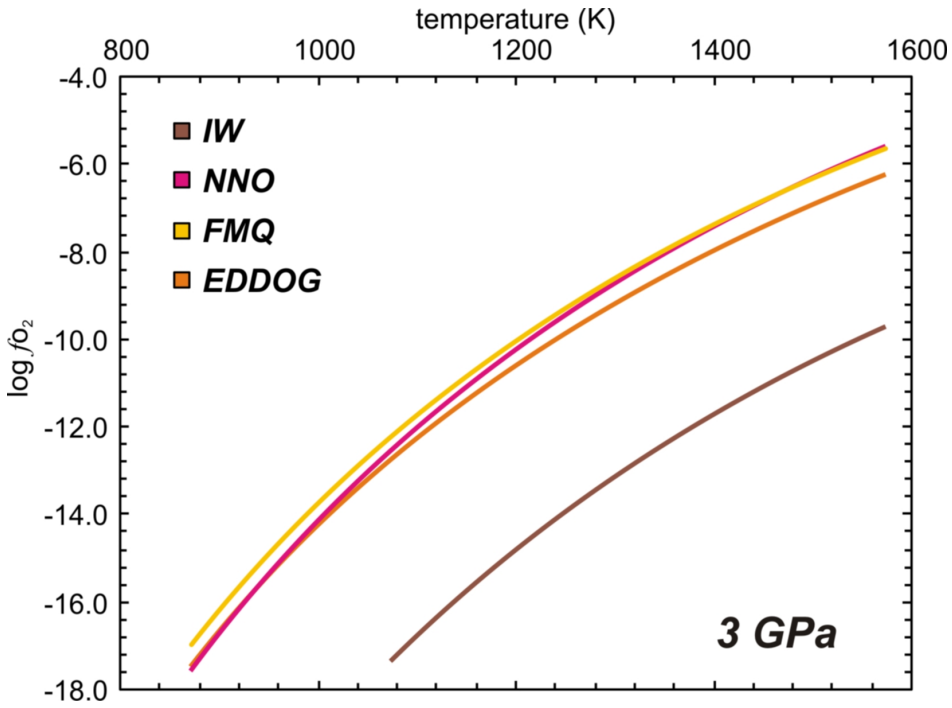

Figure 1.3 Shown are curves relative to buffer equilibria plotted as function of temperature (Kelvin) versus the logarithm of the oxygen fugacity and calculated at a fixed pressure of 3 GPa. The equilibria are reported with the acronyms explained in the text (Eq. 1.2-1.4).

Rock-forming minerals are widely characterized by the presence of heterovalent elements, such as iron, chromium, vanadium, and carbon. Their occurrence in oxidized or reduced form can be used to infer the redox state at which certain rocks have crystallized. An important goal in experimental

geochemistry is, therefore, to investigate the behavior of these elements with respect to oxygen fugacity and develop interpretative models, for extracting the change of redox conditions in the Earth over the geological time scale from the analysis of heterovalent cation concentrations in mantle rocks (Delano, 2001; Li and Lee, 2004). In figure 1.3 four buffer equilibria are plotted which are extensively used in petrology to describe redox conditions at which common silicates and oxides coexist in the Earth's interior. These equilibria are conventionally written with the high entropy side, which includes oxygen, on the right and are commonly referenced by their acronyms as follows,

$2Fe_3O_4 + 3SiO_2 = 3Fe_2SiO_4 + O_2$ (FMQ; O'Neill and Wall, 1987) (1.2)
spinel quartz olivine

$2Mg_2Si_2O_6 + CaMg(CO_3)_2 = 2Mg_2SiO_4 + CaMgSi_2O_6 + 2C + 2O_2$ (EDDOG/D; Eggler and Baker, 1982) (1.3)
enstatite dolomite olivine diopside graph/diam

$2FeO = 2Fe + O_2$ (IW**;** Huebner, 1971; O'Neill, 1987a) (1.4)
wüstite iron

$2NiO = 2Ni + O_2$ (NNO; Huebner and Sato, 1970) (1.5)

The above equilibria can also be used in a natural context. Equilibrium (1.2), for example, could be used to determine the oxygen fugacity from a mineral assemblage (figure 1.3) from consideration of the activity of each component in the phases. The standard Gibbs free energy of the reaction is a function of the oxygen fugacity through the equilibrium condition,

$$\Delta G^\circ_{(1.2)} = -RT\ln K = -RT\ln\left(\frac{a_{Fay}^3}{a_{SiO_2}^3 \cdot a_{Mt}^2} \cdot fo_2\right) \quad (1.6)$$

hence, we have that

$$\log fo_2 = -\frac{\Delta G^\circ_{[1.2]}}{\ln(10)RT} - 3\log a_{Fay} + 3\log a_{SiO_2} + 2\log a_{Mt} \quad (1.7)$$

with $\Delta G°_{[1.2]}$ standard Gibbs free energy of reaction (1.2), R is the gas constant (8.3144 J $mol^{-1}K^{-1}$), T is the temperature in Kelvin and a_i^J is the activity of the component *i* in the phase *j* (*j* is omitted in case of pure end members, as in eq. 1.7).

In the case of a pure assemblage of phases such as for equilibrium (1.2), the activity of each phase is 1 and the log fo_2 is simply expressed as a function of the Gibbs free energy of the reaction as,

$$\log fo_2 = \frac{\Delta H^o - T\Delta S^o + \Delta V(P-1)}{\ln(10)RT} \quad (1.8),$$

which requires knowledge of enthalpy, entropy and volume change with pressure and temperature of the given reaction. Thermodynamic databases are provided by Holland and Powell (1990), Robie et al. (1995) and Fabrichnaya et al. (2004). A simple parameterisation is often used to express the oxygen fugacity as function of pressure and temperature derived from (1.8),

$$\log fo_2 = \frac{a}{T} - b + \frac{c \cdot (P-1)}{T} \quad (1.9).$$

Since natural minerals are commonly complex solid solutions, in this case the activity is calculated from the chemical composition (by electron microprobe, for example) of each phase in (1.2) as,

$$a_i^j = x_i \cdot \gamma_i \quad (1.10)$$

where x_i is the mole fraction of the component in a given phase and γ_i the activity coefficient which is 1 in case of ideal mixing between sites. In case of non-ideality (γ_i used) the excess of energy due to the

mixing behaviour between atoms of different elements in a crystalline structure can be described using the general formulation,

$$RT \ln \gamma_i = (1 - X_i)^2 W \qquad (1.11)$$

with W being an interaction parameter called a Margules parameter, which represents an interchange energy (J mol^{-1}) between cations in case of symmetrical solid solutions (Wood and Fraser, 1977; Cemič, 2005). Interaction parameters used to calculate the oxygen fugacity in this study are listed in each chapter.

As shown in Figure 1.3 most buffers (1.2), (1.3), (1.4) and (1.5) follow a similar trend as a function of temperature, which results from the enthalpy change associated with oxidation being similar for most assemblages. For this reason fo_2 measurements are usually normalized to a given buffer, such as FMQ to eliminate the effect of temperature from the buffer curves.

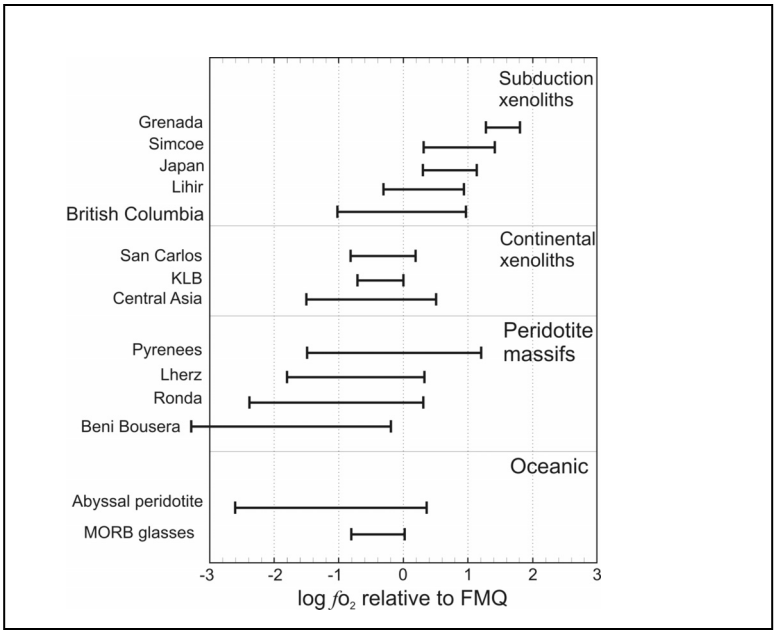

Figure 1.4 Shown is the oxygen fugacity range calculated from spinel-bearing peridotite rocks from different geological settings (Frost and McCammon, 2008 modified). References are provided by Frost and McCammon (2008).

Figure 1.4 shows the oxygen fugacity measured in natural spinel-bearing peridotites from different localities determined mainly using the following equilibrium calibrated by Nell and Wood (1991),

$$\underset{\text{opx}}{3Fe_2Si_2O_6} + \underset{\text{spinel}}{2Fe_3O_4} = \underset{\text{olivine}}{6Fe_2SiO_4} + O_2 \qquad (1.12)$$

The oxygen fugacity calculated by (1.12) requires the ferric iron content of spinel to be measured in order to determine the activity of the Fe_3O_4 component. $Fe^{3+}/\sum Fe$ of natural spinel ranges between 15 and 34 wt.%, while in the other phases, particularly olivine, the ferric iron concentration is negligible (Canil and O'Neill, 1996). As shown in figure 1.4, the oxygen fugacity of spinel-bearing xenoliths covers a range between -3 and +2 log units with respect to the FMQ buffer. This wide range reflects in part the heterogeneity of the mantle likely resulting from different processes, such as partial melting or contamination by metasomatic agents. However, it appears that there is also a link to the geological settings with xenoliths from subduction zones being more oxidized as a result of the high activity of water-bearing fluids perhaps, while the most reducing fo_2 are recorded by the abyssal peridotites, which are a residue of significant mantle melting (Frost and McCammon, 2008).

Spinel peridotite rocks record pressures corresponding to depths between 30 and 60 km. Knowledge of the mantle redox state at deeper conditions requires measurements on garnet-bearing peridotites, which are mainly found as xenoliths in kimberlites (Luth et al., 1990). The oxygen fugacity of garnet peridotites can be determined using the equilibrium calibrated by Gudmundsson and Wood (1995),

$$\underset{\text{garnet}}{2Fe_3Fe_2^{3+}Si_3O_{12}} = \underset{\text{olivine}}{4Fe_2SiO_4} + \underset{\text{opx}}{2FeSiO_3} + O_2 \qquad (1.13)$$

where the oxygen fugacity is,

$$\log fo_2 = \frac{-\Delta G_r^o}{\ln(10)RT} + 2\log a_{Fe_3Fe_2Si_3O_{12}}^{Gt} - 2\log a_{FeSiO_3}^{Opx} - 4\log a_{Fe_2SiO_4}^{olivine} \quad (1.14)$$

The volume change of equilibrium (1.13) is positive, which means that increasing pressure stabilizes the $Fe_3Fe_2^{3+}Si_3O_{12}$ skiagitic garnet (Gudmundsson and Wood, 1995; Woodland and Peltonen, 1999). As a consequence, the fo_2 will tend to drop with pressure, as shown in figure 1.5 (Frost and McCammon, 2008). This basic trend, which originates from the volume change, has been observed in mantle xenoliths from diamondiferous localities such as Kapvaal and Slave Craton with the conclusion that, the cratonic lithosphere falls mostly into the diamond stability field (Woodland and Koch, 2003; McCammon and Kopylova, 2004).

Calculations by Frost and McCammon (2008) provide a model (shown as the red line in figure 1.5) for the mantle fo_2 profile with depth for a fixed bulk composition and assuming a fixed $Fe^{3+}/\sum Fe$ ratio of 0.03 (BSE, McDonough and Sun, 1995). The profile is calculated along a continental geotherm and predicts the depth at which the lowest plausible mantle oxygen fugacity is reached, the so-called nickel precipitation curve (O'Neill and Wall, 1987). Although cratonic xenoliths show that there is a pressure effect on the fo_2 of garnet peridotite rocks, this is not related to composition but simply arises from the volume change of the ferric/ferrous equilibria (1.13). This means that, likely, the same pressure effect should operate in the asthenosphere, which is in general made out of the same mineral phases as many cratonic xenoliths, such as PHN1611 (Nixon and Boyd, 1973). This change of fo_2 with depth implies that the valence of heterovalent elements other than Fe most likely changes as regions of oceanic mantle undergo adiabatic decompression.

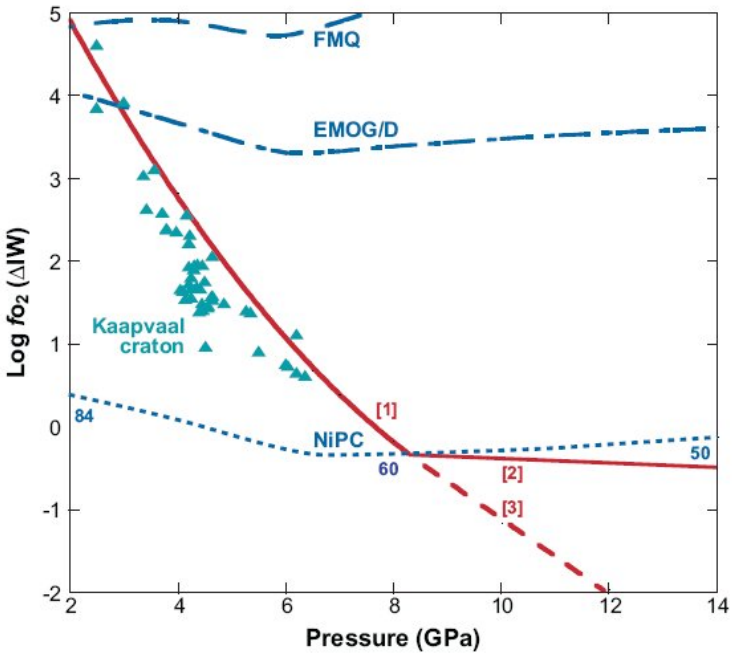

Figure 1.5 The diagram from Frost and McCammon (2008) shows the oxygen fugacity (red line) calculated for a four-phase garnet peridotite assemblage along a cratonic geotherm relative to the IW buffer. The fo_2 of the Ni precipitation curve (NiPC) is also shown for a peridotite assemblage with indicated values for the metal Ni content expressed in mol % (blue numbers) of the precipitating metal. Line 1 is the fo_2 calculated for garnet peridotite using Equation 1.6. Line 2 is the fo_2 calculated for a garnet peridotite assemblage once the NiPC curve is crossed and Ni-Fe metal forms. Line 3 is a metastable extrapolation of the fo_2 calculated using equation 1.14 when no metal precipitation is assumed. The FMQ buffer is by O'Neill and Wall (1987), while the EMOG/D buffer is by Eggler and Baker (1982).

1.5 The speciation of carbon as a function of redox state

The concentration and residence time of carbon in the mantle will depend on the form that it will take as a function of pressure, temperature and redox conditions of the interior. Redox conditions will control whether carbon exists in reduced elemental form (graphite or diamond) or as oxidized carbonate or CO_2-bearing species. In the form of diamond and graphite carbon is relatively immobile and can reside in the interior of the Earth for millions to billions of years (Holloway, 1998). However, oxidation to carbonate can promote the formation of magmas even at depths far below those where the dry mantle solidus is encountered, which can erupt to the surface, therefore mobilizing and removing carbon from the mantle. The amount of carbon removed by melting of rocks depends not only on the

depth at which this takes place (McKenzie, 1984) but, also on the solubility of CO_2 relative to the melt composition. Several studies have proposed that mid-ocean ridge basalts may originate from graphite-saturated mantle (Blundy et al., 1991; Holloway, 1998) at oxygen fugacity conditions described by the coexistence of graphite and CO_2 species.

In the pure C-O system the oxidation of graphite or diamond to pure CO_2 is described by the reaction,

$$C + O_2 = CO_2 \qquad (1.15).$$

This equilibrium is described by the acronym GCO or DCO if diamond is the stable carbon phase (Frost and Wood, 1997a). GCO is a buffering assemblage when the gas phase is pure CO_2. Graphite and diamond can only be stable at a fo_2 below this buffer. However, in the C-O-H system in equilibrium with graphite the fo_2 depends on the fluid composition. Figure 1.6a, shows the speciation of fluids in equilibrium with graphite or diamond as a function of depth following the fo_2 profile shown in figure 1.5 determined for the upper mantle. It can be observed that at low pressure where more oxidised conditions prevail the concentration of carbon dioxide in the fluid is dominant but as the mantle becomes more reducing H_2O and CH_4 fluids become dominant. Taylor and Green (1988) proposed that the more oxidised fluid compositions were likely to lower the melting temperature of mantle rocks to a greater extent than the reduced component CH_4. They argued that oxidation of CH_4 and C in the mantle due to adiabatic up welling and the increase in the fo_2 would cause the on set of melting, which they termed redox melting. In reality figure 1.6a is unlikely to reflect the real mantle because it ignores the reaction of CO_2 with mantle rocks to produced carbonates as shown in figure 1.6b.

The coexistence of graphite (diamond) and carbonate with mantle silicates in a peridotite assemblage is buffered by equilibrium (1.3) and

$$\underset{\text{opx}}{MgSiO_3} + \underset{\text{magnesite}}{MgCO_3} = \underset{\text{olivine}}{Mg_2SiO_4} + \underset{\text{graph/diam}}{C} + O_2 \qquad (1.16).$$

While equilibrium (1.16) is representative of a harzburgite assemblage, equilibrium (1.3) defines the fo_2 at which carbon and carbonate coexist with mantle silicates in a Ca-bearing (lherzolitic) peridotite assemblage (Luth, 1993). Both equilibria were calibrated by Eggler and Baker (1982) based on a set of thermodynamic data for each pure phase. These potentially buffering equilibria are calculated at 1200 °C and plotted as a function of pressure in figure 1.6b. One important issue is that equilibria involving solid carbonate are only applicable at temperatures within the stability field of a subsolidus assemblage for a carbonated peridotite. Above the melting temperature of a carbonated peridotite or harzburgite (classification given by Carter, 1970) the fo_2 will not be buffered by equilibria (1.3) or (1.16). Thermodynamic data are difficult to determine for liquid carbonate phases, the composition of which is sensitive to the temperature, particularly at temperatures where silicates start to dissolve in the initially carbonate melt. However, knowledge of the equilibrium fo_2 between reduced carbon and melts is required in order to better understand possible redox melting mechanisms and processes responsible for diamond formation (see figure 1.5). In addition carbonate-rich melts such as carbonatite or kimberlite can only originate from more oxidised sources than this fo_2. At pressures compatible with the transition zone and the lower mantle, diamond is observed to be the stable carbon phase. However, there are evidences for the presence of carbonate, either liquid (Walter et al., 2008) or solid (Brenker et al., 2007), as inclusion in natural diamonds, which would suggest oxygen fugacities at these depths are

close to those buffered by equilibrium similar to (1.16) involving high-pressure polymorphs of opx and olivine.

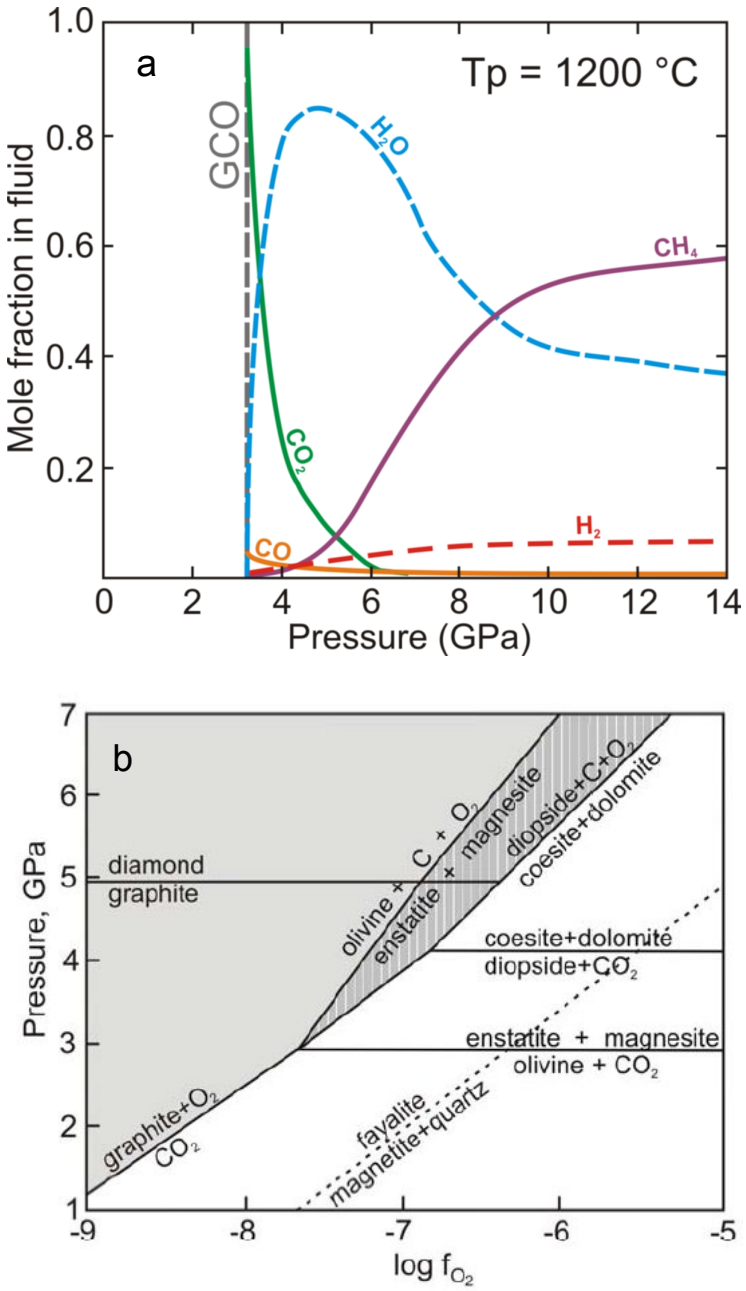

Figure 1.6 a) The speciation of the C-O-H fluid phase in equilibrium with graphite/diamond calculated as a function of pressure in the upper mantle along an adiabat with a potential temperature of 1200 °C and at an assumed fo_2 as in Figure 1.5. Vertical dark line indicates the oxygen fugacity corresponding to the CCO. b) The graph shows the location of buffering equilibria concerning the stability of C-bearing phases in the mantle on a pressure-log fo_2 projection at 1200 °C (after Luth, 1993). Shaded region represents P-fo_2 space where graphite and diamond are stable. Dark gray area corresponds to the conditions at which diamond is stable in eclogitic mantle but carbonate in peridotitic assemblage.

1.6 Aims of this study

The aim of this work was to establish the fo_2 of the carbon/carbonate equilibria as a function of pressure and temperature in synthetic mantle assemblages. Experiments were performed to provide important explanations both for the origin of CO_2-rich magmas and for the deep carbon cycle in the Earth's interior. Recent determinations of the solidus of carbonated peridotite and eclogite rocks argue for the possible origin of carbonate liquids at pressures well below those suggested by previous studies (Dasgupta and Hirschmann, 2006) and compatible even with the top of the lower mantle (Ghosh et al., 2009; Litasov et al., 2009, 2010). These studies, however, ignore that the stability of carbonate melts will also depend on the oxygen fugacity. Melting of carbonate can only occur once the oxygen fugacity is high enough in the mantle to ensure oxidation of diamond or graphite. In contrast, in this thesis melting phase relations and oxygen fugacity are considered in the determination of where carbonate-bearing melts might form in mantle assemblages. The origin of rare magmas such as carbonatitic and kimberlitic melts are examined with relation to the redox conditions of the mantle (Chapter 3).

Many studies have argued that the oxygen fugacity of the deep mantle may be more reduced than that of the upper mantle due to the increase in solubility of ferric iron in dominant deep-mantle silicates like garnet, wadsleyite, ringwoodite and magnesium silicate perovskite which, in turn, cause the precipitation of metallic Fe-Ni alloy at depths over ~200 km. Carbonate minerals such as magnesite have been shown to be stable to pressures and temperatures compatible with the lower mantle (Kraft et al., 1991; Biellman et al., 1993; Isshiki et al., 2004; Ono et al., 2005-2007). Further, studies of natural diamonds have revealed the occurrence of carbonate phases as inclusions, which likely have formed in the transition zone and lower mantle (Brecker et al., 2007; Walter et al., 2008; Kaminsky et al., 2009; Bulanova et al., 2010). However, there are no experimental data collected through which to assess the oxygen fugacity at which carbonate minerals would be reduced at such high pressure. The aim of this

study is also to determine the oxygen fugacity at which magnesite will be reduced to diamond in the transition zone and lower mantle. A comparison of this oxygen fugacity with the plausible oxygen fugacity of the mantle is also discussed based on ferric iron measurements in typical mantle silicates equilibrated with carbon and carbonate with important implications for the redox state of the mantle (Chapter 4). The oxygen fugacity constrained in these experiments also allowed a test of a widely used garnet-bearing oxybarometer to be made at pressures much higher than previously performed (Chapter 5).

Finally, the more frequent occurrence of diamonds in eclogite xenoliths than in peridotite xenoliths is still debated and may imply the possibility for carbonate to be reduced to carbon as a result of the pressure effect on equilibria involving mineral phases in eclogitic settings, such as garnet and clinopyroxene. While a number of experimental studies have been designed to examine the effect of pressure on the redox state of peridotitic mantle, very little attention has been paid to similar effects in eclogitic mantle applicable to subducting oceanic crust. This would be a key step in the cycling of carbon in the Earth. In this study the redox state of carbon/carbonate equilibria in eclogitic rocks was examined. These results might be used to assess the stability of carbonates in subducting slabs and to determine an oxygen thermobarometer for eclogitic rocks (Chapter 6).

2. Methods

2.1 High-Pressure experiments

The data discussed in this thesis represent the results of high pressure and temperature experiments performed using multianvil presses and piston cylinder devices. In multianvil experiments two stages of anvils are used to focus a force of up to 1200 tonnes, generated by a hydraulic press on a relatively small volume occupied by a ceramic high-pressure octahedral assembly. A sample is placed inside the assembly within a cylindrical resistance heater. In this study the sample was enclosed in a graphite capsule, wrapped by a metal foil (rhenium). Details and descriptions of this technique can be found in Kawai and Endo (1970), Walker (1991), Rubie et al. (1993) and Keppler and Frost (2005).

The pressure medium is usually made of MgO doped with 5 wt. % Cr_2O_3 and contains a hole filled with a zirconia sleeve as a thermal insulator and a heater (generally $LaCrO_3$ or graphite). A set of eight corner-truncated tungsten carbide cubes (first-stage anvils) is used to compress the pressure medium and pyrophyllite gaskets are glued on to the edges of each truncation. This set of cubes is then compressed by six outer tool-steel anvils (second stage), which are driven by a hydraulic press in a uniaxial direction. A sketch of the employed pressure cell in this study is presented in Figure 2.1. In this study, presses capable of producing loads of 500, 1000 and 1200 tonnes have been used to generate pressures up to 25 GPa, corresponding to pressures in the upper part of the Earth's lower mantle.

A range of pressures between 3 and 25 GPa was reached using different OEL (octahedron edge length)/TEL (truncation edge length) that imply a different sample volume. The 25/17 and 18/11 pressure cells were used in the 500 tonnes Voggenreiter press, which employs a Walker type module (Walker et al. 1990). These cell configurations employed stepped $LaCrO_3$ heaters to minimize thermal gradients. The capsule dimension in these pressure cells is 4 mm and 2 mm in outer diameter, respectively, and up to 3.5 mm in length.

For experiments at pressures corresponding to the Earth's transition zone (16 GPa) a 14/8 pressure cell with a stepped $LaCrO_3$ heater and capsule of 1.6 mm diameter was used. Finally, pressures of 24-25 GPa were reached using a smaller configuration with the 10/4 assembly and with a straight $LaCrO_3$ heater and ZrO_2 thermal insulation. In this case capsules were 1 mm in diameter and 1.4 mm in length.

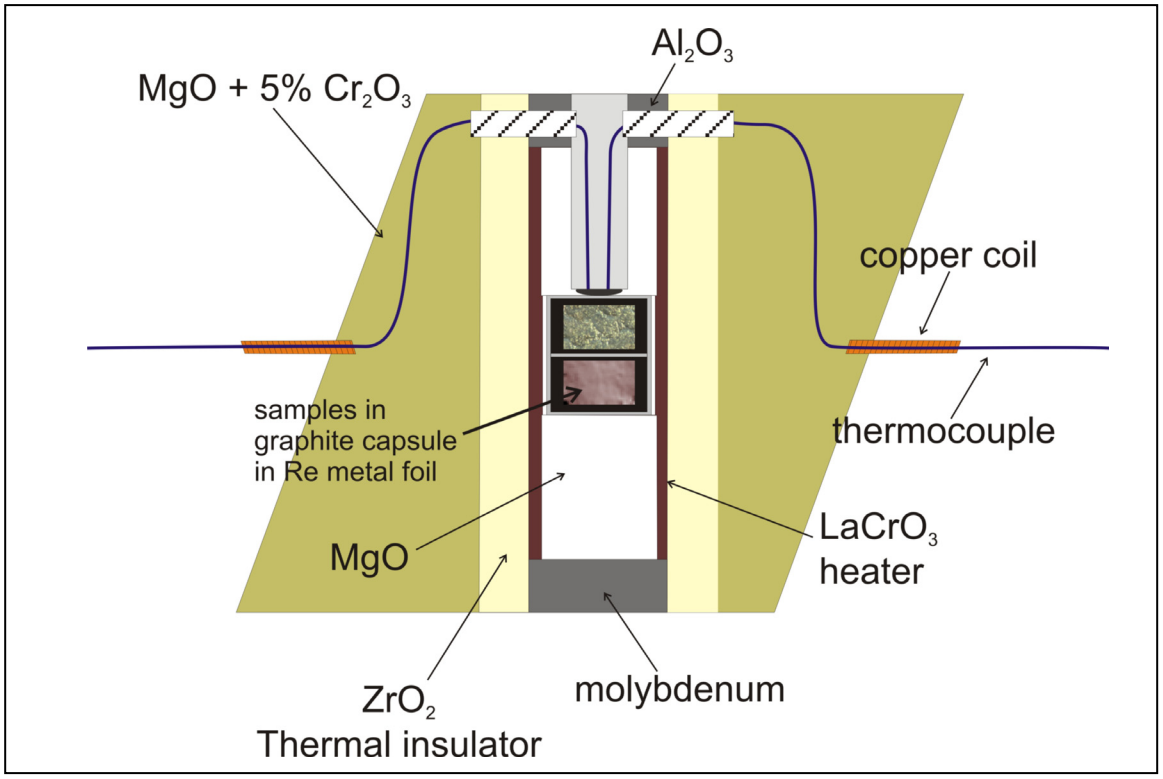

Figure 2.1 Schematic cross-section (not at scale) of a modified pressure cell for multi-anvil experiments (18/11 assembly) employing two capsules simultaneously.

For the aim of this study all experiments were carried out with graphite capsules filled with powdered starting materials and wrapped by Re foil (25 μm thick foil). This was done in order both to maintain the desired redox conditions during each run and to avoid loss of iron. Further, the graphite capsule acted as a trap for the escaping liquid produced during melting experiments. Figure 2.2 shows experiments that demonstrate the mobile character of CO_2-rich melts through graphite.

Therefore, a Re disk was use to isolate the two assemblages simultaneously employed in the same run. Further, rhenium appeared to be an extremely chemically inert material when in contact with liquids.

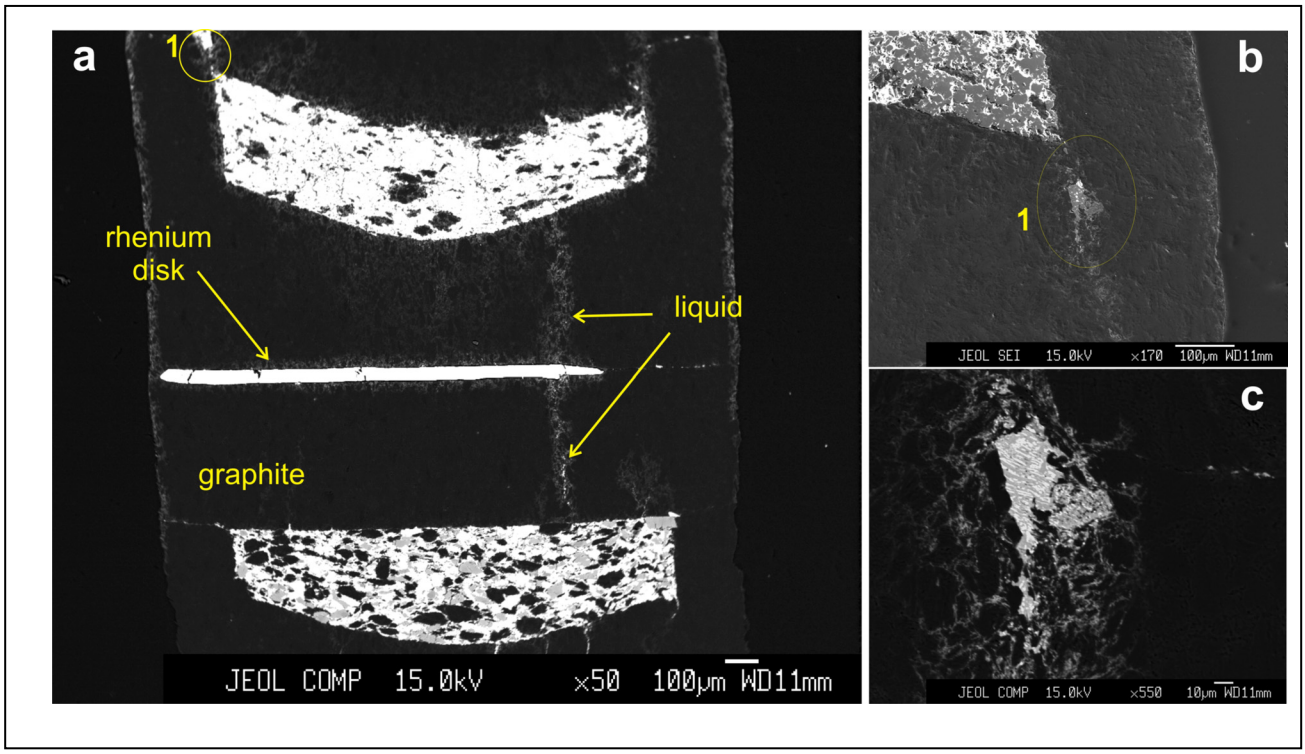

Figure 2.2 (a) Back scattered electron image, showing two different peridotite assemblages (Ca-bearing at the top and Ca-free at the bottom) separated by a Re disk in 25/17 assembly. Arrows indicate the migrating liquid through the graphite capsule like in 1. (b) and (c) are zoomed area showing the trapped melt phase (a CO_2-rich liquid) between grains of graphite.

Temperatures in all assemblies were measured using an axially inserted W97%Re3%-W75%Re25% thermocouple (D-type). In cases where the thermocouple broke during the compression stage or became unstable during heating, the experimental temperature was estimated from the electrical power to the furnace based on its linear relationship with temperature and compared with other experiments performed on the same pressure cells. The effects of the uncertainty due to temperature and pressure on the oxygen fugacity measurements are discussed in detail in the next chapters.

During this study it was also possible to perform experiments at pressure and temperature conditions of the Earth's mid lower mantle (~1200 km in depth) using a DIA-type multianvil guide

block system at the Geodynamic Research Center (Ehime, Japan). The advantage of the MADONNA press is that the displacements of all the six anvils can be measured and the differential ram pressures can be controlled with the main ram load. Therefore, higher pressures as well as a homogenous and stable hydrostatic regime are reached during compression. High-pressure cell assemblies were optimised for use with sintered diamond anvils and employed an MgO pressure medium doped with 5 wt. % chromium with fired pyrophyllite gaskets (Tange et al., 2008). High temperatures were reached using a cylindrical $LaCrO_3$ furnace (see figure 2.3).

Temperature was measured with a conventional D-type thermocouple in contact with the bottom of the graphite capsule. After quenching, a long decompression time (30 hours) was employed in order to prevent breakage of the sintered diamond anvils. Details of the pressure calibration are discussed in chapter 4.

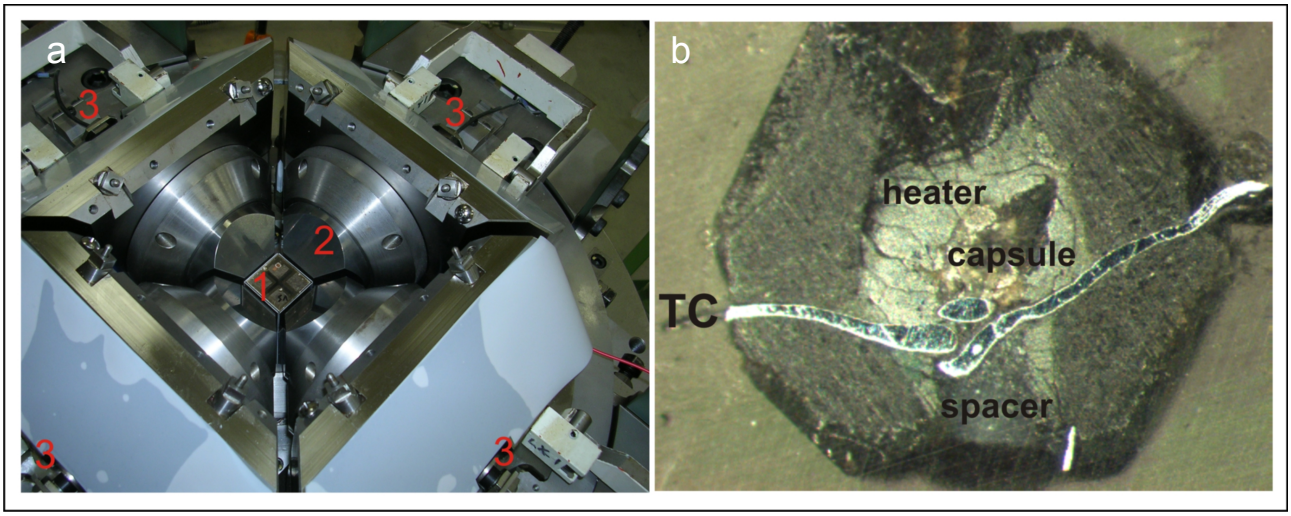

Figure 2.3 (a) Image showing technical details of the D-DIA Madonna press with the first anvil stage (1) represented by a set of eight sintered diamond cubes and the second stage (2) made by four WC anvils. 3 indicate the four sensors capable to reveal the displacement of the anvils during compression and decompression. (b) Image at optical microscope by reflected light showing a cross section of the cell employed for experiments at 45 GPa. The capsule is graphite transformed to diamond during the run.

Finally, experiments were also performed at pressures below 3 GPa using a piston cylinder device with a modified cell configuration with a stepped furnace, as in figure 2.4. The piston-cylinder apparatus (Boyd and England, 1960) available at Bayerisches Geoinstitut consists of two hydraulic rams, one to provide a confining end load and the other to advance a piston into the high-pressure chamber. Pressure is applied to the sample by pumping oil into a bridge, which advances a tungsten carbide piston. The sample, which is inside a soft pressure assembly, is compressed by the piston in an enclosed bomb consisting of a tungsten carbide core with a hole of either 3/4 (pressure to 15 kbar) or 1/2 (pressure to ~40 kbar) inches in diameter. The core is surrounded by several press-fit hardened steel rings first and then by a soft steel safety ring in the outermost part, to prevent explosive fracture of the inner rings. A retaining plate is placed on the top of the bomb and contains a central hole to allow access of the thermocouple into the sample volume of the underlying bomb. An overlying spacer is used to fill the gap between the thermocouple plate and the upper (end-loading) ram. Cooling-water pipes are then connected between these parts.

The pressure medium is a cylindrical sleeve made of either talc, NaCl or $BaCO_3$, while the heater is graphite. A Pyrex sleeve is placed between the pressure medium and the heater and acts as a thermal insulator. Finally, a steel plug is placed on top of the assembly to complete the heating circuit. The plug is electrically isolated from the out side of the core by a pyrophyllite sleeve.

The nominal pressure of an experiment might be calculated by $(R_{large}/R_{small})^2$, where R_{large} is the radius of the part of the ram upon which the oil acts and R_{small} is the radius of the piston applying force to the sample. However, due to the stress produced by all the cell components, a certain amount of friction would occur which needs to be taken into account and estimated by experimental pressure calibration using phase transitions (kyanite-sillimanite or quartz-coesite).

Experimental details concerning this study are further discussed in chapter 3.

All the recovered run products were mounted in epoxy resin and then ground and polished for analytical investigations using ethanol to preserve the carbonate phases (solid and melt). In the case of graphite containers employed at P> 6 GPa, the capsule material transformed to diamond. The preparation of suitable samples for analytical investigations required the use of diamond polishing plates.

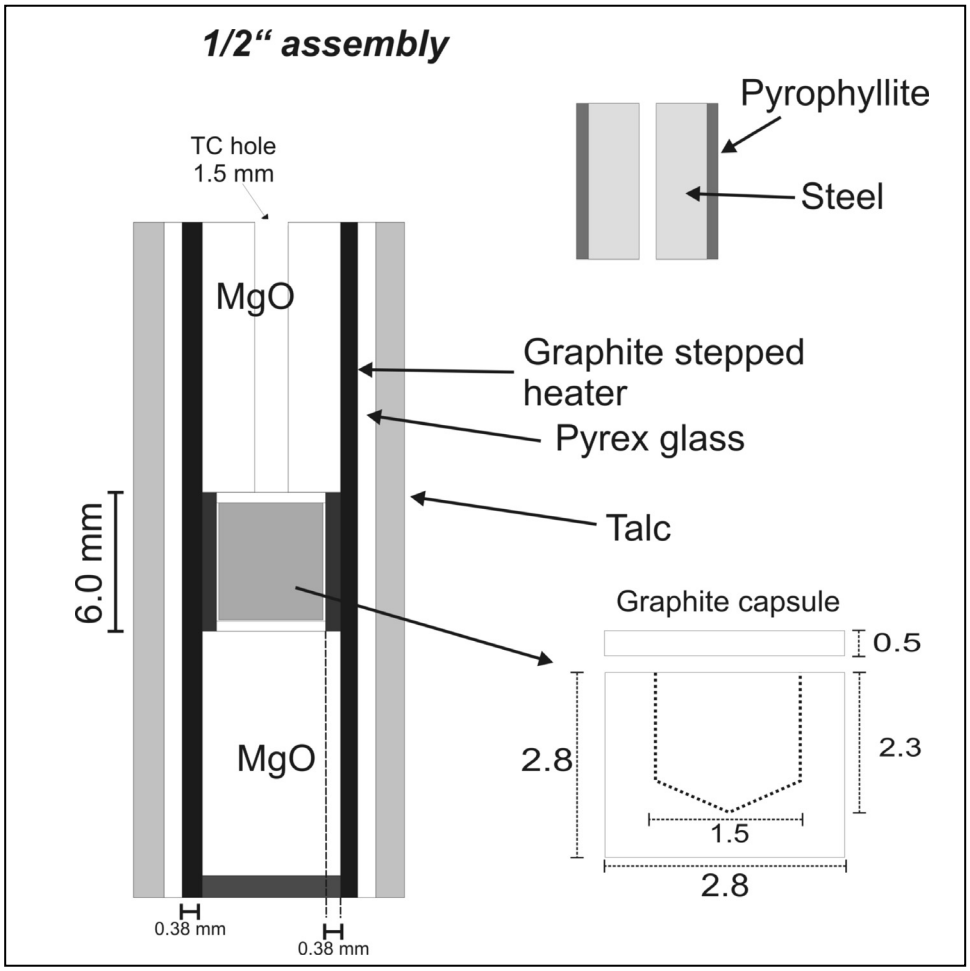

Figure 2.4 Schematic cross section of a modified piston cylinder assembly used in this study to perform experiments at pressure below 3 GPa.

2.2 Analytical techniques

2.2.1 Electron microprobe analysis

Major and minor element concentrations of coexisting phases were determined using a five-spectrometer Jeol JXA 8200 microprobe. In this technique a focused electron beam generated by a tungsten hairpin filament is accelerated on to the sample to be analysed. Electrons penetrate a volume of the sample whereby the incident higher energy electrons displace the inner shell electrons of the constituent atoms of the specimen and, therefore, cause characteristic X-rays emissions when electrons from the outer shell fall back to fill the inner shell vacancies created by the bombardment. Characteristic X-rays are then analysed by crystal spectrometers (wavelength dispersive mode). A detailed explanation to this analytical technique is given by Reed (2005).

Run products recovered from experiments were polished and then coated with a 10 nm thick carbon layer to avoid electrical charging of the surfaces. Analyses were performed using an acceleration voltage of 15 kV and variable beam currents and diameters depending on the investigated phases. Details are given in each experimental paragraph of the following chapters. The following synthetic minerals and oxides were used as standards: Si: enstatite; Mg: forsterite; Al: spinel; Ca: wollastonite; Fe, Ni, Re and Ir: pure metals; Cr: Cr_2O_3; Ti: rutile; Na: albite; C: vitrified carbon. During this study major elements were detected with the following spectrometers: TAP (thallium acid phthalate), PETH (pentaerythritol), LIF (lithium fluoride) and LDE2 (layered dispersion element).

The use of carbon as a standard was required in order to measure any possible concentration within the iridium-iron alloy redox sensor (chapter 3-4), which might affect measurements of fo_2. These measurements were performed employing industrial steel with known carbon content (0.8 wt. %) as a second standard to verify the accuracy of the standard calibration. In this case, no carbon coating was employed on the samples but copper tape was used to ensure the conductivity of the specimen and

prevent charging under electron bombardment. A complete table with the compositions of coexisting phases and liquids is provided within each chapter, with further tables of analyses in the appendix.

2.2.2 Scanning electron microscopy

In this fairly standard technique an electron beam is scanned across a specimen generating secondary electrons, back-scattered electrons and auger electrons. In case of the secondary electrons, they are emitted from the near-surface atoms of the sample so that, a quick three-dimensional image of the selected area can be quickly obtained. Further, the morphology of the sample causes the contrast in the image. X-rays are also generated in this process as the electron beam interacts with atoms of the sample causing transitions in the electron shells. The emitted X-rays with characteristic energies are measured in terms of energy spectrum (EDX) rather than wavelength (WDS) and this allows a qualitative analysis (Reed, 2005).

This technique was used in this study for a qualitative determination of the mineral composition in the run products and to obtain information on the textural indications for the attainment of equilibrium. With this aim secondary electron images were acquired which showed topographic features of the sample inside the capsule mounted in epoxy resin or simply on a stub using carbon tape such as in figure 2.5. Energy dispersive X-ray analyses were also performed to identify major elements of the minerals. SEM analyses were performed using a LEO Gemini 1530 equipped with a Schottky emitter.

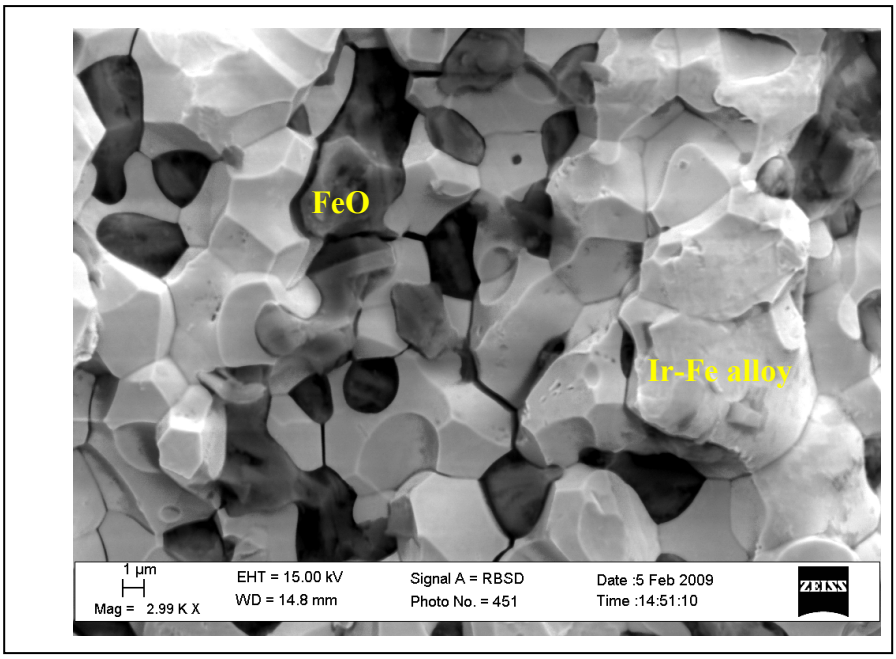

Figure 2.5 SEM image showing crystals of $Ir_{0.85}Fe_{0.25}$ alloy (bright) coexisting with FeO (dark) at high resolution. The edge-effect is also visible as consisting of bright contours where more secondary electrons can escape.

2.2.3 Raman spectroscopy

This technique is based on the inelastic scattering of light known as the Raman effect. A light that interacts with a specimen excites the constituent molecules. As a result the light is scattered with a different wavelength. This inelastically scattered light is the Raman scatter, which results from the changed molecular motions of the sample. The difference in energy between the incident light and Raman scattered light is equal to the energy absorbed by the scattering molecule and will be characteristic of a molecule and its environment in a specimen. By plotting the energy difference and the intensity of scattered light we obtain a Raman spectrum (Nasdala et al., 2004).

In the present study a LABRAM Raman spectrometer with a He-Ne laser with the 632 nm red line excitation was used to verify the presence of diamond relative to graphite as function of pressure (Kennedy and Kennedy, 1979) and to identify other high pressure silicate polymorphs. Raman spectra

were collected at ambient temperature with an instrumental resolution of 1 cm^{-1} for the peak positions. The obtained spectra were compared to the RUFF database (Downs, 2006) for mineral identification.

2.2.4 Mössbauer spectroscopy

The determination of the iron oxidation state in garnets equilibrated with carbon and carbonate-bearing mantle assemblages was a key topic of this study to better understand the conditions at which carbon oxidizes to carbonate and infer the likely redox profile applicable to the Earth's mantle (see chapter 5). The $Fe^{3+}/\sum Fe$ ratio in garnets recovered from high-pressure experiments was, therefore, investigated using Mössbauer spectroscopy.

This technique employs monochromatic γ (gamma) radiation with an energy of 14.41 keV provided by a conventional radioactive ^{57}Co source with a half-life of 270 days. The gamma rays interact with the sample (absorber), as they pass through it due to resonant vibration of the nuclei in the sample material. The source is moved relative to the sample by a certain velocity in order to shift the energy of the emitted γ radiation based on the Doppler effect, which maintains a constant resonance. A detector is then placed behind the sample that records the count rate as a function of source velocity (mm/sec) as resonance absorption takes place (figure 2.6). The resulting spectrum provides information on two important spectral parameters: the isomer shift δ_0 (or chemical shift) and the quadrupole splitting, which are strictly dependent on the valence state, spin state and coordination of the absorber atoms (figure 2.7).

In the specific case of iron, its electronic configuration is characterized by a filled [Ar]-like core ($1s^2 2s^2 2p^6 3s^2 3p^6$) with six 3d electrons that partially fill the five 3d orbitals plus two electrons in the 4s orbital ($[Ar]3d^6 4s^2$), which are removed to form iron atoms with a different oxidation state. Therefore,

ferrous iron Fe^{2+} will be represented by an electronic configuration such as $[Ar]3d^6$, while the ferric iron Fe^{3+} will have a $[Ar]3d^5$ configuration.

The 3d orbitals in a solid crystal structure will be characterized by an energy that can be either lower (t_{2g} orbitals) or higher energy (e_g orbitals) and associated to the occupancy of the electrons.

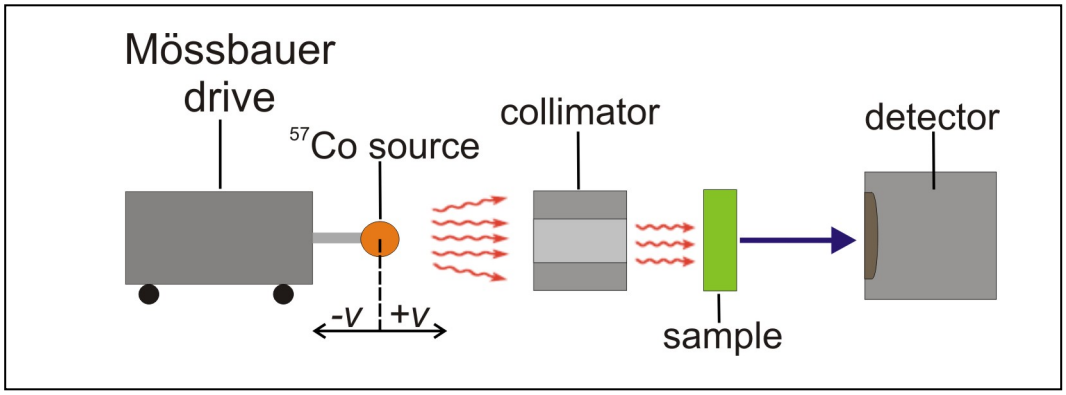

Figura 2.6 Typical geometry used in this study for measurements in transmission mode on a constant acceleration Mössbauer spectrometer (Bancroft, 1973) and with the sample placed between a ^{57}Co source and the detector.

The interaction between electrons and nuclei (hyperfine interaction) can affect the re-distribution of electron energy levels (shifted and split apart) and depends on a number of factors, including the number of electrons (Fe^0, Fe^{2+}, Fe^{3+}), the number of coordinating anions and the symmetry of the site. Transitions between split-levels will result in more complex absorption spectra than the single-line pattern (figure 2.8). Therefore, a typical Mössbauer spectrum will consist of sets of peaks (usually doublets and sextets) with hyperfine parameters corresponding to an iron nucleus in a specific environment in the sample (figure 2.7).

In this study samples were always double polished to account for about 5 mg Fe/cm^2 absorber thickness and avoid saturation effects. Mössbauer spectra were recorded at room temperature (298 K) in transmission mode on a constant acceleration Mössbauer spectrometer. The velocity scale was calibrated at 5 mm/s relative to 25 μm α-Fe foil using the positions certified for National Bureau of Standards for the outer lines of α-Fe obtained at room temperature. Spectra were fitted using a

Lorentzian curve (figure 2.9). More details concerning how the spectra were fitted are discussed in chapters 4 and 5.

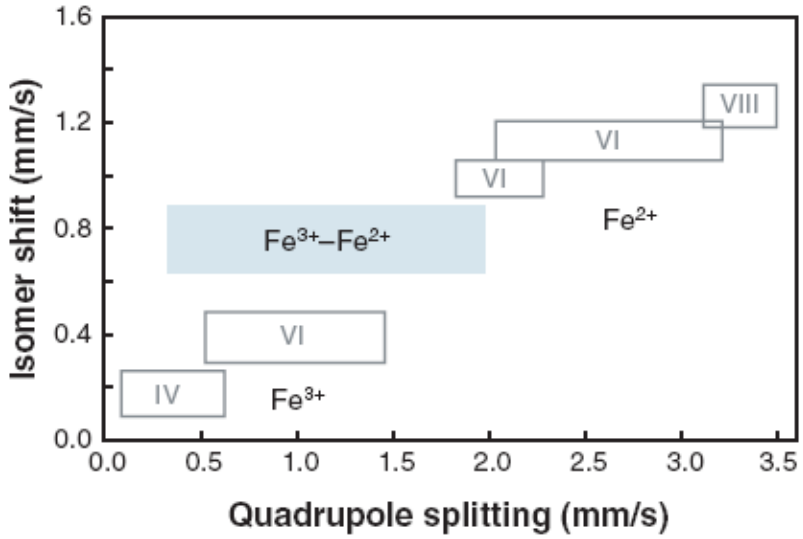

Figura 2.7 Room temperature isomer shift versus quadrupole splitting data for common rock-forming minerals, taken from Burns and Solberg (1988) and Dyar et al. (2006). The highlighted boxes indicate typical range of values used to infer valence state and coordination number of Fe atoms in minerals from the hyperfine parameters (from Dyar et al., 2006).

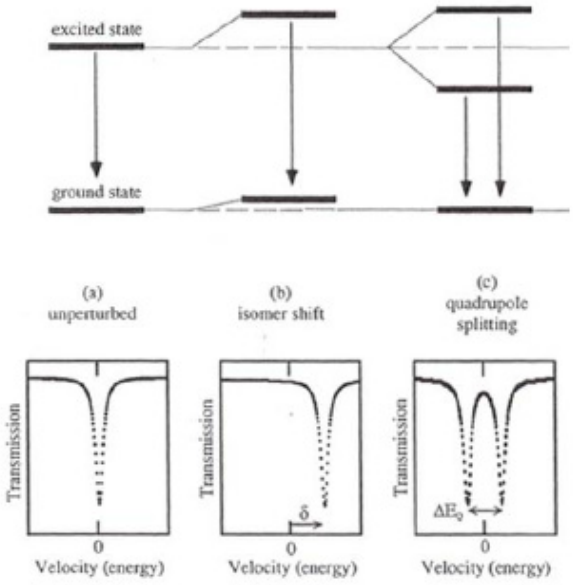

Figura 2.8 Mössbauer spectra illustrate the hyperfine parameters isomer shift and quadrupole splitting resulting from the above nuclear energy level diagram (McCammon, 2000).

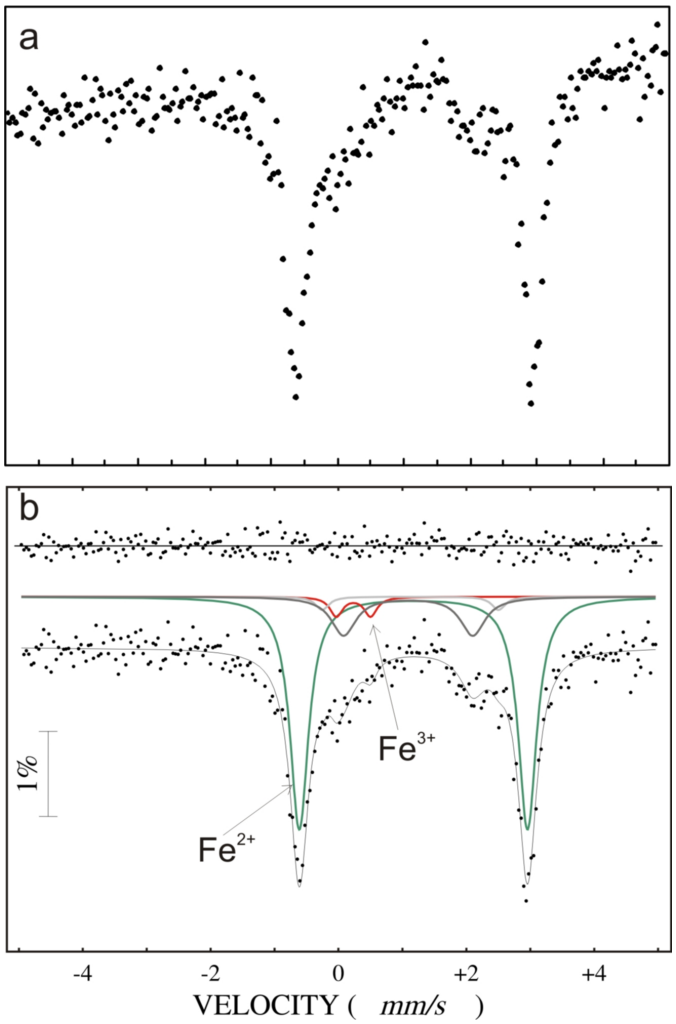

Figure 2.9 a) Shown is a typical experimental raw spectrum collected over 512 channels. Peaks indicate the presence of iron in the sample. b) Same spectrum as a) after fitting using Lorentzian curves. Doublets correspond to ferric iron in garnet (red), ferrous iron in garnet (green), opx (light gray) and olivine (dark gray).

2.2.5 Focused Ion Beam

This technique allows micron-sized wafers, referred to as foils, of material to be cut from an experimental sample in order that it can be thinned for transmission electron microscope examination. This was particularly useful in this study as traditional thin sections for TEM milling are impossible to produce from samples that contain diamond, as in the experiments recovered from 45 GPa, described in

chapter 4. Sample wafers can be cut under constant observation by SEM. The recovered wafers can be easily manipulated and secured inside the device, which prevents sample loss.

A solid gallium source is heated to its melting point (29.8 °C) producing a liquid, which flows to the tip of a tungsten needle and is held by surface tension. A strong electric field (108 V/cm) applied to the end of the tungsten tip causes the liquid Ga to form a point source of ions approximately 2-5 nm in diameter. The Ga ions are accelerated in an electrical field (up to 30 keV) to the target sample material from which atoms are sputtered. A continuous flow of liquid Ga to the tip replaces the extracted Ga^+ ions resulting in a constant ion current.

The bombardment results in a number of interactions of the ions with the target material, which is associated with energy loss of the ions. For instance, inelastic scattering of the incident Ga^+ ions with the target material produces secondary electrons used for imaging by collecting the electrons with a continuous dynode electron multiplier detector. However, semiconductor or insulator materials require a thin coating with a conducting material (e.g., carbon, gold) prior to FIB milling to enhance the observation by secondary electrons.

A thin protective layer (1-2 μm) of platinum is deposited onto a selected rectangular area of interest where the foil is to be cut. The platinum deposition is performed by decomposing an organic Pt-gas (Trimethyl-Platinum used for chemical vapor deposition). The aim of applying a platinum layer is to protect the foil from being sputtered by the Ga^+ ion beam, particularly during the final stage of the preparation sequence when the foil thickness is of the order of 100 nm.

After completion of the sputtering process the sample is then tilted at about 45° with respect to the ion beam and the foil is cut on both sides and at the bottom to allow lifting-out. Lift-out of the foil from its excavation site is performed using an internal manipulator inside the Dual Beam FIB/SEM device with a fixed tungsten tip. After touching the foil with the tip, the foil is attached by depositing platinum, lifted out and transferred to a special TEM grid, where it is also fixed by Pt deposition. After

attaching the foil to the grid, the connection of the tungsten tip with the foil is released using the ion beam. A standard TEM foil has typical dimensions of 15x10x0.150 μm with a final thickness of approximately 80-100 nm. QUANTA 3D FEG focused ion beam was used in this study (see chapter 4). Details about the preparation are shown in figure 2.10.

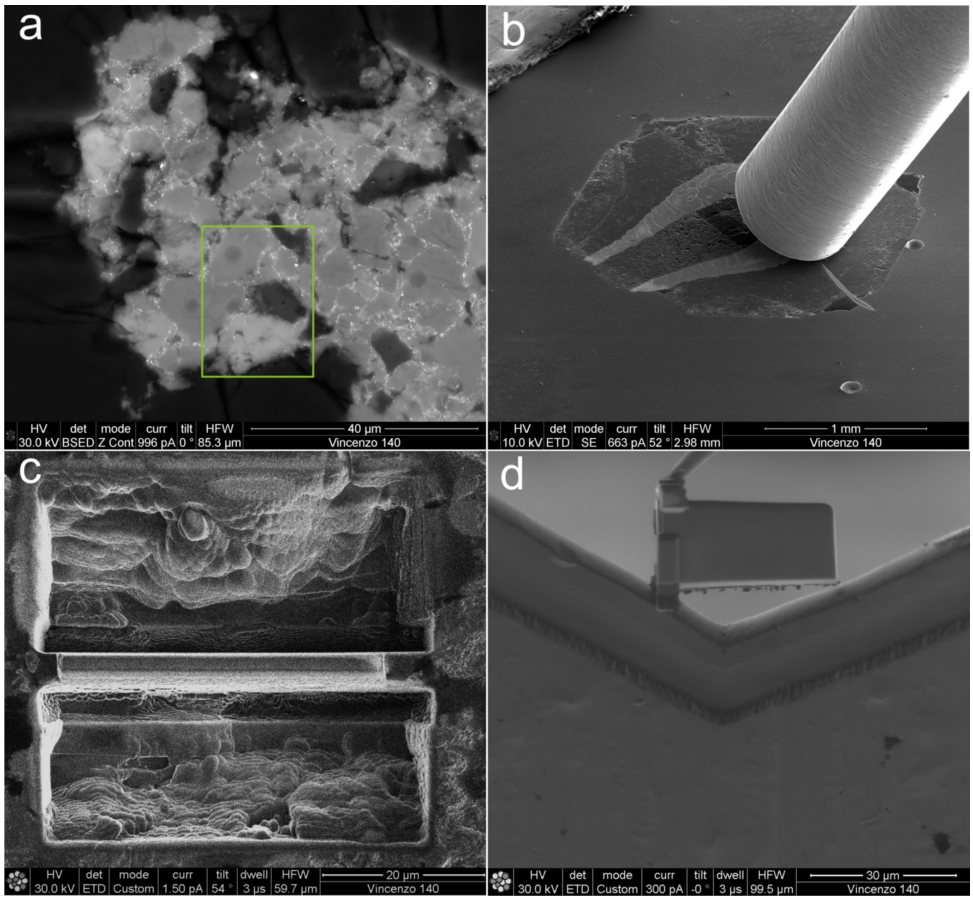

Figure 2.10 (a) Selected area to be milled by focused ion beam on the recovered run from 45 GPa and 1700 °C. b) SE image of the Pt deposition on the selected area. c) SE image of the platinum strip deposited on the surface with the two pits formed during milling. d) SE image of the foil welded by Pt deposition to the TEM grid after being lifted out and ready for final polishing.

2.2.6 Electron Energy Loss Spectroscopy

This technique is based on the analysis of the energies of the transmitted electrons that have inelastically interacted with the specimen. The loss of energy between the incident electrons and the

inelastically scattered electrons depends on the interaction process. In particular, measurement of characteristic energy loss in the transmitted electron beam after electron interactions with the sample provides information on the coordination of cations, the bonding types and the valence states of elements owing to the high energy resolution at the scale of eV.

In this project, the FIB assisted the preparation of samples for TEM analysis for the study of the iron valence state using EELS (Electron Energy-Loss Spectroscopy) in a perovskite sample recovered from 45 GPa and 1700 °C.

The ferric to total iron ratio was determined following the procedure described by van Aken et al. (2002). It requires the integration over two energy windows of the L_3 and L_2 ionisation edges of iron. The intensity ratio of the L_3 and L_2 ionisation edge yields the ferric to total iron ratio. ELNES spectra were collected using an energy-loss spectrometer (Gatan PEELS 666). Depending on the ferric iron content, the obtained ELNES spectra show a strong double peak at 707.8 eV and 709.5 eV energy loss, which represents the ferrous and ferric iron maxima at the FeL_3-edge, respectively. The peak shape of the FeL_3-edge changes according to the relative abundance of ferric and ferrous iron, i.e. an equal ratio of Fe^{2+} and Fe^{3+} results in two equal peaks of the FeL_3-edge.

Experimental details are reported in chapter 4.

2.3 Control of the oxygen fugacity during experiments

Oxygen fugacity in experimental studies is controlled mainly following two approaches: the first is based on the use of solid mineral or metal oxide assemblages that buffer the oxygen fugacity at certain know values (see chapter 1, section 1.4); the second approach employs metals as sliding redox sensors to measure the oxygen fugacity from the recovered run at a given pressure and temperature.

In detail, the different techniques can be summarized as follow:

a) double capsules where an outer capsule contains a metal oxide buffer and H_2O and an inner capsule contains the sample plus H_2O. A Pt inner capsule ensures permeability of H_2 between the buffering outer capsule and the inner. By fixing the f_{H2} in the outer capsule the fo_2 of the inner is fixed (Eugster, 1957; Ulmer and Luth, 1991; Bromiley et al., 2004);

b) metal capsules such as Fe or Re have been shown to influence the redox state of samples (McCammon and Ross, 2003);

c) buffering assemblages such as Re and ReO_2 can be added to the sample powder (Rubie, 1999);

d) sliding redox sensors where the fo_2 is measured although not fixed by the redox sensor which normally comprises an Fe-noble metal alloy (Taylor et al., 1992; Woodland and O'Neill., 1997).

A mixture of gases is generally employed in experiments at one atmosphere to oxidize or reduce the employed solid assemblage (Deines et al., 1974); the required redox conditions are imposed at a given temperature by changing the ratio between the gases employed, such as hydrogen, carbon dioxide or carbon monoxide. This is a quite well known technique that has been used either to synthesize minerals with a certain Fe^{3+}/Fe^{2+} ratio or to conduct room pressure experiments at controlled atmosphere. Gas mixing furnaces have been also employed for solid-electrolyte double-cell techniques to measure the

oxygen fugacity of natural rocks, such as the Layered Skaergaard intrusions containing graphite (Sato and Valenza, 1980).

In this study, we measured the oxygen fugacity at which carbon and carbonates (solid or melts) coexist. The experimental approach to deal with this important thermodynamic variable is accurately described in previous papers (Eugster, 1957; Taylor et al., 1992**;** Frost and Wood, 1997; Woodland and O'Neill, 1997) and it is mainly based on the use of metal-metal oxide reactions or noble metal alloys (PGE, Au and Ag) as sliding redox sensors. Both cases involve the use of double capsules that are made of different materials in order to control the fo_2. In our experiments, the oxygen fugacity was internally fixed by the coexistence of carbon and solid carbonates as shown in the equilibria (1.3) and (1.16) described in chapter 1. Measurements of the fo_2 were made by adding 5 wt. % of pure iridium metal as a redox sensor to the starting material. During the experiments metallic iron (contained in the phase assemblage) is reduced and alloys with the Ir metal to shift the oxygen fugacity of the Fe and FeO bearing equilibrium to that imposed by the presence of carbonate melt and graphite (or diamond). The amount of Fe alloying with Ir depends on the oxygen fugacity (figure 2.11a by Borisov and Palme, 2000). The resultant lowering of the activity of the Ir metal component is consequence of the redox conditions imposed by the carbon-carbonate equilibrium as function of pressure and temperature and the evolving melt composition, and displaces the equilibria (1.3) and (1.16) to more oxidizing or reducing conditions, respectively. An equation is derived to calculate the oxygen fugacity, as fully explained in the next chapter:

$$\log fo_2 = \frac{-\Delta G^{\circ}_{r}}{\ln(10)RT} + \log a^{Ol}_{Fe_2SiO_4} - \log a_{SiO_2} - 2\log a^{metal}_{Fe} \qquad (2.1)$$

The activity of Fe in the alloy was derived from the composition by electron microprobe with the activity-composition relations of (γ)Fe-Ir from literature data by Swartzendruber (1984). In principle, many noble metals might be used as a redox sensor as long as their solid solution with Fe is well defined in terms of temperature and pressure (at least at 1 bar) and the activity-composition relations for the binary systems are known. In this study, the Ir-Fe system was preferred to both Pt-Fe (Gudmundsson and Holloway, 1993) and Pd-Fe since the binary T-X diagram is well known and only one phase (γ-fcc) is stable over a large temperature range (figure 2.11b). The solubility of Re (chosen as outer capsule material) and C in Ir was regularly tested and found to be negligible. This is a remarkable aspect to take into account since the accuracy of the sensor is largely dependent on the reliability of activity-composition relations in the binary system.

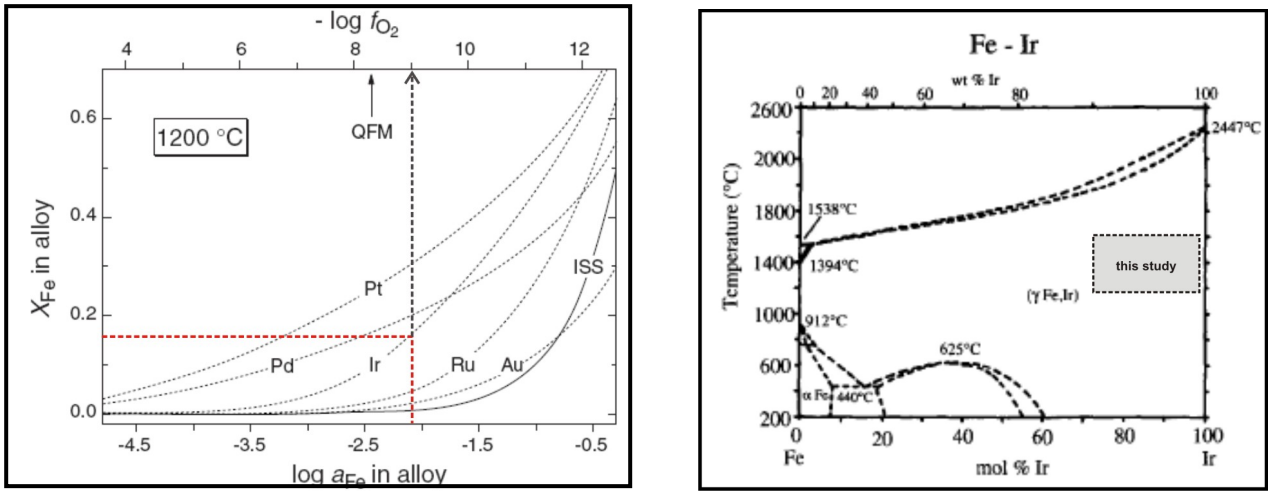

Figure 2.11 a) Composition of alloys plotted as function of the oxygen fugacity at 1200 °C by Borisov and Palme (2000) modified. The XFe vs. log aFe plot is referred to AuFe, PdFe, IrFe (red dotted line), RuFe, and PtFe alloys. b) Phase diagram for the Fe-Ir system at 1 bar by Swartzendruber (1984) modified. The grey square indicates the range in temperature and composition approached in this study.

3. Carbon speciation in the asthenosphere: experimental measurements of the redox conditions at which carbonate-bearing melts coexist with graphite or diamond in peridotite assemblages

3.1 Introduction

The residence time of carbon in the mantle and its flux both into and out of the interior will depend crucially on the conditions under which it partitions into mobile melts or fluids, compared with conditions under which it forms solid mineral phases. Numerous studies have been performed to understand decarbonation and the onset of melting in CO_2-bearing mantle rocks (Dalton and Wood, 1993; Dalton and Presnall, 1998a; Gudfinnsson and Presnall, 2005; Dasgupta and Hirschmann, 2006) with a view to understanding the speciation of carbon in the mantle. A carbonated peridotite in the simplified CMAS+CO_2 system will produce carbonate melts at pressures above 2 GPa, and temperatures close to approximately 1200 °C, where dolomite is the solidus carbonate (Wyllie and Huang, 1976). At higher temperatures the silicate content of these melts increases and they evolve towards silicate liquids (Dalton and Presnall, 1998b; Moore and Wood, 1998; Gudfinnsson and Presnall, 2005; Dasgupta et al., 2007; Brey et al., 2008). Studies have examined the melting of carbonated mantle assemblages at conditions up to 32 GPa (Ghosh et al., 2009; Litasov and Ohtani, 2009) and numerous studies have examined the stability of carbonate mineral structures up to deep lower mantle conditions (e.g. Biellmann et al., 1993). However, both oxidised and reduced forms of carbon are known to exist in the mantle (Pearson et al., 1989; Pearson et al., 1994; Ionov et al., 1996) but very little attention has been paid to the redox stability of oxidised carbonate minerals and melts with respect to reduced diamond and graphite (Luth, 1993; Dalton and Wood 1995). In the Mg-Si-O-C system the equilibrium between the carbonate mineral magnesite ($MgCO_3$) and graphite or diamond in a mantle assemblage is,

$$\underset{\text{enstatite}}{MgSiO_3} + \underset{\text{magnesite}}{MgCO_3} = \underset{\text{olivine}}{Mg_2SiO_4} + \underset{\text{graph/diam}}{C} + O_2 \qquad (3.1),$$

which takes the acronym EMOG (EMOD in the diamond stability field). At a given pressure and temperature, this equilibrium defines a fixed oxygen fugacity above which carbonates become stable. Eggler and Baker (1982) determined that the oxygen fugacity buffered by this equilibrium is approximately 1 log unit below the fayalite magnetite quartz (FMQ) oxygen buffer at 2.9 GPa.

In mantle lherzolite assemblages at pressures below 4 GPa, dolomite will be the stable carbonate phase at temperatures below the solidus and the governing carbonate-carbon reaction will therefore be,

$$\underset{\text{enstatite}}{2Mg_2Si_2O_6} + \underset{\text{dolomite}}{CaMg(CO_3)_2} = \underset{\text{diopside}}{CaMgSi_2O_6} + \underset{\text{olivine}}{2Mg_2SiO_4} + \underset{\text{graph/diam}}{2C} + 2O_2 \qquad (3.2),$$

which buffers fo_2 at a value very close to the EMOG buffer (Luth, 1993). Along an adiabat compatible with mantle up welling beneath a mid oceanic ridge, temperatures are most likely above the carbonated-peridotite solidus at depths shallower than 300 km (Dasgupta and Hirschmann, 2006). The governing redox equilibrium just above the carbonated peridotite solidus is most likely similar to equation (3.2), i.e.:

$$\underset{\text{opx}}{2Mg_2Si_2O_6} + \underset{\text{melt}}{(Ca,Mg)(CO_3)_2} = \underset{\text{cpx}}{CaMgSi_2O_6} + \underset{\text{olivine}}{2Mg_2SiO_4} + \underset{\text{graph/diam}}{2C} + 2O_2 \qquad (3.3),$$

although the stoichiometry of the reaction will change depending on the Ca/Mg ratio of the melt. With increasing temperature, or decreasing pressure along an adiabat, increasing degrees of melting will dilute the carbonate component of the melt with silicates (e.g. Dasgupta et al., 2007), thus influencing the fo_2 of equilibrium (3.3), and, as described later, leading to more reducing conditions where carbonate-bearing melt may coexist with diamond or graphite. The fo_2 buffered by equation (3.3) will therefore be a function of the carbonate-bearing melt composition. No experimental data currently exist through which to assess the fo_2 behaviour of such an equilibrium involving carbonate-bearing melt.

It has been suggested that small-degree carbonate-rich melts are the first liquids produced during adiabatic mantle up welling beneath mid-ocean ridges (McKenzie, 1985). Unlike hydrogen, carbon has a vanishingly small solubility in mantle silicate minerals (Shcheka et al., 2006) and can, therefore, form small degree melts, in principle, once the carbonated mantle solidus is crossed. Such melts may scavenge trace elements from deeper, and therefore larger, portions of the mantle than are affected by the main phase of basalt genesis. Recently, Dasgupta and Hirschmann (2006) argued that carbonate melts would be formed in up welling magnesite-bearing peridotite at 300 km although based on plausible carbon contents for the mantle melt fractions would likely be less than 0.02 wt. %. Several lines of geophysical evidence support the presence of melts at depths between 200 and 300 km beneath ridges based on seismic anisotropy (Evans et al., 1999; Dunn et al., 2001; Gu et al., 2005) and electrical conductivity measurements near ridge axes (Baba et al., 2006; Gaillard et al., 2008).

Oxy-thermobarometry equilibria indicate that the mantle should become increasingly more reduced compared to the FMQ buffer with depth. If this is the case it is possible that the stable carbon host at 300 km is in fact diamond and that the onset of melting in the mantle is not marked by the carbonate peridotite solidus but by a redox reaction between diamond or graphite and ferric iron in the silicate assemble that forms carbonate-rich melt. This process, which has been termed redox melting (Taylor and Green, 1988), may be ubiquitous in the mantle.

We have performed multianvil experiments to determine the fo_2 at high pressure and temperature where elemental carbon coexists with carbonate melt. We have examined how this fo_2 varies with melt composition as the solidus carbonate melt evolves towards a silicate liquid with increasing temperature. The results combined with an assessment of the fo_2 of the mantle from oxy-thermobarometry allow us to constrain: 1) the diamond/graphite stability field in the upper mantle; 2) the minimum fo_2 at which carbonate-bearing melts (carbonatites or kimberlites) can form in the mantle; 3) the depth at which carbonate-bearing melts would be formed in adiabatically up welling

mantle as a result of redox melting; 4) the level to which the carbonate-melt component must be diluted for melts to be stable at particular mantle oxygen fugacities.

3.2 Experimental technique

Two starting materials were employed for the majority of the experiments. A simplified carbonated harzburgite in the system Fe-Mg-Si-O-C was assembled from a mineral mixture of San Carlos enstatite, synthetic magnesite, San Carlos olivine and pure graphite (EMOG1), in the molar ratio 3:2:1:1. A simplified lherzolite composition in the system Fe-Ca-Mg-Si-O-C was assembled from the same components as EMOG1 but with $CaSiO_3$ (glass) added in the same proportion as $MgCO_3$ to provide an assemblage that would produce both dolomite and diopside (EDDOG2).

In some experiments layers of either Ca-bearing or Ca-free glass of garnet composition were added to the experiments, sandwiched between layers of either the EDDOG2 or EMOG1 compositions respectively. $Py_{85}Alm_{15}$ and $Py_{79}Alm_{16}Gr_5$ composition glasses were prepared from dried high purity MgO, Al_2O_3, $CaCO_3$, Fe_2O_3 and SiO_2. After weighing the oxide mixture was ground under ethanol in an agate mortar. The dried mixture was placed into a platinum crucible and decarbonated by heating at a rate of 150 °C/hour to 1000 °C. The powder was then glassed by quenching rapidly from 1600 °C and then ground again to a powder. This process of melting, quenching and grinding was repeated a further 3 times to ensure homogeneity of the powdered sample.

Table 3.1 Experimental run conditions and products

Run no.	Comp.	P (GPa)	T (°C)	Time (hr)	phases						
H289a*	EDDOG2	2.5	1100	23	Ol	Opx	Cpx	G		Liq	vap
H298a*	EDDOG2	2.8	1265	24	Ol	Opx	Cpx	G		(Liq)	
V588a	EDDOG2	3	1100	24	Ol	Opx	Cpx	G	Dol		
V538a	EDDOG2	3	1200	24	Ol	Opx	Cpx	G		Liq	
V426a	EDDOG2	3	1250	24	Ol	Opx	Cpx	G		Liq	
V403a	EDDOG2	3	1300	24	Ol	Opx	Cpx	G		Liq	
V406a	EDDOG2	3	1350	24	Ol	Opx	Cpx	G		Liq	
V511a	EDDOG2	3	1400	24	Ol	Opx	Cpx	G		Liq	
V542a	EDDOG2	3	1400	12	Ol	Opx	Cpx	G		Liq	
V550a	EDDOG2	3	1400	6	Ol	Opx	Cpx	G		Liq	
V512a	EDDOG2	3	1450	24	Ol	Opx	Cpx	G		Liq	
V514a	EDDOG2	3	1500	4	Ol	Opx	Cpx	G		Liq	
V592a	EDDOG2	3	1500	24	Ol	Opx	Cpx	G		Liq	
V569a	EDDOG2	3	1550	24	Ol			G		Liq	
V587a	EDDOG2	3	1400	24	Ol	Opx	Cpx	G		Liq	Gnt
V538b	EMOG1	3	1200	24	Ol	Opx		G	Mst		
V496b	EMOG1	3	1250	24	Ol	Opx		G	Mst	Liq	
V406b	EMOG1	3	1350	24	Ol	Opx		G		Liq	
V511b	EMOG1	3	1400	24	Ol	Opx		G		Liq	
V514b	EMOG1	3	1500	24	Ol	Opx		G		Liq	
S4135a	EDDOG2	6	1240	12	Ol	Opx	Cpx	G/D	Mst	(Liq)	
V567a	EDDOG2	6	1285	12	Ol	Opx	Cpx	G/D	Mst	Liq	
V543a	EDDOG2	6	1300	12	Ol	Opx	Cpx	G/D		Liq	
V539a	EDDOG2	6	1350	12	Ol	Opx	Cpx	G/D		Liq	
V525a	EDDOG2	6	1450	12	Ol	Opx	Cpx	G/D		Liq	
V457a	EDDOG2	6	1500	24	Ol	Opx	Cpx	G/D		Liq	
V553a	EDDOG2	6	1560	2	Ol	Opx	Cpx	G/D		Liq	
V606a‡	EDDOG2	6	1150	23	Ol	Opx	Cpx	G/D	Mst		Gnt
V604a‡	EDDOG2	6	1300	11	Ol	Opx	Cpx	G/D		Liq	Gnt
V605a‡	EDDOG2	6	1450	12	Ol	Opx	Cpx	G/D		Liq	Gnt
V615a‡	EDDOG2	6	1200	12	Ol	Opx	Cpx	G/D	Mst		Gnt
V617a‡	EDDOG2	6	1400	16	Ol	Opx	Cpx	G/D		Liq	Gnt
V586a	*(+ FeS)*	6	1200	12	Ol	Opx	Cpx	G/D	Mst	Liq	Sulph
V578a	*(+ FeS)*	6	1400	12	Ol	Opx	Cpx	G/D		Liq	Sulph(liq)
V576a	*(+ P_2O_5)*	6	1350	12	Ol	Opx	Cpx	G/D		Liq	Apatite
V573a	*(+ P_2O_5)*	6	1400	12	Ol	Opx	Cpx	G/D		Liq	Apatite
V585a	*(+ NaCl)*	6	1400	12	Ol	Opx	Cpx	G/D		Liq	NaCl
V539b	EMOG1	6	1350	12	Ol	Opx		G/D	Mst		
V541b	EMOG1	6	1450	12	Ol	Opx		G/D	Mst	Liq	
V458a‡	EDDOG2	7	1350	12	Ol	Opx	Cpx	G/D	Mst	(Liq)	Gnt
V492a‡	EDDOG2	7	1400	12	Ol	Opx	Cpx	G/D		Liq	Gnt
V517a‡	EDDOG2	7	1500	12	Ol	Opx	Cpx	G/D		Liq	Gnt
V564a‡	EDDOG2	7	1600	12	Ol	Opx	Cpx	G/D		Liq	Gnt
S4402 ‡	*(+ H_2O)*	7	1400	6	Ol	Opx	Cpx	G/D		Liq	Gnt
H2759b‡	EMOG1	7	1400	12	Ol	Opx		G/D	Mst		Gnt
V493b‡	EMOG1	7	1400	12	Ol	Opx		G/D	Mst		Gnt
V524b‡	EMOG1	7	1500	12	Ol	Opx		G/D	Mst		Gnt
V565a‡	EDDOG2	11	1400	12	Ol	Cl-en	Cpx	D	Mst	(Liq)	Gnt
S4230a‡	EDDOG2	11	1500	12	Ol	Cl-en	Cpx	D		Liq	Gnt
S4232b‡	EMOG1	11	1500	12	Ol	Cl-en		D	Mst		Gnt

Notes: Ol olivine, Opx orthopyroxene, Cpx clinopyroxene, Cl-en clinoenstatite, Gnt garnet, G graphite, D diamond, Mst magnesite, Dol dolomite, Liq CO_2-bearing melt and Vap CO_2 vapour. Phases difficult to analyzed or inferred by textural evidence are in brackets. a and b suffixes after the run number arise from the fact that both EMOG1 or EDDOG2 compositions were run in separate capsules in the same experiment. * Piston cylinder runs.

‡ Experiments with a garnet layer sandwiched between assemblages of EMOG1 or EDDOG2 composition.

Table 3.2 Phase compositions and measured oxygen fugacities

	T (°C)	P (GPa)	XFe_{Ol}	XFe_{En}	XFe_{alloy}	XCO_2	logfO_2	residuals
EDDOG2								
H289a	1100	2.5	0.089(4)	0.078(4)	0.080	0.50	-8.85(3)	0.16
H298a	1265	2.8	0.071(4)	0.068(1)	0.088(5)	0.50	-7.26(12)	0.08
V588a	1100	3	0.092(5)	0.073(3)	0.083(2)	0.50	-8.64(7)	0.09
V538a	1200	3	0.080(2)	0.067(1)	0.095(4)	0.49	-7.83(8)	0.03
V426a	1250	3	0.090(3)	0.080(4)	0.105(4)	0.46	-7.37(8)	0.03
V403a	1300	3	0.084	0.072(1)	0.109(6)	0.44	-7.01(8)	0.01
V406a	1350	3	0.073(2)	0.075(2)	0.113(4)	0.43	-6.74(7)	0.08
V511a	1400	3	0.068(1)	0.063(2)	0.112(4)	0.28	-6.38(6)	0.11
V542a_12hr	1400	3	0.060(1)	0.049(1)	0.097(3)	0.28	-6.30(5)	-
V550a_6hr	1400	3	0.085(6)	0.065(4)	0.086(6)	0.35	-5.85(14)	-
V512a	1450	3	0.073(2)	0.064(5)	0.137(5)	0.24	-6.23(7)	0.00
V514a	1507	3	0.056(2)	0.057(5)	0.132(4)	0.17	-5.98(7)	0.05
V592a	1500	3	0.052(1)	0.050	0.142(6)	0.21	-6.20(8)	0.13
V569a	1550	3	0.038(1)	-	0.103(4)	0.15		-
V587a (*gnt layer)*	1400	3	0.083(1)	0.074(2)	0.094(5)	0.29	-5.98(8)	0.49
EMOG1								
V538b	1200	3	0.077(2)	0.071(5)	0.078(3)	0.50	-7.59(7)	0.10
V496b	1250	3	0.075(1)	0.070(1)	0.081(6)	0.44	-7.17(11)	0.05
V406b	1350	3	0.074(1)	0.068(2)	0.100(2)	0.40	-6.56(4)	0.16
V511b	1400	3	0.071(1)	0.061(1)	0.103(3)	0.31	-6.23(5)	0.07
V514b	1500	3	0.074(1)	0.068(5)	0.117(4)	0.26	-5.63(5)	0.04
EDDOG2								
S4135a	1240	6	0.094(2)	0.076(7)	0.076(2)	0.50	-5.75(4)	0.15
V567a	1285	6	0.093(4)	0.068(3)	0.081	0.46	-5.46(3)	0.16
V543a	1300	6	0.081(5)	0.065(4)	0.084(1)	0.45	-5.49(6)	0.03
V539a	1350	6	0.076(1)	0.052(1)	0.087(6)	0.48	-5.20(10)	0.03
V525a	1450	6	0.066(1)	0.056	0.102(2)	0.31	-4.79(4)	0.03
V457a	1500	6	0.061(1)	0.058	0.115(5)	0.23	-4.68(7)	0.06
V553a	1560	6	0.041(5)	0.033(4)	0.078(6)	0.17	-4.17(18)	-
V606a (*gnt layer*)	1150	6	0.097(2)	0.084(8)	0.098(5)	0.50	-6.90(8)	-
V604a (*gnt layer*)	1300	6	0.083(2)	0.075(3)	0.091(10)	0.49	-5.56(16)	0.07
V605a (*gnt layer*)	1400	6	0.094(2)	0.078(3)	0.113(7)	0.36	-4.98(10)	0.01
V615a (*gnt layer*)	1200	6	0.100(2)	0.082(6)	0.109(5)	0.50	-6.54(8)	-
V617a (*gnt layer)*	1400	6	0.084(1)	0.067(3)	0.097(6)	0.42	-4.87(9)	0.05
V586a (*sulph*)	1200	6	0.128(8)	0.122(10)	-	-	-	-
V578a (*sulph*)	1400	6	0.149(4)	0.114(7)	-	-	-	-
V585a (*NaCl*)	1400	6	0.045(5)	0.037(1)	0.109(4)	0.47	-5.55(14)	0.68
V576a(*P*)	1350	6	0.069(1)	0.067(5)	0.094(4)	0.49	-5.36(6)	0.20
V573a(*P*)	1400	6	0.060(1)	0.050(1)	0.098	0.25	-5.17(1)	0.03
EMOG1								
V539b	1350	6	0.083(3)	0.075(5)	0.075(4)	0.50	-4.92(9)	0.14
V541b	1450	6	0.060(1)	0.047(3)	0.078(4)	0.43	-4.54(7)	0.02
EDDOG2								
V458a	1350	7	0.091(6)	0.076(4)	0.083(4)	0.50	-4.60(11)	0.07
V492a	1400	7	0.087(1)	0.073(3)	0.094(3)	0.37	-4.43(5)	0.08
V517a	1500	7	0.086(1)	0.073(4)	0.096(5)	0.32	-3.81(7)	0.07
V564a	1600	7	0.067(1)	0.055(3)	0.087(2)	0.26	-3.33(4)	0.31
S4402a (+ H2O)	1400	7	0.081	0.057(3)	0.084(2)	0.45	-4.36(3)	0.06
EMOG1								
H2759b	1400	7	0.063(2)	0.063(4)	0.091(3)	0.50	-4.65(6)	0.30
V493b	1400	7	0.074(1)	0.063(2)	0.082(2)	0.50	-4.40(4)	0.05
V524b	1500	7	0.062(1)	0.055(1)	0.077(2)	0.50	-3.82(4)	0.02
EDDOG2								
V565a	1400	11	0.086(2)	0.073(4)	0.087(6)	0.50	-2.93(10)	0.42
S4230a	1500	11	0.080(3)	0.069(4)	0.093(6)	0.46	-2.50(11)	0.38
EMOG1								
S4232	1500	11	0.089(4)	0.078(9)	0.105(3)	0.50	-2.57(7)	0.28

Notes. *XFe* in opx and ol is the molar Fe/(Fe+Mg) ratio and in Ir-Fe alloy Fe/(Fe+Ir). XCO_2 is the mole fraction of CO_2 in the melt, set as 0.5 for solid carbonate. Log fO_2 is the value calculated using equation (3.6) with uncertainties propagated from the mineral and metal compositions. The residual is the difference between the experimental log fO_2 and that determined using equations (3.14) or (3.15).

The final glass was reduced in a controlled H_2-CO_2 atmosphere at 800 °C at an oxygen fugacity equivalent to the Ni-NiO oxygen buffer. Ten weight % of either the EDDOG2 or EMOG1 assemblage was mixed within the garnet layer to ensure equilibrium. All starting compositions were mixed with 5 wt. % pure iridium metal powder (≤ 5 μm) that acted as a sliding redox sensor. Starting powders were loaded into graphite containers that were enclosed in rhenium foil capsules. In many experiments two graphite containers with different mineral assemblages (labelled a and b in Table 3.1) were enclosed in the same Re capsule, separated by a Re disk.

Experiments were performed between 3 and 7 GPa in a 500-ton Walker- type multi anvil press, while a 1000-ton Kawai-type press was employed for experiments between 7 and 11 GPa. Tungsten carbide anvils of 11 mm truncation edge length (TEL) were used with standard 18 mm edge length Cr_2O_3-doped octahedra. The capsule was placed in the central portion of a stepped graphite or lanthanum chromite furnace, surrounded by an MgO sleeve and spacers. The temperature was monitored with a W97Re3–W75Re25 (D type) thermocouple inserted within an alumina sleeve, with the junction in contact with the top of the capsule. Pressure calibrations were performed using the phase transitions of quartz to coesite**,** $CaGeO_3$ garnet to perovskite and coesite to stishovite (Keppler and Frost, 2005). The temperature variation over the sample capsule was calibrated using the coexisting compositions of ortho and clinopyroxene (Brey et al., 1990), and found to be within 50 °C of the thermocouple temperature. Experiments were performed between 1100-1600 °C for periods of between 6 and 24 hours. The experiments were quenched by turning off the power to the furnace. Recovered samples were mounted in epoxy resin, sectioned and polished parallel to the axial furnace direction. Samples were polished under ethanol.

Two experiments at 2.5 and 2.8 GPa (H289 and H298) were performed in a piston-cylinder device at the Bayerisches Geoinstitut following the hot piston-out methodology (Johannes et al., 1971; Presnall et al., 1978). Experiments were performed in half-inch talc-Pyrex pressure cells and using stepped graphite heaters and porous MgO inserts. Graphite capsules were filled with the

EDDOG2 starting material and inserted into Au-Pd tubes that were welded at one end and crimped closed at the other. Pressure calibrations were performed using the plagioclase-spinel and spinel-garnet transitions in a peridotite bulk composition at the solidus in the CaO-MgO-Al_2O_3-SiO_2 system (Presnall et al., 1979; Milholland and Presnall, 1998). The plagioclase-spinel and spinel-garnet peridotite solidus transitions were located at 0.93 GPa/1305 °C and 2.95 GPa/1585 °C in agreement with Longhi (2005), which implied a friction correction of approximately 7%. Experimental temperatures were measured using type D thermocouple wires. Temperature was controlled to within ± 1 °C of the target temperature.

Textural observations of the recovered run products were performed using a scanning electron microscope; while the chemical compositions of liquid and mineral phases were obtained using a Jeol JXA-8200 electron microprobe equipped with five wavelength-dispersive spectrometers. An accelerating voltage of 15 kV and a beam current of 5-20 nA were employed; counting times varied between 20 and 10 s on peak and background (35 and 15 for Ir-Fe metal) with a focused electron beam for mineral phases and defocused beam (1-10 μm) for melt analysis. Standards were Fe and Ir metal, chromite, and natural silicates and the PRZ correction was applied. The concentration of CO_2 in carbonate melts was estimated from the deficit in the microprobe analysis totals. Raman spectroscopy was used to confirm the presence of diamond and clinoenstatite in some samples.

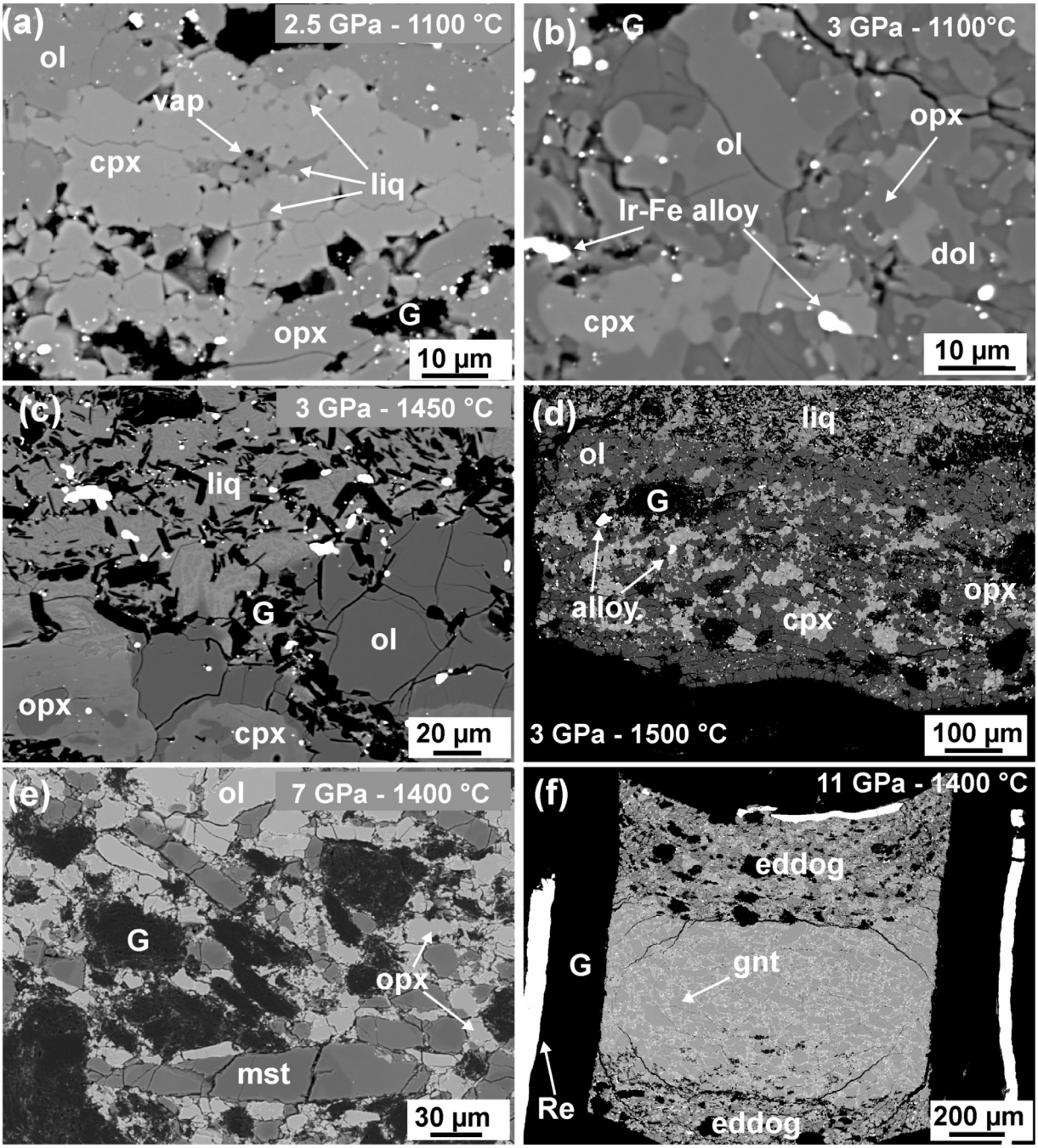

Figure 3.1 Back-scattered electron images of experimental run products, with run conditions indicated on each figure. **(a)** Run H289a: a small amount of interstitial carbonate-rich melt is present, possibly with vapour bubbles. **(b)** Run V588a is characterized by a subsolidus dolomite bearing assemblage. **(c)** Run V512a contains silica-bearing carbonate melt coexisting with graphite, olivine, cpx and opx. **(d)** Run V592a shows an upper pool of separated quenched carbonate-rich melt. **(e)** Run V493 a subsolidus magnesite bearing assemblage. **(f)** Run V565 contains a garnet layer sandwiched between fo_2 buffering assemblages of the EDDOG2 composition. Approximately 10 % of the EDDOG2 assemblage has also been mixed within the garnet layer to ensure equilibrium. The outer graphite and Re foil capsule can be seen. Abbreviations: Ol, olivine; Opx, orthopyroxene; Cpx, clinopyroxene; Gt, garnet; Liq, liquid; Vap, CO_2 vapor phase; Mst, magnesite; Dol, dolomite; G, graphite; Re, rhenium foil capsule.

3.3 Results

3.3.1 Phase relations and compositions

Experimental conditions and recovered phase assemblages are listed in Table 3.1. Average mineral Fe/(Fe+Mg) ratios and melt CO_2 contents are listed in Table 3.2. Full chemical analyses are given in Tables S3.1, S3.2 and S3.3 in the Appendix. Experiments performed on the Ca-bearing EDDOG2 composition contained olivine, orthopyroxene, clinopyroxene and either solid carbonate or melt, which evolved from being carbonate rich at low temperature to containing a significant silicate component at higher temperature. In addition, all experiments contained grains of graphite or diamond and Ir-Fe alloy dispersed throughout the charge. Partial melts segregated and formed analysable pools towards the top of the capsules. Melts quenched to a coarse intergrowth of silicate and carbonate phases (Fig. 3.1c-d), which could be analysed by increasing the diameter of the electron beam to a level larger than the dimensions of the quench crystals. The solidus at 3 GPa for the EDDOG2 composition was crossed between 1100 °C and 1200 °C where subsolidus dolomite broke down to produce SiO_2-poor CaO-rich carbonate melt of similar composition to that reported in previous studies (Dalton and Presnall, 1998b; Moore and Wood, 1998; Dasgupta et al., 2007). Between 1200 and 1350 °C the carbonate melt remained SiO_2-poor (<5 wt. %) but the MgO content increased at the expense of CaO. Between 1350 and 1550 °C the SiO_2 content of the melt increased from 4-34 wt. % and a silicate melt composition was approached at temperatures close to the carbonate free solidus. At 6 GPa magnesite occurred in the subsolidus assemblage and the solidus was crossed between 1240 and 1285 °C. Near solidus melt compositions were slightly higher in MgO than at 3 GPa, again inline with previous studies (Dalton and Presnall, 1998b; Dasgupta et al., 2007; Brey et al., 2008). Experiments at 7 and 11 GPa contained garnet layers sandwiched between EDDOG2 composition layers. At 7 GPa the solidus was crossed between 1350 and 1400 °C, while at 11 GPa melt was first observed at 1500 °C. Near-solidus melts at 11 GPa were CaO-poor.

Experiments using the Ca-free EMOG1 composition produced a similar phase assemblage but without clinopyroxene. Magnesite was the subsolidus carbonate and the solidus was crossed at temperatures approximately 50-100 °C higher than the EDDOG2 composition at 3 and 6 GPa. The SiO_2 content of melts in the EMOG1 composition is slightly higher than for EDDOG2 at a given temperature.

In figure 3.2a-c SiO_2 and CaO contents of melts are compared as a function of temperature with previous studies. Over the conditions investigated the compositions of near-solidus melts are similar to those determined by Dalton and Presnall (1998b) in the CMAS system and Brey et al. (2008), in natural complex systems. Similarly, the evolution in SiO_2 and CaO content of melts with temperature is very similar to that reported by Dasgupta and Hirschmann (2007) as is the Fe/(Fe+Mg+Ca) distribution coefficient (K_D) between melt and olivine (figure 3.2d). The distribution coefficient appears relatively pressure independent but is quite strongly dependent on composition. The only significant deviations are found in comparison to the study of Foley et al. (2009), most likely due to the additional presence of H_2O in this previous study.

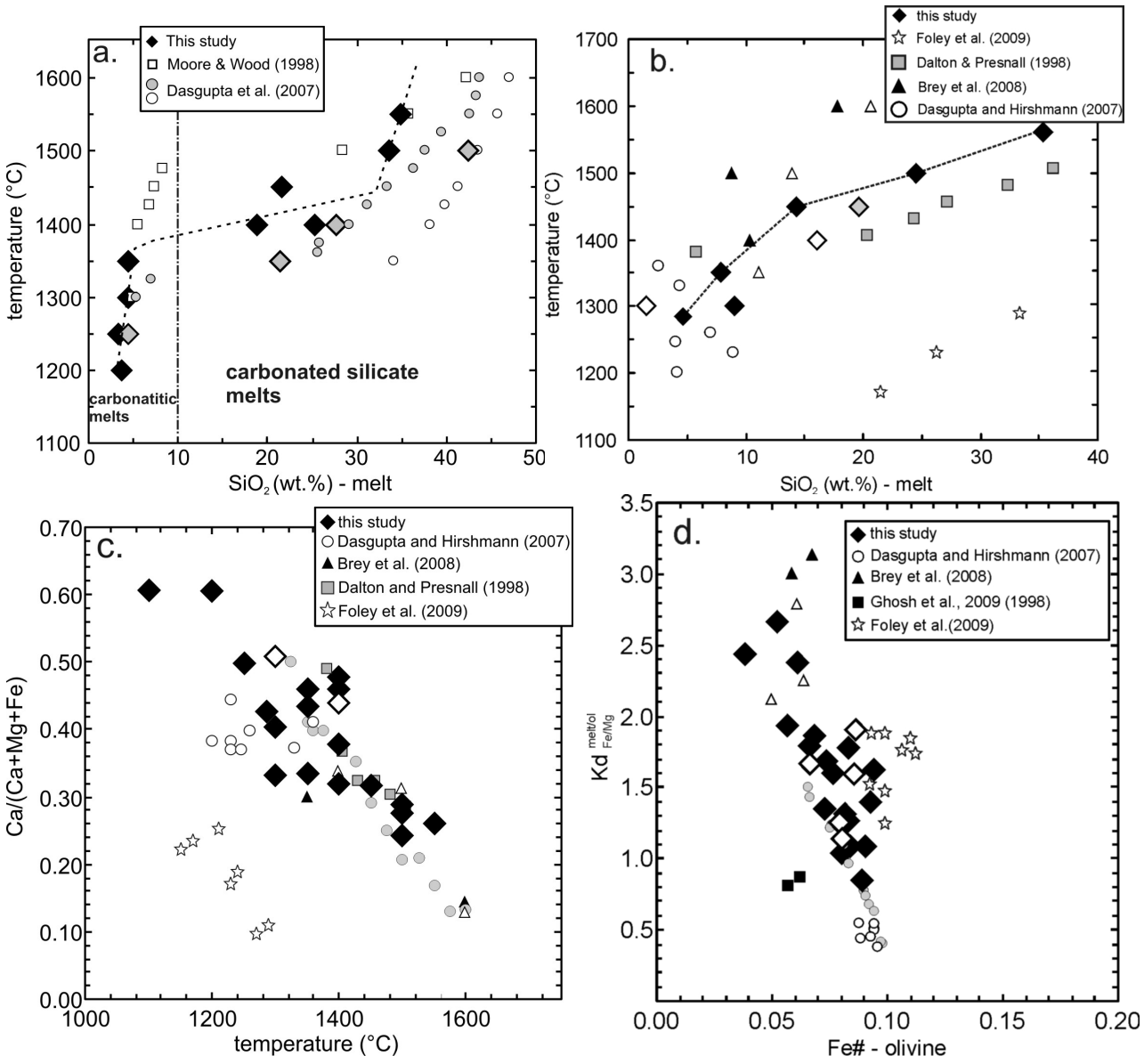

Figure 3.2 (a) Melt SiO_2 contents from experiments performed at 3 GPa as a function of temperature. Ca-free EMOG1 and Ca-bearing EDDOG2 assemblages are shown as grey and black diamonds respectively. Melt compositions from the studies of Dasgupta et al., (2007) (PERC, grey circles; PERC3, white circles) and Moore and Wood, (1998) are shown for comparison. **(b)** Melt compositions at 6 GPa symbols the same as in (a) with additional white diamonds indicating garnet-bearing runs (V604 and V605 in Table 3.1). Data are compared to previous studies on simplified (Dalton and Presnall, 1998) and natural systems (Dasgupta and Hirschman, 2007; Brey et al., 2008) and a study that also contains H_2O (Foley et al., 2009). Black and white triangles are different bulk compositions of Brey et al., (2008). **(c)** Calcium concentration in melts from this and previous studies between 2.5 and 6 GPa. Symbols as in previous figures. **(d)** The Fe-Mg distribution coefficient between melt in the Ca-bearing system and olivine is defined as $K_D=(X_{Fe(melt)}.X_{Mg(olivine)})/(X_{Fe(olivine)}.X_{Mg(melt)})$ where for example $X_{Fe(melt)}=Fe/(Fe+Mg+Ca)$. Black squares are from Ghosh et al. (2009) at 12.5 and 13.5 GPa.

3.3.2 Determination of oxygen fugacity

At pressures below approximately 2 GPa where CO_2 becomes increasingly insoluble in melts and carbonate minerals are unstable, the fo_2 will be constrained by the coexistence of graphite and a CO_2 vapour phase. At higher pressures the bulk compositions examined in this study were not CO_2-vapour saturated and carbon in the form of either graphite or diamond coexisted with either carbonate minerals, carbonate melts or melts that were transitional between carbonate liquids and silicate liquids. The oxygen fugacity was therefore buffered in each experiment by the coexistence of carbon and carbonate phases or melt species, which can be simply described by the equilibrium,

$$\underset{\text{graph/diam}}{C} + \underset{\text{mineral/melt}}{O^{2-}} + O_2 = \underset{\text{mineral/melt}}{CO_3^{2-}} \quad (3.4)$$

The oxygen fugacity was determined in each experiment by using Fe-Ir alloy as a sliding redox sensor (Taylor et al., 1992; Woodland and O'Neill, 1997; Borisov and Palme, 2000) and employing the equilibrium,

$$\underset{\text{olivine}}{Fe_2SiO_4} = SiO_2 + \underset{\text{alloy}}{2Fe} + O_2 \quad (3.5)$$

At equilibrium the oxygen fugacity is related to the activity of the various components and ΔG^0, the Gibbs free energy of the pure end-member equilibrium (3.5) i.e.

$$\log fo_2 = \frac{-\Delta G^\circ_{[3.5]}}{\ln(10)RT} + \log a^{Ol}_{Fe_2SiO_4} - \log a_{SiO_2} - 2\log a^{metal}_{Fe} \quad (3.6)$$

$a^{Ol}_{Fe_2SiO_4}$, a^{metal}_{Fe} and a_{SiO_2} are the activities of the olivine Fe_2SiO_4 component, Fe in Fe-Ir alloy and silica respectively. The silica activity is determined from the equilibrium,

$$\underset{\text{olivine}}{Mg_2SiO_4} + SiO_2 = \underset{\text{orthopyroxene}}{Mg_2Si_2O_6} \quad (3.7)$$

i.e.

$$\log a_{SiO_2} = \frac{\Delta G^\circ_{[3.7]}}{\ln(10)RT} + \log a^{orthopyroxene}_{Mg_2SiO_4} - \log a^{olivine}_{Mg_2SiO_4} \quad (3.8)$$

The ΔG^0 terms for equations (3.6) and (3.8) are determined at the P and T of interest from the thermodynamic and equation of state data given in Table 3. A Birch-Murnaghan equation of state is employed. $a^{Ol}_{Fe_2SiO_4}$ and $a^{Ol}_{Mg_2SiO_4}$ are $(X_{Fe}.\ \gamma_{Fe})^2$ and $(X_{Mg}.\ \gamma_{Mg})^2$ respectively where X_{Fe}=Fe/(Fe+Mg) and the activity coefficients for olivine (γ) are determined from,

$$RT\ln\gamma_a = W^{ol}(1-X_a)^2 \quad (3.9)$$

where W^{ol} is 2000 J/mol (Frost, 2003). The orthopyroxene solid solution is considered to be ideal, a safe assumption given that $Mg_2Si_2O_6$ is the dominant component. This is the main motivation for employing equilibrium (3.7) to determine the silica activity, rather than using the less well-constrained $Fe_2Si_2O_6$ component (O'Neill and Wall, 1987).

Table 3.3 End member thermodynamic data used for calculating oxygen fugacity

	Ref. T(K)	$\Delta_f H^\circ_{298}$ (Jmol^{-1})	H_T-H_{298} (Jmol^{-1})	S_T (JK^{-1}mol^{-1})	Heat Capacity (Cp) terms a	b	c	d	e	Source
Fe_2SiO_4 (Ol)	1000	-1477100	118432	349.23	176.0	-0.008808	-3.89E-06	0.00	2.47E-05	1
Fe (FCC)	1200	0	35543	76.91	24.0	0.008360	0		0	1
Mg_2SiO_4 (Ol)	298	-2173000		94.1	192.1	0.010848	-2.51E+06	-838	1.18E-06	2,3
$Mg_2Si_2O_6$ (Opx)	298	-3091200		133.5	356.2	-0.002990	-5.97E+05	-3185	0	2,3
O_2	298	0		205.15	48.3	-0.000691	4.99E+05	-421	0	1

	V (cm^{3}mol^{-1})	K_o(bar)	K'	dK/dT (barK^{-1})	α_0	α_1	α_2	
Fe_2SiO_4 (Ol)	46.31	1269000	5.25	-0.0281	2.39E-05	1.15E-08	-0.0518	4,5
Fe (FCC)	6.835	1653000	5.5	-0.0363	6.40E-05	0	0	5,6
Mg_2SiO_4 (Ol)	43.66	1274000	4.2	-0.028	3.89E-05	4.47E-10	-0.81408	7,8
$Mg_2Si_2O_6$ (Opx)	62.62	1027000	10.2	-0.0199	2.66E-05	7.20E-09	0	5

Notes: [1] O'Neill (1987); [2] Robie and Hemingway (1995); [3] Holland and Powell (1990); [4] Fei (1995); [5] Fabrichnaya et al. (2004); [6] Komabayashi and Fei (2010); [7] Katsura et al. (2009); [8] Boffa Ballaran and Frost unpublished data. $Cp=a+bT+cT^{-2}+dT^{-0.5}+eT^{-2}$, $\alpha=\alpha_0+\alpha_1 T+\alpha_2/T^2$.

The activity coefficient for Fe in the Fe-Ir alloy (γ_{Fe}^{metal}) was determined from the data of Swartzendruber (1984) with a determination of the pressure dependence from excess molar volume data of Schwerdtfeger and Zwell (1968). The combined expression is,

$$RT\ln\gamma_{Fe}^{metal}=(1-X_{Fe})^2\,[(-51814+0.0736P)-21964X_{Fe}] \quad (3.10)$$

where P is pressure in bars. The equation is a combined form of the expressions given by Woodland and O'Neill (1997). The pressure term determined from the excess volume of mixing data contributes only 0.15 log units to the determined log fo_2 at 11 GPa. Many noble metals that form solid solutions with Fe could have been used as a redox sensor. We prefer Fe-Ir because a single FCC structured phase is known to be stable over the entire solid solution at 1 bar and certainly Fe exists in the FCC structure over the experimental pressure and temperature range of this study (Komabayashi and Fei, 2010). X-ray diffraction patterns determined for our Ir-Fe alloys recovered from a range of pressures and temperature, and even up to 25 GPa and 1500 °C, were found to fit

the FCC structure. These lattice parameters were also consistent with those determined for the same alloy compositions at 1 bar (Schwerdtfeger and Zwell, 1968). Ir has also been shown to remain in the FCC structure to pressures of at least 65 GPa (Cerenius and Dubrovinsky, 2000) at room temperature. Although we cannot exclude that a non-quenchable phase transformation in the alloy occurs, there is no evidence to indicate that this is the case. Further, the solubility of C in Ir is known to be negligible at 1 bar and no carbide is known in the Ir-C system (Vol and Kagan, 1976). No evidence was found even using a transmission electron microscope, for the presence of carbides in this study or for the solubility of measurable amounts of C in the alloy.

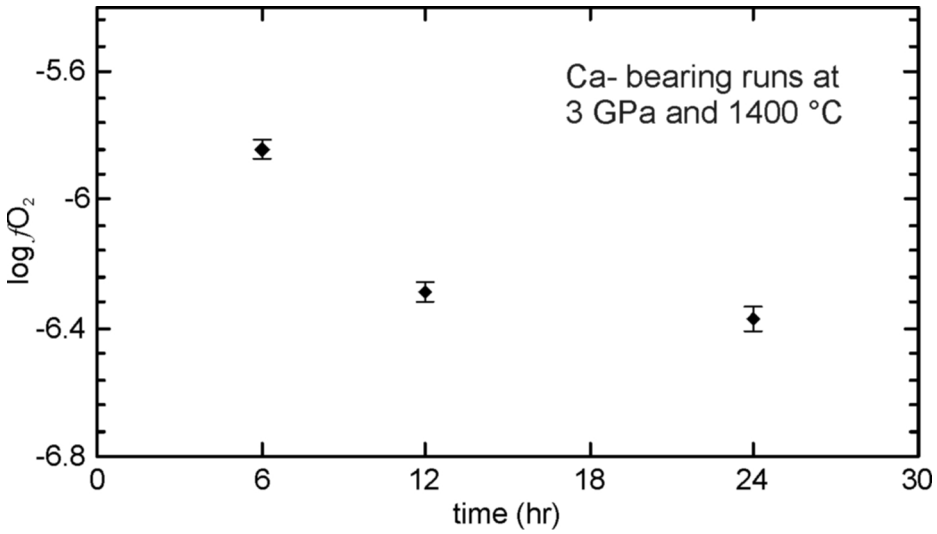

Figure 3.3 A time series showing the evolution of the oxygen fugacity measured for the EDDOG2 assemblage using the Fe-Ir redox sensor. Error bars arise from uncertainties in the chemical composition of olivine, orthopyroxene and the Fe-Ir alloy. Equilibrium values appear to be reached after approximately 12 hours.

During the experiment the fo_2 is fixed by the carbon-carbonate equilibrium (3.4) and Fe dissolves into the initially Fe-free Ir metal to equilibrate with this imposed fo_2. In figure 3.3 the fo_2 determined from equation (3.6) for a time series of experiments performed at 3 GPa and 1400 °C is shown. It can be seen that time scales of the order of 12-24 hours are required for the equilibrium fo_2 to be obtained. An important aspect in facilitating equilibrium is to keep the grain size of the initial Ir metal at approximately 5 μm in order to minimize the required change in the Fe/(Fe+Mg)

ratio of the surrounding silicate minerals. There are further indications that mineral and melt compositions approach equilibrium. The experiments were performed for similar durations as those of Dasgupta et al. (2007) and Brey et al. (2008) and similar liquid and mineral compositions are obtained. The compositions of minerals and melts show variation trends over ranges of pressure and temperature, which are also consistent with previously observed equilibrium behaviour. In addition no evidence of zoning in silicate minerals was observed.

Uncertainties in oxygen fugacities measured using equation (3.6) arise from uncertainties in the experimental temperatures, pressures and chemical analyses of the mineral and metal phases, in addition to uncertainties in thermodynamic properties used in the calculation. Although realistic uncertainties in temperature of 50 °C propagate to log fo_2 uncertainties of 0.3 log units, such uncertainties become small once values are normalized against a similarly temperature dependent buffer such as FMQ. This is also the case for uncertainties in pressure of up to 0.5 GPa. The major uncertainties are therefore those arising from the mineral and metal compositions, which are propagated in Table 3.2. In general these are <0.2 log units. Absolute uncertainties arising from the thermodynamic properties employed in equation (3.6) are harder to assess and potentially large if propagated from each experimentally determined uncertainty. However, we can compare our determinations for the solid EDDOG and EMOG/D assemblages at 3, 6 and 7 GPa with the equations of Eggler and Baker (1982) and internally consistent thermodynamic calculations based on data from Holland and Powell (1990) employing a Birch-Murnaghan equation of state. At all three pressures the agreement between our experiments and these previous studies for both solid assemblages is better than 0.3 log units. By employing the same thermodynamic data in table 3 that is also employed in the calculation of FMQ and the fo_2 determination of many xenoliths, the fo_2 determinations become internally consistent and absolute uncertainties on the thermodynamic data become much less important.

Data collected at 2.5 and 2.8 GPa are at conditions close to the decarbonation ledge where carbonate minerals and melts decarbonate to produce CO_2 vapour saturated silicate assemblages. EMOG and EDDOG assemblages at conditions close to decarbonation should buffer the fO_2 close to the CCO buffer, i.e. close to the equilibrium $C+O_2=CO_2$ (vapour). At these conditions we determined a log fO_2 of -0.84 (ΔFMQ), which is in excellent agreement with the value of -0.83 for the CCO buffer at the same conditions from the results of Ulmer and Luth (1991) or -0.91 from Frost and Wood (1997). We conclude that as our fO_2 determinations are in good agreement with thermodynamic and previous experimental data on the fO_2 of solid assemblages, that the redox sensor technique should also provide accurate measurements relative to FMQ when the carbonate phase is molten.

3.3.3 Oxygen fugacity dependences

In figure 3.4 oxygen fugacities determined using equation (3.6) are plotted as a function of inverse temperature for experiments performed between 3 and 11 GPa and 1100–1600 °C and are compared with the EMOG/D equation of Eggler and Baker (1982). As stated previously, while the carbonate bearing assemblage is subsolidus the agreement between the Eggler and Baker (1982) curve and the experimentally determined fO_2 is very good, however, once the assemblage melts the determined oxygen fugacities deviate from the predicted solid assemblage to lower values.

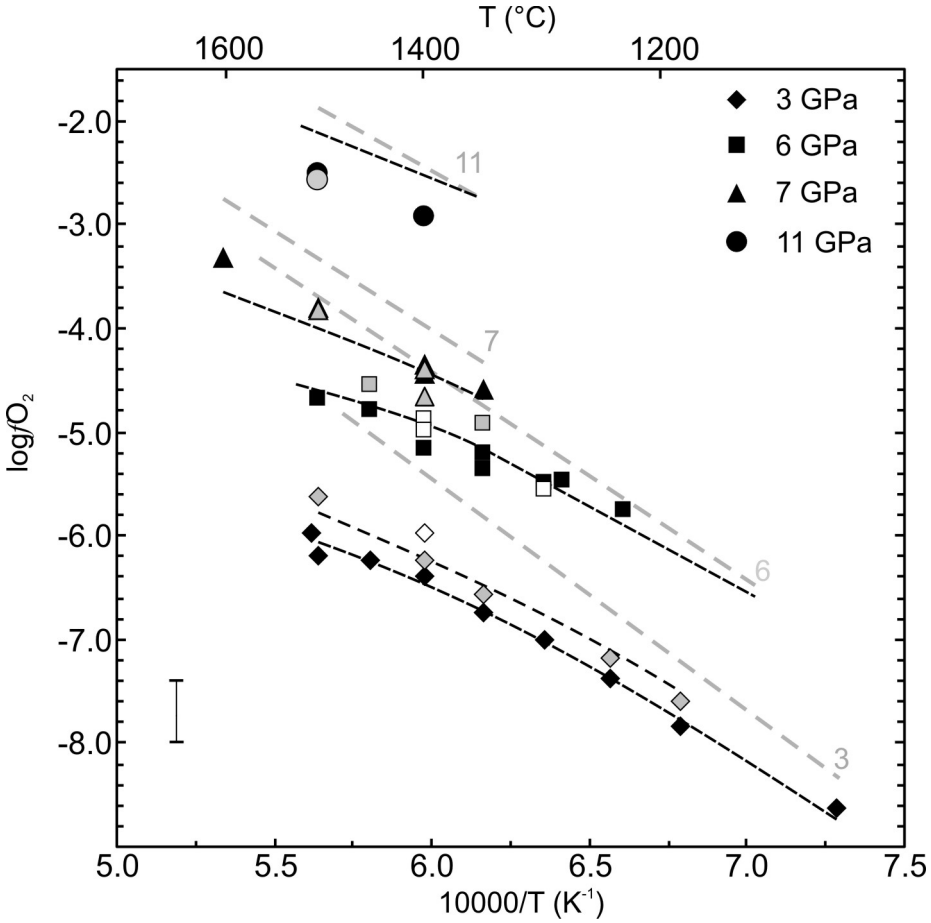

Figure 3.4 (a) Measured oxygen fugacities for the Ca-bearing EDDOG2 composition (black symbols), Ca-free EMOG1 composition (grey symbols) and garnet-bearing EDDOG2 assemblages (open symbols). The fit of equations (3.14) at all pressures, and (3.15) at 3 GPa, are indicated by dashed black curves. With increasing temperature melts become less carbonate rich as the SiO_2 content increases, which flattens the fo_2 dependence compared to the extrapolation of the sub-solidus EMOG/D buffer determination of Eggler and Baker (1982; shown with dashed grey curves).

A similar relation can be seen for both EMOG1 and EDDOG2 assemblages although the former are displaced to slightly higher oxygen fugacities. The flattening out of the oxygen fugacity dependence at high temperature most likely results from a decrease in the CO_2 content of the melt phase with temperature. This effect can be seen more clearly in figure 3.5 where some of the fo_2 temperature dependence has been removed by normalizing against the FMQ buffer (O'Neill, 1987; Ballhaus et al., 1991) using the equation,

$$\text{Log } fo_2 = 82.75+0.00484T-30681/T-24.45\text{Log}(T)+0.094P/T-0.000002P \quad (3.11)$$

where T is in K and P in bars. With increasing temperature the SiO_2 content of the melt phase increases as the melt evolves from a pure carbonate melt, at the near-solidus, towards more SiO_2-rich melts at higher temperatures. This lowers the activity of the carbonate component in the melt, which drives the equilibrium fo_2 down compared to the extrapolations to higher temperature of the solid assemblage buffer (Eggler and Baker, 1982). At 6 GPa and 1500 °C the melt phase contains 35 wt. % SiO_2 and the fo_2 is over 1 log unit below the extrapolated EMOG/D curve.

If the dilution of the carbonate melts by silicate lowers the fo_2 of the graphite-carbonate bearing assemblage, then other melt diluents should have a similar effect. Carbonate melts in the mantle may contain a range of incompatible components such as phosphorus, halogens, H_2O and FeS, (Prins, 1973; Dawson and Fuge, 1980; Le Bas, 1981; Shushkanova and Litvin, 2008) and diamond inclusions also attest to the presence of such components in melt or fluid phases (Deines and Harris, 1995; Klein-BenDavid et al., 2006). In two experiments apatite was added to the EDDOG2 mixture at 6 GPa, which resulted in 11 and 19 wt. % P_2O_5 in the melt phase at 1350 and 1400 °C respectively. As shown in figure 3.5 the addition of P_2O_5 to the melt also lowered the oxygen fugacity of the graphite-melt equilibrium by approximately 0.2 log units. As coexisting olivine contained approximately 0.8 wt. % P_2O_5, however, it would seem that P_2O_5 is not sufficiently incompatible to be present in mantle carbonate liquids at concentrations that would significantly influence the fo_2 of the graphite-melt equilibrium.

The addition of only 2.5 wt. % NaCl to the melt had a similar effect on the fo_2 as P_2O_5. This has two plausible explanations: either NaCl mixes in a strongly non-ideal manner in carbonate melt and, therefore, has a disproportionately large influence on the carbon-carbonate equilibrium, or as melt pockets were small and hard to analyse the NaCl composition of the melt may have been underestimated. Given the occurrence of NaCl in diamond fluid inclusions (Kopylova et al., 2010), however, the effect warrants further investigation.

As sulphide inclusions are the most common syngenetic inclusions observed in diamonds (Sharp, 1966; Deines and Harris, 1995) we also investigated the possibility that sulphide may mix with carbonate melt. Experiments were carried out at 6 GPa by adding ~ 6 wt. % FeS powder. Two runs at 1200 °C and 1400 °C showed clear immiscibility between a carbonate-rich melt and Fe-rich sulphide liquid, which also dissolved the entire Ir-Fe redox sensor. The concentration of S in the carbonate melt at the fo_2 defined by the equilibrium with diamond was negligible, however, which means that FeS cannot influence the fo_2. Although 2 wt. % H_2O was added to one experiment (S4402a) performed at 7 GPa and 1400 °C it was, as expected, impossible, to measure the H_2O content of the quenched melt, although a very small drop in fo_2 was noted compared to the dry experiment.

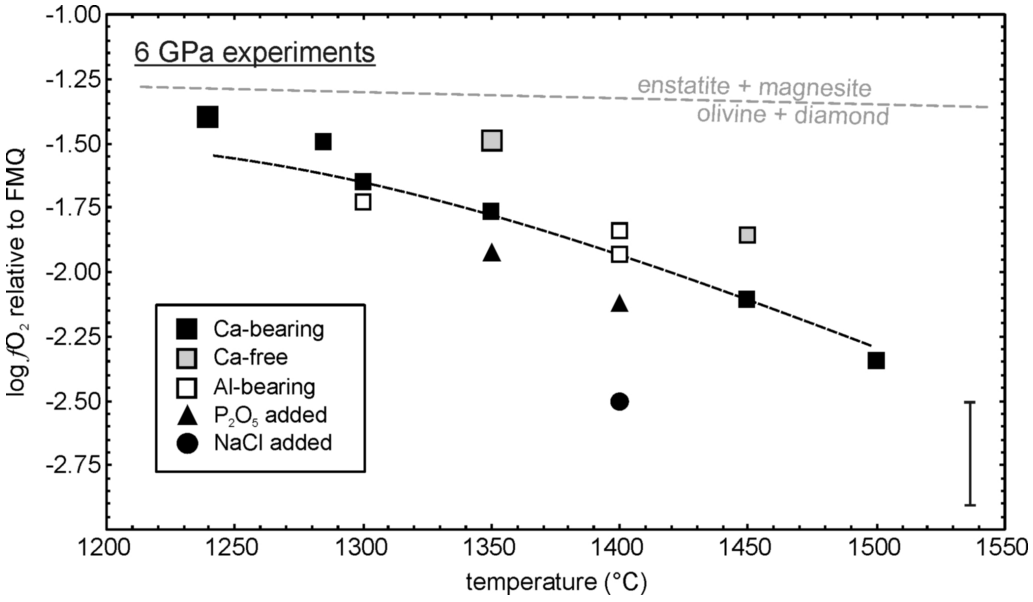

Figure 3.5 Oxygen fugacities (FMQ normalised) determined for carbonate-melt bearing assemblages coexisting with diamond are shown as a function of temperature from experiments performed at 6 GPa. Black symbols are runs in the EDDOG2 Ca-bearing system; grey symbols are EMOG1 Ca-free runs; white symbols are runs performed with garnet layers sandwiched between EDDOG2 assemblages. The slightly larger squares indicate subsolidus assemblages. The effects of adding P_2O_5 and NaCl to the assemblages are shown. The horizontal dashed grey curve is the EMOD buffer calculated from the equation of Eggler and Baker (1982), while the black dashed curve is calculated from equation (3.14).

3.4 Discussion

3.4.1 Parameterisation of the carbon/carbonate-melt fo_2 as a function of P, T and CO_2 melt content

Our experimental results indicate that close to the solidus of carbonated peridotite the fo_2 buffered by the coexistence of graphite or diamond and carbonate melts is close to that of the subsolidus EMOG/D buffer assemblage. However, at higher temperatures an increase in the silicate content of the melt and a decrease in the carbonate activity lead to a decrease in the fo_2 compared to the extrapolated trends for the EMOG/D buffer. A simple parameterisation of these fo_2 results can be performed based on the equilibrium,

$$\underset{\text{graph/diam}}{C} + O_2 = \underset{\text{melt}}{CO_2} \qquad (3.12)$$

where,

$$\log fo_2 = \frac{\Delta H^o + T\Delta S^o + P(V-1)}{\ln(10)RT} + \log a_{CO_2} \qquad (3.13)$$

We assumed that a_{CO_2}, the activity of CO_2 in the melt is equal to the mole fraction of CO_2 in the melt (XCO_2). An excellent fit is obtained between this equation and the experimental results between 2.5 and 11 GPa for the Ca-bearing EDDOG2 assemblage, which reproduces the experimental results to better than 0.3 log units in most cases. When simplified this becomes,

$$\text{Log } fo_2 = 5.44 - 21380/T + 0.078(P-1)/T + \text{Log } (XCO_2) \qquad (3.14)$$

where P is in bars and T is in K. The equation also reproduces fo_2 where P_2O_5 was added to the melt; however, it gives a slightly poorer fit to the Ca-free EMOG1 assemblage results, which were therefore fitted separately to give,

$$\text{Log } fO_2 = 5.7 - 21000/T + 0.067(P-1)/T + \text{Log } (XCO_2) \quad (3.15)$$

Both equations are in very good agreement with the EMOG/D buffer equation of Eggler and Baker (1982) below the carbonate solidus if the value of XCO_2 is fixed at 0.5. Note that neither expression is presented normalized against FMQ.

Figure 3.6 shows how equation (3.14) varies with temperature and CO_2 content of the melt at 3 GPa and a comparison with the experimental data reveals how the CO_2 content of the melt is varying with temperature. The implication of this variation is that with increasing temperature CO_2 melt species will become more stable, with respect to graphite, towards lower oxygen fugacities. The graphite stability field will therefore shrink with respect to fO_2 once large degree melts are formed and the CO_2 melt content becomes dilute. A further implication is that ideal mixing of CO_2 in silicate-carbonate melts is a reasonable approximation when assuming a pure CO_2-melt standard state.

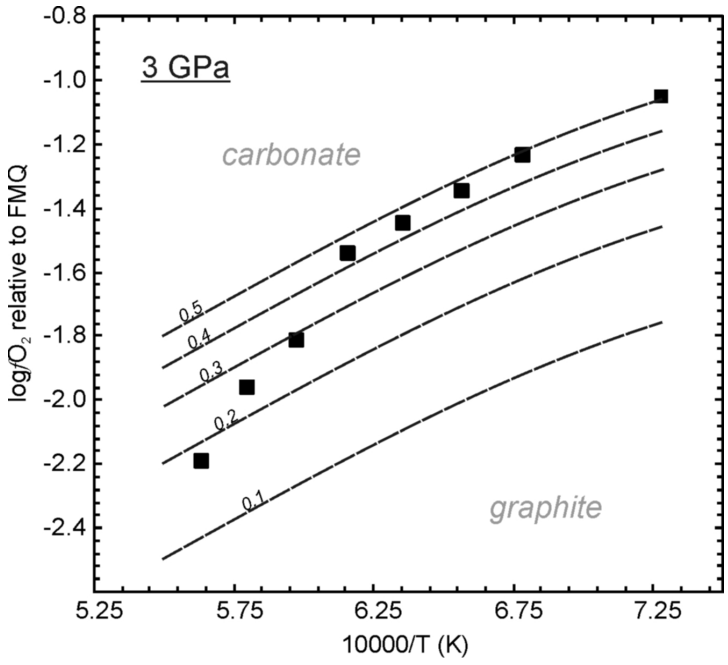

Figure 3.6 Experimentally determined oxygen fugacities for the graphite/carbonate-rich melt assemblage as a function of temperature are shown by the solid symbols. Dashed curves show the fO_2 calculated using equation (3.14) for XCO_2 melt values indicated by each curve. The diagram demonstrates the relationship between fO_2 and CO_2-melt dilution.

3.4.2 Carbon speciation with respect to the mantle redox state and the onset of redox melting

In order to determine the stability of graphite or diamond in the mantle and estimate the depth for the onset of carbonate-dominated melting in up welling asthenospheric mantle, we must compare our experimental results for the fO_2 of the carbon/carbonate-bearing melt equilibrium with a plausible estimate for the fO_2 of the mantle with depth.

Estimates for mantle fO_2 can come from analyses of the $Fe^{3+}/\Sigma Fe$ ratios of fresh MORB glasses, the concentrations of heterovalent elements in asthenospheric melts or from oxy-thermobarometry measurements on xenoliths or peridotite massifs. MORB melts are likely to provide the most direct information on the asthenospheric fO_2 because xenoliths and massifs are sections of the lithospheric mantle, where the fO_2 may have been influenced by multiple stages of melting and metasomatism. Analyses of $Fe^{3+}/\Sigma Fe$ ratios of MORB glasses imply an fO_2, corrected to conditions of the MORB source region, of approximately FMQ ± 0.5 (Bezos and Humler, 2005; O'Neill et al., 2006). Oxy-thermobarometry of abyssal peridotites, which are considered to be residues of MORB melting, reveals a range of fO_2 that extends to lower values, i.e. FMQ +0.5 to FMQ –2.5 (Bryndzia and Wood, 1990). A recent calibration of the partitioning behaviour of vanadium as a function of fO_2 implies that basalts from a range of settings, including island arcs, formed at oxygen fugacities in the range FMQ ± 1, although MORB samples fall consistently between FMQ and FMQ –1 (Mallmann and O'Neill, 2009), in line with previous similar studies (Lee et al., 2005). Using this MORB source fO_2 range and oxy-thermobarometry methods we can estimate that the bulk $Fe^{3+}/\Sigma Fe$ ratio of MORB source peridotite is likely in the range 0.02-0.03, which is consistent with estimates for the melt-residue partition coefficient of Fe^{3+} and with estimates based on mantle xenoliths (O'Neill et al 1993; Canil et al., 1994; Canil and O'Neill 1996).

At pressures greater than that considered for MORB genesis (i.e. 1.5 GPa) the only mantle fO_2 determinations come from oxy-thermobarometry measurements on garnet lherzolite xenoliths from cratonic lithosphere (e.g. Woodland and Koch, 2003; McCammon and Kopylova, 2004; Creighton et al., 2009). Such determinations are interesting not because the fO_2 of the cratonic lithosphere necessarily reflects that of the asthenosphere but because they show a general trend of decreasing fO_2 with depth that is caused mainly by a crystal-chemical effect, which should also be reflected in asthenospheric mantle. The fO_2 of garnet lherzolite xenoliths can be determined using the oxy-thermobarometer calibrated by Gudmundsson and Wood (1995) based on the equilibrium,

$$\underset{\text{garnet}}{2Fe_3Fe_2^{3+}Si_3O_{12}} = \underset{\text{olivine}}{4Fe_2SiO_4} + \underset{\text{opx}}{2FeSiO_3} + O_2 \qquad (3.16)$$

Figure 3.7 shows oxygen fugacities determined using this equilibrium for xenoliths from various cratons as a function of equilibration depth. At each depth fO_2 ranges are recorded, which correlate to some extent with mineral $Fe^{3+}/\sum Fe$ ratios. There is, however, a general decrease in fO_2 with depth, which does not correlate with either mineral or whole rock $Fe^{3+}/\sum Fe$ ratios. Some of the deepest xenoliths record the lowest fO_2 but display some of the highest garnet $Fe^{3+}/\sum Fe$ ratios (Luth et al., 1990; Woodland and Koch, 2003). The main cause of this general fO_2 decrease is the volume change of equilibrium (3.16), which, with increasing pressure causes the equilibrium to favour the formation of the $Fe_3Fe_2^{3+}Si_3O_{12}$ garnet component. This effect drives down the fO_2 with depth (Wood., 1991; Ballhaus, 1995). At depths beyond the onset of melting the asthenospheric mantle should behave in a similar fashion, as it seems most likely that fO_2 is an intrinsic function of the mantle bulk composition, rather than being fixed by any open system exchange. It is possible, therefore, to estimate the plausible evolution of fO_2 with depth by assuming a fertile mantle bulk composition and calculating the fO_2 using equilibrium (3.16) after assigning mineral chemical

compositions using literature partitioning data (O'Neill and Wood, 1979; von Seckendorff and O'Neill, 1993). Such a calculation is shown in figure 3.7 as a solid grey curve tending downwards with depth. It is performed along an adiabat with a potential temperature of 1320 °C using the bulk silicate Earth (BSE) composition of McDonough and Sun (1995) and assuming a fixed garnet $Fe^{3+}/\sum Fe$ ratio of 0.12, which corresponds to a bulk rock $Fe^{3+}/\sum Fe$ ratio of approximately 0.03, using Fe^{3+} mineral partition coefficients from Canil and O'Neill (1996). The decrease in fo_2 predicted by this calculation with depth arises solely due to the volume change of equilibrium (3.16). While fo_2 is not a function of the bulk rock $Fe^{3+}/\sum Fe$ ratio, at a given depth and temperature for a BSE bulk composition the fo_2 will vary as a function of garnet $Fe^{3+}/\sum Fe$ ratio, when calculated with equilibrium (3.16). Therefore, in order to determine conservative bounds for the asthenospheric fo_2 the shaded region in figure 3.7 is calculated assuming garnet $Fe^{3+}/\sum Fe$ ratios of 0.08 and 0.4. This maximum bound would produce a bulk rock $Fe^{3+}/\sum Fe$ ratio of at least 0.1, which is close to that observed in MORB glasses and must be a safe maximum value for the $Fe^{3+}/\sum Fe$ ratio of the depleted MORB source asthenosphere. It is interesting to note that some cratonic xenolith samples in figure 3.7 plot close to this determined maximum fo_2 bound. These high xenolith fo_2 values do not result from the same extreme level of garnet Fe^{3+} enrichment, however, but instead arise mainly from lower olivine and orthopyroxene iron contents than calculated for the BSE composition.

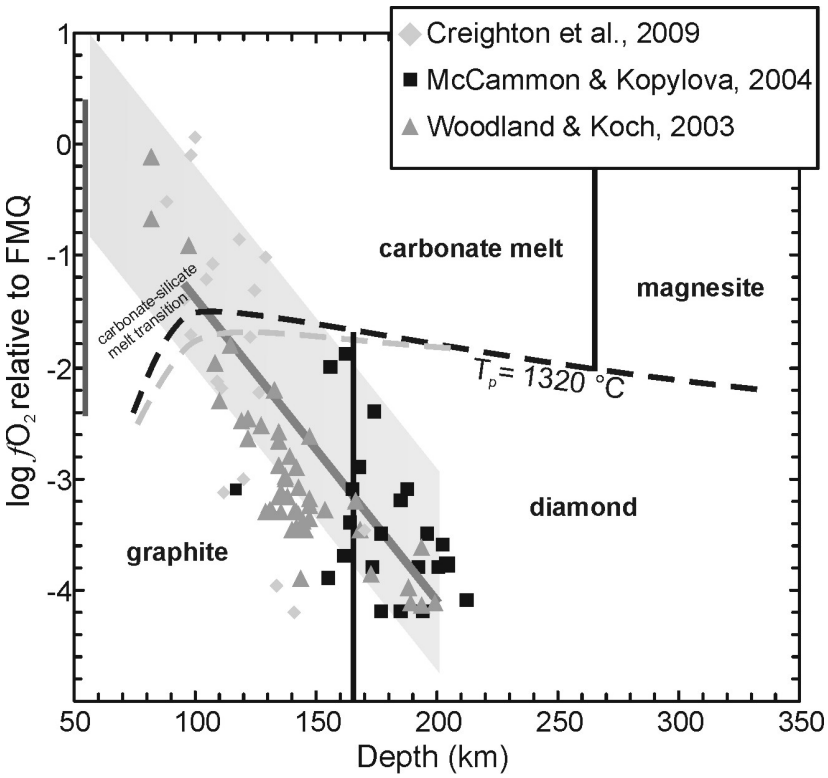

Figure 3.7 The speciation of carbon in the mantle. The two dashed curves indicate the fo_2 of the assemblage buffered by diamond or graphite coexisting with carbonate minerals or melts in a peridotite bulk composition. The dashed curves are calculated along an adiabat with a potential temperature of 1320 °C with the black dashed curve assuming the melt CO_2 contents determined as a function of temperature in this study and the grey dashed curve using melts compositions determined by Dasgupta and Hirschmann (2006; 2007). Carbonates or carbonate-bearing melts can only be stable along an adiabat at oxygen fugacities above these curves. The downward bend in the fo_2 at 100 km results from the transition from carbonate-bearing to silicate dominated melts. The fo_2 calculated between 100 and 200 km for a mineral assemblage with a bulk silicate Earth composition containing garnet with a $Fe^{3+}/\sum Fe$ ratio of 0.12 is shown as the solid grey line. The shaded region around this curve is calculated in the same way but assuming a garnet $Fe^{3+}/\sum Fe$ ratio of 0.08 for the lower bound and 0.4 for the upper. The shaded region, which is extrapolated between 50 and 100 km, represents the range of plausible oxygen fugacities for the asthenospheric mantle, following the oxy-thermobarometer of Gudmundsson and Wood (1995).
The vertical line at 50 km shows the range of fo_2 recorded by abyssal peridotites (Bryndzia and Wood, 1990). Symbols correspond to oxy-thermobarometry measurements for the fo_2 of mantle xenoliths from subcratonic lithosphere.

In figure 3.7 two dashed curves are shown for the fo_2 followed by an equilibrium diamond (or graphite) and carbonate-bearing melt assemblage (from equation 3.14), calculated along a 1320 °C potential temperature adiabat for melt compositions determined in this study (bold dashed line) and that of Dasgupta and Hirschmann (2007; grey dash). At oxygen fugacities above these curves carbonate-bearing melts can be stable, while below the curves diamond or graphite are stable. At depths just shallower than approximately 270 km small degree carbonate melts would form at temperatures compatible with the mantle adiabat and oxygen fugacities higher than approximately

FMQ -2. However, the range determined for the asthenospheric mantle fO_2 at this depth is firmly within the diamond stability field and continues to be up to approximately 150 km, where the fO_2 enters the stability of carbonate-bearing melts and redox melting (Taylor and Green, 1988) would occur. Only when up welling mantle reaches this depth will graphite start to oxidize, through reduction of Fe_2O_3 in silicates, to form a carbonate melt containing 3-15 wt. % SiO_2. This range in melt SiO_2 contents arises from differences in melt compositions as a function of temperature between this study and that of Dasgupta and Hirschmann (2006). At shallower depths still, larger degrees of melting cause the fO_2 of the equilibrium to bend sharply to lower values and graphite would be completely oxidized from the MORB source at depths compatible with the main phase of basalt genesis. The most important implication of this analysis is that carbonate melting should commence through a redox reaction with mantle silicates only at depths <150 km. It should be noted that this depth is constrained by the highest plausible estimate for the mantle bulk rock $Fe^{3+}/\sum Fe$ ratio of approximately 0.1, more typical xenolith $Fe^{3+}/\sum Fe$ ratios of 0.03 (Canil and O'Neill, 1996) constrain redox melting to only occur at depths <100 km. In peridotite assemblages carbonate melts could only be stable in exceptionally oxidized mantle at depths greater than this. Taking into account mineral/melt partition coefficients and proposed mantle abundances of H, Cl and P the presence of these components will not effect this conclusion significantly. Melts such as kimberlites which form at depths ≥ 150 km are, therefore, predicted to arise from either exceptionally oxidized mantle or have initial molar CO_2 contents in the range 1-5 mole %. At reducing conditions where melt-CO_2 concentrations should be low it is also possible that melt CH_4 concentrations become significant.

In the calculation of the mantle fO_2 shown in figure 3.7 it is assumed that fO_2 is intrinsically controlled by the ferric/ferrous equilibrium (3.16) and that the bulk $Fe^{3+}/\sum Fe$ ratio remains constant over the depth interval of the calculation. In reality, however, the mantle ferric/ferrous ratio will

change as carbon undergoes the redox transition from graphite to carbonate-bearing melt and this will affect the fO_2. During up welling carbon oxidation will reduce the Fe_2O_3 content of the mantle causing the fO_2 to be buffered by the graphite/carbonate-bearing melt equilibrium for some depth interval until graphite is exhausted. The extent to which this is important depends on the mantle carbon content, for which estimates for the upper mantle range from approximately 20-250 ppm (Trull et al., 1993; Saal et al., 2002; Hirschmann and Dasgupta, 2009). Carbon contents at the lower end of this estimate will not affect the fO_2 evolution significantly. However, if the mantle contained 250 ppm carbon then complete carbon oxidation would require the reduction of approximately 0.6 wt. % Fe_2O_3. This would require an initial mantle $Fe^{3+}/\sum Fe$ ratio of approximately 0.1, which corresponds to a fO_2 that is still just within the shaded region in figure 3.7, but which is much higher than estimates based on shallow mantle xenoliths and basalts. It would also cause the fO_2 to be buffered by the graphite-melt equilibrium for a depth interval between approximately 100 and 150 km. Although most recent studies on the depleted MORB source seem to favour carbon contents at the lower end of the range (Saal et al., 2002; Hirschmann and Dasgupta, 2009), the sources of ocean island basalts and enriched MORB may have carbon contents closer to the higher estimate (Dixon et al., 1997; Aubaud et al. 2005). A heterogeneous distribution of carbon in the MORB source would result in buffering along the graphite-melt fO_2 curve to varying depths, which could easily explain the range of fO_2 displayed by abyssal peridotites.

A major caveat for the calculation and comparison of mantle fO_2 shown in figure 3.7 is the accuracy in the calibration of equilibrium (3.16) for the measurement of fO_2 in garnet bearing peridotites. While this oxy-thermobarometer has been calibrated at pressures up to 3.5 GPa (Gudmundsson and Wood, 1995), the predicted oxygen fugacities have not been experimentally confirmed at higher pressures, where the volume change of the equilibrium is predicted to significantly lower mantle fO_2. While further studies are warranted we note that the behavior predicted by the volume change of equilibrium (3.16) is at least consistent with recent

measurements by Rohrbach et al. (2007), which indicate that high ferric-Fe bearing garnet is in equilibrium with Fe-metal at pressures above 6 GPa. The results of Rohrbach et al. (2007) imply that the mantle may become saturated in Fe-rich metal at pressures greater than 6 GPa. Our results indicate that at these conditions, close to the IW oxygen buffer, the mantle should be in the diamond stability field. However, carbides or Fe metal-bearing species may be the major hosts for C at these conditions.

3.5 Conclusions

The fO_2 buffered by equilibria involving both elemental carbon (graphite or diamond) and carbonate minerals or melts has been determined in both Ca-bearing and Ca-free model peridotite compositions at pressures between 2.5 and 11 GPa and temperatures at and above the carbonated peridotite solidus (1100-1600°C). The results show that as carbonate melts evolve to more silicate-rich compositions with temperature, the fO_2 buffered by the equilibrium between the melt and graphite or diamond is lowered in comparison to an extrapolation of the solid EMOG or EMOD buffering assemblages. This lowering of the fO_2, which expands the melt stability field with respect to reduced carbon, results from the dilution of the carbonate component in the melt phase. We parameterise our results into an equation for $\log fO_2$ as a function of pressure, temperature and mole fraction of CO_2 in the melt phase. Our parameterisation reproduces our experimental results to within 0.3 log units and can be used to determine the fO_2 of any assemblage where elemental carbon coexists with a CO_2-bearing melt between 2.5-11 GPa.

Garnet-peridotite oxy-thermometry predicts that the range of fO_2 in the asthenospheric mantle should become more reduced with depth as a result of the volume change of the governing ferric/ferrous equilibrium in the silicate assemblage. If correct this means that carbonate melting will only commence in adiabatically up-welling asthenospheric mantle, once the plausible range of

mantle fO_2 crosses the fO_2 constrained by the equilibrium between carbonate melt and graphite or diamond. Our results indicate a depth interval for the onset of carbonate-rich redox melting of 100-150 km, with the deeper value corresponding to a highly oxidised mantle assemblage. Over this depth interval Fe_2O_3 in mantle silicates will react with diamond to produce carbonate rich melts. Redox melting therefore limits the depth interval over which carbonate-rich melts can form in the melting column beneath mid ocean ridges.

If current estimates for the range in mantle fO_2 are correct, diamond and graphite should be the dominant host for carbon at depths >150 km, although arguments for the presence of metal in the mantle above 200 km may imply that carbon is then hosted in this metal phase or as iron carbide (Rohrbach et al. 2007; Frost and McCammon, 2008). In peridotite assemblages carbonates should only exist at depths >150 km in highly oxidised regions or as dilute melt species.

Estimates for the $Fe^{3+}/\sum Fe$ ratio of the deep mantle are strongly dependent on the source carbon content. If determinations of high carbon contents (>100 ppm) in the sources of ocean island basalts and enriched MORB are correct then these up welling sources must initially have much higher $Fe^{3+}/\sum Fe$ ratios in the deeper mantle before the on set of diamond/graphite oxidation, than assumed from the analysis of rocks and basalts from the shallower mantle.

4. Carbon/carbonate equilibrium in the transition zone and lower mantle as function of the oxygen fugacity

4.1 Introduction

The speciation, mobility and residence time of carbon bearing species in the mantle will depend strongly on the oxygen fugacity. Reduced carbon species such as diamond and graphite, for example, are immobile, while oxidized species such as CO_2 fluid and carbonate melt can migrate. It is therefore important to understand the oxygen fugacity at which redox reactions involving C-bearing species occur as a function of pressure and temperature.

Many studies have argued that the oxygen fugacity of the deep mantle may be more reduced than that of the upper mantle due to the increase in solubility of ferric Fe in dominant deep-mantle minerals (Luth et al., 1990; O'Neill et al., 1993; Ballhaus, 1995). Garnet, wadsleyite, ringwoodite and magnesium silicate perovskite, for example, all contain significant quantities of ferric iron even in equilibrium with metallic iron. It has been proposed that this affinity may cause the mantle to become saturated in metallic Fe-Ni alloy at depths greater than 200 km. The oxygen fugacity revealed by mantle xenoliths in cratonic lithosphere has also been found to drop with increasing pressure. This is mainly a result of the effect of pressure on heterogeneous ferric-ferrous equilibria involving mantle minerals. This pressure effect may exert a dominant influence over the oxygen fugacity and is also consistent with the occurrence of Fe-Ni metal at depths of approximately 200 km in the mantle (Ballhaus, 1995; Rohrbach et al., 2007; Frost and McCammon, 2008).

Stagno and Frost (2010) compared the oxygen fugacity where carbonate minerals and melts reduce to diamond or graphite with a plausible oxygen fugacity profile for the upper-mantle and concluded that carbon would be in the reduced form as graphite or diamond at depths between 100 and 300 km.

At higher pressures, however, there are no experimental data through which to assess the oxygen fugacity at which carbonate minerals would be reduced. Carbonate minerals such as magnesite have been shown to be thermally stable in laser heated-diamond anvil cell experiments to pressures of ~115 GPa and temperatures to 2700K (Kraft et al., 1991; Biellman et al., 1993; Isshiki et al., 2004; Ono et al., 2005, 2007), but the oxygen fugacity in these experiments has not been considered.

Recent studies on natural samples, on the other hand, have revealed the occurrence of carbonate phases as inclusions in diamond that are argued to have formed in the transition zone and lower mantle (Brecker et al., 2007; Walter et al., 2008; Kaminsky et al., 2009; Bulanova et al., 2010). CO_2-rich melts migrating from the lower mantle have also been implicated in the origin of isotopic heterogeneity displayed by kimberlites, carbonatites and OIB magmas (Collerson et al., 2010).

In the simplified Mg-Si-O-C system the oxygen fugacity at which magnesite ($MgCO_3$) and diamond coexist in the wadsleyite stability field of the transition zone (410-520 km) will be governed by the equilibrium,

$$\underset{\text{clinoenstatite}}{MgSiO_3} + \underset{\text{magnesite}}{MgCO_3} = \underset{\text{wadsleyite}}{Mg_2SiO_4} + \underset{\text{diamond}}{C} + O_2 \qquad (4.1)$$

In the lower mantle the same oxygen fugacity will be governed by the equilibrium,

$$\underset{\text{magnesite}}{MgCO_3} = \underset{\text{periclase}}{MgO} + \underset{\text{diamond}}{C} + O_2 \qquad (4.2)$$

The oxygen fugacity buffered by equilibria (4.1) and (4.2) could be calculated using thermodynamic data, however, uncertainties in the thermodynamic and equation of state data for magnesite introduces significant uncertainties into such a calculation. The aim of this study is to determine the oxygen fugacity at which the carbonate mineral magnesite will be reduced to diamond in the transition zone

and lower mantle. A comparison of this oxygen fugacity with the plausible oxygen fugacity of the mantle is then used to identify the likely host for carbon in the bulk of the mantle and discuss the origin of inclusions in deep mantle diamonds.

4.2 Experimental methods

Experiments were carried out at pressures of 16, 23, 25 and 45 GPa and temperatures ranging between 1500 and 1700 °C using different starting materials. Equilibrium (4.1) was studied at 16 and 23 GPa employing a carbonated harzburgite starting composition (Eq1) in the system Fe-Mg-Si-O-C assembled from a mineral mix of San Carlos olivine, San Carlos enstatite, synthetic magnesite and pure graphite, in the molar ratio 3:2:1:1. In addition, in each experiment a layer of olivine mixed with enstatite and magnesite (2:1:1) was added sandwiched between two layers of the Eq1 mix to facilitate Mössbauer measurements. 5 wt. % iridium metal powder (≤ 5 μm) was added to all layers to act as a sliding redox sensor.

Equilibrium (4.2) was studied at 25 and 45 GPa employing a mineral mixture in the system Fe-Mg-O-C (Eq2) comprising synthetic $MgCO_3$, pre-synthesized ferropericlase (Fe/{Fe+Mg}=0.17) and pure graphite powder. 5 wt. % pure iridium metal was also added.

At 45 GPa one run (M140) was also performed with Al-bearing glass powder added to the Eq2 mixture, in order to crystallize aluminous magnesium silicate perovskite with a composition similar to that crystallised from pyrolitic bulk compositions (Kesson et al., 1998). This glass was prepared from high purity MgO, Al_2O_3, Fe_2O_3 and SiO_2. After weighing, the oxide mixture was ground for 1 hour under ethanol in an agate mortar. The dried mixture was decarbonated by heating at a rate of 150 °C/hour to 1000 °C and then glassed at 1650 °C. The recovered and ground glass was then reduced in a

controlled H_2-CO_2-Ar atmosphere at 1000 °C at an oxygen fugacity equivalent to the Ni-NiO oxygen buffer for 24 hours.

Further experiments at 25 and 45 GPa employed the Eq2 bulk composition but 3 wt. % Ni metal was added instead of Ir metal in order to test a second type of sliding redox sensor.

Experiments between 16 and 25 GPa were performed in 1000 and 1200 tonne Kawai-type multianvil presses at the Bayerisches Geoinstitut.

Tungsten carbide anvils of 8 and 4 mm truncation edge length (TEL) were used with standard 14 and 10 mm edge length of Cr_2O_3-doped MgO octahedra. Starting powders were loaded into a graphite container that was enclosed in a rhenium foil capsule. The capsule was placed in the central portion of a straight lanthanum chromite furnace, surrounded by an MgO sleeves and spacers. The temperature was monitored with a $W_{97}Re_3$–$W_{75}Re_{25}$ (D type) thermocouple inserted within an alumina sleeve, with the junction in contact with the top of the capsule. Experiments were performed between 1500-1700 °C for 1-15 hours.

Experiments at 45 GPa (M131 and M140) were carried out using the MADONNA D-DIA (1500 tons) press installed at the Geodynamics Research Center (Ehime University, Japan) employing 14 mm edge length sintered diamond anvils. In these runs the starting powder was placed in a graphite capsule and compressed inside an MgO pressure medium (OEL 2.0 mm) doped with 5 wt. % Cr_2O_3. Fired pyrophyllite gaskets were used. Further experimental details are described by Tange et al. (2008). High temperatures were reached using a cylindrical $LaCrO_3$ furnace. Temperature was measured with a$W_{97}Re_3$−$W_{75}Re_{25}$ thermocouple in contact with the bottom of the graphite capsule. The experiments were run for approximately 1 hour during which the temperature was manually controlled to within ±5 °C. After quenching, a long decompression time (30 hrs) was employed in order to prevent breakage of the sintered diamond anvils.

Pressure calibrations at the Bayerisches Geoinstitut are reported in Keppler and Frost (2005). Sample pressures in experiments performed at 45 GPa were calibrated as a function of oil pressure based on *in situ* synchrotron X-ray diffraction experiments performed using the SPEED-Mk.II multianvil press installed at the BL04B1 beam line in SPring-8 (Katsura et al., 2004). Au was used as an internal pressure standard (Tsuchiya, 2003) and calibrations were performed up to ~62 GPa between 1700 and 2100 K. This calibration was further tested off-line by monitoring semiconductor to metal transitions in ZnS (15.5 GPa; Onodera and Ohtani, 1980), GaP (22.5 GPa; Dunn and Bundy, 1978), Zr (α-γ and β-γ transitions) and Fe_2O_3. Off-line calibration was consistent with synchrotron experiments (figure 4.1).

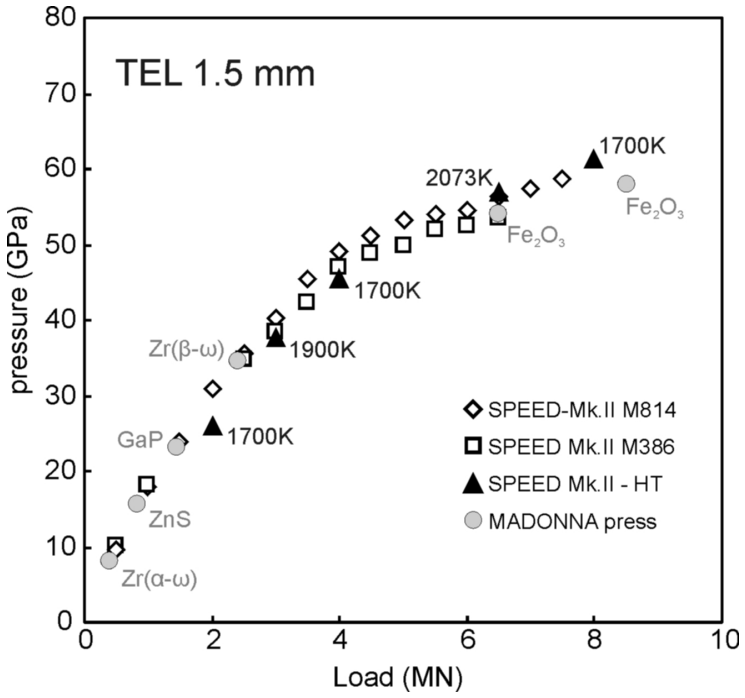

Fig 4.1 Pressure calibration for the 1.5 mm truncated edge length (TEL) assembly using laboratory and *in situ* X-ray diffraction experiments and the equation of state of gold (Tsuchiya, 2003). HT means high temperature. See text for further details.

Recovered samples were mounted in epoxy resin, sectioned and polished parallel to the axial furnace direction under ethanol to preserve carbonate phases. Textural observations of the recovered

run products were performed using FEG Scanning Electron Microscopy (Bayerisches Geoinstitut) and Field Emission Scanning Electron Microscopy (Geodynamic Research Center-Ehime), while the chemical composition of each phase was obtained using a Jeol JXA-8200 electron microprobe equipped with five wavelength dispersive spectrometers. An accelerating voltage of 15 kV and a beam current of 5-20 nA was employed and counting times varied between 20 and 10 s on peak and background (30 and 15 s for Ir-Fe metal) with a focused electron beam. Standards were natural silicates and metals (Ir, Fe and Ni). The PRZ correction was applied. The carbon content of metallic phases in the recovered samples was also randomly detected following the procedure described in Dasgupta and Walker (2008) and employing vitrified carbon (purity >99.99 % provided by Alfa) as standard.

The ferric/ferrous ratios within layers of wadsleyite (at 16 GPa) and Al-bearing perovskite (at 45 GPa) were determined at room temperature and pressure using ^{57}Mössbauer spectroscopy in transmission mode on a constant acceleration with a nominal 370 MBq ^{57}Co high specific activity source. The effective Mössbauer thickness was estimated from the composition. The velocity scale was calibrated relative to 25 μm thick α-Fe foil. Spectra were fitted to a Lorentzian line-shape using the fitting program NORMOS written by R.A. Brand (distributed by Wissenschaftliche Elektronik, Germany). Spectra were collected for periods of between 3-7 days over a sample region of approximately 250 μm in diameter.

Additionally, the iron valence state in minerals from experiment M140 were measured by Electron Energy Loss Spectroscopy on a thin film extracted using QUANTA 3D FEG focused ion beam. The Fe $L_{2,3}$-edge energy-loss near-edge structure (ELNES) of the sample was examined using a 200 kV analytical scanning transmission electron microscope equipped with a parallel electron energy-loss spectrometer. ELNES spectra were collected in diffraction mode with convergence and collection semi angles of $\alpha = 4$ mrad and $\beta = 1.45$ mrad, an energy dispersion of 0.1 eV per channel and 5 - 10 seconds integration time per read-out. The incident beam current was about 16 nA, and the fluence rate was

$1.26x10^3$ e/Å^2/sec. To reduce electron irradiation damage during EELS measurements especially on perovskite grains, the TEM thin foil was cooled to nearly liquid nitrogen temperature (ca. -160 °C) in a Gatan cooling holder. To evaluate the intensity ratio of $L_{2,3}$ –edges, the energy resolution of 0.8-0.9 eV was measured as the width of the zero-loss peak (ZLP) at half height. The energy scale of the core-loss spectrum was fixed using the Fe L_3-edge maxima of predominantly Fe^{2+}- and Fe^{3+}-bearing phases, ferropericlase and magnesium silicate perovskite, at 707.8 eV and 709.5 eV, respectively. Spectral processing included subtraction of the dark current, alignment and summation of offset spectra to reduce channel-to-channel gain variations, background subtractions of the form AE-g, deconvolution of the ZLP to remove the multiple scattering effect on the core-loss edge, and subtraction of the continuum intensity beneath the Fe $L_{2,3}$ edge using a double arctangent function with two fixed inflection points at 708.65 eV and 721.65 eV. Quantification of the Fe $L_{2,3}$-ELNES was made using an empirically-calibrated universal curve (van Aken and Liebscher, 2002).

4.3 Results

Experimental conditions and recovered phase assemblages are listed in Table 4.1, with full chemical analyses reported in Table S4.1 and S4.2 in the Appendix. In all experiments the graphite capsule transformed to polycrystalline diamond. Experiments were performed below the carbonated solidus for the various compositions and no indication of melting was observed (see figure 4.2).

At 16 GPa products from the study of equilibrium (4.1) contained wadsleyite, clinoenstatite, magnesite and diamond in addition to Ir-Fe alloy. At 23 GPa in the Ca-Mg-Si-Fe-O-C system ringwoodite and stishovite supplanted wadsleyite and clinoenstatite and coexist with Mg- and Ca-perovskite. At 25 and 45 GPa products included ferropericlase, magnesite, diamond and Ir-Fe alloy. Experiment M140 at 45 GPa additionally contained Al-perovskite, while run H2981 at 25 GPa and

M131 at 45 GPa, which initially contained Ni instead of Ir, contained no metal phase after the experiment as all Ni oxidized and partitioned mainly into ferropericlase.

Tabella 4.1 Experimental conditions and run products

Run no	P (GPa)	T (°C)	Time (hr)	phases				
S4226	16	1500	12	wads	Cl-En	mst	C	
S4278	16	1550	12	wads	Cl-En	mst	C	
H3102	23	1600	1	ringw	Mg/Ca-Pv	mst	C	Stish
H2946	25	1500	12	Fe-pc	-	mst	C	
H2982	25	1500	16	Fe-pc	-	mst	C	
H2887	25	1550	12	Fe-pc	-	mst	C	
S4807	25	1600	1	Fe-pc	-	mst	C	
H2981*	25	1500	12	Fe-pc	-	mst	C	
M131*	45	1700	1	Fe-pc	-	mst	C	
M140	45	1700	1	Fe-pc	Mg-Pv	mst	C	

Notes: *Wads* = wadsleyite, Rinw = ringwoodite, *Cl-en* = clino-enstatite, *C* = diamond, *Mst* = magnesite, Mg/Ca-*Pv* = Mg, Ca-bearing perovskite, *Stish* = stishovite, Fe-pc = ferropericlase. * Runs containing nickel.

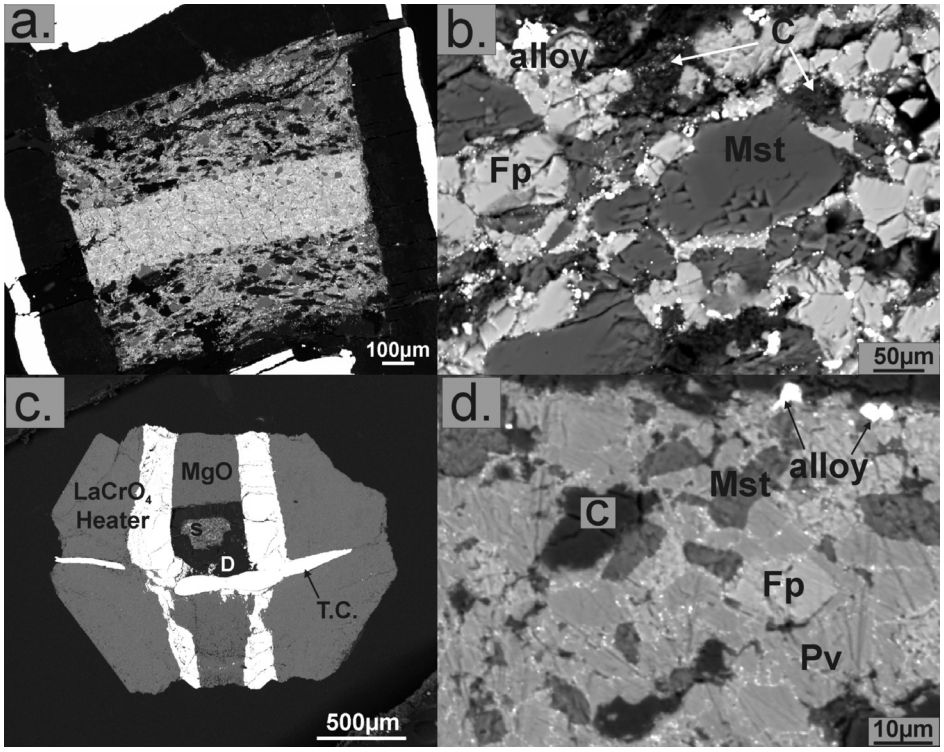

Fig 4.2: a) recovered sectioned run product S4226 (16 GPa/1500 °C) showing the wadsleyite-rich layer. b) H2946 run (25 GPa/1500 °C) showing a heterogeneous mineral assemblage with: magnesite (mst), Fe-periclase (Fe-pc), diamonds (dark grains) and the iron-iridium alloy (bright phase). c) Assembly used for experiments with sintered diamond anvils. d) Run M140 (45GPa/1700°C) showing ferropericlase (Fe-pc), magnesite (Mst), diamonds (C) and Mg-perovskite (Pv).

The TEM image in figure 4.3 shows part of the product from M140 at 45 GPa where coarse-grained ferropericlase is in contact with smaller well crystallized perovskite grains. Although only run for one hour M140 shows evidence for textural equilibrium. In addition the determined $K_D^{Fe/Mg}$ between perovskite and ferropericlase ($=\left\{X_{Fe}^{Pv}/X_{Mg}^{Pv}\right\}/\left\{X_{Fe}^{Fp}/X_{Mg}^{Fp}\right\}$) of 0.54 is in excellent agreement with values determined by Irifune et al. (2010) at similar pressures and temperatures (figure 4.4a). The Fe-Mg partition coefficient between magnesite and silicate minerals was found to decrease as the silicate phases transform to progressively higher-pressure polymorphs as shown in figure 4.4b. The Fe-Mg partition coefficient between magnesite and ferropericlase remained constant between 25 and 45 GPa, which seems to preclude any significant effects resulting from changes in the spin state of Fe in ferropericlase on Fe-Mg partitioning over this pressure range (Badro et al., 2003).

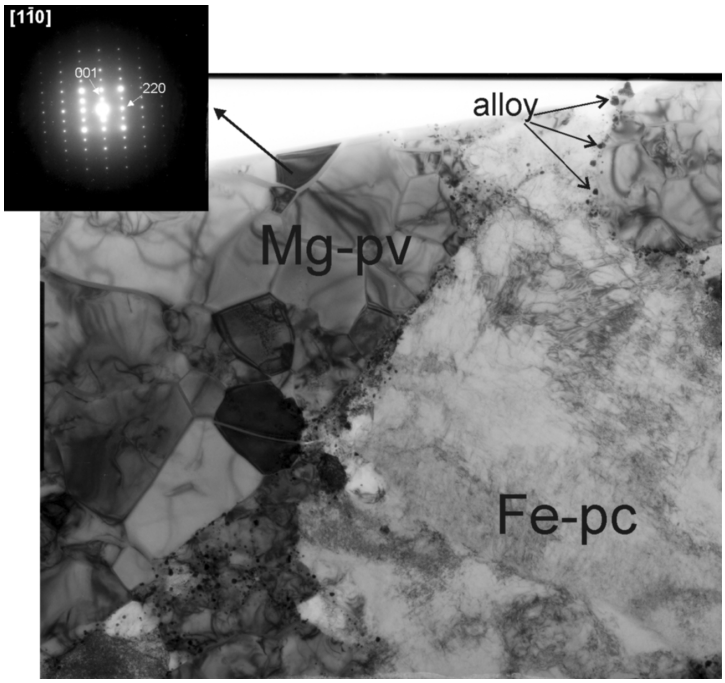

Fig 4.3: Bright-field image of the film recovered from run M140 along a [1-10] zone axis. Inclusions are shown (Mg-Pv magnesio-perovskite, Fe-pc ferropericlase and iridium-iron alloy), while dark lines and dots are clearly distributed on the ferropericlase grain and representative of dislocation features. On upper left part a SAED pattern is shown for Mg-Pv grain used for EELS analysis.

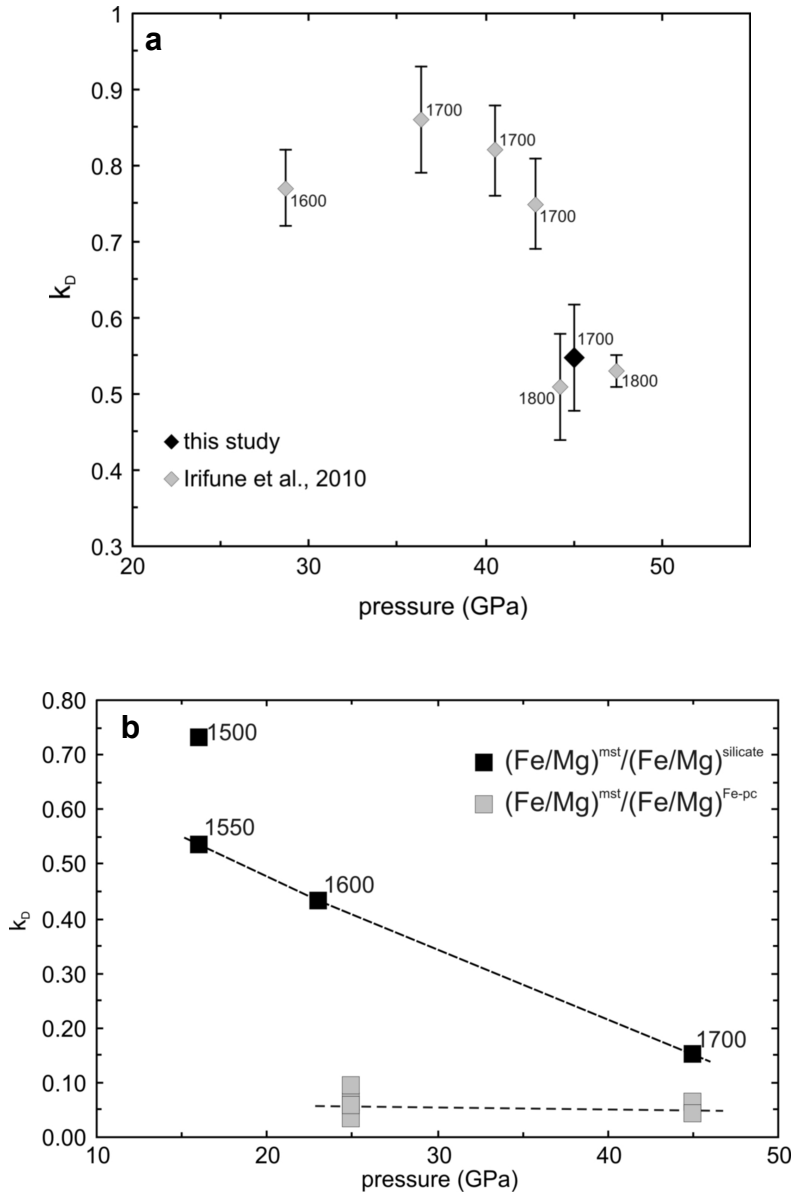

Fig 4.4: a) Shown is the Fe/Mg partition coefficient calculated for Mg-Pv and ferropericlase as compared to data by Irifune et al. (2010); b) the Fe/Mg K_D is shown between magnesite and silicates (clinoenstatite and Mg-Pv) and between magnesite and ferropericlase as function of pressure.

Mössbauer spectra for wadsleyite and aluminous silicate perovskite from 16 and 45 GPa respectively are shown in fig. 4.5a-b. Spectra for wadsleyite (S4226, S4278) were fitted to one quadruple doublet for Fe^{2+} in M1 and M2 site and one for Fe^{3+} in the M3 site. The $Fe^{3+}/\sum Fe$ ratio of wadsleyite was found to be 0.04 (2) in the two samples examined. Spectra for aluminous perovskite (M140) were fitted to

four quadrupole doublets, two for Fe^{2+} and one for Fe^{3+} in perovskite and a further doublet for Fe^{2+} in coexisting ferropericlase. The corresponding $Fe^{3+}/\sum Fe$ ratio is 0.79 (±0.1). Further measurements were made on both perovskite and ferropericlase from the same sample using EELS (Fig. 4.5c-d). Measurements on perovskite grains yielded a $Fe^{3+}/\sum Fe$ ratio of 0.68(3), which is just within the uncertainty of the Mössbauer measurement. The $Fe^{3+}/\sum Fe$ ratio for coexisting ferropericlase was 0.02(5).

In each experiment the oxygen fugacity was buffered by the coexistence of diamond and magnesite through the Fe-bearing equivalents of equilibrium (4.1) at 16 and 23 GPa and equilibrium (4.2) at 25 and 45 GPa. The oxygen fugacity was then measured in each experiment using a sliding redox buffer based on the Fe content of Ir-Fe alloy measured after the experiment (Stagno and Frost, 2010). The redox sensor in the wadsleyite stability field employs the equilibrium,

$$\underset{\text{wadsleyite}}{Fe_2SiO_4} = SiO_2 + \underset{\text{alloy}}{2Fe} + O_2 \qquad (4.3)$$

where the oxygen fugacity is therefore calculated through,

$$\log fo_2 = \frac{-\Delta G^{o}[4.3]}{\ln(10)RT} + \log a^{Wads}_{Fe_2SiO_4} - \log a_{SiO_2} - 2\log a^{metal}_{Fe} \qquad (4.4)$$

where $a^{Wadsl}_{Fe_2SiO_4}$, a^{metal}_{Fe} and a_{SiO_2} are the activities of the Fe_2SiO_4 component in wadsleyite, Fe in the Ir-Fe alloy and silica respectively. The silica activity is determined from the equilibrium,

$$\underset{\text{wadsleyite}}{Mg_2SiO_4} + SiO_2 = \underset{\text{clino-enstatite}}{Mg_2Si_2O_6} \qquad (4.5)$$

i.e.

$$\log a_{SiO_2} = \frac{\overset{o}{\Delta G}[4.5]}{\ln(10)RT} + \log a^{clinoen}_{Mg_2Si_2O_6} - \log a^{Wads}_{Mg_2SiO_4} \quad (4.6)$$

$a^{Wads}_{Fe_2SiO_4}$ and $a^{Wads}_{Mg_2SiO_4}$ are $(X_{Fe}.\ \gamma_{Fe})^2$ and $(X_{Mg}.\ \gamma_{Mg})^2$ respectively where X_{Fe}=Fe/(Fe+Mg) and the activity coefficients (γ) are determined from,

$$RT\ln\gamma_a = W^{wads}(1-X_a)^2 \quad (4.7),$$

where W^{wads} the wadsleyite Fe-Mg interaction parameter is 2 kJ/mol (Frost, 2003). The Mg-Fe clinoenstatite solid solution is considered to be ideal. The activity coefficient for Fe in the Fe-Ir alloy (γ^{metal}_{Fe}) was calculated from,

$$RT\ln\gamma^{metal}_{Fe} = (1-X_{Fe})^2 \cdot (-51814+0.0736P-21964X_{Fe}) \quad (4.8),$$

where P is pressure in bars (Schwerdtfeger and Zwell, 1968; Swartzendruber, 1984).

At 23 GPa in the ringwoodite stability field an equilibrium analogous to (4.3) is employed to calculate fo_2, with the SiO_2 activity fixed by the presence of stishovite. At 25 and 45 GPa the fo_2 was measured by using the equilibrium,

$$\underset{\text{wustite}}{2FeO} = \underset{\text{alloy}}{2Fe} + O_2 \quad (4.9)$$

with the expression,

$$\log fo_2 = \frac{-\overset{o}{\Delta G}[4.9]}{\ln(10)RT} + 2\log a^{Fp}_{FeO} - 2\log a^{metal}_{Fe} \quad (4.10)$$

a_{FeO}^{Fp}, the activity of FeO in ferropericlase, is (X_{Fe} γ_{Fe}) and the activity coefficient γ_{Fe} is,

$$RT\ln\gamma_{Fe}=W^{Fp}(1-X_a)^2 \quad (4.11)$$

where W^{Fp} is 11 kJ/mol (Frost, 2003). The ΔG^0 terms for equilibria (4.4), (4.6) and (4.10) are determined using the thermodynamic and equation of state data given in Table 4.3.

Uncertainties in measured oxygen fugacities arise from uncertainties in the experimental temperatures, pressures and chemical analyses of the mineral and metal phases, in addition to uncertainties in thermodynamic data used in the calculation. Errors due to the standard deviation in chemical analysis are reported in table 4.2 and are in general less than 0.1 log units. Pressure-temperature uncertainties are even smaller once the results are normalized against the IW buffer. The reproducibility in the experiments seems to be approximately 0.3 log units. Uncertainties propagated from those in the thermodynamic data used are by far the largest source of error. However, these uncertainties can be addressed by comparing thermodynamic data from various sources. For equilibrium (4.3) when two independent sources of end-member thermodynamic data are compared the difference in calculated oxygen fugacity is approximately 0.2 log units in the wadsleyite stability field and 0.47 in the ringwoodite field. For equilibrium (4.9) at lower mantle conditions there is no uncertainty in the end member thermodynamic data once the fO_2 is normalized against IW. Only the uncertainties in the activity-composition relations are important for equilibrium (4.9) and of these only the uncertainty in the Fe-Ir activity coefficient is significant. The high-pressure extrapolation of the Fe-Ir activity coefficient employs the excess volume of mixing of the solid solution at room temperature and pressure. Propagating the uncertainty on this value at 45 GPa results in an fO_2 uncertainty of 0.4 log units. In addition to this, however, we have no information on how pressure might affect the excess volume of mixing. If we make the extremely conservative assumption that pressure causes Fe-Ir mixing

to become ideal then at 45 GPa the resulting fo_2 uncertainty is 0.8 log units, which is the value we employ in figure 4.6.

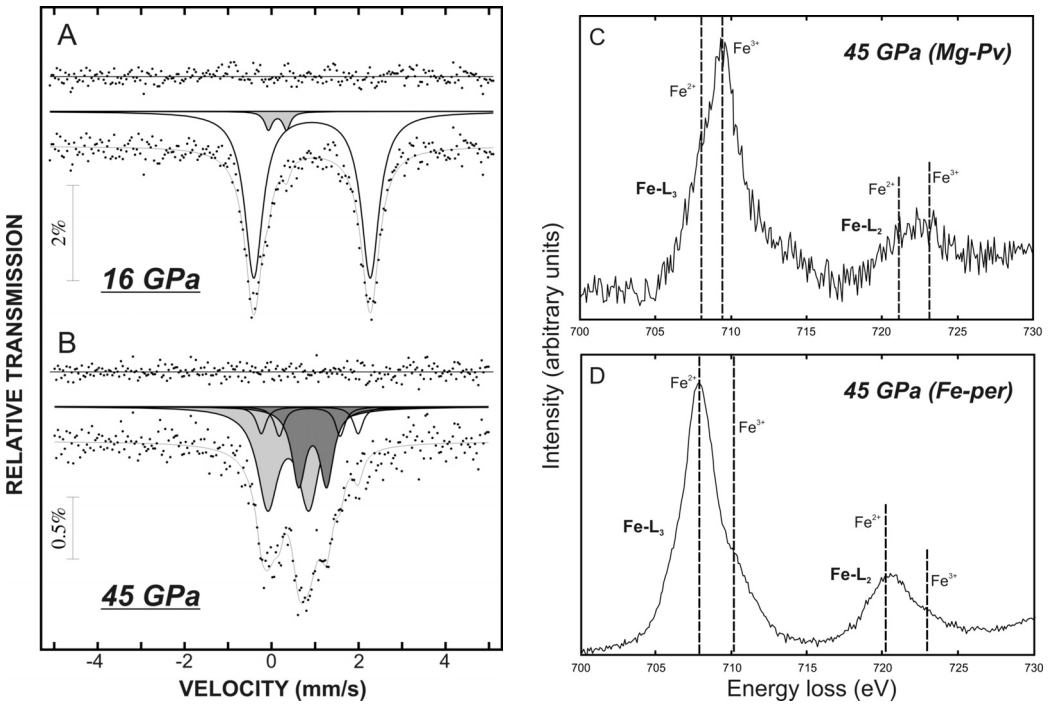

Fig 4.5: a) Mössbauer spectra, the doublets corresponding to Fe^{3+} in Mg-Pv and Fe^{2+} in Fe-Per are shaded light gray and dark gray, respectively; the remaining doublets correspond to Fe^{2+} in Mg-Pv. c) Fe $L_{2,3}$-edge energy-loss near-edge structure spectra based on EELS measurements of a run product at 45 GPa for ferropericlase (Fe-Per) and d) Mg-perovskite (Mg-Pv).

Table 4.2 Experimental results and calculated oxygen fugacities

Run No.	T (°C)	P (GPa)	$XFe_{wads/Ringw}$	$XFe_{Clen/Fe\text{-}pc}$	XFe_{alloy}	fo_2	fo_2(IW)
S4226	1500	16	0.095(1)	0.057(5)	0.099	-1.06(1)	2.88(1)
S4278	1550	16	0.090(2)	0.051(3)	0.125	-1.09(1)	2.56(1)
H3102	1600	23	0.101(4)	-	0.101(5)	1.45(2)	2.98(3)
H2946	1500	25	-	0.175(4)	0.110(10)	1.17(9)	2.63(9)
H2982	1500	25	-	0.149(4)	0.128(17)	0.88(13)	2.34(14)
H2887	1550	25	-	0.178(5)	0.136(10)	1.09(7)	2.32(7)
S4807	1600	25	-	0.175(4)	0.115(17)	1.44(15)	2.46(15)
H2981	1500	25	-	0.273(5)	-	-1.58	0.22
M131-1	1700	45	-	0.232(12)	-	3.61	0.03
M131-2	1700	45	-	0.349(2)	-	3.57	-0.01
M140	1700	45	-	0.151(5)	0.073	6.18(2)	2.16(2)

Table 4.3 End member thermodynamic data used for calculating oxygen fugacity

	Ref. T(K)	$\Delta_f H^o$ ($Jmol^{-1}$)	H_T-H_{298} ($Jmol^{-1}$)	S_T ($JK^{-1}mol^{-1}$)	a	b	c	d	Source
Fe (FCC)	1200	0	35543	76.91	24.0	0.008360	0		1
FeO	298	-262133		63.46	390.8	0.008574	-7.325E+05	246.6	2
$Mg_2Si_2O_6$ (Cpx)	298	-3089646		131.0	380.06	-0.011287	63506	-3687.6	5
O_2	1000	0	22694	205.15	48.3	-0.000691	4.99E+05	-421	1
Fe_2SiO_4 (wads)	298	-1468000		141.80	272.67	-2639.6	0	4.48E08	5
Mg_2SiO_4 (wads)	298	-2140500		95.00	216.44	-1472.40	0	-5.58E+08	5
Fe_2SiO_4 (wads)	1673	$G_{(Tr)}$= -1955055-438.59*(T-Tr)-0.074*$(T-Tr)^2$							4
Mg_2SiO_4 (wads)	1673	$G_{(Tr)}$ =-2514481-354.00*(T-Tr)-0.054*$(T-Tr)^2$							4

	V (cm^3mol^{-1})	K_o(bar)	K'	dK/dT ($barK^{-1}$)	α_0	α_1	α_2	α_4	
Fe (FCC)	6.835	1653000	5.5	-363	6.40E-05	0	0		5,6
FeO	12.25	1500000	4.3	-264+0.02(T-Tr)	3.481E-05	2.968E-9	-0.0806	-0.00144	2,3
$Mg_2Si_2O_6$ (Cpx)	62.62	1250000	4	-213	3.92E-05	4.32E-09	-1.6577		5
Fe_2SiO_4 (wads)	43.15	1660000	4	-281	8.77E-05	-2.61E-09	4.435	-3.4E-02	
Mg_2SiO_4 (wads)	40.51	1725000	4	-351	1.77E-05	1.10E-08	-0.0083		5
Fe_2SiO_4 (wads)*	44.779	1400000	4		4.30E-05				4
Mg_2SiO_4 (wads)*	42.206	1462000	4.21		4.20E-05				4

[1] O'Neill (1987); [2] Hass and Hemingway (1992); [3] refined from the data of Seagle et al. (2008); [4] Frost (2003); [5] Fabrichnaya et al. (2004) [6] Komabayashi and Fei (2010); * values at 1673 K. $Cp=a+bT+cT^{-2}+dT^{-0.5}+eT^2$, $\alpha=\alpha_0+\alpha_1T+\alpha_2/T^2+\alpha_3/T$.

4.4 Discussion and conclusions

Figure 4.6 shows the experimentally determined fO_2 (ΔIW), also reported in Table 4.2 at which diamond and magnesite coexist in a bulk silicate Earth composition (BSE) assemblage to pressures of 45 GPa. The results indicate the lowest fO_2 at which magnesite can be stable and show that, although this fO_2 initially increases with pressure, above 10 GPa there is a gradual decrease. For comparison a band showing the plausible fO_2 of the mantle is also shown. The fO_2 in the mantle below 300 km is considered to be at or below the IW buffer (Frost and McCammon, 2008). In the lower mantle this low fO_2 arises from the fact that aluminous silicate perovskite, the dominant lower mantle mineral, displays a $Fe^{3+}/\sum Fe$ ratio of over 0.5 even when coexisting with metallic Fe (Frost et al., 2004). This means that, if whole mantle convection occurs and the total oxygen content of the upper mantle is similar to the lower mantle, then metallic Fe-Ni alloy would be forced to precipitate in the lower mantle to provide

sufficient Fe^{3+} to account for the equilibrium perovskite $Fe^{3+}/\sum Fe$ ratio. $Fe^{3+}/\sum Fe$ measurements on upper mantle and transition zone minerals also imply that the fo_2 of the mantle must be similarly reduced below 300 km (Rohrbach et al., 2007).

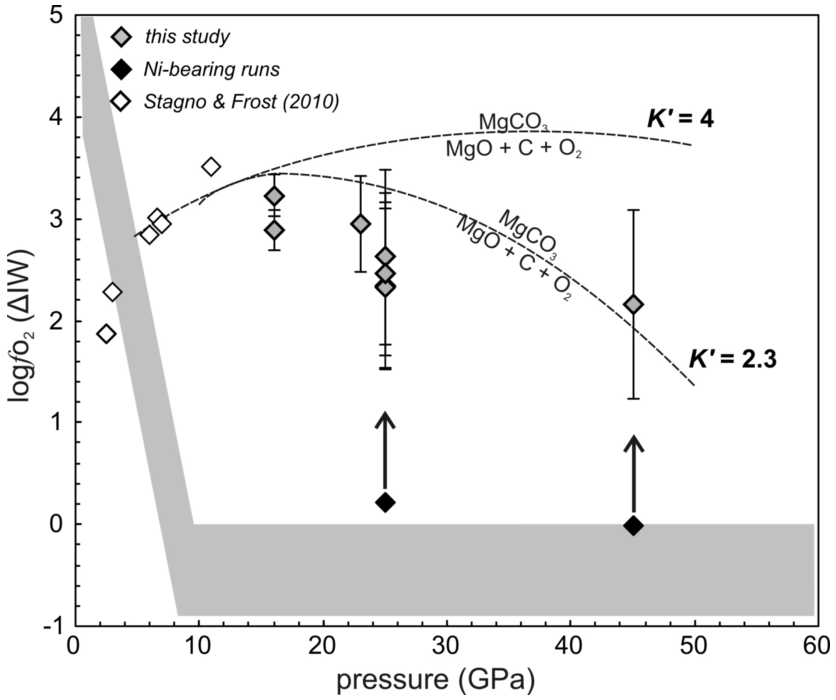

Fig 4.6: Shown are measured fo_2 using the iridium-iron redox sensor and normalized to the IW buffer as function of pressure and compared to thermodynamic calculations for equilibrium (4.2). The grey line indicates the fo_2 of the mantle (Frost and McCammon, 2008; Stagno and Frost, 2010).

Figure 4.6 indicates that the mantle below 150 km depth is within the diamond stability field and that magnesite should not exist in the deep interior, except in regions that are exceptionally oxidized. The fo_2 of magnesite stability is determined to be approximately 2 log units above the IW buffer at 45 GPa. In order to provide additional confirmation of the oxidized nature of magnesite stability an experiment at 45 GPa was performed (M131) where Ir metal was replaced in the starting powders by Ni metal. If the minimum fo_2 of magnesite stability were compatible with the presence of Fe-Ni metal in the lower mantle a metallic phase should persist in the experiment alloyed with Fe. However,

although diamond and magnesite were found to exist in the run products, Ni metal was completely oxidized and partitioned strongly into ferropericlase. By considering thermodynamic properties of the FeO and NiO ferropericlase end-members and data for Fe-Ni alloys it is possible to calculate that the highest fO_2 where Fe-Ni metal can coexist with ferropericlase at 45 GPa is almost exactly IW. This experiment, therefore, categorically demonstrates that the minimum fO_2 for magnesite to be stable must be above IW at 45 GPa, which is further confirmation of the results shown in figure 4.6.

The reversal in pressure dependence of the fO_2 at which diamond and magnesite coexist can be rationalized as arising from the high compressibility of magnesite. A thermodynamic calculation for the fO_2 of equilibrium (4.2) predicts a similar pressure trend reversal as displayed by experimental data. However, the pressure at which the reversal occurs is dependent on the value of *K'* (*dK/dP*) for magnesite employed for which literature values vary between 2.3 - 4 (Fiquet et al., 1994; Litasov et al., 2008; Ross, 1997). A linear extrapolation of the results shown in figure 4.6 infers that at pressures above approximately 100 GPa magnesite may coexist with Fe-Ni metal at an fO_2 below IW and, therefore, would be the dominant host for carbon at the very base of the mantle in the so called D" region.

An important aspect for the redox state of the deep mantle is to understand how the fO_2 relates to the $Fe^{3+}/\sum Fe$ ratio of the mineral phases and the metal content of the mantle. Wadsleyite and garnet synthesized at the conditions where they would coexist in the transition zone have $Fe^{3+}/\sum Fe$ ratios of 0.02 and 0.1 respectively in the presence of metallic Fe (Rohrbach et al., 2007; O'Neill et al., 1979). Given that the $Fe^{3+}/\sum Fe$ ratio of the upper mantle is considered to be <0.03 this means that metallic Fe-Ni alloy must form through FeO disproportionation in the transition zone to produce Fe_2O_3. However, our results show that at 16 GPa and an fO_2 approximately 3 log units above IW where magnesite is stable, wadsleyite has only a slightly higher $Fe^{3+}/\sum Fe$ ratio of 0.04, i.e. once any accompanying metal

had been oxidized a relatively large increase in fO_2 would occur as a result of a relatively small oxidation of wadsleyite. A similar situation would exist in the lower mantle where aluminous perovskite and ferropericlase have $Fe^{3+}/\sum Fe$ ratios of approximately 0.6 and 0.02 in the presence of metallic Fe. If upper mantle bulk oxygen content is assumed this would require disproportionation of FeO to produce 1 weight % Fe-Ni alloy. However in the presence of magnesite the $Fe^{3+}/\sum Fe$ ratios of both phases are essentially the same. The implication is that once Fe-Ni metal has either been oxidized or separated in the lower mantle, relatively little further oxidation would be necessary to raise the fO_2 3 log units from below IW to the magnesite stability field. This observation underlines the fact that Fe-Ni metal will buffer the oxygen fugacity in the lower mantle but once the metal is oxidized the fO_2 of the lower mantle would be very poorly buffered and could be very heterogeneous.

Finally, it is interesting to note that some ferropericlase inclusions in diamond, which are proposed to have been trapped in the lower mantle, exhibit high Ni contents of up to 1-2 weight % (Harte et al., 1999). This implies formation of the inclusions at conditions above Fe-Ni metal stability and similar to those where magnesite could be stable. This might imply that the inclusions were trapped at the top of the lower mantle where the aluminium content of silicate perovskite is lower, due to the presence of garnet, which results in lower perovskite Fe^{3+} contents. If the perovskite Fe^{3+} content is lower little or no metallic Fe may be required to form and mantle oxygen fugacities above IW would be quite plausible. Alternatively the high Ni contents may imply that some regions of the lower mantle are free of metallic Fe as a result of extreme oxidation to levels where $Fe^{3+}/\sum Fe$ ratios of over 0.5 are possible without disproportionation of FeO to form metallic Fe.

In conclusion, this study provides information on the redox conditions at which diamond and carbonate exist at depths to ~1100 km with respect to the expected fO_2 of the mantle. Experimental data were used to test the validity of thermodynamic data applied to equilibrium (4.2) and imply that K^1 (the

pressure derivative of the bulk modulus) is likely to be less than 4. The results indicate that carbonates might become the stable host for carbon at the base of the mantle.

5. Fe^{3+}/Fe_{tot} measurements of garnets equilibrated with carbon and carbonate in a peridotite assemblage

5.1 Introduction

Redox conditions of the Earth's mantle can be determined by either combining $Fe^{3+}/\sum Fe$ measurements of fresh basalt glasses with calibrations for the Fe^{3+}- fO_2 relationship of mantle melts (Sack et al., 1980; Jayasuriya et al., 2004) or by performing oxy-thermobarometry determinations on mantle xenoliths, which employ heterogeneous equilibria involving oxidation of Fe-bearing minerals (O'Neill and Wall, 1987; Luth et al., 1990; Nell and Wood, 1991; Luth and Canil, 1993). To date most measurements have employed oxy-thermobarometry on spinel-bearing xenolith samples, which indicate that shallower regions of the upper mantle (<50 km depth) are typically characterized by an oxygen fugacity in the range +1 to -3 log units relative to the FMQ buffer (Frost and McCammon, 2008).

The origin of this range in fO_2 remains obscure, however, and it is clear that the mantle seems not to be buffered at a particular fO_2 but displays a range of values potentially resulting from the actions of partial melting and metasomatism (McCammon et al., 2001).

The fO_2 of deeper-formed garnet-bearing xenoliths brought to the surface generally by kimberlitic magmas, can be determined using the equilibrium,

$$\underset{\text{garnet}}{2Fe_3Fe_2^{3+}Si_3O_{12}} = \underset{\text{olivine}}{4Fe_2SiO_4} + \underset{\text{opx}}{2FeSiO_3} + O_2 \qquad (5.1)$$

This equilibrium requires the determination of the ferric iron content of natural garnets, which allows the proportion of the skiagite ($Fe_3Fe_2^{3+}Si_3O_{12}$) garnet end-member to be calculated. The thermodynamic treatment of equilibrium (5.1) was accurately described by Luth et al. (1990), and then calibrated by Gudmundsson and Wood (1995) through a series of experiments where garnet peridotite

samples were equilibrated at measured oxygen fugacities. Recovered garnet layers from within the experimental samples were analysed using Mössbauer spectroscopy to determine the $Fe^{3+}/\sum Fe$ ratio. Other heterogeneous equilibria have been proposed as potential oxybarometers such as:

$$\underset{\text{cpx}}{4CaFe^{3+}AlSiO_6} + \underset{\text{opx}}{3Fe_2Si_2O_6} = \underset{\text{cpx}}{2CaAl_2SiO_6} + \underset{\text{cpx}}{2CaFeSi_2O_6} + \underset{\text{olivine}}{4Fe_2SiO_4} + O_2 \qquad (5.2)$$

or

$$\underset{\text{garnet}}{2Ca_3Fe_2^{3+}Si_3O_{12}} + \underset{\text{opx}}{6MgSiO_3} + \underset{\text{opx}}{4FeSiO_3} = \underset{\text{cpx}}{6CaMgSi_2O_6} + \underset{\text{olivine}}{4Fe_2SiO_4} + O_2 \qquad (5.3).$$

Their use, however, is limited by the lack of thermodynamic data relative to the Fe^{3+}-bearing end members owing to the complexity of the appropriate activity-composition models in multisite phases like garnet and clinopyroxene.

Oxygen fugacity determinations of xenolith rocks from kimberlites are of obvious interest due to the presence of both diamond and carbonate in such samples (Mitchell, 1986) and the need to understand the diamond formation process. Kimberlitic xenoliths are sampled from a range of depths in the Archean (2.5 billion years old) lithosphere, which can also be assessed from the use of thermobarometers. Therefore, the variation of fo_2 through the lithosphere with depth can be studied. A number of studies have demonstrated a general decrease in the fo_2 of garnet peridotite rocks measured using equilibrium (5.1) as a function of equilibration depth in various Archean cratons (Woodland and Koch, 2003). This mainly arises from the effect of pressure on equilibrium (5.1) as the volume change for this equilibrium has been determined to be positive (Gudmundsson and Wood, 1995). This positive volume change will drive the calculated oxygen fugacities for equilibrium (5.1) down with pressure for a constant bulk composition and oxidation state. This has been noted by many authors (Wood et al., 1990; O'Neill et al., 1993b; Ballhaus, 1995) and it has even been proposed that the decrease in fo_2 with

depth caused by the positive volume change of (5.1) may result in fO_2 conditions low enough for metallic Fe-Ni alloy to form in the mantle at depths greater than 200 km (Rohrbach et al., 2007).

The calibration of equilibrium (5.1) by Gudmundsson and Wood (1995) implies that if the fO_2 buffered by a garnet peridotite assemblage is to remain constant relative to the FMQ buffer with increasing pressure, then the Fe^{3+} content of garnet has to increase. In chapter 3 it was shown that the EMOG/D buffer remains lower but broadly parallel to the FMQ buffer with increasing pressure.

Therefore, if the oxygen fugacity of a garnet-peridotite assemblage is buffered by the coexistence of graphite and carbonate then by 6 GPa the garnet $Fe^{3+}/\sum Fe$ ratio should increase to approximately 40%. Such high ferric iron levels have never been observed in natural samples, even in those that have experienced metasomatism (McCammon et al. 2001; Creighton e al., 2009). Hence, the suspicion exists that oxygen fugacities determined using equilibrium (5.1) might be underestimated at pressures far from the conditions at which equilibrium (5.1) was calibrated.

The aim of this study was, therefore, to investigate the iron oxidation state of garnet equilibrated with carbonate and graphite/diamond in a typical mantle assemblage where the oxygen fugacity was fixed at known values as a function of pressure and temperature. Through these measurements the validity of the Gudmundsson and Wood (1995) calibration for equilibrium (5.1) can be tested at pressures much higher than those at which it was calibrated. A re-evaluation of the calibration can also be performed and the effect on fO_2 determinations of natural samples can also be examined.

5.2 Experimental methods

Starting materials were similar to those described in Chapter 3 with the addition of a layer of garnet composition material sandwiched between layers of the buffering carbon/carbonate bearing assemblages (EDDOG2 and EMOG1), either lherzolitic or harzburgitic and placed inside a graphite

capsule. $Py_{85}Alm_{15}$ and $Py_{79}Alm_{16}Gr_5$ garnet solid solutions were prepared as glasses from dried high purity MgO, Al_2O_3, $CaCO_3$, Fe_2O_3 and SiO_2 as representative of a simplified fertile garnet composition (Nixon and Boyd, 1973). After weighing, the oxide mixture was ground under ethanol in an agate mortar. The dried mixture was placed into a platinum crucible and decarbonated by heating at a rate of 150 °C/hour to 1000 °C. The powder was then glassed by heating for 2 hrs at 1600 °C and then quenched in a steel plate filled with water and ice. The recovered glass was crushed into small chips in a steel mortar, cleaned by a magnet to remove steel shards and then re-glassed in a repeat of the described procedure to ensure homogeneity. A few fragments of each glass were collected for microprobe measurements to monitor the composition and the iron loss as a function of time. The use of temperatures significantly above the melting point is required in order to quench a glass free of crystals. Preliminary observations using an electron microscope were necessary in order to exclude the presence of quench crystals, e.g. spinels. The final glass was crushed, ground dry in an agate mortar for 30 min and reduced in a gas-mixing furnace at 800 °C for several hours in a gaseous mixture of CO_2/CO and CO_2/H_2 corresponding to the NNO buffer, to obtain a low initial ferric Fe content. The final powder was stored in a desiccator ready for use.

Two experiments (V615a and V620a) were performed using a natural chromium-bearing garnet (FSM1 garnet by Woodland and Koch, 2003) and H_2O was added to one experiment (S4402) by adding $Mg(OH)_2$ to the starting material. Compositions of starting glasses and natural Cr-bearing garnets are shown in Table 5.1. Experimental details (pressure media, multi anvil devices and pressure calibration) are described in more detail in Chapters 2 and 3. Experiments were performed between 3 and 11 GPa and temperatures of 1150-1600 °C, then quenched by turning off the power to the furnace after a period of between 6 and 25 hours.

In order to test equilibrium (5.1) we conducted experiments using three different starting mixtures as sandwiched layers: 1) with only garnet glass as in Gudmundsson and Wood (1995); 2) adding 20%

of magnesite + opx + Ir mixed with the garnet; 3) adding 20% of the buffering carbon-carbonate assemblage (olivine + magnesite + opx + Ir) mixed within the garnet layer (see Table 5.2).

Chemical compositions of the mineral phases including garnet were obtained using the electron microprobe (technical procedure as described in chapters 2 and 3).

Table 5.1 Starting composition of garnet.

Wt. %	Ca-bearing [22]	Ca-free [17]	Cr-rich ($^{+}$FSM1)
SiO_2	43.20(22)	44.60(41)	42.60
Al_2O_3	22.73(15)	24.13(23)	21.33
Cr_2O_3	-	-	1.87
FeO*	8.20(8)	5.91(10)	7.28
MgO	21.33(11)	25.65(23)	21.86
CaO	4.52(6)	-	4.38
Na_2O	-	-	0.04
NiO	-	-	0.01
Tot.	99.98(38)	100.28(38)	99.37
$Fe^{3+}/\sum Fe$	-	-	0.088
Fe#	0.16	0.11	0.13

Notes: Figures in parentheses [ ] indicate total number of analyses; numbers in parentheses ( ) are standard deviations. (*) Total Fe as FeO. ($^{+}$) Garnet composition as reported by Woodland and Koch (2003). Fe# calculated as *XFe/(XFe+XMg+XCa)*.

The ferric/ferrous iron ratio of the sandwiched garnets in the recovered run products was determined by ^{57}Fe Mössbauer spectroscopy. Thick sections were prepared of the samples and polished to a thickness of approximately 200-300 μm to provide Fe levels of less than 5 mg Fe/cm^2 and avoid saturation effects in Mössbauer measurements (Long et al., 1983). Spectra were collected at 298 K using a nominal 370 MBq ^{57}Co point source (McCammon, 1994). Mirror image spectra were collected over 512 channels using a multichannel analyser for between 2 and 6 days over a sample region of 200-500 μm in diameter. A velocity range of -5 to +5 mm/s was always used. The velocity scale was

calibrated relative to a 25 μm thick α-Fe foil. No spectra were collected at 77 K since it has been demonstrated that the temperature dependence of the ratios of recoil-free fractions in dodecahedral and octahedral sites can be neglected (Gudmundsson and Wood, 1995). Finally, spectra were folded and fitted to Lorentzian line-shapes (as described in chapter 2) using the fitting program NORMOS written by R.A. Brand (distributed by Wissenschaftliche Elektronik, Germany).

Spectra were fitted using one asymmetric doublet for ferrous iron in the dodecahedral site and one symmetric doublet for ferric iron in the octahedral site (Amthauer et al., 1976; Luth et al., 1990) with the hyperfine parameters left unconstrained. Although most layers consisted primarily of garnet, the contribution of ferric iron could be better resolved when hyperfine parameters for opx and olivine were included in the fit for experiments where these minerals were also present in the layer. Relative areas could be determined with good precision by including symmetrical doublets for ferrous iron corresponding to each phase, with hyperfine parameters as reported by O'Neill et al. (1993). Small amounts of metallic iron dissolved in the iridium alloy redox sensor or iron in minor amounts of diopside were not taken into account while fitting the spectra.

Table 5.2 Conditions and run products of garnet sandwiched layer experiments.

Run no	P (GPa)	T (°C)	Duration (hr)	Phases										
				before					after					
V621a	3	1250	25	Ol	Opx	Gnt	Mst	Ir	Ol	Opx	Cpx	Gnt	Liq	alloy
V621b	3	1250	25	Ol	Opx	Gnt		Ir	Ol	Opx		Gnt		alloy
V587a	3	1400	24		Opx	Gnt	Mst	Ir	Ol	Opx	Cpx	Gnt	*Liq/G	alloy
V606a	6	1150	23	Ol	Opx	Gnt	Mst	Ir	Ol	Opx	Cpx	Gnt	mst	alloy
V604a	6	1300	11	Ol	Opx	Gnt	Mst	Ir	Ol	Opx	Cpx	Gnt	mst	alloy
V605a	6	1400	12	Ol	Opx	Gnt	Mst	Ir		Opx	Cpx	Gnt	Liq	alloy
V615a	6	1200	12	Ol	Opx	Gnt	Mst	Ir	Ol	Opx	Cpx	Gnt	mst	alloy
V620a	6	1350	19	Ol	Opx	Gnt	Mst	Ir		Opx		Gnt	Liq/G	alloy
V458a	7	1350	12			Gnt						Gnt		
V517a	7	1500	12		Opx	Gnt	Mst	Ir	Ol	Opx	Cpx	Gnt	*Liq	alloy
S4402a	7	1400	6			Gnt						Gnt	(*Liq)	
V492a	7	1400	12		Opx	Gnt	Mst	Ir		Opx	Cpx	Gnt	Liq/G	alloy
V564a	7	1600	12		Opx	Gnt	Mst	Ir		Opx	Cpx	Gnt	Liq/G	alloy
H2759b	7	1400	12			Gnt						Gnt		
V493b	7	1400	12		Opx	Gnt	Mst	Ir		Opx		Gnt	mst	alloy
V524b	7	1500	12		Opx	Gnt	Mst	Ir		Opx		Gnt	*mst	alloy
V565a	11	1400	12		Opx	Gnt	Mst	Ir		*Opx	Cpx	Gnt	mst	alloy
S4230a	11	1500	12			Gnt						Gnt		
S4232b	11	1500	12			Gnt						Gnt		

Notes: (*) indicates phases of which the chemical composition was not measurable due to the small size. a and b indicate Ca-bearing and Ca-free assemblages, respectively.

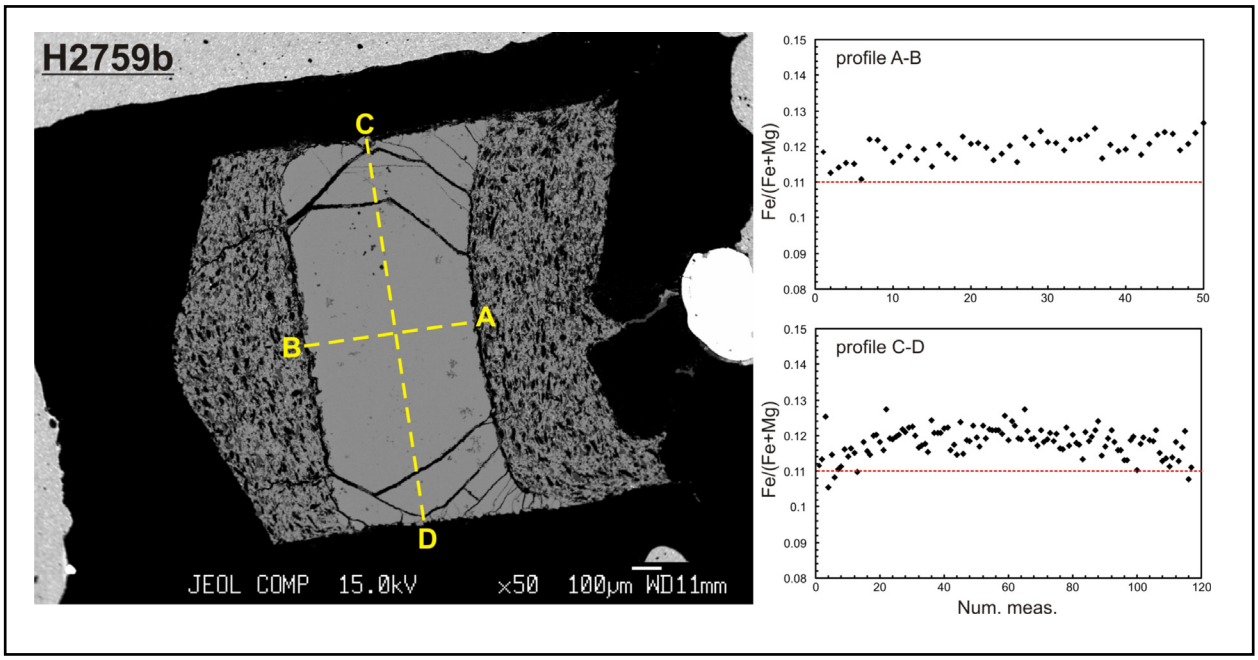

Figure 5.1 (Left panel) BSE image of run H2759b (Ca-free assemblage) with a sandwiched layer made of garnet. Yellow dashed lines indicate the measuring profiles. (Right panel) Shown is the variation of the Fe/(Fe+Mg) ratio along A-B and C-D lines measured along the garnet layer by steps of ~5 µm. Red dashed lines referred to the nominal Fe/(Fe+Mg) ratio.

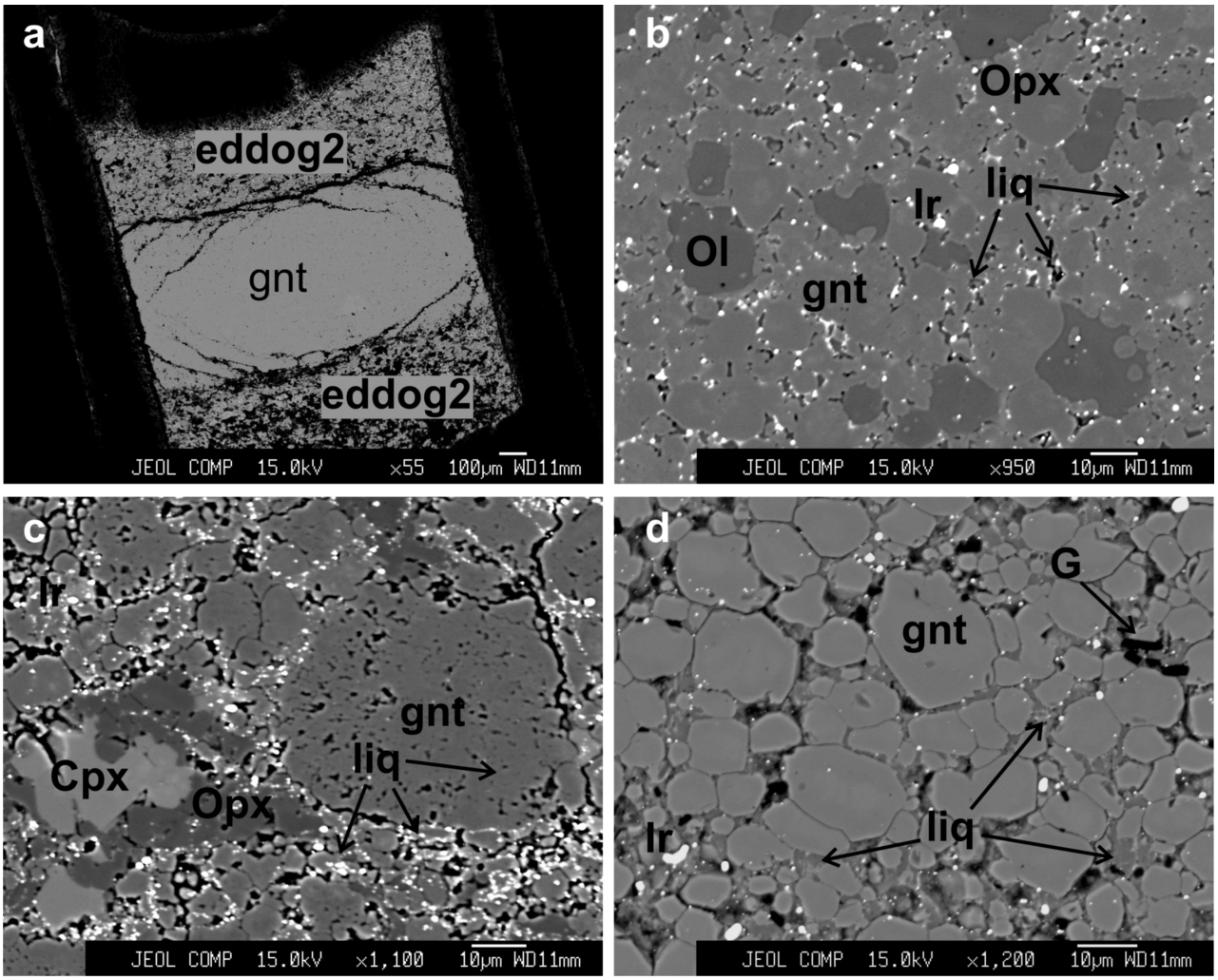

Figure 5.2 (a) BSE image showing the garnet layer experiment recovered from S4402a run (plus H_2O) at 7 GPa and 1400 °C. (b) Run V621a shows the coexistence of interstitial liquid (Ca/ (Ca+Mg+Fe) of 0.55) along with other silicate phases. The bright phase is the Ir-Fe alloy redox sensor. (c) Run V492a (7 GPa/1400 °C) shows cpx surrounded by opx and in contact with garnet. Small dark spots are interpreted as traces of melt removed during polishing and tiny graphite laths. (d) Run V620 (6 GPa and 1350 °C) shows the occurrence of melt around grains of garnet. It is noteworthy the presence of graphite (G) crystallized from a Ca-rich carbonate liquid.

5.3 Results

5.3.1 Phase compositions and attainment of divalent cation equilibrium

Each recovered experiment contained a central garnet-rich layer sandwiched between layers of a nominally garnet free C-bearing peridotite assemblage. Some garnet layers consisted solely of garnet; however, in most experiments opx, magnesite and olivine were added to the layer, in addition to Fe-Ir

alloy. In some experiments melt was present in the layer and, sometimes clinopyroxene and graphite were formed. Experimental conditions and phase assemblages of the sandwiched layer are summarized in Table 5.2 while, chemical compositions of the run product layers are reported in Table S5.1 and S5.2 of the Appendix. Tables S3.1 and S3.2 of the Appendix list compositions of phases in the layers above and below the garnet layer, as small variations exist between the layers.

Recovered garnet textures and iron contents reflected the initial glass starting composition. For instance, experiments performed using only glass produced crystals greater than about 10 μm in diameter with a *Fe/(Fe+Mg)* corresponding on average to the nominal value of 0.16 (Ca-bearing) and 0.11(Ca-free). Iron contents in garnet from experiments at higher temperature were lower, most likely as a result of loss of iron to the melt. Some profile measurements randomly conducted across garnet layers showed a gradual change in composition from the center to the top and bottom layers and even laterally in contact with the graphite capsule (figure 5.1). These can be explained by varying degrees of disequilibrium with the surrounding layers and by thermal gradients across the sample.

When possible measurements were made on phases found within the garnet layers. Only where phases were missing from the garnet layer was it necessary to consider compositions of phases from the adjacent layers.

As shown in Table 5.2, in most garnet layers magnesite and opx were added to ensure the presence of sufficient oxidant and to buffer the silica activity. In Ca-bearing experiments this led to the formation of clinopyroxene (figure 5.2c) as a product of the reaction,

$$Ca_3Al_2Si_3O_{12} + 6MgSiO_3 \rightarrow Mg_3Al_2Si_3O_{12} + 3CaMgSi_2O_6 \qquad (5.4).$$

Although clinopyroxene is known to have a relatively high $Fe^{3+}/\sum Fe$ in peridotite rocks (Luth and Canil, 1993; Woodland, 2009), we can safely neglect the contribution of this phase to Mössbauer measurements due to its small modal concentration and low total iron content <4 wt. %. The chemical

composition of resultant clinopyroxene was consistent with the composition of clinopyroxenes formed in the garnet-free upper and lower layers of samples reported in Chapter 3. Experiments above the melting temperature of magnesite produced liquids with a composition (when measurable) similar to those produced in the top or bottom layers although characterized by a smaller melt fraction due to either the initial lower abundance of carbonate in the layer starting mixture or expulsion of the melt from the garnet-rich layer.

Figures 5.3a and b show the Fe-Mg distribution coefficient (K_D) calculated between garnet and olivine in experiments with both Ca-bearing and Ca-free assemblages and plotted versus temperature. Curves calculated from the experimentally calibrated model of O'Neill and Wood (1979) are shown for comparison. The K_D value was calculated as follows,

$$K_D = \frac{X_{Mg}^{ol} \cdot X_{Fe}^{gt}}{X_{Mg}^{gt} \cdot X_{Fe}^{ol}} \qquad (5.5)$$

It can be observed that the experimental data and the predicted trends are quite consistent particularly for experiments at pressures of 6 and 7 GPa. In addition the effect of pressure on the K_D is consistent with the calibrated model, with only a few outliers. A similar result is observed for experiments in the Ca-free assemblage (Figure 5.3b). Figure 5.3c summarizes all the data in terms of the experimental versus predicted distribution coefficients, calculated to fully account for the Ca and Fe contents of the phases in each experiment. Where discrepancies occur these can be generally attributed to experiments where olivine was not present in the garnet-rich layer and olivine compositions were taken from analyses of the adjacent garnet-free layers. The Ca-Mg exchange between garnet and clinopyroxene (figure 5.3d) apparently increases slightly as a function of temperature but most values are well

clustered around the previously observed range (Luth et al., 1990; Mukhopadhyay, 1991; Woodland, 2009).

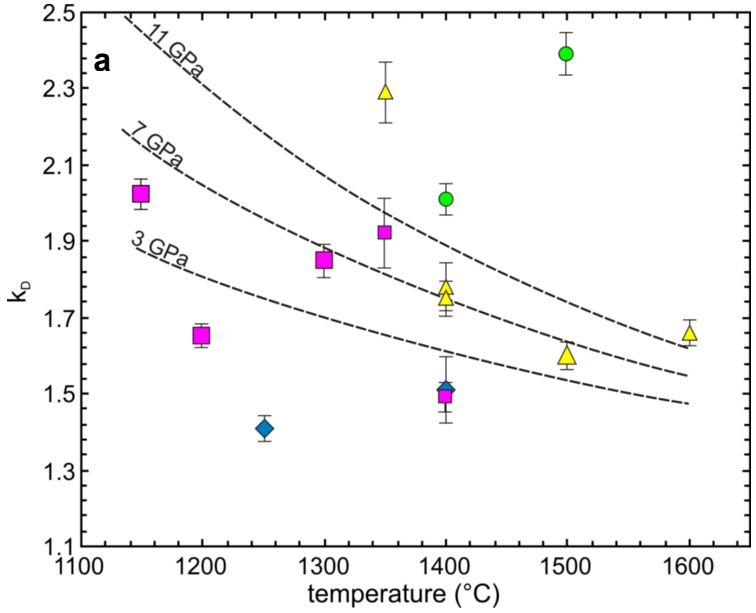

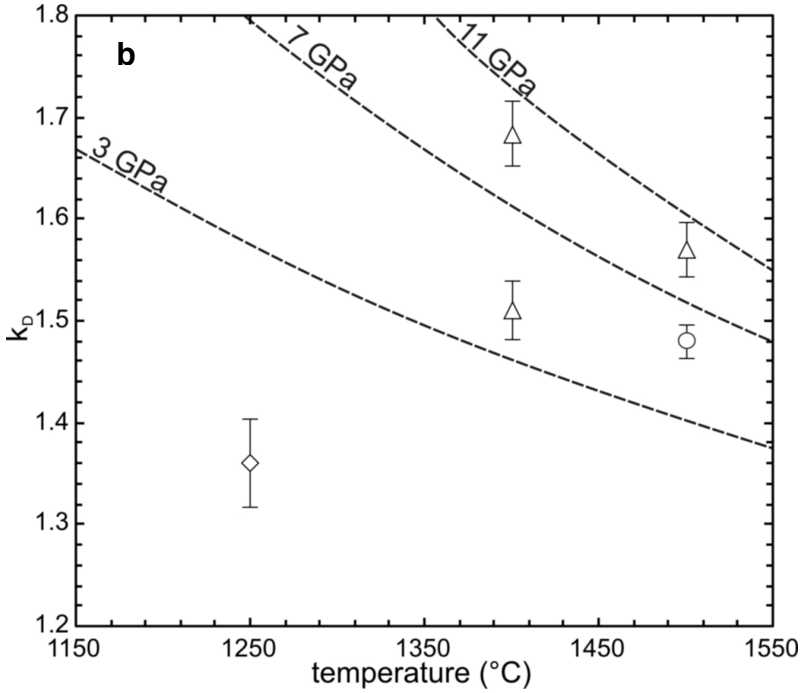

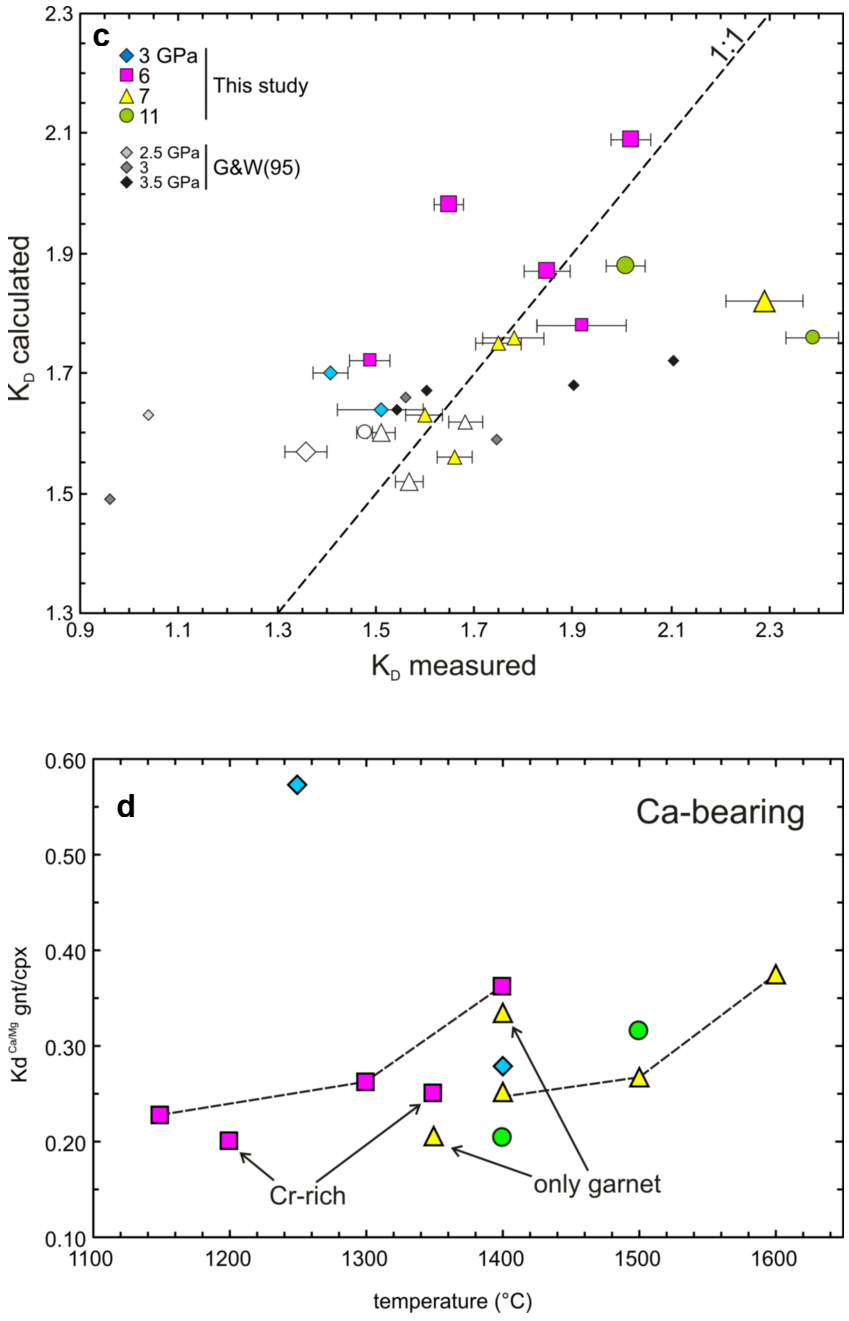

Figure 5.3 (a) The Fe-Mg distribution coefficient between garnet and olivine is plotted as function of temperature. Symbols as follow: blue diamonds indicate runs at 3 GPa; pink squares runs at 6 GPa; yellow triangles 7 GPa runs; 11 GPa are indicated with green circles. Dashed lines are drawn based on the model by O'Neill and Wood (1979). b) Same symbols as above but gray to indicate Ca-free assemblage. (c) The K_D calculated from garnet and olivine run products is plotted versus the predicted values using the corrected equation given by O'Neill and Wood (1979). Along the dashed line the ratio between the K_D calculated and measured is equal to 1. (d) The Ca-Mg distribution coefficient is calculated as $[(X_{Ca})gnt \cdot (X_{Mg})cpx]/ [(X_{Ca})cpx \cdot (X_{Mg})gnt]$ and plotted versus temperature for experiments in the Ca-bearing system. "Only garnet" refers to monomineralic sandwiched layers. Symbols like for figure 3a.

5.3.2 Oxygen fugacity measurements employing iridium as redox sensor

The oxygen fugacity was buffered in each experiment through the coexistence of carbon (graphite or diamond) and carbonate phases (dolomite or magnesite) or melts species (Chapter 3). Therefore, the garnet ferric iron contents should have equilibrated with the imposed oxygen fugacity. Subsolidus buffering assemblages were,

$$\underset{\text{opx}}{MgSiO_3} + \underset{\text{magnesite}}{MgCO_3} = \underset{\text{olivine}}{Mg_2SiO_4} + \underset{\text{graph/diam}}{C} + O_2 \qquad (5.6)$$

in a Ca-free assemblage and

$$\underset{\text{enstatite}}{2Mg_2Si_2O_6} + \underset{\text{dolomite}}{CaMg(CO_3)_2} = \underset{\text{diopside}}{CaMgSi_2O_6} + \underset{\text{olivine}}{2Mg_2SiO_4} + \underset{\text{graph/diam}}{2C} + 2O_2 \qquad (5.7)$$

in a typical lherzolitic assemblage. Solid carbonates were replaced by carbonate melts at temperatures above the solidus, which evolved to become more Si-rich with temperature. Oxygen fugacities were determined experimentally using the Ir-Fe alloy redox sensor. The technique is extensively discussed in Chapter 3 of this thesis along with the propagation of the uncertainties. In most cases mineral Fe/(Fe+Mg) ratios were calculated from olivine and orthopyroxene found within the garnet layer, as with Fe/(Fe+Ir) ratios from the alloy. However, in some instances where additional mineral phases were not added to the garnet layer, it was necessary to use compositions analyzed in the adjacent layers to determine the oxygen fugacity. In experiments where it was possible to determine the oxygen fugacity from phases both within the garnet layer and in the surrounding garnet-free layers, very little difference in the determined fo_2 was observed. Experiments performed as a function of time to test equilibrium of the iridium-iron alloy redox sensor have been discussed in chapters 3.

5.3.3 Ferric iron content of garnets and attainment of redox equilibrium

Results of Mössbauer determinations of the ferric/ferrous iron ratios in garnet-rich layers are shown in Table 5.3 as determined from the relative areas of Fe^{3+} and Fe^{2+} doublets; hyperfine parameters are also reported. When compared to garnet spectra analysed by both Luth et al. (1990) and Gudmundsson and Wood (1995), the I.S. and the Q.S. (isomer shift and quadrupole splitting) appear very similar (figure 5.4a), although some discrepancies arise most likely due to difficulties in fitting spectra with either small ferric iron concentrations or due to interference from the presence of other iron-bearing phases in the layer. In experiments where magnesite, opx and olivine were added to the layer garnet is assumed to be the only ferric iron-bearing phase in the assemblage. This is a safe assumption since no significant amount of Fe^{3+} has been previously reported either for olivine or orthopyroxene (O'Neill et al., 1993).

Table 5.3 Hyperfine parameter for Mössbauer measurement of ferric iron

Sample	Fe^{2+}		Fe^{3+}		$Fe^{3+}/\sum Fe$	χ^2
	I.S.	*Q.S.*	*I.S.*	*Q.S.*		
V587a	1.18	3.56	0.20	0.54	0.066	1.05
V621a	1.16	3.58	0.25	0.32	0.039	1.00
V621b	1.18	3.57	0.20	0.30	0.010	1.06
V606a	1.17	3.56	0.19	0.36	0.049	1.11
V604a	1.21	3.67	0.22	0.27	0.061	0.99
V605a	1.17	3.57	0.23	0.54	0.054	1.22
V615a	1.17	3.63	0.25	0.24	0.102	1.17
V620a	1.21	3.66	0.21	0.33	0.106	0.95
V458a	1.18	3.55	0.10	0.32	0.120	1.08
V517a	1.19	3.57	0.13	0.51	0.113	1.06
S4402a	1.19	3.60	0.23	0.45	0.150	1.04
V492a	1.18	3.57	0.22	0.24	0.075	1.07
V564a	1.17	3.60	0.20	0.25	0.089	0.99
H2759b	1.18	3.64	0.21	0.31	0.050	1.16
V493b	1.17	3.6	0.21	0.31	0.126	0.99
V524b	1.17	3.53	0.10	0.17	0.056	1.22
V565a	1.2	3.63	0.23	0.34	0.060	1.26
S4230a	1.19	3.64	0.24	0.31	0.124	1.06
S4232b	1.17	3.60	0.30	0.40	0.027	1.19

Notes: I.S. stays for isomer shift, while Q.S. for quadrupole splitting. Both are reported in mm/s and measured relative to the α-Fe metal at 298 K. X^2 is the chi-squared referred to the fitted spectra. Results of ferric iron in garnets are characterized by an uncertainty of ±0.02.

The accuracy of the ferric iron determinations was tested with run V587a by taking two different spectra: one measurement carried out over the entire cross section of the sample; a second measurement limited to the layer containing garnet. Fitted spectra are shown in figure 5.4b and both results are consistent and give about 6 % of ferric iron in garnet. The uncertainty in the ideal thickness calculated to reduce the saturation effect was tested collecting a few spectra after re-polishing the samples and resulted in a value within the uncertainty for the measured $Fe^{3+}/\sum Fe$ (±2%). Finally, small amounts of ferric iron measured in recovered garnets (V621b and S4432b) seem to confirm the absence of significant Fe^{3+} in the starting glasses.

Figure 5.5 shows $Fe^{3+}/\sum Fe$ ratios of garnets as a function of pressure compared to $Fe^{3+}/\sum Fe$ ratios of garnet-bearing mantle peridotites from different localities. $Fe^{3+}/\sum Fe$ ratios are also shown from the calibration experiments of Gudmundsson and Wood (1995). It is noteworthy that the ferric/ferrous contents of garnets equilibrated in this study cover a similar range to measurements made on garnets from mantle xenoliths. $Fe^{3+}/\sum Fe$ garnet ratios from the calibrations of Gudmundsson and Wood (1995), on the other hand, are in general more oxidized than most natural samples.

The relationship between the garnet $Fe^{3+}/\sum Fe$ ratio and the fo_2 determined with the iridium redox sensor (FMQ normalized) is shown in figure 5.6. The results of the calibration experiments of Gudmundsson and Wood (1995) are also shown for comparison. In the study of Gudmundsson and Wood (1995) the final garnet $Fe^{3+}/\sum Fe$ ratios were approached from natural garnet starting materials that had both higher and lower initial $Fe^{3+}/\sum Fe$ ratios, as shown in figure 5.6. However, reversals were not performed in this previous study at the same oxygen fugacities and at the fo_2 comparable with the current study $Fe^{3+}/\sum Fe$ ratios were only approached from compositions with initial higher levels of Fe^{3+}. Gudmundsson and Wood (1995) also state that reducing garnet ferric Fe contents was extremely sluggish and only a very limited shift in the garnet $Fe^{3+}/\sum Fe$ ratio was possible. In the current study starting garnet glass compositions were employed for most experiments that had initial Fe^{3+} levels

below detection limits and thus, equilibrium was approached from the opposite direction to those of Gudmundsson and Wood (1995).

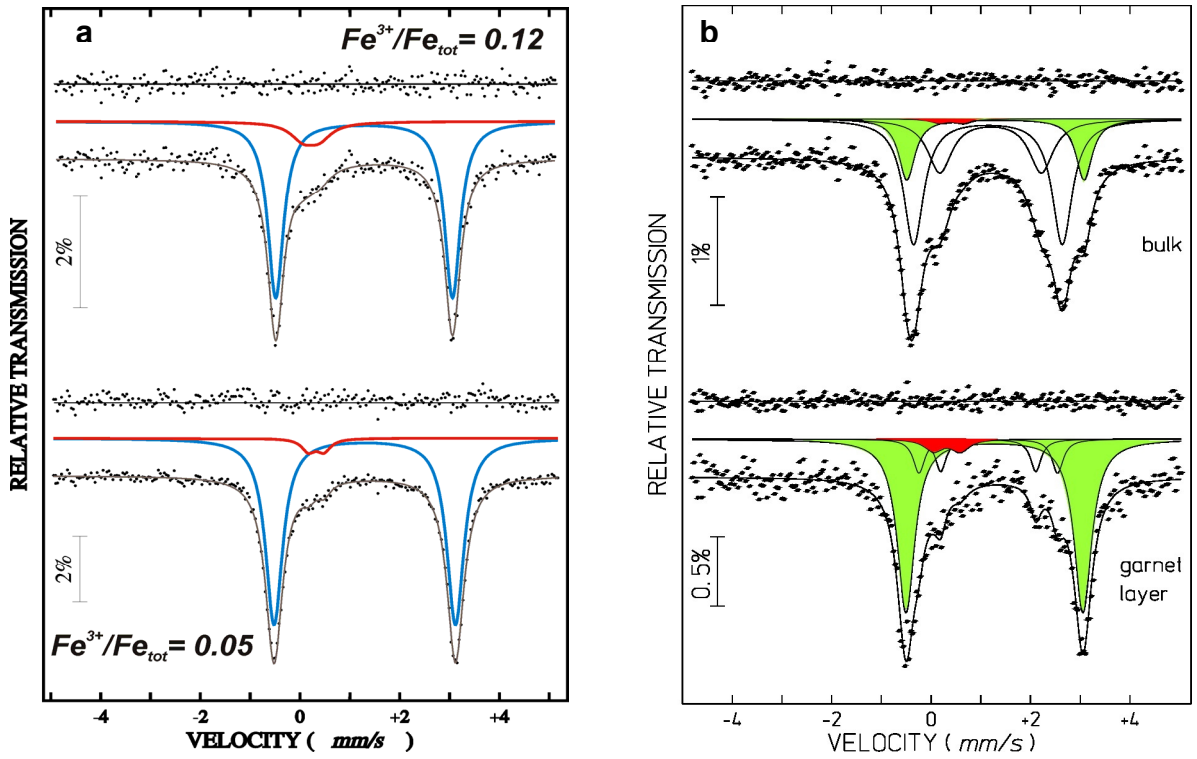

Figure 5.4 (a) Mössbauer spectra of garnet V458a and H2759b at 298 K with ferric iron doublets shown in red. b) Spectra collected from V587a showing differences in line widths and relative areas between a spectrum collected over the entire sectioned sample (bulk) and the spectrum collected only from the garnet-bearing layer. Green and red doublets are representative of ferrous and ferric iron measured in garnet. Small white doublets are also shown, which represent ferrous iron-bearing phases (olivine and orthopyroxene).

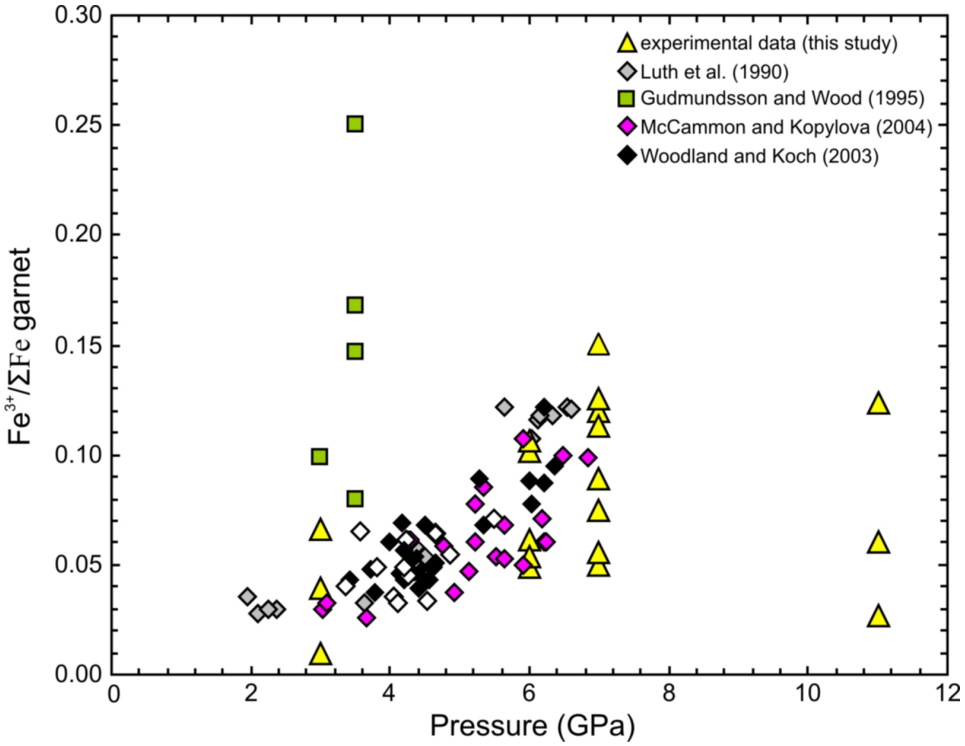

Figure 5.5 Shown is the increase of ferric iron content of recovered synthetic garnets measured by Mössbauer spectroscopy as function of pressure. Ferric iron contents of natural garnets from mantle xenoliths (Kaapvaal Craton, Vitim Plateau, Slave Craton; see legend for references) are also shown for comparison. Green squares are experimental data used to calibrate eq. (5.1) and reported by Gudmundsson and Wood (1995).

As several different experimental configurations were employed in this study, by comparing the extent of garnet oxidation with the reversals of Gudmundsson and Wood (1995) it is possible to assess which of the configurations from this study are likely to have reached equilibrium. Firstly, some of the lowest garnet $Fe^{3+}/\sum Fe$ ratios occurred in experiments where magnesite was not added to the garnet layer and the temperatures were too low for melting to occur. These experiments (i.e., V621b, H2759b) therefore, likely did not reach redox equilibrium with the buffering carbon-carbonate assemblage due to the lack of local oxidizing agent and are excluded from further consideration. Secondly, subsolidus experiments appear also to result in low $Fe^{3+}/\sum Fe$ ratios that can be excluded (V606a). A number of experiments were performed at 1400 °C and 6-7 GPa, which although performed at almost identical conditions resulted in varying levels of garnet Fe^{3+} content. The highest levels of Fe^{3+} were reached when either H_2O was added to the sample (S4402a) or when the sample was Ca-free (V493b).

However, in a few experiments it is unclear why similar conditions rendered garnet Fe^{3+} contents that were so different. Experiment V524b for example performed in a Ca free system at 7 GPa and 1500 °C produced garnet with a $Fe^{3+}/\sum Fe$ ratio of only 0.055, where as experiment V493b, which was identical except being run at 100 °C lower in temperature, produced garnet with a $Fe^{3+}/\sum Fe$ ratio of 0.126. In several instances, however, the highest levels of Fe^{3+} were reproducible from different starting materials such as at 6 GPa and 1350°C where garnet $Fe^{3+}/\sum Fe$ ratios of 0.12 and 0.11 were obtained from synthetic glass and natural garnet starting compositions respectively. From the consistency of these repeated experiments it is assumed equilibrium was achieved.

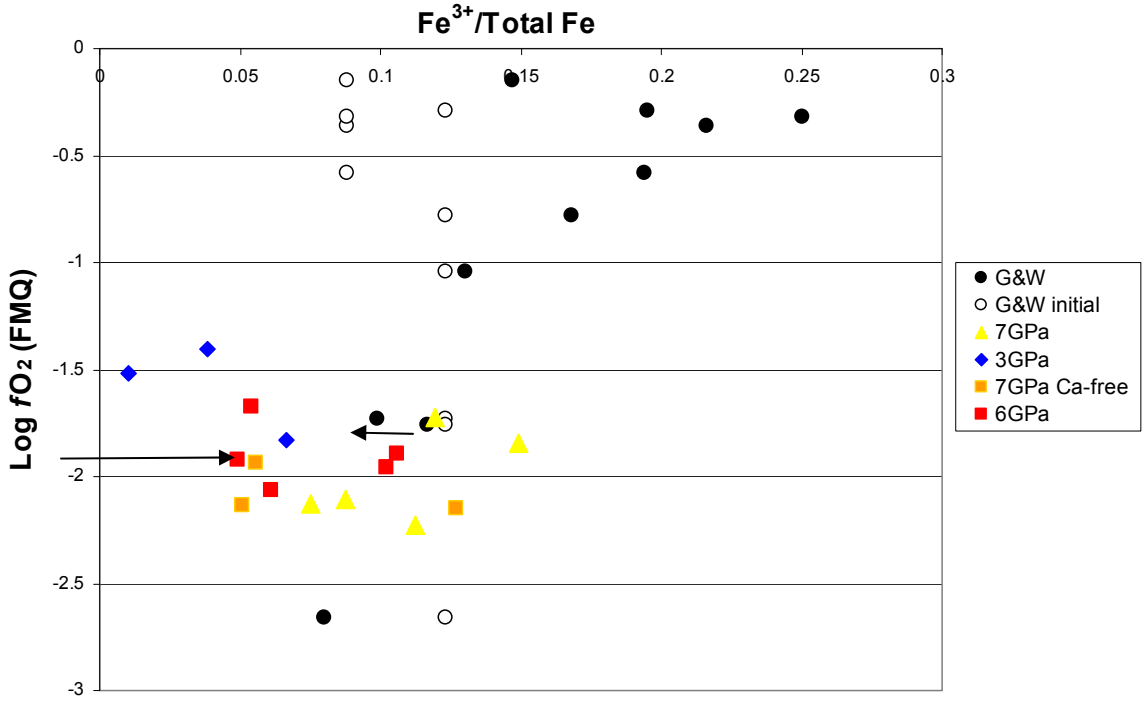

Figure 5.6 $Fe^{3+}/\sum Fe$ ratio of garnets from experiments performed at different pressures plotted against oxygen fugacity determined from the Ir-alloy redox sensor normalized to FMQ. G&W refers to the previous measurements of Gudmundsson and Wood (1995) from samples equilibrated at 3 - 3.5 GPa and 1300 °C. Arrows indicate the approach to equilibrium for two experiments performed at approximately the same conditions from this study and that of Gudmundsson and Wood (1995). Open circles indicate G&W starting garnet compositions.

5.4 Oxygen-thermobarometry measurements on the experimental garnet peridotite assemblages

The fo_2 within the garnet-bearing layers of the experiments can be calculated using the oxy-thermobarometer given by equilibrium (5.1) in order to test the validity of the extrapolation of the calibration of Gudmundsson and Wood (1995) for this equilibrium to pressures greater than 3.5 GPa. The fo_2 is calculated from the expression,

$$\log fo_2 = \frac{-\Delta G^{o}_{r}}{\ln(10)RT} + 2\log a^{Gt}_{Fe_3Fe_2Si_3O_{12}} - 2\log a^{Opx}_{FeSiO_3} - 4\log a^{olivine}_{Fe_2SiO_4} \qquad (5.8)$$

where $a^{Gt}_{Fe_3Fe_2Si_3O_{12}}$, $a^{Opx}_{FeSiO_3}$ and $a^{olivine}_{Fe_2SiO_4}$ are the Fe-end member activities of each silicate phase and ΔG^{O}_{r} is the standard state free energy of equilibrium (5.1). The activity of fayalite was calculated using a single-site symmetric regular solution equation,

$$a_{Fay} = X_{Fay} \cdot e^{\frac{W(1-X_{Fay})^2}{RT}} \qquad (5.9)$$

with X_{Fay} calculated as Fe/(Fe+Mg) from the olivine composition and the interaction parameter W^{Ol} is 3.7 kJ/mol (Wiser and Wood, 1991). The exponential term corresponds to the activity coefficient of fayalite. The activity of ferrosilite in opx was calculated assuming ideal mixing between M1 and M2 sites as follow,

$$a_{Fs} = X^{M2}_{Fe} \cdot X^{M1}_{Fe} \cdot \gamma_{Fe_2Si_2O_6} \qquad (5.10)$$

with γ_{Fs} equal to 1 (Wood and Banno, 1973). Activities for both phases are listed in Table S5.1 (Appendix). The activity of skiagite in garnet was calculated using the corrected expression for the skiagite activity coefficient given by Woodland and Peltonen (1999) where non-ideal mixing is assumed between cubic and octahedral sites and appropriate reciprocal reactions are also employed (Luth et al., 1990) involving grossular, andradite, pyrope and skiagite (Wood and Nicholls, 1978).

The ΔG_r^O of (5.1) is determined by sum of the free energy of formation of reagents and products in equilibrium (5.1) calculated at a given pressure and temperature and it is related to the equilibrium constant of the reaction (5.1) by,

$$\log K_1 = \frac{-\Delta G_r^O}{RT\ln(10)} \qquad (5.11),$$

with P in bars and T in Kelvin.

Gudmundsson and Wood (1995) formulated an equation for $\log K_1$ expressed as function of pressure and temperature, as follow

$$\log K_1 = 9.79\text{-}20400/T\text{-}0.045P/T \qquad (5.12),$$

derived by combining the free energy of the following reaction (Woodland and O'Neill, 1993),

$$1/3Fe_3Fe_2Si_3O_{12} = 5/3Fe + SiO_2 + O_2 \qquad (5.13),$$

with the free energies of fayalite-iron-quartz (O'Neill, 1987) and quartz-fayalite-ferrosilite (Wood, 1987) reactions and extrapolating the obtained value of $\log K_1$ at 1 bar taking into account the volume and entropy changes over the pressure and temperature of interest of skiagite, opx , olivine (Moecher et al., 1988) and oxygen (Robie et al., 1978).

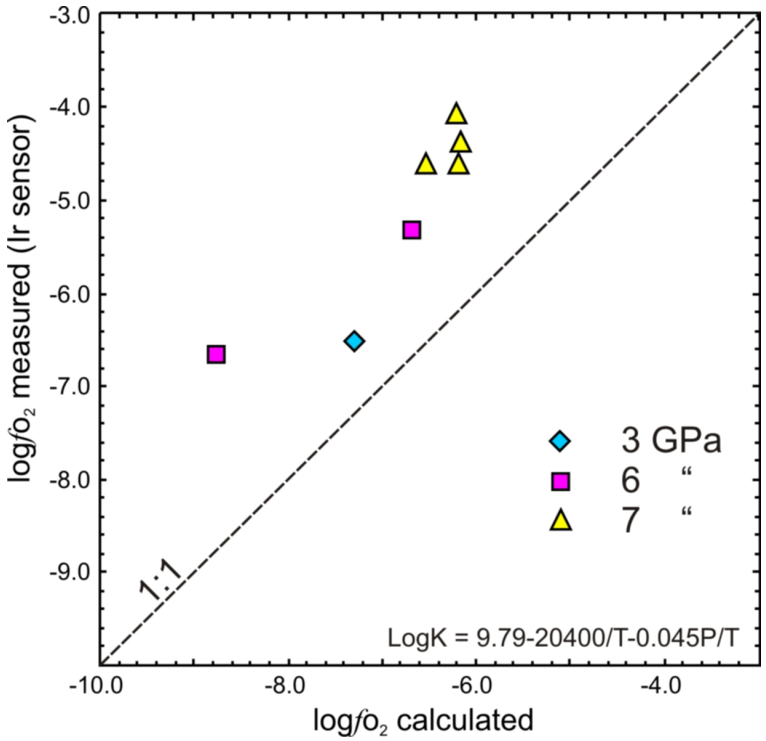

Figure 5.7 Comparison of fO_2 measured with Ir-Fe sensor with fO_2 calculated from eq. (1).

A comparison between fO_2 measured using the Ir-Fe alloy sensor and calculated using expression (5.8) with the data of Gudmundsson and Wood (1995) is shown in figure 5.7. Uncertainties for the alloy sensor are ~0.3 log units taking into account uncertainties in pressure and temperature from experimental runs (0.5 GPa and ± 50 °C), chemical composition of the run products and from thermodynamic data. The calibration of Gudmundsson and Wood (1995) has a stated uncertainty of 0.5 log units. The oxygen fugacities calculated using the previous model are inconsistent with those measured using the Ir-Fe alloy sensor. The divergence is greatest at 6 and 7 GPa with the reversal at 3 GPa being in the best agreement with the model. This implies that the pressure dependence of the Gudmundsson and Wood model may be in error.

Table 5.4 Composition of Ir-Fe alloy and determined oxygen fugacities.

Run no	X_{Fe}(Ir-Fe)	log$f$O$_2$ alloy	log$f$O$_2$ calc	log$f$O$_2$ (EMOG/D)$^+$
V621a	0.125(5)	-7.45	-9.55	-7.36
V621b	0.122(8)	-7.57	-11.31	-7.20*
V587a	0.081(4)	-6.51	-7.29	-6.48
V606a	0.115(5)	-7.10	-9.98	-6.60
V604a	0.120(8)	-5.90	-8.35	-5.49
V605a	0.099(4)	-4.73	-8.23	-4.99
V615a	0.112(5)	-6.66	-8.75	-6.20
V620a	0.102(3)	-5.33	-6.67	-5.22
V458a	0.083(4)	-4.60	-6.18	-4.67
V517a	0.119	-4.06	-6.22	-4.03
S4402a	0.084(2)	-4.36	-6.15	-4.42
V492a	0.120(8)	-4.64	-7.31	-4.51
V564a	0.087(2)	-3.31	-5.80	-3.64
H2759b	0.091(3)	-4.65	-7.60	-4.35
V493b	0.108(5)	-4.61	-6.53	-4.35
V524b	0.074(1)	-3.77	-6.73	-3.80
V565a	0.117	-3.31	-8.13	-2.51
S4230a	0.093(6)	-2.50	-5.66	-2.12
S4232b	0.104(3)	-2.71	-9.22	-2.29

Notes: (*) V621b is a magnesite free run. fO$_2$ was, therefore, calculated using the CCO buffer of Frost and Wood (1997). Numbers in parentheses ( ) are standard deviations from chemical composition of the alloy. (+) fO$_2$ calculated using Stagno and Frost (2010) equations.

5.5 Discussion

5.5.1 Parameterisation of logK as function of pressure and temperature

As shown in figure 5.7 there is a discrepancy between the fO$_2$ determined using the oxy-thermobarometer of Gudmundsson and Wood (1995) on the garnet-layer experimental samples and the determination of fO$_2$ using the Ir-Fe alloy sliding redox sensor. This discrepancy apparently increases with pressure to give discrepancies of the order of 2 log units at 7 GPa. The calibration experiments of Gudmundsson and Wood (1995) were performed mainly at 3 GPa and 1300 °C and at oxygen fugacities between FMQ and FMQ-3. Because these experiments were performed at basically the same pressure and temperature they mainly tested the suitability of the activity-composition model employed for garnet, i.e. they examined the reliability of the fO$_2$ extrapolation rather than the effects of pressure and temperature. The calibration of Gudmundsson and Wood (1995) relies on thermodynamic (O'Neill, 1987; Wood, 1987; Moecher et al., 1988) and volume data (Wood, 1987; Woodland and O'Neill, 1993)

to determine the pressure and temperature dependence of the equilibrium constant K_1 for (5.1), i.e. to obtain equation (5.14). Using the oxygen fugacity and compositional data determined in this study it is possible to calculate the equilibrium constant K_1 in equation (5.11) at each pressure and temperature. In detail, this is performed by rearranging equation (5.8) to calculate ΔG_r^O using the activity models formulated by Gudmundsson and Wood (1995) and the fo_2 determined for each experiment using the Ir-Fe alloy sensor. K_1 is related to ΔG_r^O as in equation (5.11). Results of such a calculation are shown in figure 5.8. Uncertainties propagated from the uncertainty on both the log fo_2 determination and the compositional measurements, including $Fe^{3+}/\sum Fe$, are 0.6 log units.

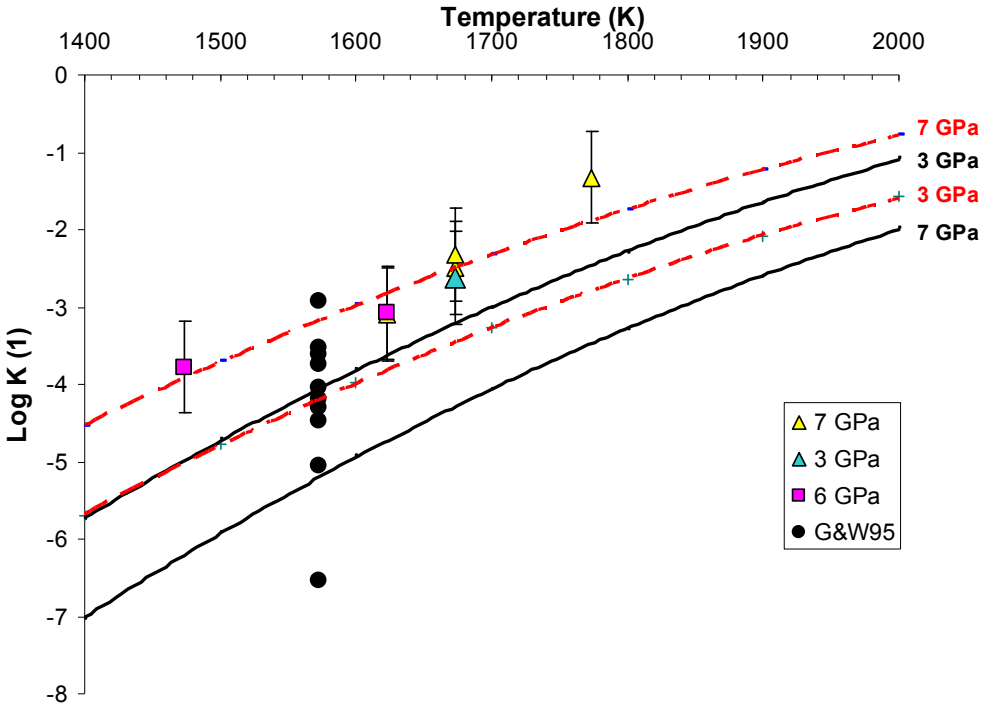

Figure 5.8: Log $K_{(1)}$, the equilibrium constant for equilibrium (5.1) is plotted against temperature for experiments performed between 3 and 7 GPa. $K_{(1)}$ is calculated using the compositional data determined in this study and the fo_2 determined from the Ir-alloy sensor. Similar calculations are shown performed for the Gudmundsson and Wood (1995) study (G&W95). Two solid black curves are shown calculated from the Gudmundsson and Wood (1995) formulation for Log $K_{(1)}$ at 3 and 7 GPa. Red dashed curves are a new fit to experimental data from both studies.

The implication of figure 5.8 is that the pressure dependence of $LogK_1$ is opposite to that proposed from the determined volume change of equilibrium (5.1). The experimental data allow a re-formulation of the expression for logK of equilibrium (5.1) as a function of pressure and temperature as follows,

$$\log K_1 = 8.019 - 20400/T + 0.04P/T \qquad (5.14)$$

with P in bars and T in Kelvin. The recalculated fo_2 values are plotted versus the measured fo_2 using the Ir-Fe alloy sensor and shown in figure 5.9. The only inconsistent data are represented by V587a at 3 GPa that recorded the lowest amount of ferric iron.

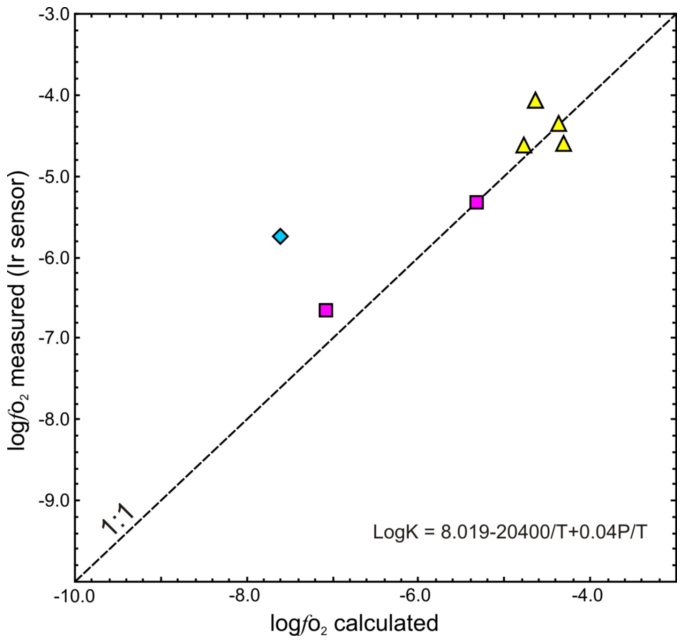

Figure 5.9 Comparison of measured fo_2 with values calculated from eq. (5.1) using (5.14). Symbols as in figure 5.8.

In addition, oxygen fugacities calculations using eq. (5.14) differ by less than 1 log unit on average with respect to the fo_2 obtained using equilibria (5.6) and (5.7).

As previously stated, experiments from Gudmundsson and Wood (1995) were performed at basically isobaric and isothermal conditions and the effects of pressure and temperature on equilibrium (5.1) were assessed using thermodynamic data to derive an expression for the K_D of equilibrium (5.1) given in

equation (5.12). The results of this study indicate that the predictions of the Gudmundsson and Wood (1995) calibration are in error at high pressure and the simplest procedure to recalibrate this error is to redefine the equation for K_D, which is then given as equation (5.14). It must be noted, however, that there are two other alternative possibilities. Firstly, although in this study similar garnet $Fe^{3+}/\sum Fe$ ratios in the recovered samples were obtained from starting materials with very different initial $Fe^{3+}/\sum Fe$ ratios, the experiments were not strictly reversed, due to the sluggish nature of Fe^{3+} reduction reported for garnet (Gudmundsson and Wood, 1995) and it is possible that equilibrium was not achieved. This possibility, although unlikely given the reproducibility of the results, remains to be further tested. Secondly, it is possible that the erroneous by predicted garnet $Fe^{3+}/\sum Fe$ ratios do not arise from an incorrect expression for K_D but, instead result from an uncorrected calibration for the activity composition relations of $2Fe_3Fe_2^{3+}Si_3O_{12}$ garnet. In particular the calibration of Gudmundsson and Wood (1995) ignores excess volume contributions to the non-ideality of mixing. It is possible that the inclusion of these terms, if found to be significant, could lead to a different pressure dependence for the Gudmundsson and Wood model. This could be assessed in the future by examining the volumes of garnets on the join $Fe_3Fe_2^{3+}Si_3O_{12}$-$Mg_3Fe_2^{3+}Si_3O_{12}$. Thermodynamic data on the garnet end member $Mg_3Fe_2^{3+}Si_3O_{12}$ would allow the calibration of further oxy-thermobarometers that would be closer in composition to natural samples. However, given the data available a recalibration of the $K_{D(1)}$ is by far the simplest way to bring the experimental observations into agreement with the calibration for equilibrium (5.1).

5.5.2 The redox profile of the upper mantle revisited

To date equilibrium (5.1) has been extensively used to determine the oxygen fugacity at which mantle xenoliths from cratonic areas have equilibrated. A common procedure consists of first determining equilibrium pressures using geobarometers, such as the alumina content in opx and garnet (Mac

Gragor, 1974; Brey and Köhler, 1990); then, the temperature is determined using common geothermometers, such as clinopyroxene-orthopyroxene (Finnerty and Boyd, 1987; Brey and Köhler, 1990). Finally, fo_2 is calculated using equilibrium (5.1), which is suitable for the majority of mantle xenoliths, which record equilibrium pressures of at least of ~2.1-2.3 GPa (Luth et al., 1990).

The fo_2 in natural garnet peridotitic rocks can be determined using the expression for the K_D of equilibrium (5.1) derived from the experiments described in this section. Figure 5.10 shows the oxygen fugacity calculated for mantle xenoliths (Luth et al. 1990) employing both the original Gudmundsson and Wood calibration (blue diamonds) and the recalibrated K_D, equation (5.14), from this study (pink squares). Based on this K_D reformulation the oxygen fugacity of mantle xenoliths does not follow the steep decrease with pressure because the volume change of the new K_D expression has the opposite sign. Instead, fo_2 remains relatively constant with pressure, just below but subparallel with the carbon-carbonate equilibrium. Although the sign of the K_D expression changes fo_2 does not increase with pressure due to increasing equilibration temperature of the natural samples with pressure. This is a striking contrast with the previous study and implies that the lithospheric mantle does not become more reducing with depth. One interpretation of the xenolith samples, based on the results of chapter 3, is that the oxygen fugacity of the lithospheric sample results from equilibrium between diamond or graphite and fluids or melts, where the activity of the carbonate component is variable between pure carbonate and liquids containing <10 % carbonate.

These results, if correct, apparently weaken arguments developed in chapter 3 concerning oxidation of the mantle during decompressive up welling as a result of the shift in equilibrium (5.1) with pressure. If the volume change of equilibrium (5.1) is indeed in the opposite direction then during decompression changing equilibrium ferric iron contents in garnet will have no propensity to oxidise the mantle as described in chapter 3. However, the results of Rohrbach et al. (2007) indicate that at

pressures between 8 and 15 GPa garnets with significant ferric Fe contents, up to 35 %, are in equilibrium with metallic Fe, i.e. oxygen fugacities even lower than in the experiments performed in this chapter. As our study indicates that this is not the case at 6 GPa the most likely explanation is that ferric Fe contents do start to increase above 6 GPa or as Rohrbach et al. (2007) propose once the garnet-majorite transition starts. It is therefore likely that oxygen fugacities do decrease at high pressures as a result of the stability of ferric Fe containing garnet and that up welling mantle undergoes oxidation, although potentially at higher pressures than indicated by the arguments in chapter 3.

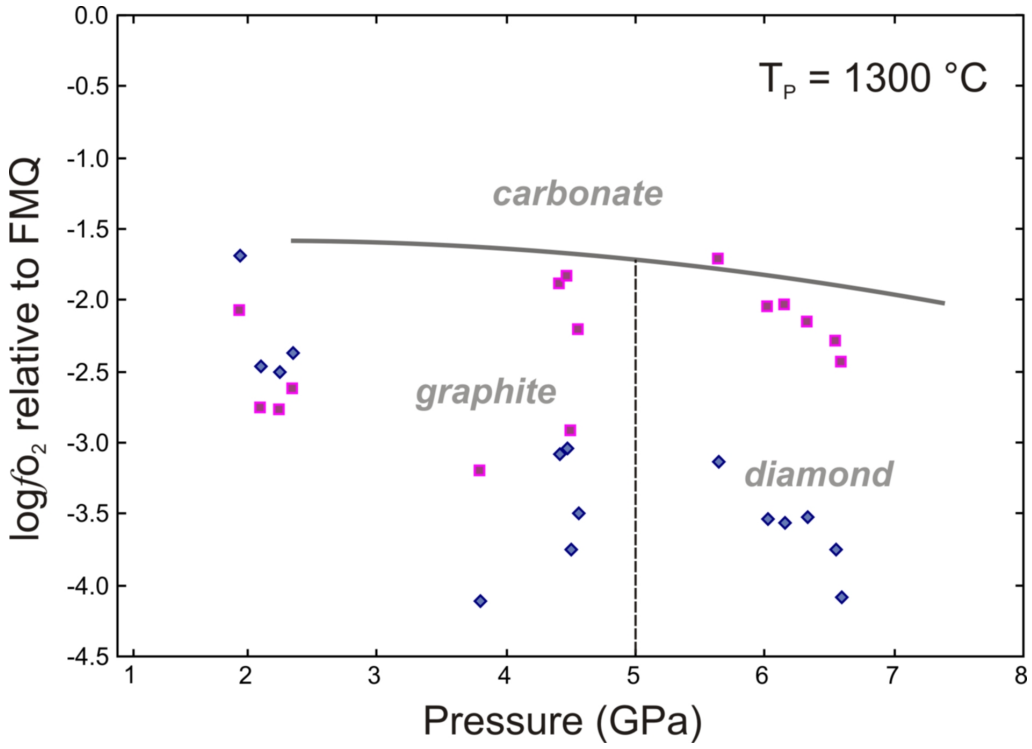

Figure 5.10 Blue and pink symbols indicate oxygen fugacity of natural mantle xenoliths calculated using equilibria (5.1), while equations (5.12) and equation (5.14) respectively for $K_{D(1)}$ and plotted as function of pressure. The grey curve is calculated using the EMOG/D buffer modified by Stagno and Frost (2010) along an adiabat at a potential temperature (T_P) of 1300 °C. Dotted line indicates the transition from graphite to diamond calculated using the equation form Kennedy and Kenney (1979).

5.6 Conclusions

The fO_2 buffered by equilibria involving the skiagite end-member in garnet peridotite has been reviewed in both Ca-bearing and Ca-free model peridotite compositions at pressures between 3 and 7 GPa and temperatures at 1150-1600 °C. Results show a minor pressure dependence of the logK relative to equilibrium (5.1) previously calibrated by Gudmundsson and Wood (1995). This implies that skiagite is even stable at more oxidizing conditions compared to previous studies. Therefore, a new equation of logK is proposed based on measured oxygen fugacities using the iridium-iron alloy redox sensor. This new equation reproduces our experimental results along with data reported by Gudmundsson and Wood (1995).

Based on garnet-peridotite oxy-thermometry the range of fO_2 in the asthenospheric mantle should become more reduced with depth as a result of the volume change of the governing ferric/ferrous equilibrium in the silicate assemblage. We argued that carbonate melting will only commence in adiabatically up welling asthenospheric mantle, once the plausible range of mantle fO_2 crosses the fO_2 constrained by the equilibrium between carbonate melt and graphite with a depth interval for the onset of carbonate-rich redox melting of 100-150 km. However, our new assessment of the redox profile of the upper mantle implies that melting might occur in a broader depth interval where a lower Fe_2O_3 in mantle silicates is required to produce carbonate-rich melts by reaction with elemental carbon.

Although diamond and graphite remain the dominant hosts for carbon in the upper mantle, based on these results the presence of metal might be only limited to locally highly reducing conditions.

However, further results might be needed to investigate if ferric iron contents in garnets increase more above 6 GPa or as Rohrbach et al. (2007) propose once the garnet-majorite transition starts.

6. Carbon and carbonate equilibrium in eclogitic assemblage: preliminary results

6.1 Introduction

The term eclogite usually refers to metamorphic mineral assemblages, "facies" (Eskola, 1914), characterized by a bulk composition that ranges from basaltic to picritic and by a bimineralic assemblage consisting of garnet (typically a solid solution of pyrope-grossular-almandine) and omphacite (clinopyroxene with a variable concentration of the jadeitic component). Eclogite is also the original host rock from which diamond was first recovered (Bonney, 1899) and diamond with eclogitic affinity dominates the diamond population at some localities as shown by the presence of eclogitic inclusions in the diamonds (Cartigny, 2005).

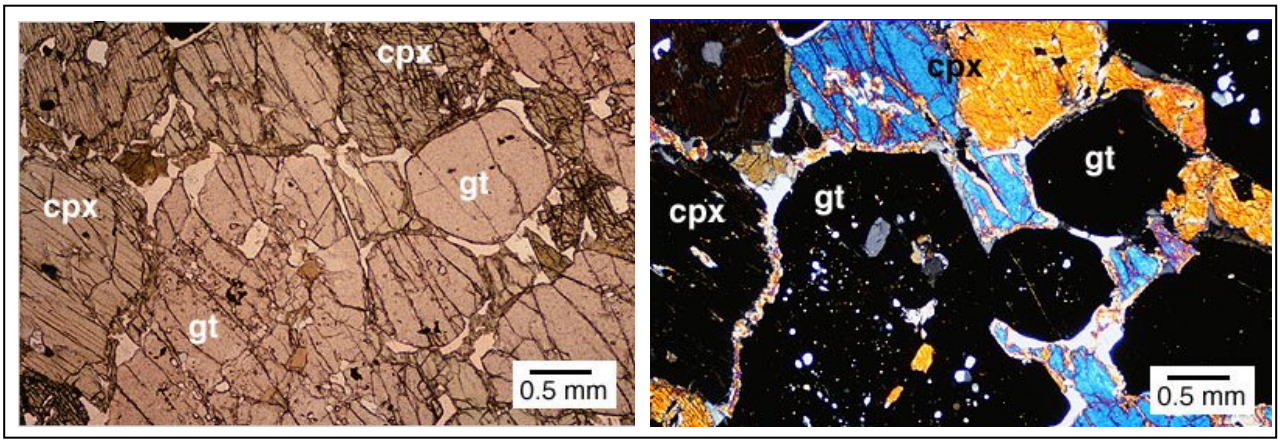

Figure 6.1. a) Optical microscope image with transmitted light with parallel nichols showing eclogitic texture with coexisting garnet and omphacitic clinopyroxene. b) The same thin section is shown with crossed nichols. Micrometer sized crystals are present as inclusions in garnet grains. The shown sample (SA 19) is a xenolith from South Africa kimberlites.

These rocks show a diagnostic granoblastic texture (see fig. 6.1a-b) imposed by garnet and clinopyroxene accompanied by the presence of secondary minerals like kyanite, quartz/coesite (O'Hara, 1960) and accessories like rutile, zircon or apatite likely associated either to exsolution

processes occurring within the rock-forming minerals (garnet and clinopyroxene) or to retrograde metamorphism (e.g. amphibole in contact with clinopyroxene).

Although eclogitic rocks are easily distinguishable both by naked eye and mineralogy, their petrogenesis is made quite complex due to the variety of geological settings in which they occur, as summarized by the following classification (Coleman et al., 1965),

- Eclogite inclusions in kimberlites (Robert Victor mine, Zagadocnaya, Basutoland);
- Eclogite inclusions in alkali basalts (Hawaii);
- Eclogite inclusions in peridotite (Norway, Japan, Czech Republic);
- Granulite facies eclogite (Varberg);
- Amphibolite facies eclogite (Bavaria, Norway, Spain, Scotland);
- Eclogite in glaucophanitic metamorphic terranes.

A generalized reaction can explain the compositional similarities between these groups (Ringwood, 1975) originally starting from an igneous rock, called protolith, as follows:

$$\text{plagioclase} + \text{pyroxene} \pm \text{olivine} \rightarrow \text{omphacite} + \text{garnet} \pm \text{quartz} \qquad (6.1)$$

Among the different eclogites listed above, those found as xenoliths in kimberlites have been estimated to represent less than 1 volume % of the overall abundance and potentially provide important information since they likely come from subcratonic mantle, as suggested by the presence of high pressure phases, e.g. diamond and coesite. These eclogitic inclusions are mostly Archean in age and show geochemical evidence for an origin from plagioclase-bearing protoliths and oxygen isotopic features consistent with seawater alteration of a subducted oceanic crust. In contrast, eclogite xenoliths from Kuruman, South Africa, and Sierra Leone stem from protoliths that were picritic cumulates from

intermediate pressures of 1-2 GPa and were subsequently transposed to higher pressures within the subcratonic mantle (Jacob, 2004).

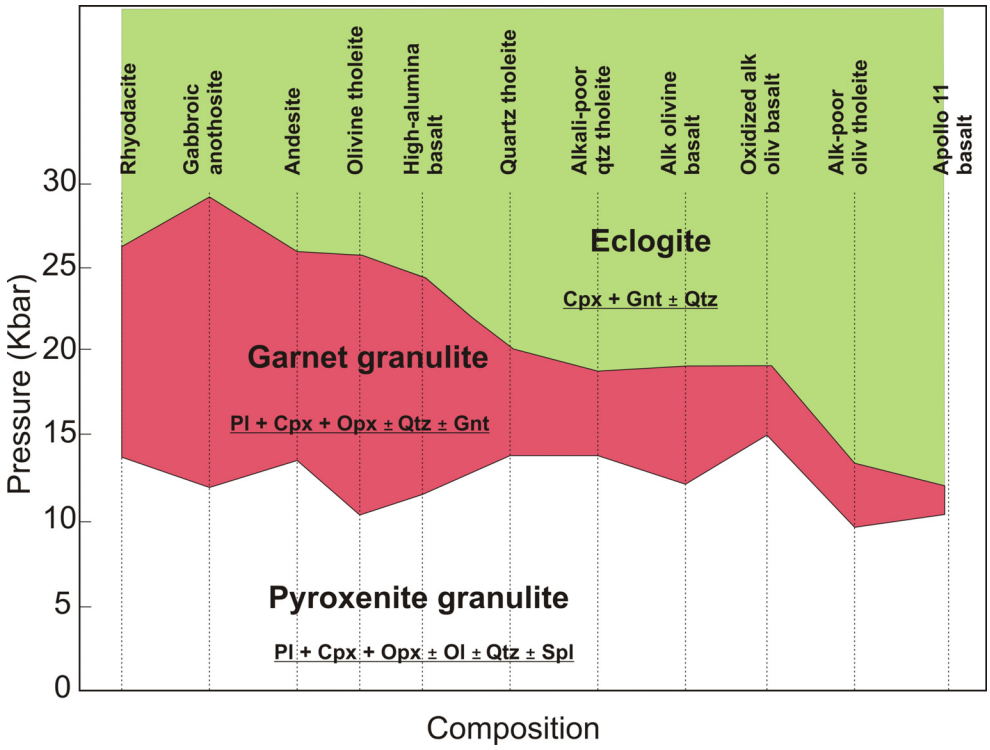

Figure 6.2 Diagram showing the pressure of granulite to eclogite transition as function of the composition of igneous rocks at 1100 °C (Ringwood, 1975-modified).

Although the Fe-Mg distribution (k_D) between garnet and clinopyroxene is helpful to identify this wide variety of eclogitic assemblages, values might also overlap between eclogites from different geological settings (Banno, 1970); while the use of geothermo-barometers is limited and made complex due to the compositional dependence of the starting protolith that affect the origin of eclogites (see figure 6.2). In particular, diamondiferous eclogites are often differentiated based on the high concentrations of Na_2O and K_2O (McCandless and Gurney, 1989), which have been experimentally demonstrated to be incorporated in the cpx structure as a function of pressure (Erlank and Kushiro, 1970; Sobolev and Lavrentev, 1971; Harlow, 1997).

Several hypotheses converge to infer that MORB basalts may preserve their carbon content, generated by hydrothermal processes (Alt and Teagle, 1999), during subduction until a carbonated eclogite has crystallized. It has been proposed, for example, that the low $\delta^{18}O$ isotopic signature (between 2 and 8 ‰) of diamond-bearing eclogites may be explained by sea-water alteration (Gregory and Taylor, 1981; Alt et al., 1989). Experimental studies conducted by Yaxley and Brey (2004), Dasgupta et al., (2004; 2005 and 2006) and Hammouda (2003) provided useful information about the carbon storage in eclogitic reservoirs and its contribution to the origin of carbonatitic intrusions in cratonic areas by determining the solidus of a carbonated eclogite as function of pressure, temperature and composition. Its location below the solidus of a carbonated peridotite and the possible melting might result in the formation of carbonatitic liquid that act as metasomatic agents with respect to the overlying mantle peridotite with important consequences for mantle heterogeneity as well as the main carriers for CO_2 all over the mantle.

Figure 6.3 shows the results of Dasgupta et al. (2005) on the melting of various carbonated-eclogitic compositions that mainly differ in their Ca# (Ca/(Ca+Mg) ratio). The eutectic has a Ca# of approximately 0.65 and is centered well within the range of eclogite compositions and causes large differences in melting temperatures depending on the exact Ca content of the bulk composition. This can explain large differences between carbonated eclogite melting temperatures determined in the literature. The preservation of carbonate within subducted eclogitic crust will depend to some extent on the carbonated eclogite melting temperature. Low melting temperatures will favor loss of carbonate from the slab into the overlying mantle. However, carbon might also be preserved within slabs as a result of reduction of carbonates to form graphite or diamond.

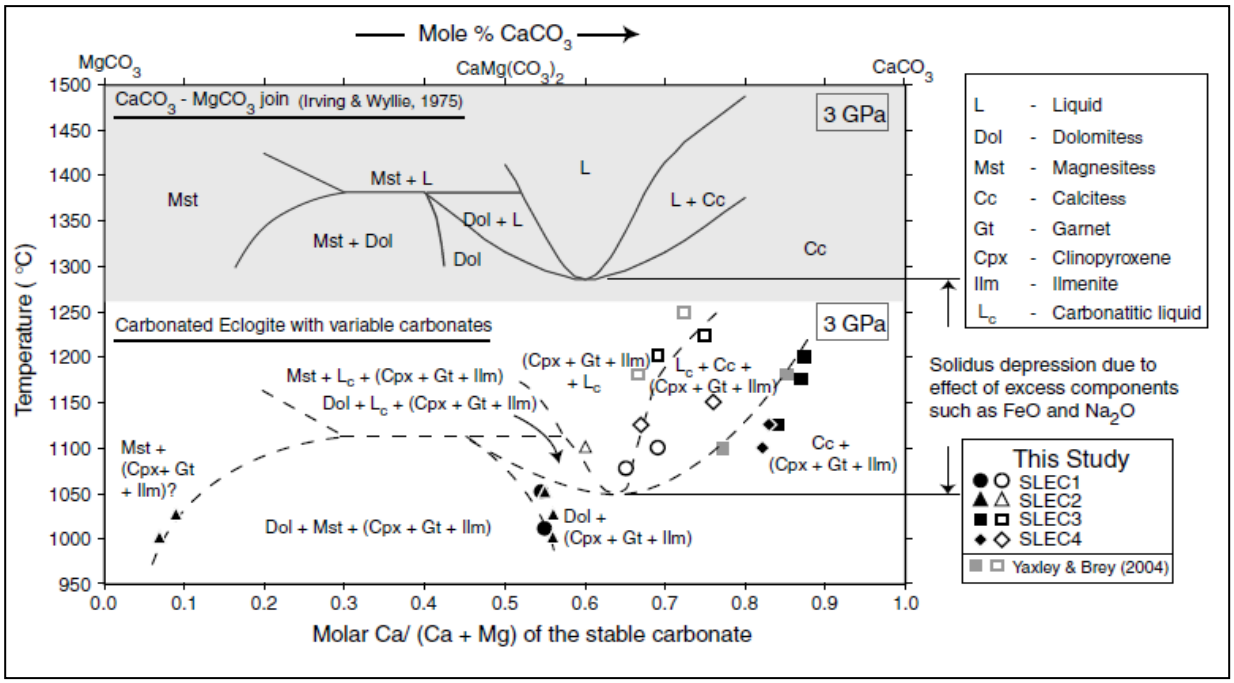

Figure 6.3 From Dasgupta et al. (2005) showing the variability in the solidus of carbonated eclogite in a natural bulk composition compared to the higher temperature melting relations in the simplified $CaCO_3$-$MgCO_3$ at 3 GPa.

This and the prevalence of diamond associated within eclogitic assemblages emphasize the importance of understanding the oxygen fugacity at which diamond and carbonate are stable in eclogitic rocks. Luth (1993) performed the only analysis to date of the stability of diamond and carbonate in eclogitic versus peridotitic rocks. Luth (1993) showed that at subsolidus conditions the diamond-carbonate transformation in eclogite rocks can be described in end-member terms by the equilibrium:

$$CaMg(CO_3)_2 + 2SiO_2 = CaMgSi_2O_6 + 2C + O_2 \qquad (6.2)$$

dolomite coesite diopside graphite/diamond

which is termed DCDG/D. Although the above equilibrium assumes SiO_2 saturation, most proposed MORB compositions would crystallize with excess silica and even quite SiO_2-poor eclogite compositions can crystallize coesite at high pressures and temperatures (Yaxley and Brey, 2004). Luth calculated the oxygen fugacity buffered by this reaction using thermodynamic data as shown in figure

6.4. The calculation, which assumes different activities for dolomite and diopside, indicates that diamond has a larger stability field with respect to oxygen fugacity in eclogitic rocks than in peridotites. Luth (1993) argued that this implies that carbonates infiltrating from peridotitic rocks would be reduced on entering eclogites, thus explaining why diamond and graphite are often associated with eclogites rather than peridotites. However, the calculation of Luth (1993) involves several large uncertainties. Firstly, eclogitic pyroxenes and carbonates have compositions different from the end members in (6.2) and activity-composition relations are complex for the solid solutions. Secondly, it is likely that diamonds grow from liquids, therefore it is important to understand the equilibrium analogous to (6.2) which controls diamond stability above the solidus of a carbonated eclogite.

In this section exploratory experiments are described to test suitable reactions for the measurement of fo_2 buffered by the coexistence of graphite and near solidus carbonate melts within eclogitic bulk compositions. The first problem faced in determining the oxygen fugacity of an eclogite assemblage is finding a redox sensitive reaction for which the thermodynamic data are relatively well known. This is a challenge for eclogites where the two main phases are complex solid solutions for which lengthy activity models introduce large uncertainties into the calculations. In this project a carbonated eclogite composition was saturated in additional phases that allowed more reliable redox equilibria to be used to determine the fo_2 buffered by the natural equivalent of equilibrium (6.2). In separate starting compositions an eclogite composition was saturated in kyanite and rutile. In addition all experiments contained Ir metal, which formed an Ir-Fe alloy sliding redox sensor, similar to that described in chapters 3, 4 and 5. These experiments were performed to develop an experimental strategy for determining fo_2 in eclogite composition experiments, with the ultimate goal of determining the fo_2 of natural eclogitic rocks.

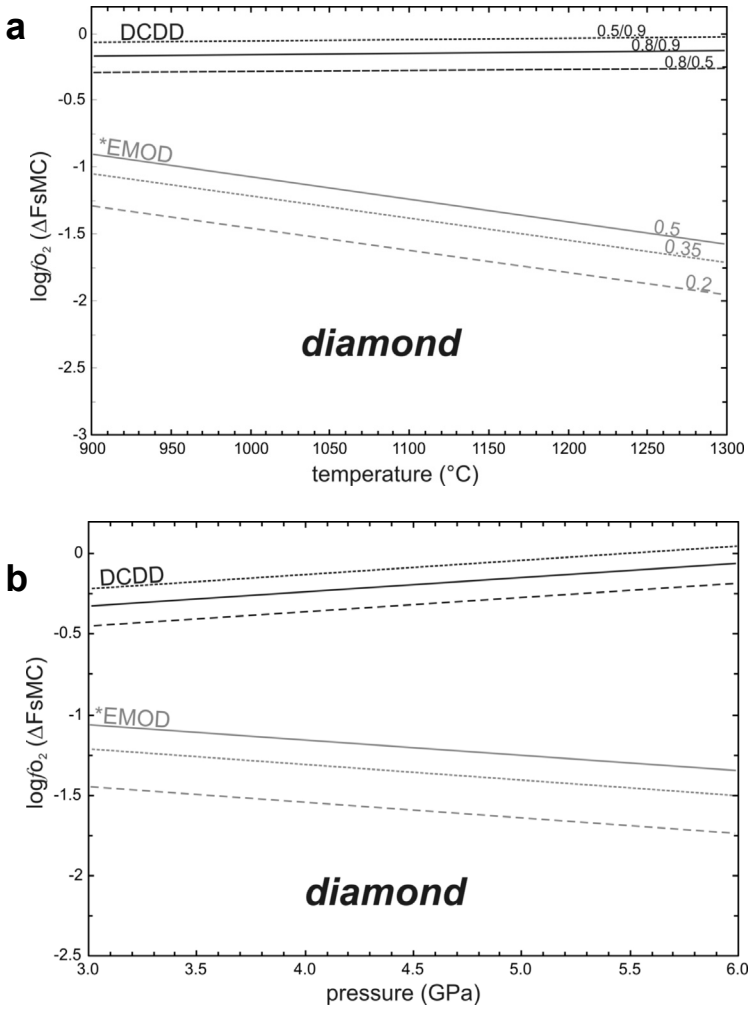

Figure 6.4 (a) Shown is the predicted fO_2 using eq. 6.2 (DCDD) by Luth (1993) as function of temperature at 5 GPa. Numbers close to each line indicate values used for a(Di)/a(Dol) which are the activity of diopside and dolomite in cpx and solid carbonate respectively. Shown is also the calculated fO_2 for a peridotite assemblage (EMOD) modified after Stagno and Frost (2010). In this case numbers indicate the fixed value of aCO_2. (b) Calculated fO_2 as function of pressure at 1100 °C. Values are normalized to the ferrosilite-magnetite-coesite buffer employed by Luth (1993) which is almost coincident with FMQ.

6.2 Experimental method

For all experiments an eclogite composition was employed similar to the G2 composition of Pertermann and Hirschmann (2003) in the system SiO_2-Al_2O_3-MgO-FeO-CaO-Na_2O. The composition was assembled from oxides with a deficit of MgO, CaO and FeO in order that 10 % carbonate phases could be later added. The composition was then melted and quenched to glass and reduced in a gas

mixing furnace. This carbonated eclogite composition was finally mixed with 5 wt. % Ir metal powder and 10 % graphite powder to make a starting composition called START 1.

The first starting composition used in the experiments was produced by mixing START 1 with natural kyanite (~10 wt. %) from Minas Gerais (Brazil) to make START 2. A second composition was produced by mixing START 1 with, 10 wt. % TiO_2 and $FeTiO_3$ to make START 3 in order that both rutile and ilmenite are stabilized as observed in some experiments on natural eclogite compositions (Dasgupta et al. 2004; Zhang et al. 2003). Starting compositions are given in Table 6.1. Experiments were performed at 3 GPa in a multianvil press at 950 and 1000 °C employing an 18/11 assembly. The large assembly allowed two capsules to be employed in each experiment so both compositions (START 2 and 3) were run simultaneously. Experimental and analytical techniques employed were the same than those described in the previous chapters.

Table 6.1 Starting materials and comparison with compositions used in previous studies.

	This study				Previous studies		
	START1[27]	START1 (normalized to 100)	START1 +CO2	Kyanite [12]	(Yasuda et al., 1994)	G2 (Pertermann et al., 2003)	GA1(Yaxley and Green, 2004)
SiO_2	56.09(40)	**57.33**	**49.85**	37.31(17)	**49.71**	**50.05(23)**	50.35
MgO	5.66(12)	**5.78**	**7.11**	-	**8.43**	**7.90(12)**	7.94
Al_2O_3	15.66(15)	**16.00**	**13.91**	63.27(29)	**15.68**	**15.76(24)**	16.53
CaO	8.70(19)	**8.89**	**10.17**	-	**11.73**	**11.74(20)**	9.60
FeOtot	8.35(13)	**8.53**	**10.11**	0.14(5)	**9.46**	**9.35(19)**	9.83
Na_2O	3.39(9)	**3.47**	**3.02**	-	**2.76**	**3.04(10)**	3.49
TiO_2	-	**-**	**-**	-	**1.71**	**1.97(9)**	1.49
CO_2	-	**-**	**5.83**	-	**-**	**-**	-
Total	97.85(47)	**100**	**100**	100.86(32)	**99.48**	**100**	99.23

Notes: Figures in parentheses [ ] indicate total number of analyses; numbers in parentheses ( ) are standard deviations.

Table 6.1 Experimental run conditions and products.

Run no.	P (GPa)	T (°C)	Time (hr)	phases						
V636a	3	950	~42	Omph	Gnt	Coe	G	Ky	Cc	Liq
V637a	3	950	120	Omph	Gnt	Coe	G	Ky	Cc	Liq
V624a	3	1000	~31	Omph	Gnt	Coe	G	Ky		Liq
V636b	3	950	~42	Omph	Gnt	Coe	G	Rut	Cc	
V637b	3	950	120	Omph	Gnt	Coe	G	Rut	Cc	
V624b	3	1000	~31	Omph	Gnt	Coe	G	Rut		Liq

Notes: Omph, omphacite; Gnt, garnet ; Coe, coesite; G, graphite; Ky, kyanite; Rut, rutile; Cc, carbonate s.s.; Ilm, ilmenite; Liq, melt.

6.3 Results

Experimental run conditions and resulting assemblages are shown in Table 6.2. Phase compositions including melt and alloy are reported in Table S6.1 and S6.2 (Appendix). Recovered samples from both compositions showed crystallization of the main silicate phases, such as omphacitic clinopyroxene and garnet. Grain sizes ranged between 5 and 20 μm. Small grains of coesite were also observed in addition to Ir-Fe alloy and graphite dispersed in a matrix or occurring as inclusions in garnet inline with previous studies. In experiments employing the START 2 composition kyanite was present. At 950 °C a carbonate melt was produced in equilibrium with cpx, garnet, kyanite and coesite. The melt contained approximately 6 wt. % SiO_2 and had Ca# of 0.64, which is similar to the eutectic carbonate composition described by Dasgupta et al. (2005) and shown in figure 6.3. Melt composition was estimated also at 950 °C but after 120hr (V637a) to test the attainment of equilibrium between solid phases, liquid and alloy composition. The Ca# of this melt remained constant with a slight increase of MgO from 8.40 wt. % after 42 hr to 10.32 wt. % after 120hr accompanied by a simultaneous decrease of CaO (~ 2 wt. %) while FeO remained constant. Although melt was observed at 1000 °C run, its composition was not measurable.

Rounded garnet crystals occurred always strictly in contact with euhedral omphacitic cpx. The Mg number of garnet, calculated as Mg/(Mg+Fe), increased with temperature from 0.40 to 0.50 in agreement with experiments recovered both from carbonated systems (Yaxley and Green, 1994) and dry systems (Pertermann et al., 2003) with CaO content being stable and likely dependent on the bulk composition. The alumina content in clinopyroxene was approximately 15 wt. %, which is higher than the more typical 5 wt. % observed in previous carbonated eclogite experiments at the same conditions (Dasgupta et al. 2005), due to kyanite saturation but in agreement with cpx crystallized from the same MORB-like bulk composition (Pertermann et al., 2003) with a Mg number of ~0.78. Further, the Na_2O content of cpx is observed to decrease from 7.17 to 5.75 wt. %, while the CaO content increases from 11.72 to 14.43 wt. % mainly as consequence of the increased melt fraction.

In experiments performed using the START 3 composition, rutile was identified along with cpx, garnet, coesite and carbonate phases, while ilmenite was not found as expected from results of previous studies on a similar bulk composition (Yaxley and Green, 1994; Pertermann et al., 2003). Carbonate phases observed in the short run at 950 °C are siderite and siderite-magnesite-calcite solid solutions, which show evidence of disequilibrium, as they appear dissociated each other and dispersed within other phases. After 120 hr siderite still occurs along with other carbonate, such as a siderite-magnesite and a calcite-siderite-magnesite solid solution. At 1000 °C no solid carbonates are found and a glass is produced which is not analysable but might have a composition reported by the already mentioned authors. The Al_2O_3 content of the omphacitic cpx is observed to increase with temperature from 9.80 to 13.22 wt. % while the other oxides do not change. Much more Fe is contained in cpx, about 8 wt. %, compared to the kyanite-bearing assemblage. Finally, garnet has an Mg number ranging from 0.36 to 0.42 as temperature increases from 950 to 1000 °C. However, garnet has more Fe than START 2, while the TiO_2 content is about 1.0 wt. %, a bit higher when compared with experiments where garnet

coexists with ilmenite (Dasgupta et al., 2005). Neither TiO_2 is observed to dissolve in the iridium-iron alloy or iridium into the rutile phase.

The partitioning of Fe-Mg between garnet and clinopyroxene in both series of experiments is compared with the equation calibrated by Ellis and Green (1979) calculated for the same compositions in figure 6.6. As shown in this figure the value is usually observed to decrease as a function of temperature and it is strongly dependent on the composition. Kyanite-bearing runs are for the main part in better agreement than those containing rutile.

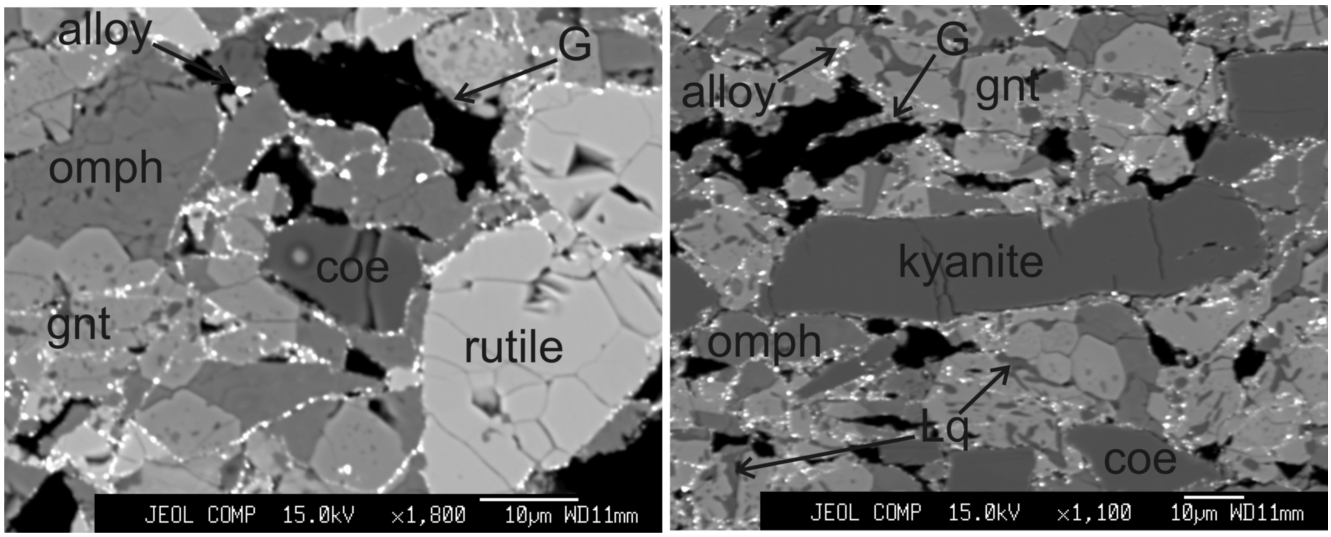

Figure 6.5. Left) recovered sectioned run product V636b (3 GPa/950 °C) showing a Ti-bearing assemblage with rutile after 42 hr. Right) V637a run (3 GPa/950 °C) showing a heterogeneous mineral assemblage after 120 hr with kyanite. Notes: coesite (coe), garnet (gnt), graphite (G), liquid (Lq) and the iron-iridium alloy (bright phase).

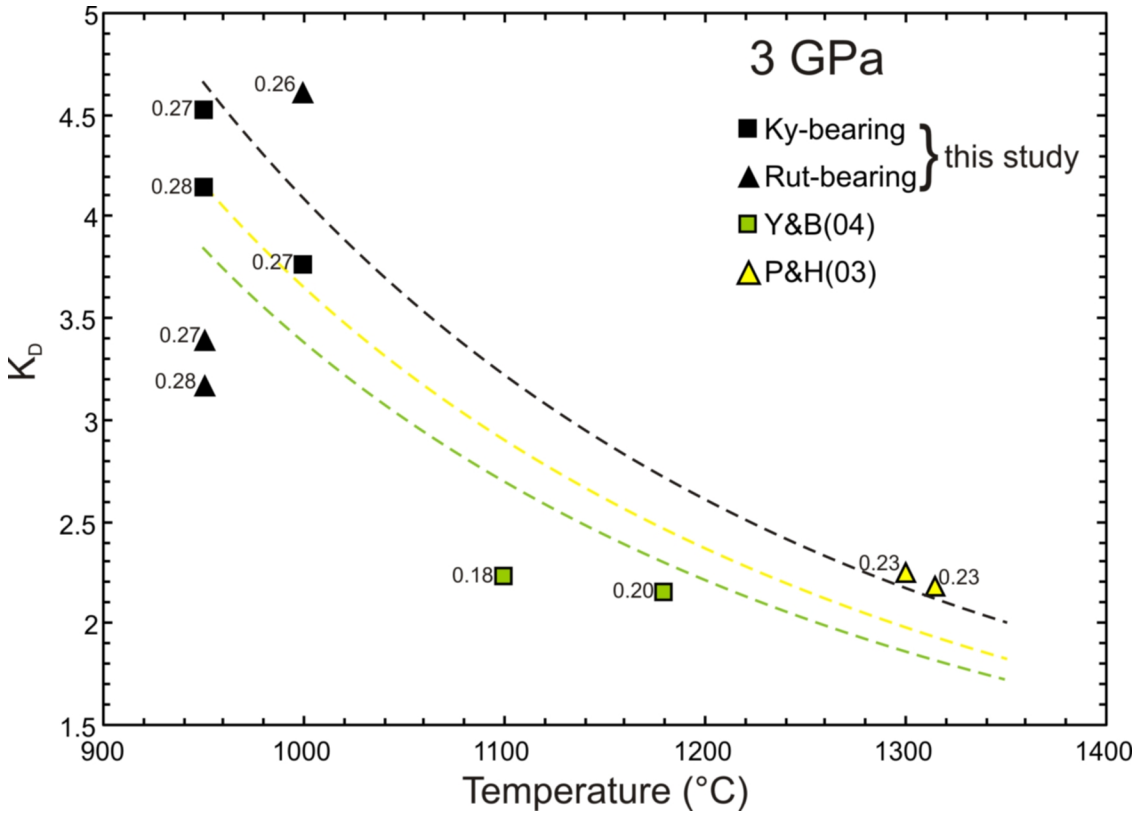

Figure 6.6 The Fe-Mg distribution coefficient calculated between garnet and cpx as function of temperature. Dotted curves are calculated using Ellis and Green (1979) with XCa representative of the appropriate experiment (see legend). Green curve with a XCa of 0.2; yellow curve is 0.23 and black curve is 0.27. Small numbers indicate XCa in garnet.

6.4 Oxygen fugacity determination

In these experiments the fo_2 was buffered by the presence of graphite and a carbonate-bearing phase coexisting nominally with cpx, garnet and coesite in an analogous equilibrium to (6.2). The fo_2 of this equilibrium can be measured, however, using a second equilibrium employing the phases present plus Ir-Fe alloy. In experiments with kyanite (START 2) the oxygen fugacity can be measured using equilibrium,

$$\underset{\text{garnet}}{Fe_3Al_2Si_3O_{12}} = \underset{\text{kyanite}}{Al_2SiO_5} + \underset{\text{coesite}}{2SiO_2} + \underset{\text{alloy}}{3Fe} + 1.5O_2 \qquad (6.3)$$

For this equilibrium only the activities of $Fe_3Al_2Si_3O_{12}$ and Fe must be considered and both are well known. End member thermodynamic data used in addition to that used in previous chapters is listed in Table 6.3. The fo_2 is then calculated from the expression,

$$\log f_{O_2} = \frac{-\Delta G^o_{[6.3]}}{1.5RT\ln(10)} - 2\log a^{metal}_{Fe} + \frac{2}{3}\log a^{Garnet}_{Fe_3Al_2Si_3O_{12}} \quad (6.4)$$

The determination of a^{metal}_{Fe}, the Fe activity in Ir-Fe alloy, has been previously described. The activity of the $Fe_3Al_2Si_3O_{12}$ garnet component is calculated from,

$$a^{Garnet}_{Fe_3Al_2Si_3O_{12}} = (X_{Fe}.\gamma_{Fe})^3 \quad (6.5)$$

Where X_{Fe} is the molar *Fe/(Fe+Mg+Ca)* in garnet and γ_{Fe} is the activity coefficient determined using the model of O'Neill and Wood (1979) from,

$$RT\ln\gamma_{Fe}=X_{Mg}^2W_{Mg\text{-}Fe}+X_{Ca}^2W_{Ca\text{-}Fe}+X_{Ca}X_{Mg}(W_{Mg\text{-}Fe}+W_{Ca\text{-}Fe}-W_{Ca\text{-}Mg}) \quad (6.6)$$

Where $W_{Mg\text{-}Fe}$, $W_{Ca\text{-}Fe}$, $W_{Ca\text{-}Mg}$ are Margules interaction parameters with the values 800, 0 and 11000 J mol^{-1} respectively.

The oxygen fugacity in the second series of Ti-bearing experiments can be calculated using the equilibria

$$\underset{\text{ilmenite}}{FeTiO_3} = \underset{\text{rutile}}{TiO_2} + \underset{\text{alloy}}{Fe} + 0.5O_2 \quad (6.7)$$

Unfortunately, ilmenite was not actually found in the experiments, however if we assume its presence the fo_2 can be calculated from the relation,

$$\log fo_2 = \frac{-\Delta G^o_{[6.7]}}{RT\ln(10)} - \log a^{metal}_{Fe} + \log a^{Ilmenite}_{FeTiO_3} \qquad (6.8)$$

Rutile in the recovered experiments is relatively pure. The activity of $FeTiO_3$ in ilmenite is unknown as no analyses could be made. However, in the similar experiments of Dasgupta et al. (2005) ilmenite was observed and estimates of the likely activity can be made. Variations in ilmenite activity do not affect the fo_2 determined from (6.8) significantly.

Table 6.3 End member thermodynamic data used for calculating oxygen fugacity

	Ref. T(K)	$\Delta_f H^o$ (Jmol^{-1})	H_T-H_{298} (Jmol^{-1})	S_T (JK^{-1}mol^{-1})	a	b	c	d	e	Source
$Fe_3Al_2Si_3O_{12}$ (Gt)	298	-5271940		342.6	863.0	-0.008290	1.70E+06	-8870	0	1
Fe (FCC)	1200	35543	35543	76.91	24.0	0.008360	0		0	2
Al_2SiO_5 (Ky)	298	-2596196		82.30	342.08	-0.03956	-2.59E+05	-3567.5	8.19E-06	4,6
SiO_2 (Coe)	298	-906400		40.60	150.05	-0.02957	6.38E+05	-1822.1	6.07E-06	6
O_2	1000	0	22694	205.15	48.3	-0.000691	4.99E+05	-421	0	2
$FeTiO_3$ (Ilm)	298	-1232000		108.9	262.7	-8.00E-02	3.83E+05	-2538.00	3.39E-05	3
TiO_2 (Rut)	298	-944000		50.6	84.6	5.99E-04	-1.10E+06	-295.70	0	3

	V (cm^{3}mol^{-1})	K_o(bar)	K'	dK/dT (barK^{-1})	α_0	α_1	α_2	α_3	
$Fe_3Al_2Si_3O_{12}$ (Gt)	115.32	1500000	4.305	-0.0450	3.08E-05	6.66E-09	0.64532	-6.11E-03	5
Fe (FCC)	6.835	1653000	5.5	-0.0363	6.40E-05	0	0		6,7
Al_2SiO_5 (Ky)	44.15	1500000	4	-0.0300	5.40E-05	-2.06E-10	1.553	-0.015053	4,6
SiO_2 (Coe)	20.64	800000	8	0	5.43E-06	7.60E-09	0	0	6
O_2									
$FeTiO_3$ (Ilm)	31.69	1770000	4	-0.022	2.69E-05	3.48E-09	0	0	5
TiO_2 (Rut)	18.82	2160000	4.24	-0.022	2.89E-05	0	0	0	5

Notes: [1] O'Neill and Wood (1979) [2] O'Neill (1987) [3] Robie and Hemingway (1995) [4] Holland and Powell (1990) [5] Fei (1995) [6] Fabrichnaya et al. (2004) [7] Komabayashi and Fei (2010).

6.5 Discussion

In figure 6.7 oxygen fugacities calculated from both kyanite and rutile bearing experiments using equilibria (6.4) and (6.8) are shown. In one kyanite bearing experiment no metal alloy could be analysed. The DCDG curve is equilibrium (6.2) calculated from the pure end-member thermodynamic data. The EMOG curve, which describes the fO_2 where graphite and carbonate coexist in peridotitic assemblages, is shown calculated from the equation given in chapter 3. Melting of carbonated peridotite commences at approximately 1300 K but no account has been made of this in figure 6.7 as the mole fraction of CO_2 in the EDDOG equation from chapter 3 has been fixed at 0.5.

The agreement between Fe-Mg partitioning between cpx and garnet shown in figure 6.6 with previous models indicates a close approach to equilibrium for the kyanite-bearing experiments, while those from rutile-bearing experiments are in poorer agreement. No ilmenite could be found in the recovered rutile-bearing samples, so the fO_2 calculation for these samples must be considered less reliable. In addition, the carbonate phase in the rutile-bearing experiments was very Fe rich. It is possible that the Fe-enrichment in the carbonate phase resulted in higher determined oxygen fugacities but this melt is anyway inconsistent with previous carbonate phases measured in eclogites at similar conditions (Dasgupta et al. 2005). In the kyanite bearing experiments carbonate melt was analysed, which was consistent with previous studies. In addition as Ir metal is Fe free in the starting compositions, more reduced results have been displaced further from the starting material and are therefore likely to be closer to equilibrium. For these reasons the kyanite results are considered to be more reliable than the rutile-bearing experiments.

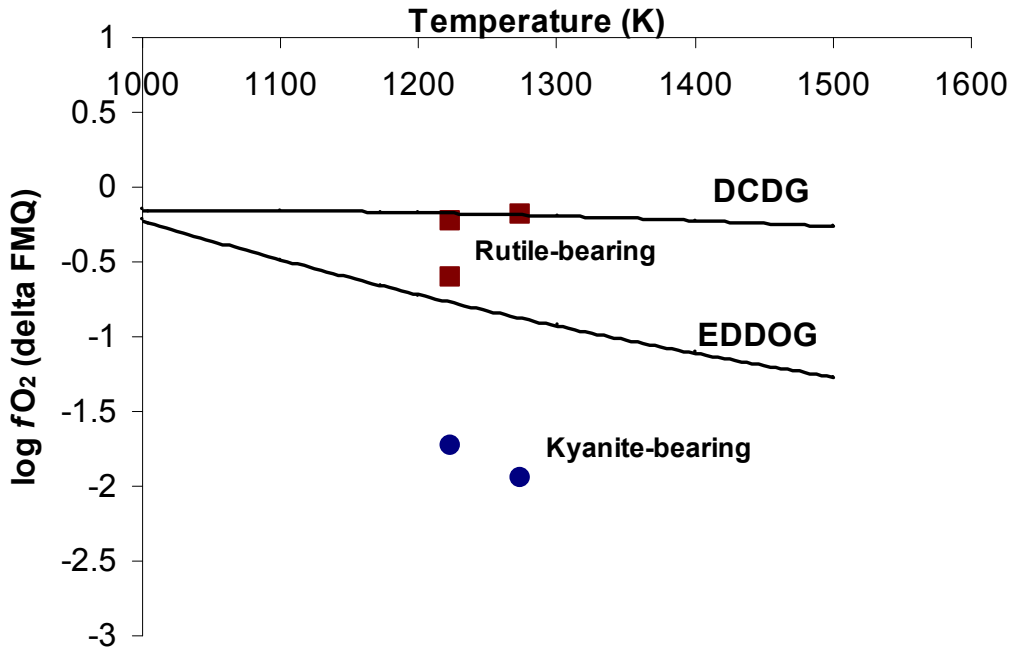

Figure 6.7 Oxygen fugacities calculated from kyanite (blue circles) and rutile (brown squares) bearing experiments using equilibria (6.4) and (6.8) respectively. Values are compared with calculations of the DCDG equilibrium (6.2) from thermodynamic data and the determination of the EDDOG buffer from chapter 3. Uncertainties propagated from compositional measurements are of the order of 0.2 log units.

Luth (1993) argued that the DCDG buffer was at a fo_2 above that of EDDDOG and that for a fixed oxygen fugacity eclogitic rocks could be in the graphite/diamond stability field while peridotites could be in the carbonate field. Similarly carbonate melts infiltrating from peridotites might therefore be reduced to diamond/graphite on entering eclogites, thus supporting the observation of diamonds being hosted disproportionately by eclogitic rocks in some localities. The results from kyanite-bearing experiments do not support this hypothesis, however, because the fo_2 buffered by the coexistence of carbonate melt and graphite in these experiments is below the EDDOG buffer and thus carbonates would be stable at even lower oxygen fugacities in eclogites compared to peridotites. An additional issue not considered by Luth (1993) is that as the carbonated solidus in eclogitic rocks is at least 200 °C lower than in peridotites carbonate liquids infiltrating from a peridotite would likely flux a much greater proportion of melting on entering eclogitic rocks. At similar temperatures carbonate melts in

eclogites contain a larger silicate component than in peridotitic rocks and, therefore, as seen in chapter 3, the fO_2 for graphite/diamond formation will be driven to even lower values by the dilution of the CO_2 component in the melt.

For the previously described reasons it is, therefore, unlikely that the diamond-eclogite association in some localities arises from a difference in the graphite-carbonate buffering reaction between peridotites and eclogites. One possibility for the association is that carbonates, initially associated with eclogites during subduction, remain at low enough temperatures for a solid-state transformation to diamond to occur. However, this is implausible as diamond is a metasomatic mineral and growth rings imply growth from a liquid or fluid. A further possibility is that carbonate liquids entering eclogites are forced to reduce due to redox reaction with the silicate minerals. Garnet in eclogites, for example, is more Ca-rich than in peridotites and a plausible carbonate reduction reaction might consider the andradite component i.e.

$$\underset{\text{melt}}{CaCO_3} + \underset{\text{cpx}}{2CaSiO_3} + \underset{\text{cpx}}{2FeSiO_3} = \underset{\text{garnet}}{Ca_3Fe_2Si_3O_{12}} + \underset{\text{coesite}}{SiO_2} + \underset{\text{graphite/diamond}}{C} \qquad (6.9)$$

In order to determine whether such a reaction could take place the fO_2 of the oxidation reaction involving andradite would need to be determined. The most straight forward method to achieve this would be to measure the andradite component in garnets produced in similar experiments to those described in this chapter.

6.6 Conclusions

The oxygen fugacity at which graphite coexists with solid carbonate or melt in eclogitic assemblages has been determined at 3 GPa and temperatures in the range between 950-1000 °C using iridium as redox sensor. Preliminary results are presented for two different eclogitic assemblages, which are thought to originate by metamorphism of MORB basalt (kyanite and TiO_2-bearing). This assemblage might represent a potential carrier for carbon down into the mantle in subduction zones. However, conditions at which carbonate or graphite/diamond may persist at depth need to be investigated based on the proposed study. Preliminary results show also compositions of coexisting silicate phases, which are in agreement with previous studies where MORB-like bulk compositions were used. On the other hand, results are in contrast with studies that considered alterated MORB basalts as starting composition. Finally, experiments carried out using a kyanite-bearing assemblage show fo_2, which are more reliable than TiO_2-bearing and appear in contrast with previous predictions on the equilibrium between diamonds and carbonate in these rocks. However, results from TiO_2-bearing system can be improved by determining the concentration of ferric iron in garnet at a given fo_2 and fixing the oxygen fugacity with the coexistence of ilmenite.

Further results will provide the basis for determining whether with increasing pressure during subduction there will be a tendency for carbonates to reduce to graphite (diamond) in eclogitic rocks as a result of pressure favouring the formation of Fe^{3+} components in garnet and clinopyroxene.

7. General conclusions

The investigation of the Earth's mantle is crucial to our understanding of the geochemical and petrological processes generating oxidation of the mantle, which in turn can affect volcanic eruptions and loss of volatiles to the atmosphere. To date, knowledge concerning the mantle composition and structure has come mainly from the study of seismic wave velocities through the Earth's interior in addition to the interpretation of mantle xenoliths and erupted magmas. Xenoliths, unfortunately, arise from depths <200 km into the mantle and can be influenced by melting and metasomatic processes. Magmas are often altered and influenced by processes of magmatic differentiation, assimilation and mixing. A great deal more information can be provided by natural mineral and melt inclusions in erupted xenocrysts and diamonds. Some diamond inclusions, for example, are considered to be direct samples of the mantle from depths greater than 600 km and show the presence of solid carbonate. These inclusions provide important information not only about the mineralogy of the region of the mantle where they formed but rather unique information on the most oxidized conditions at which diamond can be stable along with mantle silicates.

In the course of this thesis, the conditions at which carbonate minerals and melts form from either graphite or diamond were studied as a function of pressure, temperature and oxygen fugacity in typical mantle peridotite assemblage. These conditions not only define those that are likely prevalent during diamond growth but also identify the conditions under which reduced carbon in up welling mantle would become oxidized to produce carbonate minerals and melts. In addition the redox state of carbon/carbonate equilibria was determined with respect to the proportion of ferric iron-bearing mineral components of the upper mantle, transition zone and lower mantle, which in turn can be used to refine oxy-thermobarometry equilibria for determining the redox state of the mantle.

7.1 The oxidation of elemental carbon to carbonate beneath mid-ocean ridges

Carbonatites or carbonate-rich melts are likely to be the first liquids produced during mantle up welling (McKenzie, 1985). Though they are implicated in the origins of kimberlitic magmas, it is possible that mid ocean ridge melting also commences with the production of small degree carbonate rich melts

at conditions much deeper in the mantle than the main phase of silicate partial melting. Seismological and geoelectrical anomalies represent the evidence for deep melting in MOR settings and are confirmed by experimental studies, which showed a typical high electrical conductivity of CO_2-rich liquid.

The depth of 200-300 km beneath the East Pacific Rise where this body characterized by high electrical conductivity was identified has been also the subject of experimental petrology. In order to explain deep melting, experimental studies suggested that the melting of a peridotite source with 2.5 % of CO_2 is able to produce carbonatitic melts in small amounts occurring when the mantle adiabat intersects the solidus curve of the appropriate mantle assemblage. However, the crucial role of oxygen fugacity in the upper mantle was totally neglected. While it is possible that the coexistence of carbonate and graphite/diamond may buffer the oxygen fugacity of the mantle, as a result of the relatively low carbon content, ferric/ferrous equilibria probably exert a more dominant influence and may drive the oxygen fugacity of the mantle down with increasing depth. In this scenario the onset of carbonatitic melting in upwelling mantle will be controlled by the point where the ambient oxygen fugacity crosses the oxygen fugacity imposed by the appropriate carbon-carbonate equilibria, rather than the solidus of carbonate-bearing mantle.

Using MORB glasses as a source to determine the fo_2 range in the asthenosphere and oxy-thermobarometry methods we estimated that the bulk $Fe^{3+}/\Sigma Fe$ ratio of MORB source peridotite is likely in the range 0.02-0.03, which is consistent with estimates for the melt-residue partition coefficient of Fe^{3+} and with estimates based on mantle xenoliths (O'Neill et al 1993; Canil et al., 1994; Canil and O'Neill 1996).

We assume that the general trend of decreasing fo_2 with depth found in mantle xenoliths from cratonic areas might also reflect the fo_2 in asthenospheric mantle in down welling when a whole convection mantle is considered. Calculations were performed along an adiabat with a potential temperature of 1320 °C using the bulk silicate Earth (BSE) composition of McDonough and Sun

(1995) and assuming a fixed garnet $Fe^{3+}/\sum Fe$ ratio of 0.12, which corresponds to a bulk rock $Fe^{3+}/\sum Fe$ ratio of approximately 0.03.

By determining the fO_2 buffered by equilibria involving both elemental carbon (graphite or diamond) and carbonate minerals or melts at pressures between 2.5 and 11 GPa and temperatures at and above the carbonated peridotite solidus, we are now able to determine the depth at which a redox melting may occur. Based on our results we have examined how the fO_2 of the carbon/carbonate equilibrium varies with melt composition as the solidus carbonate melt evolves towards a silicate liquid. The dilution of the carbonate component in SiO_2-bearing melts was found to lower the relative fO_2, expanding the melt stability field with respect to reduced carbon, which well applies to a context of decompression melting along an adiabat beneath mid ocean ridges. Comparing with previous studies for the plausible oxygen fugacity trend in the upper mantle based on redox equilibria involving the skiagite garnet end member, the stability of carbonate-bearing melts should enter the domain of asthenospheric mantle fO_2 at depths of approximately 120 km, where redox melting (Taylor and Green, 1988) would occur. Only when up-welling mantle reaches this depth will graphite start to oxidize, through reduction of Fe_2O_3 in silicates, to form a carbonate melt containing 3-15 wt. % SiO_2. Small fractions of CO_2-rich liquids will not affect the main production of melt from the spinel peridotite facies. Isotopic signatures and trace elements patterns, however, will record features that result from the scavenging of elements incompatible in the presence of carbonate melt from much greater volumes of the mantle than the main phase of melting involves.

However, some caution must be taken in the acceptance of the current ideas on the variation in fO_2 of the mantle with depth and the calibration of the existing oxy-thermobarometer for garnet peridotite (Gudmunnson and Wood, 1995). The garnet oxy-barometer predicts that at pressures of approximately 6 GPa garnets buffered at oxygen fugacities compatible with the presence of graphite and carbonate

melt should contain in excess of 40 % of Fe in the ferric state. However, in this study no garnet was synthesised with more than approximately 12 % ferric Fe. In fact, although greater amount of ferric iron (~40%) in garnet would be required in order to promote redox melting of a carbonated peridotite, those amounts have been shown to be totally in contrast with garnet compositions found in these experiments and even in natural rocks, which recorded coexistence with CO_2-rich melt. If results from this study are confirmed, the oxygen fugacity of the upper mantle may be in fact more oxidized than previously thought.

In this scenario, during up welling carbon oxidation will reduce the Fe_2O_3 content of the mantle causing the fo_2 to be buffered by the graphite/carbonate-bearing melt equilibrium for some depth interval until graphite is exhausted. The extent to which this is important depends on the mantle carbon content, for which estimates for the upper mantle range from approximately 20-250 ppm.

7.2 Magnesite as a deep carbon source

In this study, experiments were performed to determine fo_2 values at which diamond oxidises to carbonate in the transition zone and lower mantle. This measured oxygen fugacity was found to be approximately 3 log units above the iron-wüstite oxygen buffer (ΔIW+3). As the oxygen fugacity of the transition zone and lower mantle is most likely at or below the IW buffer this confines the stability of solid carbonate to the upper mantle or to unusually oxidized regions of the deeper mantle. The oxygen fugacity at which magnesite and diamond coexist shows a slight decrease with pressure; however, implying the possibility that magnesite may become the stable host for carbon at the very base of the lower mantle and coexist with a Fe-Ni-C alloy. However, along with the oxidation of diamond to carbonate no differences have been observed in the ferric iron content of representative

mantle minerals of the transition zone and lower mantle when compared with ferric iron contents of phases equilibrated with metallic iron.

Finally, melting processes has been reported to occur at high pressure as suggested by a mineral assemblage included in diamonds (Walter et al., 2008). In peridotite assemblages carbonate melts could only be stable in exceptionally oxidized mantle at depths greater than 120 km. Melts such as kimberlites, which form at depths ≥ 150 km are, therefore, predicted to arise from either exceptionally oxidized mantle or have initial molar CO_2 contents in the range 1-5 mole %.

7.3 Further work

During the course of this thesis a number of points have become obvious where further experimental studies would benefit our understanding.

As discussed in the previous chapter, in kimberlites diamonds occur in eclogite xenoliths more frequently than in peridotite xenoliths, but the reason for this is unclear. The redox conditions recorded by xenolith mineral assemblages as well as by diamond inclusions with peridotite or eclogite affinities may shed some light on this problem.

The redox conditions controlled by mineral phases in eclogitic settings are, in fact, still relatively uncertain; possible control factors may include silicate-carbonate-diamond reactions and ferrous minerals such as garnet and clinopyroxene. Determining the relationship between the oxygen fugacity and the Fe^{3+}/Fe^{2+} changes in a carbonated eclogitic systems, however, will yield insight not only into the formation mechanism of diamonds but also the influx of carbonate (or carbon) in the mantle by subduction of initially carbonate-rich oceanic crust. The effect of pressure on ferric iron contents of eclogitic minerals has been poorly studied and the stability of carbonate minerals with respect to carbon is also poorly understood in eclogitic systems. It is quite possible that as subduction proceeds

ferric/ferrous equilibria in the eclogitic portions of subducting slabs drive the fO_2 within the slab down, resulting in residual carbonate being reduced to diamond. This would be a key step in the cycling of carbon in the Earth.

A second important point is represented by the pressure effect on the stability of solid carbonate with respect to diamond at conditions compatible with the base of the lower mantle. In the upper mantle the oxygen fugacity revealed by xenoliths, drops with increasing pressure, mainly as a result of the effect of pressure on heterogeneous ferric-ferrous equilibria (Woodland and Koch, 2003). At these conditions C occurs mostly as graphite (or diamond). At deeper conditions an oxygen fugacity is reached where Ni-Fe alloy will precipitate. However, experiments on assemblages of diamond, magnesium carbonate, magnesiowüstite containing an Ir-Fe metal redox sensor have shown that at conditions of the lower mantle the lowest fO_2 stability of a carbonated peridotite may become very close to the fO_2 where Fe-Ni alloy is also present. It is possible that with increasing pressure the carbonate stability field intersects the fO_2 where Ni-Fe alloy would be in equilibrium with a peridotite composition mantle assemblage. This would have major implications, as it would mean that carbonate would become the dominant host for carbon at the base of the Earth's mantle and could potentially promote partial melting in the ultralow velocity zones at the core mantle boundary. Carbonate melts could then promote initial up-welling of plume material within these regions as a result of upward heat transfer away from the core mantle boundary.

Acknowledgements

I gratefully acknowledge financial support under the EU funded Marie Curie, “project 019700” PhD fellowship and the support of the DFG through grant “FR1555/5-1”.
I would like to thank Dan Frost, who always supported me with his unique motivation and real interest in what I was doing during my entire doctoral research work. Many thanks to Catherine McCammon for helping me with Mössbauer measurements and for many fruitful discussions. I am also grateful to Nobuyoshi Miyajima for his assistance in TEM study. I would also like to thank Prof. Dave Rubie for his support and interest in my research and Prof. A. Woodland for providing me a natural garnet useful for my research.
Many thanks to Shantanu Keshav and Gummi Gudfinnson, who first introduced me to the piston cylinder and multianvil community.
I am indebted to Dr. Florian Heidelbach for the German translation of my thesis summary and other related documents and Detlef Krauβe for his help and teaching during the long time spent at the electron microprobe.
I am grateful to David Dolejs, who offered me the first opportunity to join BGI people in March 2007.

I also would like to acknowledge Prof. Tetsuo Irifune, who gave me the unique opportunity to work at the Geodynamic Research Center in Matsuyama. Beautiful and unforgettable experience!

I offer my special thanks to the entire technical and administrative staff of the Bayerisches Geoinstitut for all the assistances.

Last but not least, ringrazio di cuore Paola per la pazienza e lo spirito di sacrificio mostrato in questi anni di lontananza anche, e soprattutto, dopo per aver messo al mondo quanto di piu’ prezioso ci sia nelle mia vita: Sofia.

References

Akaishi, M., Kanda, H., and Yamaoka, S., 1990. Synthesis of diamond from graphite-carbonate systems under very high temperature and pressure. J. of Crystal Growth, v. 104p. 578-581.

Allard P., Carbonelle J., Dajlevic D., Le Bronce J., Morel P., Robe M.C., Maurenads J.M., Faivre-Pierret R., Martin D., Sabroux J.C.and Zettwoog P., 1991. Eruptive and diffuse emissions of CO_2 from Mount Etna, Nature 351, pp. 387-391.

Alt, J.C., Anderson, T.F., Bonnell, L., Muehlenbachs, K., 1989. Mineralogy, chemistry, and stable isotopic composition of hydrothermally altered sheeted dikes: ODP hole 504B, Leg 111. Proc. ODP, Sci. Results 111, 27-40.

Alt, J. C. & Teagle, D. A. H., 1999. The uptake of carbon durino alteration of ocean crust. Geochimica et Cosmochimica Acta 63, 1527-1535.

Amthauer G., Annersten H., Hafner S.S., 1976. The Mössbauer spectrum of ^{57}Fe in silicate garnets. Z Kristallogr 143, 14-55.

Arima, M., Nakayama, K., Akaishi, M., Yamaoka, S., and Kanda, H., 1993. Crystallization of diamond from a silicate melt of kimberlite composition in high-pressure and high-temperature experiments. Geology, v. 21p. 968-970.

Aubaud, C., Francoise, P., Hekinian, R., Javoy, M., 2005. Degassing of CO_2 and H_2O in submarine lavas from the Society hotspot. Earth Planet. Sci. Lett. 235, 511–527.

Baba, K., Chave, A.D., Evans, R.L., Hirth, G., Mackie, R.L., 2006. Mantle dynamics beneath the East Pacific Rise at 17 S: insights from the Mantle Electromagnetic and Tomography (MELT) experiment. J. Geophys. Res. 111, B02101.

Badro, J., Fiquet, G., Guyot, F., Rueff, J.P., Struzhkin, V.V., Vanko´, G., Monaco, G., 2003. Iron partitioning in Earth's mantle: Toward a deep lower mantle discontinuity. Science, 300, 789-791.

Ballhaus, C., 1995. Is the upper mantle metal-saturated? Earth Planet. Sci. Lett. 132, 75-86.

Ballhaus, C., Berry, R.F., Green, D.H., 1991. High pressure experimental calibration of the olivine-orthopyroxene-spinel oxygen geobarometer: implications for the oxidation state of the upper mantle. Contrib. Mineral. Petrol. 107, 27-40.

Ballhaus, C.G., Stumpfl, E.F., 1985. Occurrence and petrological significance of graphite in the Upper Critical Zone, western Bushveld Complex, South Africa. Earth and Planetary Science Letters 74, 58-68.

Bancroft G.M., 1973. Mössbauer Spectroscopy; An Introduction for Inorganic Chemists and Geochemists. In: , Wiley, New York, p. 259.

Banno Sh., 1970. Classification of eclogites in terms of physical conditions of their origin. Phys. Earth Planet. Interiors 3, 405-421.

Barrenechea, J.F., Luque, F.J., Rodas, M., Pasteris, J.D., 1997. Vein-type graphite mineralization in the Jurassic volcanic rocks of the external zone of the Betic Cordillera (southern Spain). Canadian Mineralogist 35, 1379-1390.

Bezos, A., Humler, E., 2005. The $Fe^{3+}/\sum Fe$ ratios of MORB glasses and their implications for mantle melting. Geochim. Cosmochim. Acta 69, 711–725.

Biellmann, C., Gillet, P., Guyot, F., Peyronneau, J., Reynard, B., 1993. Experimental evidence for carbonate stability in the Earth's lower mantle. Earth Planet. Sci. Lett. 118, 31-41.

Blundy J.D., Brodholt J.P., Wood B.J., 1991. Carbon-fluid equilibria and the oxidation state of the upper mantle. Nature, 349, 321-24.

Bonney, T.G., 1899. The parent-rock of the diamond in South Africa. Geol. Mag. 6, 309-321.

Borisov, A., Palme H., 2000. Solubilities of noble metals in Fe-containing silicate melts as derived from experiments in Fe-free systems. Am. Mineral. 85, 1665-1673.

Bose, P.N., 1884. Geology of the Lower Narbada Valley between Nimáwar and Káwant. Geol. Surv. India, Mem. 21, 1-72.

Boyd, F.R., and England, J.L., 1960. Apparatus for phase-equilibrium measurements at pressures up to 50 kilobar and temperatures up to 1750 °C. Journal of Geophysical Research, 65, 74l-748.

Boyd, F.R. and Gurney, J., 1986. Diamonds and the African lithosphere. Science, 232, 472-477.

Brenker, F.E., Vollmer, C., Vincze, S., Vekemans, B., Szymanski, A., Janssens, K., Szaloki, I., Nasdala, L., Joswig, W., Kaminsky, F., (2007), Carbonates from lower part of transition zone or even the lower mantle. Earth Planet. Sci. Lett. 260, 1-9.

Brey, G.P., Koehler,T., Nickel, K.G., 1990. Geothermobarometry in four-phase lherzolites I. Experimental results from 10 to 60 kbar. J. Petrol. 31, 1313–1352.

Brey G.P., Köhler T., 1990. Geothermobarometry in four-phase lherzolites. II. New thermobarometers, and practical assessment of existing thermobarometers. J Petrol 3, 1353-1378.

Brey, G.P., Bulatov, V.K., Girnis, A.V., Lahaye, Y., 2008. Experimental melting of carbonated peridotite at 6-10 GPa. J. Petrol. 49, 797-821.

Bromiley G.D., Hilairet N., McCammon C., 2004. Solubility of hydrogen and ferric iron in rutile and TiO_2 (II): implications for phase assemblages during ultrahigh-pressure metamorphism and for the stability of silica polymorphs in the lower mantle. Geophys. Res. Lett. 31, L04610.

Bryndzia, L.T., Wood, B.J., 1990. Oxygen thermobarometry of abyssal spinel peridotites: the redox state and C-O-H volatile composition of the Earth's suboceanic mantle. Am. J. Sci. 290, 1093–1116.

Bulanova, G.P., Walter, M.J., Smith, C.B., Kohn, S.C., Armstrong L.S., Blundy, J., Gobbo, L., 2010. Mineral inclusions in sublithospheric diamonds from Collier 4 kimberlite pipe, Juina, Brazil: subducted protoliths, carbonated melts and primary kimberlite magmatism. Contrib. Mineral. Petrol. 160, 489-510.

Bundy, F. P., 1963b. Direct conversion of graphite to diamond in static pressure apparatus. J. Phys. Chem., 38, 631.

Bureau, H., Pineau, F., Metrich, N., Semet, M.P., Javoy, M., 1998. A melt and fluid inclusion study of the gas phase at Piton de la Fournaise volcano (Reunion Island). Chem. Geol. 147, 115-130.

Burns, R.G., and Solberg, T.C., 1988. ^{57}Fe-bearing oxide, silicate, and aluminosilicate minerals. In Spectroscopic Characterization of Minerals and Their Surfaces, L.M. Coyne, D.F. Blake, and S.W.S. McKeever, Eds. American Chemical Society Symposium, Series, pp. 263-282. Oxford: Oxford University Press.

Canil, D., O'Neill H.St.C, Pearson, D.G., Rudnick, R.L., McDonough, W.F., Carswell, D.A., 1994. Ferric iron in peridotites and mantle oxidation states. Earth Planet. Sci. Lett. 123, 205-220.

Canil, D., O'Neill, H.St.C., 1996. Distribution of ferric iron in some upper-mantle assemblages. J. Petrol. 37, 609-635.

Carter L., 1970. Mineralogy and chemistry of the Earth's upper mantle based on the partial fusion-partial crystallization model, Geol. Soc. Amer. Bull. 81, pp. 2021-2034.

Cartigny, P., Jendrzejewski, N., Pineau, F., Petit, E., Javoy, M., 2001. Volatile (C, N, Ar) variability in MORB and the respective roles of mantle source heterogeneity and degassing: the case of the Southwest Indian Ridge. Earth Planet. Sci. Lett. 194, 241-257.

Cartigny P., (2005) Stable isotopes and diamond origins. Elements, 1, 79-84.

Cartigny, P., Pineau, F., Aubaud, C., Javoy, M., 2008. Towards a consistent mantle carbon flux estimate: insights from volatile systematics (H_2O/Ce, δD, CO_2/Nb) in the North Atlantic mantle (14° N and 34° N). Earth Planet. Sci. Lett. 265, 672-685.

Cemič, L., 2005. Thermodynamics in Mineral Sciences: An Introduction. Springer. 386 p.

Cerenius, Y., Dubrovinsky, L., 2000. Compressibility measurements on iridium. J. Alloys and Compounds 306, 26-29.

Chiodini, G., M. Valenza, C. Cardellini, and A. Frigeri,2008. A New Web-Based Catalog of Earth Degassing Sites in Italy, Eos Trans. AGU, 89(37).

Coleman, R.G., Lee, D.E., Beatty, L.B., Brannock, W.W., 1965. Eclogites and eclogites: their differences and similarities. Geol. Soc. Amer. Bull. 76, 483-508.

Collerson, K.D., Williams, Q., Ewart, A.E., Murphy, D.T., 2010. Origin of HIMU and EM-1 domains sampled by ocean island basalts, kimberlites and carbonatites: The role of CO2-fluxed lower mantle melting in thermochemical upwellings, Phys. Earth Planet. Inter., 181, 112-131.

Creighton, S., Stachel, T., Matveev, S., Hoefer, H., McCammon, C.A., Luth, R.W., 2009. Oxidation of the Kaapvaal lithospheric mantle driven by metasomatism. Contrib. Mineral. Petrol. 157, 491–504.

Dalton, J.A., Presnall, D.C., 1998a. Carbonatitic melts along the solidus of model lherzolite in the system CaO-MgO-Al_2O_3-SiO_2-CO_2 from 3 to 7 GPa. Contrib. Mineral. Petrol. 131, 123-135.

Dalton, J.A., Presnall, D.C., 1998b. The continuum of primary carbonatitic–kimberlitic melt compositions in equilibrium with lherzolite: data from the system CaO–MgO–Al_2O_3–SiO_2–CO_2 at 6 GPa. J. Petrol. 39, 1953–1964.

Dalton, J.A., Wood, B.J., 1993. The compositions of primary carbonate melts and their evolution through wallrock reaction in the mantle. Earth Planet. Sci. Lett. 119, 511-525.

Dalton, J.A., Wood, B.J., 1995. The stability of carbonate under upper-mantle conditions as a function of temperature and oxygen fugacity. Eur. J. Mineral. 7, 883-891.

Dasgupta, R., Hirschmann, M.M., 2006. Melting in the Earth's deep upper mantle caused by carbon dioxide. Nature 440, 659-662.

Dasgupta, R., Hirschmann, M.M., 2007. Effect of variable carbonate concentration on the solidus of mantle peridotite. Am. Mineral. 92, 370–379.

Dasgupta, R. and Hirschmann, M. M., 2010. The deep carbon cycle and melting in Earth's interior. Earth and Planetary Science Letters (Frontiers) 298, 1-13.

Dasgupta, R., Hirschmann, M. M. and Dellas, N., 2005. The effect of bulk composition on the solidus of carbonated eclogite from partial melting experiments at 3 GPa. Contributions to Mineralogy and Petrology 149, 288-305.

Dasgupta, R., Hirschmann, M.M., Smith, N.D., 2007. Partial melting experiments of peridotite+CO_2 at 3 GPa and genesis of alkalic ocean island basalts. J. Petrol. 48, 2093-2124.

Dasgupta, R., Hirschmann, M.M., Withers, A.C., 2004. Deep global cycling of carbon constrained by the solidus of anhydrous, carbonated eclogite under upper mantle conditions. Earth Planet. Sci. Lett. 227, 73-85.

Dasgupta, R., Walker, D., 2008. Carbon solubility in core melts in a shallow magma ocean environment and distribution of carbon between the Earth's core and the mantle. Geochim. Cosmochim. Acta 72, 4627–4641.

Dawson, J.B., Fuge, R., 1980. Halogen content of some African primary carbonatites. Lithos, 13, 139-143.

Deines, P., Nafziger, R.H., Ulmer, G.C. and Woermann, E., 1974. T-O_2 tables for selected gas mixtures in the C-H-O system. In: College Earth Mineral. Sci. Bull. Exp. Station 88, The Pennsylvania State Univ.

Deines P., 1980. The carbon isotopic compositions of diamonds: relationship to diamond shape, color, occurrence and vapor composition. Geochimica et Cosmochimica Acta 44, 943-961.

Deines, P., 2002. The carbon isotope geochemistry of mantle xenoliths. Earth-Science Reviews 58, 247-278.

Deines, P., Harris, J.W., 1995. Sulfide inclusion chemistry and carbon isotopes of African diamonds. Geochim. Cosmochim. Acta 59, 3173-3188.

Delano, J.W., 2001. Redox history of the Earth's Interior since □3900 Ma: implications for prebiotic molecules. Orig. Life Evol. Bios. 31, 311-341.

Dixon, J.E., 1997. Degassing of alkalic basalts. Am. Mineral. 82, 368-378.

Dixon, J.E., Clague, D.A., Wallace, P., Poreda, R., 1997. Volatiles in alkalic basalts from the north arch volcanic field, Hawaii: extensive degassing of deep submarine-erupted alkalic series lavas. J. Petrol. 38, 911-939.

D'Orazio M., F. Innocenti, S. Tonarini and C. Doglioni, 2007. Carbonatites in a subduction system: the Pleistocene alvikites from Mt. Vulture (southern Italy), Lithos 98, pp. 313-334.

Downs R.T., 2006. The RRUFF Project: an integrated study of the chemistry, crystallography, Raman and infrared spectroscopy of minerals. Program and Abstracts of the 19th General Meeting of the International Mineralogical Association in Kobe, Japan.

Dyar, M.D., Agresti, D.G., Schaefer, M.W., Grant, C.A., and Sklute, E.C., 2006. Mössbauer spectroscopy of Earth and planetary materials. Annual Reviews of Earth and Planetary Sciences, 34, 83-125.

Dunn, K.J., Bundy, F.P., 1978. Materials and techniques for pressure calibration by resistance-jump transitions up to 500 kilobars. Rev. Sci. Instrum. 49, 365-370.

Dunn, R.A., Toomey, D.R., Detrick, R.S., Wilcock W.S.D., 2001. Continuous Mantle Melt Supply Beneath an Overlapping Spreading Center on the East Pacific Rise. Science 291, 1955–1958.

Eggler, D.H., Baker, D.R., 1982. Reduced volatiles in the system C-O-H: implications to mantle melting, fluid formation, and diamond genesis. High-Pressure Res. Geophys., 237-250.

Ellis, D. J. & Green, D. H. (1979). An experimental study of the effect of Ca upon garnet–clinopyroxene Fe-Mg exchange equilibria. Contributions to Mineralogy and Petrology 71, 13-22.

Erlank, A.J., Kushiro, I., 1970. Potassium contents of synthetic pyroxenes at high temperatures and pressures. Carnegie Inst. Washington, Yearbook 68, 433-439.

Eskola, P., 1914. On the petrology of the Orijarvi region in southwestern Finland. *Bull. Com. Geol. Fin.* 40, 274 pp.

Eugster, H. P., 1957, Heterogeneous reactions in- volving oxidation and reduction at high pressure and temperature: Jour. Chem. Physics, v. 26, p. 1720.

Evans, R.L., Tarits, P., Chave, A.D., White, A., Heinson, G., Filloux, J.H., Toh, H., Seama, N., Utada, H., Booker, J.R., Unsworth, M.J., 1999. Asymmetric electrical structure in the mantle beneath the east Pacific rise at 17 S: Science 286, 752–756.

Fabrichanaya, O., Saxena, S.K., Richet, P., Westrum, E.F., 2004. Editors, Thermodynamic Data, Models and Phase Diagrams in Multicomponent Oxide Systems, Springer.

Falloon, T.J., Green, D.H., 1989. The solidus of carbonated, fertile peridotite. Earth Planet. Sci. Lett. 94, 364-370.

Falloon, T.J., Green, D.H., 1990. Solidus of carbonated fertile peridotite under fluid saturated conditions. Geology 18, 195-199.

Fedortchouk Y., Canil D., Semenets E., 2007. Mechanisms of diamond oxidation and their bearing on the fluid composition in kimberlite magmas, American Mineralogist, 92, 1200-1212.

Fei, Y., 1995. Thermal expansion. In: Ahrens TJ (ed) Mineral Physics & Crystallography–a handbook of physical constants, 1st edn. Am. Geophys. Union, Washington, DC, pp 29-44.

Field S.W., Haggerty S.E., 1990. Graphitic xenoliths from the Jagersfontein kimberlite, South Africa: evidence for dominantly anhydrous melting and carbon deposition. Eos, Trans Am Geophys Union 71, 658.

Fine, G.J. and E.M. Stolper, 1985. Dissolved carbon dioxide in basaltic glasses: Concentrations and speciation. Earth Planet. Sci. Lett., 76, p. 263-278.

Finnerty A.A., Boyd F.R., 1987. Thermobarometry for garnet peridotites: basis for the determination of thermal and compositional structure of the upper mantle. In: Nixon PH (ed) Mantle xenoliths. Wiley, Chichester, pp 381-402.

Fiquet, G., Guyot, F., and Itié, J.P., 1994. High-pressure X-ray diffraction study of carbonates- $MgCO_3$, $CaMg(CO_3)_2$, and $CaCO_3$. American Mineralogist 79, 15-23.

Foley, S.F., Yaxley, G.M., Rosenthal, A., Buhre, S., Kiseeva, E.S., Rapp, R.P., Jacob, D.E., 2009. The composition of near-solidus melts of peridotite in the presence of CO_2 and H_2O between 40 and 60 kbar. Lithos 112, 274-283.

Frezzotti, M.L., Peccerillo, A., Panza, G.F., 2009. Carbonate metasomatism and CO_2 lithosphere-asthenosphere degassing beneath the Western Mediterranean: An integrated model arising from petrological and geophysical data. Chemical Geology 262, 108-120.

Frost, D.J., 2003. Fe^{2+}-Mg partitioning between garnet, magnesiowüstite, and $(Mg,Fe)_2SiO_4$ phases of the transition zone. Am. Mineral. 88, 387-397.

Frost, D. J., C. Liebske, F. Langenhorst, C. A. McCammon, R. G. Trønnes, and D. C. Rubie, 2004. Experimental evidence for the existence of iron-rich metal in the Earth's lower mantle. Nature, 428, 409– 412.

Frost, D.J., McCammon, C.A., 2008. The redox state of the Earth's mantle. Annual Review of Earth and Planetary Science 36, 389-420.

Frost, D.J., Wood, B.J., 1997a. Experimental measurements of the fugacity of CO_2 and graphite/diamond stability from 35 to 77 kbar at 925 to 1650°C. Geochimica et Cosmochimica Acta 61, 1565-1574.

Gaillard, F., Malki, M., Iacono-Marziano, G., Pichavant, M., Scaillet, B., 2008. Carbonatite melts and electrical conductivity in the asthenosphere. Science 322, 1363-1365.

Gerlach T.M. andGraeber E., 1985. The volatile budget of Kīlauea Volcano, Nature 313, pp. 273-277.

Ghosh, S., Ohtani, E., Litasov, K.D., Terasaki, H., 2009. Solidus of carbonated peridotite from 10 to 20 GPa and origin of magnesiocarbonatites melt in the Earth's deep mantle. Chem. Geol. 262, 17-28.

Gregory, R.T., Taylor, H.P., 1981. An oxygen isotope profile in a section of cretaceous oceanic crust, Samail ophiolite, Oman: evidence for d18O buffering of the oceans by deep (>5 km) seawater-hydrothermal circulation at mid-ocean ridges. J. Geophys. Res. 86 (B4), 2737-2755.

Gu, Y.J., Lerner-Lam, A.L., Dziewonski, A.M., Ekstrom, G., 2005. Deep structure and seismic anisotropy beneath the East Pacific Rise. Earth Planet. Sci. Lett. 232, 259-272.

Gudfinnsson G. H. and Presnall D. C., 1996. Melting relations of model lherzolite in the system CaO-MgO-Al_2O_3-SiO_2 at 2.4-3.4GPa and the generation of komatiites. J. Geophys. Res., 101, 27701-27709.

Gudfinnsson, G.H., Presnall, D.C., 2005. Continuous gradations among primary kimberlitic, carbonatitic, melilitic, basaltic, picritic, and komatiitic melts in equilibrium with garnet lherzolite at 3-8 GPa, J. Petrol. 46, 1645-1659.

Gudmundsson G., Holloway J.R., 1993. Activity-composition relationships in the system Fe-Pt at 1300 and 1400 °C and at 1 atm and 20 kbar. Am Mineral 78, 178-186.

Gudmundsson, G., Wood, B.J., 1995. Experimental tests of garnet peridotite oxygen barometry. Contrib. Mineral. Petrol. 119, 56-67.

Gurney, J.J., 1989. Diamonds. In: Ross, J. et al. (Eds.) Kimberlites and related rocks. GSA Spec. Publ. 2, 935-965.

Haas, J.L., Hemingway, B.S., 1992. Recommended standard electrochemical potentials and fugacities of oxygen for the solid buffers and thermodynamic data in the systems iron-silicon-oxygen, nickel-oxygen, and copper-oxygen. U.S. Geological Survey Open-File report 92-267, p 733.

Hamilton, D.L., Burnham, C.W., Osborn, E.F., 1964. The solubility of water and effects of oxygen fugacity and water content on crystallization in mafic magmas. Journal of Petrology 5, 21-39.

Hammouda, T., 2003. High-pressure melting of carbonated eclogite and experimental constraints on carbon recycling and storage in the mantle. Earth Planet. Sci. Lett. 214, 357-368.

Harlow, G.E., 1997. K in clinopyroxene at high pressure and temperature:an experimental study. Am. Mineral. 82, 259-269.

Harte, B., Harris, J.W., Hutchison, M.T., Watt, G.R., Wilding, M.C., 1999. Lower mantle mineral associations in diamonds from Sao Luiz, Brazil. In: Fei Y, Bertka CM, Mysen BO (eds) Mantle petrology: field observations and high pressure experimentation. Geochem Soc Spec Publ 6, 125-153.

Herzberg, C. and Zhang, J., 1996. Melting experiments on anhydrous peridotite KLB-1: Compositions of magmas in the upper mantle and transition zone. Journal of Geophysical Research 101, 8271-8295.

Hillgren, V.J., Gessmann, C.K. and Li, J., 2000. An experimental perspective on the light element in Earth's core. In: Canup, R.M. and Righter, K., Editors, 2000. Origin of the Earth and Moon, University of Arizona Press, Tucson, pp. 245-263.

Hirschmann, M. M., 2000. The mantle solidus: experimental constraints and the effect of peridotite composition. Geochemistry, Geophysics, Geosystems 1, paper number 2000GC000070.

Hirschmann, M.M., Dasgupta, R., 2009. The H/C ratios of Earth's near-surface and deep reservoirs, and consequences for deep Earth volatile cycles. Chem. Geol. 262, 4-16.

Holland, T.J.B., Powell, R., 1990. An enlarged and updated internally consistent thermodynamic dataset with uncertainties and correlations: The system K_20-Na_2O-CaO-MgO-FeO-Fe_20_3-Al_2O_3-TiO_2-SiO_2-C-H_2-O_2. J. Metamorphic. Geol. 8, 89-124.

Hollister, V.F., 1980. Origin of graphite in the Duluth Complex. Economic Geology 75, 764-766.

Holloway JR. 1998. Graphite-melt equilibria during partial melting: constraints on CO_2 in MORB magmas and the carbon content of the mantle. Chem. Geol. 147, 89-97.

Huebner, J.S., 1971. Buffering techniques for hydrostatic systems at elevated pressures. In: Research techniques for high pressure and high temperature. (G.C. Ulmer, ed.) pp. 123-178. Berlin, Heidelberg, New York, Springer.

Huebner, J.S., Sato, M., 1970. The oxygen fugacity-temperature relationship of manganese oxide and nickel oxide buffers. Am. Mineral. 55, 934-952.

Jacob, D. E., Kronz, A., Viljoen, K. S., 2004. Cohenite, native iron and troilite inclusions in garnets from polycrystalline diamond aggregates. Contributions to Mineralogy and Petrology 146, 566-576.

Javoy M., Pineau F. and Allègre C.J., 1982. Carbon geodynamic cycle. Nature (London) 300, pp. 171-173.

Johannes, W., Bell, P.M., Mao, H.K., Boettcher, A.L., Chipman, D.W., Hays, J.F., Newton, R.C., Seifert, F., 1971. An interlaboratory comparison of piston–cylinder pressure calibration using the albite-breakdown reaction. Contrib. Mineral. Petrol. 32, 24-38.

Kaminsky, F.V., Khachatryan, G.K., Andreazza, P., Araujo, D.P., Griffin, W.L., 2009. Super-deep diamonds from kimberlites in the Juina area, Mato Grosso State, Brazil. Lithos 112(2), 833-842.

Katsura, T., Shatskiy, A., Manthilake, M., Zhai, S.M., Fukui, H., Yamazaki, D., Matsuzaki, T., Yoneda, A., Ito, E., Kuwata, A., Ueda, A., Nozawa, A., Funakoshi, K., 2009. Thermal expansion of forsterite at high pressures determined by *in situ* X-ray diffraction: the adiabatic geotherm in the upper mantle, Physics of the Earth and Planetary Interiors **174**, 86-92.

Katsura, T., Funakoshi, K., Kubo, A., Nishiyama, N., Tange, Y., Sueda, Y., Kubo, T., Utsumi, W., 2004. A large-volume high-pressure and high-temperature apparatus for in situ X-ray observation, 'SPEEDMk. II'. Phys. Earth Planet. Inter., 143-144, 497-506.

Kawai, N., Endo, S., 1970. The generation of ultrahigh hydrostatic pressures by a split sphere apparatus. Rev. Sci. Instrum. 41, 1178-1181.

Kennedy, C. S., and G. C. Kennedy, 1976. The equilibrium boundary between graphite and diamond. J. Geophys. Res., 81, 2467.

Keppler, H., Frost, D. J., 2005. Introduction to minerals under extreme conditions. In: Miletich, R. (ed.) EMU Notes in Mineralogy, 7. Budapest: Eötvös University Press, pp. 1-30.

Kesson, S.E., FitzGerald, J.D., Shelley, J.M.G., 1998. Mineralogy and dynamics of a pyrolite lower mantle. Nature 393, 252-55.

Klein-Ben David, O., Wirth, R., Navon, O., 2006. TEM imaging and analysis of microinclusions in diamonds: A close look at diamond-growing fluids. American Mineralogist 91, 353-365.

Kogiso, T., Hirschmann, M. M. & Frost, D. J., 2003. High-pressure partial melting of garnet pyroxenite: possible mafic lithologies in the source of ocean island basalts. Earth and Planetary Science Letters 216, 603-617.

Komabayashi, T., Fei, Y., 2010. Internally consistent thermodynamic database for iron to the Earth's core conditions, J. Geophys. Res., 115, B03202.

Kopylova, M., Navon, O., Dubrovinsky, L., Khachatryan, G., 2010. Carbonatitic mineralogy of natural diamond-forming fluids. Earth Planet. Sci. Lett. 291, 126-137.

Kornprobst, J., Pineau, F., Degiovanni, R., and Dautria, J.M. (1987) Primary igneous graphite in ultramafic xenoliths: I. Petrology of the cumulate suite in alkali basalt near Tissemt (Eggere, Algerian Sahara). Journal of Petrology, 28, 293-311.

Koster van Groos, A. F. and Wyllie, P. J., 1963. Experimental data bearing on the role of liquid immiscibility in the genesis of carbonatites. Nature, 199, 801-802.

Kraft, S., Knittle, E., Williams, Q., 1991. Carbonate stability in the Earth's mantle: a vibrational spectroscopic study of aragonite and dolomite at high pressures and temperatures, J. Geophys. Res. 96, 17997-18010.

Ionov D. A., Dupuy C., O'Reilly S. Y., Kopylova M. G., Genshaft Y. S., 1993. Carbonated peridotite xenoliths from Spitsbergen: implications for trace element signature of mantle carbonate metasomatism. Earth and Planetary Science Letters 119, 283-297.

Ionov, D., O'Reilly, S.Y., Genshaft, Y.S., Kopylova, M.G., 1996. Carbonate-bearing mantle peridotite xenoliths from Spitsbergen: phase relationships, mineral compositions and trace-element residence. Contrib. Mineral. Petrol. 125, 375-392.

Irifune, T., Shinmei, T., McCammon, C.A., Miyajima, N., Rubie, D.C., Frost, D.J. 2010. Iron Partitioning and Density Changes of Pyrolite in Earth's Lower Mantle. Science 327, 193.

Isshiki, M., Irifune, T., Hirose, K., Ono, S., Ohishi, Y., Watanuki, T., Nishibori, E., Takata, M., Sakata, M., 2004. Stability of magnesite and its high-pressure form in the lowermost mantle. Nature 427, 60-63.

Jacob, D.E., 2004. Nature and origin of eclogite xenoliths from kimberlites. Lithos 77, 295-316.

Jayasuriya K.D., O'Neill H.S., Berry A.J., Campbell S.J., 2004. A Mossbauer study of the oxidation state of Fe in silicate melts. Am. Mineral. 89, 1597-1609.

Lee, C.T.A., Leeman, W.P., Canil, D., Li, Z.X.A., 2005. Similar V/Sc systematics in MORB and arc basalts: Implications for the oxygen fugacities of their mantle source regions. J. Petrol. 46 (11), 2313–2336.

Le Bas, M.J., 1981. Carbonatite magmas. Mineral. Mag. 44, 133-140.

Leung, I., Guo, W., Friedman, I., Gleason, J., 1990. Natural occurrence of silicon carbide in a diamondiferous kimberlite from Fuxian. Nature 346, 352-354.

Li, Z.-X.A., Lee, C.-T.A., 2004. The constancy of upper mantle fo_2 through time inferred from V/Sc ratios in basalts. Earth Planet. Sci. Lett. 228, 483-493.

Litasov, K.D., Fei, Y., Ohtani, E., Kuribayashi, T., Funakoshi, K., 2008. Thermal equation of state of magnesite to 32 GPa and 2073 K. Physics of the Earth and Planetary Interior 168, 191-203.

Litasov, K.D.,Ohtani, E., 2009a. Phase relations in the peridotite-carbonate-chloride system at 7.0-16.5 GPa and the role of chlorides in the origin of kimberlite and diamond. Chem. Geol. 262, 29-41.

Litasov, K., Ohtani, E., 2009b. Solidus of carbonated peridotite in the system $CaO–Al_2O_3–MgO–SiO_2–Na_2O–CO_2$ to the lower mantle depths. Phys. Earth Planet. Inter. 177, 46-58.

Litasov, K.D., and Ohtani, E., 2010. The solidus of carbonated eclogite in the system CaO-Al2O3-MgO-SiO2-Na2O-CO2 to 32 GPa and carbonatite liquid in the deep mantle: Earth and Planetary Science Letters, v. 295, p. 115-126.

Long, G.J., Cranshaw, T.E., and Longworth, G., 1983. The ideal Mössbauer effect absorber thicknesses. Mössbauer Effect Reference Data Journal, 6, 42.49.

Longhi, J., 2005. Temporal stability and pressure calibration of barium carbonate and talc/pyrex pressure media in a piston-cylinder apparatus. American Mineralogist 90, 206-218.

Luque, F.J., Rodas, M., Galán, E., 1992. Graphite vein mineralization in the ultramafic rocks of southern Spain: mineralogy and genetic relationships. Mineralium Deposita 27, 226-233.

Luque, F.J., Pasteris, J.D., Wopenka, B., Rodas, M., Barrenechea, J.F., 1998. Natural fluid-deposited graphite: mineralogical characteristics and mechanisms of formation. American Journal of Science 298, 471-498.

Luth, R.W., 1993. Diamonds, Eclogites and the Oxidation State of the Earth's mantle. Science, New Series, 261 n. 5117, 66-68.

Luth, R.W., Canil, D., 1993. Ferric iron in mantle-derived pyroxenes and a new oxybarometer for the mantle. Contributions to Mineralogy and Petrology 113, 236-248.

Luth, R.W., Virgo, D., Boyd, F.R., Wood, B.J., 1990. Ferric iron in mantle-derived garnets. Contrib. Miner. Petrol. 104, 56-72.

MacGregor I.D., 1974. The system $MgO-Al_2O_3-SiO_2$: solubility of Al_2O_3 in enstatite for spinel and garnet peridotite compositions. Am Mineral 59, 110-119.

Mallmann, G., O'Neill, St.C., 2009. The crystal/melt partitioning of V during mantle melting as a function of oxygen fugacity compared with some other elements. J. Petrol. 50, 1765-1794.

Marty, B. and Jambon, A., 1987. C/He^3 in volatile fluxes from the solid Earth. Implications for carbon geodynamics, Earth Planet. Sci. Lett. 83, 16-26.

Marty, B., Tolstikhin, I.N., 1998. CO_2 fluxes frommid-ocean ridges, arcs and plumes. Chem. Geol. 145, 233-248.

Mathez, E.A., 1987. Carbonaceous matter in mantle xenoliths: composition and relevance to the isotopes. Geochimica et Cosmochimica Acta 51, 2339-2347.

Mathez, E. A., Fogel, R. A., Hutcheon, I. D., Marshintsev, V. K., 1995. Carbon isotope composition and origin of SiC from kimberlites of Yakutia, Russia. Geochimica et Cosmochimica Acta 59, 781-791.

McCammon C.A., 1994. A Mössbauer milliprobe: practical considerations. Hyperfine Interact. 92, 1235-1239.

McCammon, C.A., 2000. Insights into phase transformations from Mössbauer spectroscopy. In S. Redfern, and M. Carpenter, Eds., Transformation Processes in Minerals, vol. 39, p. 241-264. Reviews in Mineralogy and Geochemistry, Mineralogical Society of America, Washington, D.C.

McCammon, C.A. and Ross, N.L., 2003. Crystal chemistry of ferric iron in $(Mg,Fe)(Si,Al)O_3$ majorite with implications for the transition zone. Physics and Chemistry of Minerals 30, 206-216.

McCammon C.A., Griffin W.L., Shee S.R., O'Neill H.StC., 2001. Oxidation during metasomatism in ultramafic xenoliths from the Wesselton kimberlite, South Africa: implications for the survival of diamond. Contrib. Miner. Petrol. 141, 287-296.

McCammon, C.A., Kopylova, M.G., 2004. A redox profile of the Slave mantle and oxygen fugacity control in the cratonic mantle. Contrib. Miner. Petrol. 148, 55-68.

McCandless, T.E., Gurney, J.J., 1989. Sodium in garnet and potassium in clinopyroxene; criteria for classifying mantle eclogites. In: Ross, J., Jaques, A.L., Ferguson, J., Green, D.H., O'Reilly, S.Y., Danchin, R.V., Janse, A.J.A. (Eds.), Kimberlites and Related Rocks. Special Publication—Geological Society of Australia, vol. 14, pp. 827-832. Perth.

McDonough, W.F., Sun, S.-s., 1995. The composition of the Earth. Chem. Geol. 120, 223-253.

McKenzie D., 1984. The generation and compaction of partially molten rock. J. Petrol. 25, 713-765.

McKenzie, D., 1985. The extraction of magma from the crust and mantle. Earth Planet. Sci. Lett. 74, 81-91.

Meyer, H.O.A., 1987. Inclusions in diamonds. In: Nixon. P.H. (Ed.). Mantle xenoliths. Chichester, England, John Wiley and Sons, pp. 501-522.

Milholland, C.S., Presnall, D.C., 1998. Liquidus phase relations in the system CaO-MgO-Al_2O_3-SiO_2 at 3.0 GPa: the aluminous pyroxene thermal divide and high-pressure fractionation of picritic and komatiitic magmas. J. Petrol. 39, 3-27.

Minissale, A., 2004. Origin, transport and discharge of CO_2 in central Italy. Earth Science Review 66, 89-141.

Mitchell, R.H., 1986. Kimberlites: Mineralogy, Geochemistry and Petrology. Plenum Press, New York, N.Y.

Moecher D.P., Essene E.J., Anovitz L.M., 1988. Calculation and application of clinopyroxene-garnet-plagioclase-quartz geobarometers. Contrib Mineral Petrol 100, 92-106.

Moore J. G., 1979. Vesicularity and CO_2 in MORB. Nature 282, 250-253.

Moore, K.R., Wood, B.J., 1998. The Transition from Carbonate to Silicate Melts in the CaO–MgO SiO_2–CO_2 System. J. of Petrol. 39, 1943-1951.

Mukhopadhyay, B., 1991. Garnet breakdown in some deep-seated garnetiferous xenoliths from the central Sierra Nevada: Petrologic and tectonic implications. Lithos, 27, 59-78.

Mysen B.O. and Richet P., 2005. Silicate Glasses and Melts-Properties and Structure, Elsevier, Amsterdam.

Nasdala, L., Smith, D.C., Kaindl, R.and Ziemann, M.A., 2004. Raman Spectroscopy: Analytical perspectives in mineralogical research. - In: BERAN, A. & LIBOWITZKY, E. (eds.): EMU Notes in Mineralogy, EMU School on Spectroscopic Methods in Mineralogy. Chap. 7, 281-343.

Nell J. and Wood B.J., 1991. High-temperature electrical measurements and thermodynamic properties of Fe_3O_4-$FeCr_2O_4$-$MgCr_2O_4$-$FeAl_2O_4$ spinels. Am. Miner. 76, 405-26.

Nixon P.H. and Boyd F.R., 1973. Petrogenesis of the granular and sheared ultrabasic nodule suite in kimberlites. In Lesotho Kimberlites, ed. PH Nixon, pp. 48-56. Maseru, Lesotho: Lesotho Natl. Dev. Corp. 350 pp.

O'Hara, M. J., 1960. A garnet-hornblende-pyroxene rock from Glenelg, Inverness-shire. Geol. Mag. 97, 145.

O'Neill, H.St.C., Wood, B.J., 1979. An experimental study of Fe-Mg partitioning between garnet and olivine and its calibration as a geothermometer. Contrib. Mineral. Petrol. 70, 59-70.

O'Neill, H.St.C., Wall, V.J., 1987. The olivine-orthopyroxene-spinel oxygen geobarometer, the nickel precipitation curve, and the oxygen fugacity of the earth's upper mantle. J. Petrol. 28, 1169-1191.

O'Neill, H.St.C., 1987a. Quartz–fayalite–iron and quartz–fayalite–magnetite equilibria and the free energies of formation of fayalite (Fe_2SiO_4) and magnetite (Fe_3O_4). Am. Mineral. 72, 67-75.

O'Neill, H.St.C., Rubie, D.C., Canil, D., Geiger, C.A., Ross, C.R., 1993b. Ferric iron in the upper mantle and in transition zone assemblages: implications for relative oxygen fugacities in the mantle. In Evolution of the Earth and Planets , ed. E Takahashi, R Jeanloz, DC Rubie, Geophys. Monogr. 74: 73-88. Washington: Int. Union Geol. Geophys. and Am. Geophys.Union.

O'Neill, H.St.C., Berry, A.J., McCammon, C.M., Jayasuriya, K.D.,Campbell, S.J., Foran, G., 2006. An experimental determination of the effect of pressure on the $Fe^{3+}/\Sigma Fe$ ratio of an anhydrous silicate melt to 3.0 GPa Am. Mineral. 91, 404-412.

Ono, S., Kikegawa, T., Ohishi, Y., Tsuchiya, J., 2005. Post-aragonite phase transformation in $CaCO_3$ at 40 GPa. Am. Mineral. 90, 667-671.

Ono, S., Kikegawa, T., Ohishi, Y., 2007. High-pressure phase transition of $CaCO_3$. Am. Mineral. 92, 1246-1249.

Onodera, A., Ohtani, A., 1980. Fixed points for pressure calibration above 100 kbars related to semiconductor-metal transitions. J. Appl. Phys. 51 (5), 2581-2585.

Otting, W. and Zahringer, J., 1967. Total carbon content and primordial rare gases in chondrites, Geochim. Cosmochim. Acta 31, 1949-1960.

Pan, V., Holloway, J.R., Hervig, R.L., 1991. The pressure and temperature dependence of carbon dioxide solubility in tholeiitic basalt melts. Geochimica et Cosmochimica Acta 56, 1875-1883.

Papale, P., 1999. Modeling of the solubility of a two-component H2O+CO2 fluid in silicate liquids, American Mineralogist, v. 84, p. 477-492.

Pearson, D.G, Davies, G.R, Nixon, P.H, Milledge, H.J., 1989. Graphitized diamonds from a peridotite massif in Morocco and implications for anomalous diamond occurrences. Nature 338, 60-62.

Pearson, D.G., Boyd, F.R., Haggerty, S.E., Pasteris, J.D., Field, S.W., Nixon, P.H., Pokhilenko, N.P., 1994. The characterisation and origin of graphite in cratonic lithospheric mantle: a petrological carbon isotope and Raman spectroscopic study. Contrib. Mineral. Petrol. 115, 449-466.

Pertermann, M. and Hirschmann, M. M., 2003. Anhydrous partial melting experiments on MORB-like eclogite: phase relations, phase compositions and mineral–melt partitioning of major elements at 2-3 GPa. Journal of Petrology 44, 2173-2201.

Pineau, F., Javoy, M., Kornprobst, J., 1987. Primary igneous graphite in ultramafic xenoliths: II. Isotopic composition of the carbonaceous phases present in xenoliths and host lava at Tissemt (Algerian Sahara). Journal of Petrology 28, 313-322.

Pineau, F., Shilobreeva, S., Hekinian, R., Bidiau, D., Javoy, M., 2004. Deep-sea explosive activity on the Mid-Atlantic Ridge near 34º 50′ N: a stable isotope (C, H, O) study. Chem. Geol. 211, 159-175.

Poirier J.P., 1994. Light elements in the Earth's outer core: A critical review, Phys. Earth Planet. Inter. 85, 319-337.

Presnall, D.C., Dixon, S.A., Dixon, J.R., O'Donnell, T.H., Brenner, N.L., Schrock, R.L., Dycus, D.W., 1978. Liquidus phase relations on the joint diopside-forsterite-anorthite from 1 atm to 20 kbar; their bearing on the generation and crystallization of basaltic magma. Contrib. Mineral. Petrol. 66, 203–220.

Presnall, D.C., Dixon, J.R., O'Connell, T.H. & Dixon, S.A., 1979. Generation of mid-ocean ridge tholeiites. J. Petrol. 20, 3-35.

Presnall, D. C., Gudfinnsson, G. H. & Walter, M. J., 2002. Generation of mid-ocean ridge basalts at pressures from 1 to 7 GPa. Geochimica et Cosmochimica Acta 66, 2073-2090.

Prins, P., 1973. Apatite from African carbonatites. Lithos 6, 133-144.

Reed, S. J. B., 2005. Electron Microprobe Analysis and Scanning Electron Microscopy in Geology, 2nd ed. xiii+192 pp. Cambridge, New York, Melbourne, Cambridge University Press.

Ringwood, A.E., 1975, *Composition and Petrology of the Earth's Mantle*, McGraw-Hill, New York, 618 pp.

Ripley, E.M., Taib, N.I., 1989. Carbon isotopic studies of metasedimentary and igneous rocks at the Babbitt Cu–Ni deposit, Duluth Complex, Minnesota, U.S.A.. Chemical Geology (Isotope Geoscience Section) 73, 319-342.

Robie RA, Hemingway BS, Fisher JR (1978) Thermodynamic properties of minerals and related substances at 298.15 K and 1 bar (10^5Pa) pressure and at higher temperature. US Geol Surv Bull 1452.

Robie, R.A., Hemingway, B.S., 1995. Thermodynamic Properties of Minerals and Related Substances at 298.15 K and 1 bar (10^5 Pascals) Pressure and at Higher Temparatures. U.S. Geol. Survey Bullettin 2131, United States Government Printing Office, Washinghton.

Roedder E., 1984. Fluid inclusions; Reviews in Mineralogy 12. Mineral. Soc. Amer.

Rohrbach, A., Ballhaus, C., Golla–Schindler, U., Ulmer, P., Kamenetsky, V.S., Kuzmin, D.V., 2007. Metal saturation in the upper mantle. Nature 449, 456-458.

Ross, N.L., 1997. The equation of state and high pressure behaviour of magnesite. American Mineralogist, 82, 682-688.

Rubie, D.C., 1999. Characterising the sample environment in multianvil high-pressure experiments. Phase Transitions 68, 431-451.

Rubie D.C., Karato S., Yan H., O'Neill H.St.C., 1993. Low differential stress and controlled chemical environment in multianvil high-pressure experiments. Phys Chem Minerals 20, 315-322.

Saal, A.E., Hauri, E., Langmuir, C.H., Perfit, M.R., 2002 Vapour undersaturation in primitive mid-ocean-ridge basalts and the volatile content of Earth's upper mantle. Nature 419, 451-455.

Sack R.O., Carmichael I.S.E., Rivers M., Ghiorso M.S., 1980. Ferric-ferrous equilibria in natural silicate liquids at 1 bar. Contrib. Miner. Petrol. 75(4), 369-76.

Salters V. J. M. and Hart S. R., 1989. The Hf-paradox, and the role of garnet in the MORB source. Nature 342, 420-422.

Sano, Y., Williams, S.N., 1996. Fluxes of mantle and subducted carbon along convergent plate boundaries. Geophys. Res. Lett. 23, 2749-2752.

Sato M. and Valenza, M., 1980. Oxygen fugacities of the layered series of the Skaergaard intrusion, East Greenland. Am. J. Sci. 280A, 134-58.

Schrauder M. and Navon O., 1993. Solid carbon dioxide in a natural diamond. Nature 365, 42-44.

Schwerdtfeger, K., Zwell, L., 1968. Activities in solid iridium-iron and rhodium-iron alloys at 1200°C. Trans. Metall. Soc. AIME 242, 631-633.

Seagle, C.T., D.L. Heinz, A.J. Campbell, V.B. Prakapenka, and S.T. Wanless, 2008. Melting and thermal expansion in the Fe-FeO system at high pressure, Earth Planet. Sci. Lett., 265, 655-665.

Sharp, W.E., 1966. Pyrrhotite: a common inclusion in South African Diamonds. Nature 211, 402–403.

Shaw, A.M., Hilton, D.R., Fischer, T.P., Walker, J.A., Alvarado, G.E., 2003. Contrasting He-C relationships in Nicaragua and Costa Rica: insights into C cycling through subduction zones. Earth Planet Sci. Lett. 214, 499-513.

Shaw, A.M., Behn, M.D., Humphris, S.E., Sohn, R.A., Gregg, P.M., 2010. Deep pooling of low degree melts and volatile fluxes at the 85°E segment of the Gakkel Ridge: evidence from olivine-hosted melt inclusions and glasses. Earth Planet. Sci. Lett. 289, 311-322.

Shcheka, S.S., Weidenbeck, M., Frost, D.J., Keppler, H., 2006. Carbon solubility in mantle minerals. Earth Planet. Sci. Lett. 245, 730–742.

Shushkanova, A.V., Litvin, Y.A., 2008. Experimental evidence for liquid immiscibility in the model system $CaCO_3$-pyrope-pyrrhotite at 7.0 GPa: the role of carbonatite and sulfide melts in diamond genesis, Canadian Mineralogist 46, 991-1005.

Smith, C.B., Gurney, J.J., Skinner, E.M.W., Clement, C.R., and Ebrahim, N., 1985. Geochemical character of the southern African kimberlites: A new approach based on isotopic constraints: Geological Society of South Africa Transactions, v. 88, p. 267-280.

Sobolev, N.V., Lavrentev, Y.G., 1971. Isomorphic sodium admixture in garnets formed at high pressure. Contrib. Mineral. Petrol. 31, 1-12.

Stachel,T. and Harris,J.W., 2008. The origin of cratonic diamonds-Constraints from mineral inclusions. Ore Geology Reviews, 34, 5-32.

Stagno, V., and D. J. Frost, 2010. Carbon speciation in the asthenosphere: Experimental measurements of the redox conditions at which carbonate-bearing melts coexist with graphite or diamond in peridotite assemblages. Earth Planet. Sci. Lett., 30, 72-84.

Stolper E.M. and J.R. Holloway, 1988. Experimental determination of the solubility of carbon dioxide in molten basalt at low pressure. Earth Planet. Sci. Lett., 87, p. 397-408.

Strens, R.G.J., 1965. The graphite deposit of Seathwaite in Borrowdale, Cumberland. Geological Magazine 102, 393-406.

Swartzendruber, L.J., 1984. The Fe-Ir (iron - iridium) system. Bull. of Alloy Phase Diagrams 5, 48-52.

Tange, Y., Irifune, T., and Funakoshi, K., 2008. Pressure generation to 80 GPa using multianvil apparatus with sintered diamond anvils, High Pressure Res., 28, 245-254.

Taylor, W.R., Green, D.H., 1988. Measurement of reduced peridotite-C-O-H solidus and implications for redox melting of the mantle. Nature 332, 349-352.

Taylor, J., Wall, V.J., Pownceby M.I., 1992. The calibration and application of accurate redox sensors. American Mineralogist 77, 284-295.

Tingle, T., 1998. Accretion and differentiation of carbon in the early Earth. Chem. Geol. 147, 3-10.

Trull, T. Nadeau, S., Pineau, F., Polve, M., Javoy, M., 1993. C-He systematics in hotspot xenoliths: implications for mantle carbon contents and carbon recycling. Earth Planet. Sci. Lett. 118, 43-64.

Tsuchiya, T., 2003. First-principles prediction of the P-V-T equation of state of gold and the 660-km discontinuity in Earth's mantle, J. Geophys. Res., 108, 2462.

Ulmer, P., Luth, R.W., 1991. The graphite-COH fluid equilibrium in P, T, fo_2 space. Contrib. Mineral. Petrol. 106, 265-272.

van Aken, P.A., Liebscher, B., 2002. Quantification of ferrous/ferric ratios in minerals: new evaluation schemes of Fe-L23 electron energy-loss near-edge spectra. Phys. Chem. Miner. 29, 188-200.

Veksler, I.V., Nielsen, T.F.D., Sokolov, S.V., 1998a. Mineralogy of crystallized melt inclusions from Gardiner and Kovdor ultramafic alkaline complexes: implications for carbonatite petrogenesis. Journal of Petrology 39, 2015-2031.

Vol, A.E., Kagan I.K., 1976. Handbook of Binary Metallic Systems - Structures and Properties. Nauka (Moskow) vol.3, 788.

Von Seckendorff, V., O'Neill, H.St.C., 1993. An experimental study of Fe-Mg partitioning between olivine and orthopyroxene at 1173, 1273 and 1423 K and 1.6 GPa. Contrib. Mineral. Petrol. 113, 196-207.

Wallace, M.E., Green, D.H., 1988. An experimental determination of primary carbonatite magma composition. Nature 335, 343-346.

Wallace, P. J. (2005). Volatiles in subduction zone magmas: Concentrations and fluxes based on melt inclusion and volcanic gas data, J. Volcanol. Geotherm. Res., 140, 217-240.

Walker, D., 1991. Lubrication, gasketing, and precision in multianvil experiments. American Mineralogist 76, 1092-1100.

Walter, M., Bulanova, G., Armstrong, L., Keshav, S., Blundy, J.D., Gudfinnsson, G., Lord, O., Lennie, A., Smith, C., Gobbo, L., 2008. Primary carbonatite melt from deeply subducted oceanic crust. Nature 454, 622-625.

Wiser N., and Wood B.J., 1991. Experimental determination of activities in Fe-Mg olivine at 1400K. Contrib Mineral Petrol 108, 146-163.

Wood B.J., 1987. Thermodynamics of multicomponent systems containing several solid solutions. (Reviews in mineralogy 17) Mineral Soc Am, Washington, DC, 71-94.

Wood, B.J., 1991. Oxygen barometry of spinel peridotites. In Oxide Minerals: Petrologic and Magnetic Significance, ed. DH Lindsley, Rev. Mineral. 25, 417-31. Washington, DC: Mineral. Soc. Am. 508 pp.

Wood B.J., Banno S., 1973. Garnet-orthopyroxene and orthopyroxene-clinopyroxene relationships in simple and complex systems. Contrib Mineral Petrol 42, 109-124.

Wood B.J., Bryndzia L.T., Johnson K.E., 1990. Mantle oxidation state and its relationship to tectonic environment and fluid speciation. Science 248, 337-345.

Wood, B.J., and Fraser, D. G., 1976. Elementary Thermodynamics for Geologists. Oxford University Press, 303 p.

Wood B.J. and Nicholls J., 1978. The thermodynamical properties of reciprocal solid solutions. Contrib Mineral Petrol 66, 389-400.

Woodland A.B., 2009. Ferric iron contents of clinopyroxene from cratonic mantle and partitioning behaviour with garnet. Lithos, 112, 2, 1143-1149.

Woodland, A.B., Koch, M., 2003. Variation in oxygen fugacity with depth in the upper mantle beneath Kaapvaal craton, South Africa. Earth Planet. Sci. Lett. 214, 295-310.

Woodland, A.B., O' Neill, H.St.C., 1997. Thermodynamic data for Fe-bearing phases obtained using noble metal alloys as redox sensors. Geochim. Cosmochim. Acta 61, 4359-4366.

Woodland AB, Peltonen P., 1999. Ferric iron contents of garnet and clinopyroxene and estimated oxygen fugacities of peridotite xenoliths from the Eastern Finland Kimberlite Province. *Proc. Int. Kimberlite Conf.*, *7th, Cape Town*, pp. 904–11. Cape Town: Red Roof Design

Woolley, A.R., 1989. The spatial and temporal distribution of carbonatites. In: K. Bell, Editor, Carbonatites, Unwin Hyman, London, pp. 15-38.

Wyllie, P. J., and Huang, W. L., 1975. Influence of mantle CO_2 in the generation of carbonatites and kimberlites. Nature, 257, 297-299.

Wyllie, P.J., Huang W.L., 1976. Carbonation and melting reactions in the system CaO-MgO-SiO_2-CO_2 at mantle pressures with geophysical and petrological applications. Contrib. Mineral. Petrol. 54, 79-107.

Yasuda, A., Fujii, T. & Kurita, K. ,1994. Melting phase relations of an anhydrous mid-ocean ridge basalt from 3 to 20 GPa; implications for the behavior of subducted oceanic crust in the mantle. Journal of Geophysical Research 99, 9401-9414.

Yaxley, G.M., Brey, G.P., 2004. Phase relations of carbonate-bearing eclogite assemblages from 2.5 to 5.5 GPa: implications for petrogenesis of carbonatites. Contrib. Mineral. Petrol. 146, 606-619.

Yoder, H. S. and C. E. Tilley, 1962. Origin of basalt magmas: an experimental study of natural and synthetic rock systems. J. of Petrol. 3, 342-532.

Zhang C. and Duan Z., 2009. A model for C-O-H fluid in the Earth's mantle. Geochimica et Cosmochimica Acta, 73 (7), 2089-2102.

Zhang, R. Y., Zhai, S. M., Fei, Y. W. & Liou, J. G., 2003. Titanium solubility in coexisting garnet and clinopyroxene at very high pressure: the significance of exsolved rutile in garnet. Earth and Planetary Science Letters, 216, 591-601.

Zhang, Y., Zindler, A., 1993. Distribution and evolution of carbon and nitrogen in Earth. Earth Planet. Sci. Lett. 117, 331-345.

APPENDIX

Table S3.1a Microprobe phase analyses.

Phase	No. points[+]	SiO_2	MgO	CaO	Al_2O_3	FeO*	IrO_2[*]	CO_2[**]	Tot.
H289a (2.5 GPa, 1100 °C)									
Liq	4	0.50(17)	14.68(91)	34.42(1.67)	0.03(1)	2.16(17)	0.36(22)	47.84	52.16(1.61)
Ol	27	41.46(21)	49.93(38)	0.15(5)	0.01(1)	8.67(39)	0.26(21)		100.48(38)
Cpx	21	55.32(38)	20.04(38)	22.49(65)	0.10(4)	2.70(27)	0.31(15)		100.96(37)
Opx	11	58.34(32)	34.91(50)	1.74(33)	0.07(1)	5.28(23)	0.38(27)		100.72(53)
H298a (2.8 GPa, 1265 °C)									
Liq	n.m.								
Ol	28	41.66(26)	51.62(51)	0.24(11)	0.01(1)	7.00(43)	0.35(24)		100.87(37)
Cpx	20	55.83(28)	20.72(50)	22.07(97)	0.18(4)	2.13(40)	0.21(20)		101.14(31)
Opx	3	58.54(30)	34.72(51)	2.96(1.06)	0.10(2)	4.49(7)			101.07(41)
V588a (3 GPa, 1100 °C)									
Dol	2	0.25(23)	20.48(1.19)	32.20(98)	0.01(1)	2.30(11)	0.34(11)	44.43	55.57(27)
Ol	19	41.41(23)	50.19(38)	0.14(4)	0.01(1)	9.03(4)	0.27(18)		101.05(33)
Cpx	19	55.55(27)	19.86(32)	22.69(42)	0.13(5)	2.73(47)	0.30(16)		101.26(35)
Opx	17	58.55(55)	35.55(47)	1.39(21)	0.07(1)	4.99(21)	0.34(24)		100.90(64)
V538a (3 GPa, 1200 °C)									
Liq	1	3.61	13.33	31.04	0.06	2.15		49.81	50.19
Ol	22	40.41(18)	50.88(26)	0.13(2)	0.02(1)	7.92(16)	0.21(15)		99.61(24)
Cpx	43	54.19(32)	20.74(39)	21.48(42)	0.14(9)	2.72(40)	0.26(18)		99.52(45)
Opx	3	57.04(13)	35.44(13)	1.57(6)	0.09(3)	4.57(4)			98.92(11)
V426a (3GPa, 1250 °C)									
Liq	30	3.39(1.82)	19.56(1.40)	29.99(1.80)	0.07(4)	3.78(1.09)	0.22(21)	43.00	57.00(2.84)
Ol	17	40.56(23)	51.53(22)	0.10(2)	0.01(1)	9.11(32)	0.23(16)		101.54(26)
Cpx	4	55.36(25)	22.31(79)	20.01(82)	0.10(1)	2.99(20)	0.21(19)		100.99(22)
Opx	17	57.32(30)	35.79(30)	1.56(23)	0.11(4)	5.53(29)	0.21(17)		100.52(35)
V403a (3GPa, 1300 °C)									
Liq	92	4.44(2.40)	24.32(2.08)	25.11(2.87)	-	4.34(84)		41.53	58.47(3.10)
Ol	5	41.38(22)	51.48(39)	0.13(9)	-	8.42(11)			101.73(40)
Cpx	2	55.74(25)	22.92(33)	18.92(11)	0.05(1)	2.71(28)	0.50(1)		100.88(40)
Opx	29	58.68(28)	36.17(36)	1.06(30)	-	5.02(10)	0.18(17)		101.11(41)
V406a (3 GPa, 1350 °C)									
Liq	30	4.05(2.38)	27.63(1.22)	21.81(1.45)	0.08(5)	5.25(69)		41.10	58.90(2.62)
Ol	10	41.36(86)	51.59(55)	0.08(2)	-	7.24(16)	0.43(38)		100.63(58)
Cpx	1	56.27	23.07	17.90	0.5	2.64	0.80		100.72
Opx	35	57.51(33)	36.66(42)	1.03(39)	0.03(2)	5.29(11)	0.23(14)		100.76(39)
V511a (3 GPa, 1400 °C)									
Liq	33	18.76(2.71)	28.23(1.83)	20.97(2.65)	0.09(2)	6.90(81)		24.88	75.12(1.83)
Ol	25	41.34(13)	52.81(18)	0.29(2)	-	6.92(13)	0.18(18)		101.54(30)
Cpx	39	55.74(61)	25.63(1.46)	15.29(2.00)	-	3.42(40)	0.17(16)		100.25(61)
Opx	30	57.84(16)	35.55(33)	2.59(42)	-	4.23(17)	0.24(17)		100.45(31)
V542a (3 GPa, 1400 °C – 12 hrs)									
Liq	2	17.44(1.87)	22.73(2.67)	26.44(2.10)	0.07(1)	8.00(1.39)		25.03	74.97(3.50)
Ol	15	41.28(17)	52.83(10)	0.29(2)	0.01(1)	5.86(9)	0.14(13)		100.41(30)
Cpx	17	56.37(21)	25.91(53)	15.45(67)	0.04(1)	2.75(10)	0.13(12)		100.64(21)
Opx	13	58.26(25)	35.80(26)	2.82(11)	0.03(1)	3.25(5)	0.19(13)		100.34(46)
V550 (3 GPa, 1400 °C – 6 hrs)									
Liq	7	1.81(1.40)	16.39(64)	33.62(1.71)	0.05(5)	3.13(87)		44.87	55.13(1.70)
Liq	1	10.83	27.57	20.58	0.20	9.10		31.61	68.39
Ol	17	40.92(21)	50.47(42)	0.12(3)	0.01(1)	8.36(60)	0.25(18)		100.13(35)
Cpx	18	55.38(23)	20.57(46)	21.63(61)	0.10(4)	2.61(15)	0.20(17)		100.50(32)
Opx	28	58.26(42)	35.34(41)	1.98(48)	0.09(3)	4.36(28)	0.14(14)		100.18(48)
V512a (3 GPa, 1450 °C)									
Liq	3	21.62(25)	28.13(30)	20.89(19)	0.31(4)	6.67(8)	-	21.66	78.34(75)
Ol	38	40.90(95)	52.33(66)	0.37(19)	-	7.37(18)	-		101.14(73)
Cpx	35	55.08(25)	21.17(62)	21.00(92)	-	2.58(16)	-		99.96(23)

Opx	27	57.75(45)	35.22(62)	2.80(68)	-	4.28(39)	0.19(15)		100.24(59)
V514a (3 GPa, 1500 °C – 4 hrs)									
Liq	8	33.54(7.91)	27.51(3.95)	17.41(3.21)	0.20(8)	5.67(1.76)	0.28(26)	15.18	84.82(4.51)
Ol	32	41.10(20)	52.85(22)	0.33(12)	-	5.64(18)	0.17(11)		100.09(27)
Cpx	20	55.10(28)	22.17(87)	19.96(1.12)	-	2.48(19)	0.14(12)		99.85(29)
Opx	28	57.91(16)	35.64(18)	2.10(34)	-	3.82(34)	0.13(11)		99.60(21)
V592 (3 GPa, 1500 °C)									
Liq	3	33.64(1.15)	26.09(1.07)	13.34(62)	1.04(4)	6.84(87)	-	18.57	81.43(1.21)
Ol	21	42.26(34)	52.63(32)	0.60(18)	0.02(1)	5.18(14)	0.24(19)		100.97(33)
Cpx	17	55.87(39)	19.86(53)	22.36(77)	0.46(2)	1.68(14)	-		100.52(54)
Opx	1	50.85	33.93	11.64	0.31	3.21	0.19		100.33
V569 (3 GPa, 1550 °C)									
Liq	21	34.77(4.82)	30.15(3.92)	16.18(2.73)	0.23(8)	5.25(74)	0.42(40)	12.90	87.10(3.30)
Ol	45	41.72(38)	53.65(42)	0.44(4)	0.1(1)	3.83(9)	0.37(21)		100.02(60)
qchOl	4	40.11(65)	51.72(81)	0.67(3)	0.2(1)	5.32(37)	0.28(16)		98.11(1.08)
V587 (3 GPa, 1400 °C)									
Liq	11	25.29(1.47)	16.99(48)	23.40(87)	4.35(32)	4.90(19)	-	24.89	75.11(1.45)
Ol	20	40.11(33)	50.26(31)	0.22(8)	0.08(5)	8.14(13)	0.18(16)		98.99(28)
Cpx	20	53.54(41)	21.05(49)	19.08(74)	2.10(54)	3.05(20)	0.20(18)		99.03(48)
Opx	16	56.37(41)	34.21(37)	1.88(21)	1.91(65)	4.74(13)	0.23(18)		99.34(32)
Gnt	29	42.48(36)	22.00(36)	5.50(28)	23.64(19)	5.67(43)	0.18(14)		99.49(32)
Ca-free assemblage									
V538b (3 GPa, 1200 °C)									
Mst	14	-	45.60(47)	1.04(20)	0.02(1)	3.63(62)	0.20(15)		50.50(52)
Ol	19	40.90(17)	51.13(22)	0.03(1)	0.02(1)	7.57(23)	0.22(10)		99.89(26)
Opx	15	57.06(31)	36.08(29)	0.29(13)	0.67(9)	4.89(37)	0.19(14)		99.19(37)
V496b (3 GPa, 1250)									
Liq	1	4.41	46.12	0.31	0.20	3.72	0.14	44.28	55.72
Mst	19	-	46.85(30)	0.54(17)	-	3.88(46)	-		51.45(17)
Ol	51	41.11(26)	52.52(28)	0.02(1)	0.05(2)	7.59(10)	0.26(18)		101.54(34)
Opx	6	56.38(47)	35.80(71)	-	1.79(85)	5.11(69)	0.22(15)		99.58(91)
V406b (3 GPa, 1350)									
Liq	4	21.31(4.12)	33.73(4.89)	-	0.15(6)	6.66(1.61)	0.27(26)		62.89(1.89)
Ol	60	40.90(45)	53.25(43)	0.10(4)	-	7.60(9)	-		101.85(71)
Opx	39	58.38(65)	36.37(43)	1.05(33)	-	4.74(13)	0.23(22)		100.73(70)
V511b (3 GPa, 1400)									
Liq	4	27.70(1.95)	37.88(2.56)	-	0.06(1)	5.41(25)	0.64(45)		71.39(4.83)
Ol	69	40.98(20)	51.87(25)	0.15(3)	0.05(4)	7.02(14)	0.27(18)		100.05(37)
Opx	46	57.70(43)	36.48(36)	0.52(20)	0.59(10)	4.23(10)	0.26(17)		99.52(50)
V514b (3 GPa, 1500)									
Liq	1	42.41	29.14	0.99	-	4.42	-	23.06	76.94
Ol	75	40.61(18)	51.36(20)	0.13(2)	-	7.32(12)	0.25(14)		99.63(29)
Opx	36	56.93(89)	35.89(42)	0.52(35)	-	4.65(33)	0.27(18)		98.22(70)
S4135a (6 GPa, 1240 °C)									
Liq	n.m.								
Mst	12	0.13(8)	44.91(1.09)	1.58(33)	-	4.39(50)	0.25(18)	48.72	51.28(96)
Ol	17	41.08(27)	49.54(20)	0.09(3)	-	9.12(22)	0.22(18)		100.06(30)
Cpx	20	55.39(30)	20.17(31)	21.50(40)	0.11(3)	3.14(20)	0.21(16)		100.53(36)
Opx	27	58.59(34)	35.32(36)	0.98(35)	0.07(2)	5.18(46)	0.14(13)		100.29(31)
V567a (6 GPa, 1285 °C)									
Liq	5	4.70(1.69)	21.16(1.28)	25.12(2.02)	0.27(14)	5.42(1.39)		43.14	56.86(1.61)
Mst	19	-	44.59(33)	2.25(25)	-	4.34(50)	0.13(9)	48.64	51.36(53)
Ol	22	38.84(37)	50.13(33)	0.10(3)	-	9.14(43)	0.14(13)		98.35(45)
Cpx	15	53.55(41)	19.87(36)	22.71(49)	0.12(3)	2.83(19)	0.12(10)		99.19(61)
Opx	11	56.48(42)	36.15(18)	0.99(19)	0.09(6)	4.70(18)	0.27(17)		98.67(63)
V543a (6 GPa, 1300 °C)									
Liq	14	9.03(2.52)	24.40(1.38)	18.80(1.04)	0.87(0.31)	5.05(0.82)			58.33(3.54)

Ol	13	41.01(24)	50.46(29)	0.16(13)	0.01(1)	7.98(52)	0.31(22)		99.92(38)
Cpx	20	55.43(22)	20.48(71)	21.70(97)	0.10(4)	2.67(24)	0.33(27)		100.70(40)
Opx	28	58.31(31)	35.21(33)	1.87(29)	0.09(3)	4.37(29)	0.21(20)		100.06(43)
V539a (6 GPa, 1350 °C)									
Liq	5	7.88(1.34)	18.30(1.81)	24.53(1.09)	0.17(3)	4.32(46)		44.56	55.19(2.10)
Ol	12	40.71(26)	50.82(29)	0.12(3)	0.02(2)	7.49(10)	0.24(13)		99.39(27)
Cpx	44	54.82(40)	21.59(23)	20.05(34)	0.13(5)	2.95(24)	0.24(18)		99.77(42)
Opx	10	57.21(24)	35.45(33)	1.74(34)	0.11(4)	4.46(14)	0.24(14)		99.22(33)
V525a (6 GPa, 1450 °C)									
Liq	4	14.39(2.34)	29.21(2.16)	21.17(3.07)	0.09(5)	6.62(2.23)		28.45	71.55(3.85)
Ol	28	41.11(22)	52.35(33)	0.17(11)	0.01(1)	6.61(8)	0.18(15)		100.44(32)
Cpx	17	55.66(26)	23.50(41)	18.17(49)	0.11(4)	2.70(7)	0.27(18)		100.27(22)
Opx	1	57.91	36.02	1.97	0.07	3.82	0.45		100.11
V457a (6 GPa, 1500 °C)									
Liq	16	24.48(3.64)	29.00(4.96)	17.77(3.63)	0.45(10)	7.97(1.75)		20.43	79.57(4.18)
Ol	28	41.68(12)	52.98(21)	0.32(4)		6.13(6)	0.23(21)		101.34(27)
Cpx	26	56.03(25)	24.76(36)	15.74(43)	-	2.80(9)			99.66(34)
Opx	2	56.90(1.11)	34.41(59)	4.43(77)	0.16	3.75(3)	0.23(6)		99.86(90)
alloy	5	-	-	0.16(4)	-	3.58(14)	95.78(81)		99.61(66)
V553a (6 GPa, 1560 °C)									
Liq	6	35.30(1.90)	45.14(2.47)	0.54(38)	0.09(5)	3.33(1.70)	0.21(13)	15.37	84.63(2.53)
Ol	6	42.15(7)	53.50(38)	0.25(4)	-	4.10(57)	0.18(10)		100.19(76)
Cpx	7	56.15(1.07)	25.15(2.02)	15.13(2.52)	0.16(7)	3.23(56)	0.25(14)		100.07(63)
Opx	6	59.12(28)	36.22(35)	2.35(16)	0.04(1)	2.23(23)			100.03(35)
V606a (6 GPa, 1150 °C)									
Mst	13	-	45.20(77)	1.96(43)	-	4.27(65)	0.19(12)	48.11	51.89(47)
Ol	29	40.97(20)	50.41(24)	0.10(3)	-	9.63(24)	0.20(13)		101.54(39)
Cpx	20	54.96(35)	19.72(32)	22.21(51)	0.38(12)	2.97(19)	0.20(12)		100.48(64)
Opx	15	58.07(60)	35.78(42)	0.95(34)	0.21(12)	5.84(59)	0.19(13)		101.11(47)
Gnt	31	42.99(26)	21.18(36)	5.36(31)	23.35(23)	8.61(26)	-		101.60(31)
V604a (6 GPa, 1300 °C)									
Liq	2	1.43(61)	17.87(51)	28.75(72)	0.23(1)	3.66(21)		47.97	52.03(91)
Ol	14	40.66(33)	51.03(36)	0.13(3)	0.03(2)	8.22(20)	0.19(13)		100.39(31)
Cpx	8	54.34(27)	21.38(67)	19.49(67)	0.64(8)	3.10(15)	-		99.09(28)
Opx	8	56.65(55)	35.24(44)	1.63(43)	0.47(14)	4.83(14)	0.31(15)		99.17(63)
Gnt	20	42.20(42)	22.00(29)	5.35(41)	22.63(40)	6.86(26)	-		99.24(60)
V605a (6 GPa, 1400 °C)									
Liq	8	16.89(2.83)	19.37(1.82)	24.80(1.87)	0.89(43)	5.84(1.16)	-	32.09	67.91(2.23)
Ol	39	40.55(22)	49.31(33)	0.22(15)	0.05(2)	9.12(17)	0.28(17)		99.71(46)
Cpx	15	54.46(39)	21.90(65)	17.80(1.05)	0.84(27)	3.70(19)	0.26(18)		99.02(47)
Opx	8	57.20(26)	34.16(16)	2.12(28)	0.87(26)	5.18(20)	0.20(16)		99.80(38)
Gnt	24	42.95(50)	23.17(42)	5.02(36)	23.22(44)	6.40(19)	-		100.96(59)
V615a (6 GPa, 1200 °C)									
Mst	6	-	44.65(1.18)	1.24(34)	-	4.40(40)	-	48.52	51.48(35)
Ol	22	40.47(24)	49.15(33)	0.13(7)	-	9.70(22)	0.26(22)		100.09(50)
Cpx	18	54.24(49)	19.03(94)	22.66(1.33)	0.09(3)	3.26(73)	-		99.75(87)
Opx	18	57.74(47)	34.85(84)	1.20(86)	0.08(4)	5.56(36)	0.26(16)		99.81(74)
Gnt	30	42.12(40)	21.63(61)	4.94(67)	21.64(40)	7.21(20)	0.23(21)		99.73(53)
V617a (6 GPa, 1400 °C)									
Liq	11	5.43(2.98)	20.79(2.41)	28.76(3.75)	0.23(13)	5.87(2.02)	-	38.85	61.15(2.29)
Ol	17	41.00(34)	50.97(41)	0.14(4)	-	8.37(16)	0.30(17)		101.09(37)
Cpx	14	54.74(33)	21.41(92)	19.77(1.37)	0.65(25)	3.16(28)	0.15(14)		100.14(43)
Opx	33	57.90(43)	35.66(44)	1.73(43)	0.49(21)	4.53(22)	0.23(20)		100.72(70)
Ca-free assemblage									
V539b (6 GPa, 1350 °C)									
Mst	22	-	45.10(93)	1.42(91)	-	3.44(68)	0.08(6)	49.94	50.06(52)
Ol	19	40.80(18)	50.22(26)	0.06(1)	0.02(1)	8.06(26)	0.28(10)		99.45(30)
Opx	17	57.26(22)	35.34(31)	0.47(16)	0.58(7)	5.12(35)	0.18(11)		98.95(19)
V541b (6 GPa, 1450 °C)									

Liq	8	19.15(4.24)	38.01(2.13)	3.70(1.19)	0.76(36)	5.81(1.15)	-	32.04	67.96(2.65)
Mst	34	-	46.28(41)	0.14(6)	-	2.80(13)	0.20(14)	50.51	49.49(53)
Ol	27	41.26(15)	51.39(19)	0.03(1)	0.04(1)	5.84(6)	0.21(12)		98.78(26)
Opx	32	58.61(30)	36.95(31)	-	0.37(17)	3.26(17)	0.19(11)		99.45(25)
V458a (7 GPa, 1350 °C)									
Mst	14	0.30(28)	45.27(88)	1.35(20)	-	3.58(36)	-	49.09	50.91(83)
Ol	10	40.64(15)	50.23(53)	0.08(2)	-	8.95(62)	-		100.55(50)
Cpx	5	54.47(85)	19.68(35)	21.63(31)	0.35(10)	2.83(11)	0.29(12)		99.29(1.16)
Opx	4	57.68(22)	35.08(76)	1.50(73)	0.24(12)	5.16(22)	0.17(14)		99.91(35)
Gnt	18	42.54(18)	21.19(34)	4.78(35)	22.88(14)	8.65(18)	-		100.11(20)
V492a (7 GPa, 1400 °C)									
Liq	31	12.52(1.94)	21.82(1.27)	24.54(1.14)	0.60(8)	7.06(2.19)	0.24(17)	33.22	66.78(2.04)
Ol	5	40.68(13)	50.40(25)	0.11(1)	0.03	8.57(18)	0.21(18)		100.17(50)
Cpx	9	54.71(83)	22.78(49)	18.87(45)	0.41(13)	3.36(19)	-		101.59(83)
Opx	19	57.67(25)	35.10(35)	1.59(37)	0.51(31)	4.89(23)	0.28(16)		100.11(39)
Gnt	16	42.94(67)	22.49(42)	4.89(37)	22.78(49)	6.82(37)	-		100.04(50)
V517a (7 GPa, 1500 °C)									
Liq	13	15.42(3.34)	28.95(2.77)	17.98(3.15)	0.15(5)	7.74(1.59)	0.16(13)	29.60	70.40(5.17)
Ol	17	40.39(19)	50.75(17)	0.15(8)	0.03(1)	8.51(9)	0.15(12)		100.14(25)
Cpx	19	54.71(13)	23.21(41)	16.68(47)	0.73(12)	3.59(23)	0.24(17)		99.20(30)
Opx	20	57.22(29)	35.41(54)	1.57(52)	0.55(22)	4.93(23)	-		99.99(30)
Gnt	37	42.78(32)	22.91(52)	4.78(58)	22.71(28)	6.44(18)	-		99.80(35)
V564a (7 GPa, 1600 °C)									
Liq	27	27.05(1.00)	23.54(1.40)	18.55(85)	1.63(29)	6.63(94)	-	22.45	77.55(95)
Ol	7	40.99(10)	50.50(17)	0.20(1)	0.08(2)	6.45(10)	0.17(15)		98.39(36)
Cpx	4	56.43(44)	26.13(1.22)	12.83(1.90)	1.11(8)	3.26(35)	0.27(20)		100.01(51)
Opx	16	58.17(33)	34.57(31)	2.35(15)	0.97(32)	3.60(16)	0.23(15)		99.87(31)
Gnt	22	44.39(34)	23.89(29)	4.69(33)	22.57(47)	5.08(17)	0.15(14)		100.78(27)
S4402a (7 GPa, 1400 °C) + wt.% H_2O									
Liq	10	21.74(6.47)	21.84(5.88)	9.57(4.31)	1.26(0.37)	3.88(1.71)	0.29(28)		58.59(6.10)
Ol	2	40.65(14)	51.19(39)	0.13(1)	0.04(2)	8.02(1)	-		100.66(7)
Cpx	7	54.41(96)	23.97(1.38)	14.84(2.15)	2.01(17)	4.65(45)	0.26(10)		100.14(46)
Opx	25	58.10(16)	36.61(31)	1.32(26)	0.40(16)	3.93(23)	0.26(16)		100.67(22)
Gnt	23	43.05(38)	23.20(44)	4.81(35)	22.64(35)	6.36(24)	-		100.14(38)
Ca-free assemblage									
H2759b (7 GPa, 1400 °C)									
Mst	22	-	47.48(50)	0.25(13)	-	2.83(53)	0.23(18)		50.83(40)
Ol	23	41.12(31)	51.97(43)	0.03(1)	0.03(2)	6.27(16)	0.23(12)		99.66(37)
Opx	28	58.21(42)	36.03(41)	0.26(8)	0.36(9)	4.29(27)	0.26(18)		99.40(63)
Gnt	74	42.74(21)	26.15(15)	-	24.03(24)	5.31(10)			98.30(33)
V493b (7 GPa, 1400 °C)									
Mst	25	0.02(1)	47.30(57)	0.28(10)	-	2.03(1.35)	0.18(12)		49.81(90)
Ol	39	40.66(18)	51.47(29)	0.02(1)	0.03(2)	7.31(11)	0.30(15)		99.80(27)
Opx	21	57.55(21)	36.61(24)	0.14(5)	0.56(7)	4.35(10)	0.17(13)		99.39(19)
Gnt	23	43.98(22)	26.31(27)	0.25(13)	23.87(30)	6.70(14)	0.22(16)		101.33(42)
V524b (7 GPa, 1500 °C)									
Mst	13	-	47.47(54)	0.20(15)	-	1.59(1.33)	0.15(8)		49.44(97)
Ol	16	40.23(54)	52.32(43)	0.02(1)	0.05(2)	6.18(7)	0.23(15)		99.04(59)
Opx	6	57.07(38)	36.66(33)	-	0.80(18)	3.78(9)	0.19(10)		98.61(80)
Gnt	23	43.42(22)	26.95(24)	0.22(8)	23.48(41)	4.99(9)	0.16(15)		99.21(58)
V565a (11 GPa, 1400 °C)									
Mst	5	-	44.50(32)	1.44(9)	-	3.59(11)	-		50.25(67)
Ol	19	40.84(33)	51.17(33)	0.14(7)	-	8.54(19)	-		100.93(60)
Cpx	7	54.30(47)	20.43(26)	21.27(41)	0.47(31)	2.89(16)	0.14(12)		99.53(54)
Opx	9	57.83(43)	36.57(38)	0.38(9)	0.13(5)	5.13(29)	0.19(18)		100.23(57)
Gnt	27	43.34(41)	22.95(39)	4.85(33)	22.11(41)	7.70(25)	-		101.07(54)
S4230a (11 GPa, 1500 °C)									
Liq	10	12.60(2.47)	32.86(99)	3.28(27)	-	6.35(36)	-	44.92	55.08(2.43)

Ol	2	40.01(44)	52.23(72)	0.12(1)	0.03(1)	8.06(2)	0.35(5)	-	100.80(88)
Cpx	1	56.11	23.01	18.21	0.14	3.49	0.37	-	101.32
Opx	9	58.78(1.00)	36.48(67)	0.58(31)	0.11(5)	4.83(29)	0.27(25)	-	100.98(91)
Gnt	29	42.96(61)	21.81(46)	5.44(20)	22.20(56)	8.04(23)	-	-	99.50(29)
Ca-free assemblage									
S4232b (11 GPa, 1500 °C)									
Mst	15	-	48.80(1.24)	0.25(12)	-	1.92(1.11)	0.16(12)		51.22(1.29)
Ol	12	40.26(1.00)	51.94(92)	0.03(1)	0.03(2)	7.38(35)	0.31(15)		99.96(1.02)
Opx	11	58.07(1.08)	36.88(1.04)	0.17(6)	0.27(21)	4.68(60)	0.32(18)		100.39(82)
Gnt	22	43.50(18)	26.12(30)	-	24.48(48)	6.83(13)	-		101.05(40)

Notes: ($^{+}$) number of points analysed. (*) Total Fe is given as FeO. (**) CO_2 calculated by difference. Errors in parentheses are 1σ of the mean, reported as least units cited; (n.m.) means not measurable.

Table S3.2 Microprobe analyses of doped experiments.

Phase	*No meas*	*SiO_2*	*MgO*	*CaO*	*Al_2O_3*	*FeO*	*P_2O_5*	*S*	*Cl*	*Na_2O*	*IrO_2*	*CO_2*	*Tot.*
V586a (6 GPa, 1200 °C) + 6 wt. % FeS													
Mst	16	0.05(4)	44.14(79)	2.16(56)	0.01(1)	6.68(67)		0.04(3)			0.08(8)	46.59	53.41(1.00)
Ol	22	38.12(49)	48.29(85)	0.10(2)	0.01(1)	12.61(70)		0.02(2)			0.30(18)		99.43(50)
Cpx	15	53.43(60)	20.07(41)	20.87(62)	0.13(4)	4.60(35)		0.02(2)			-		99.31(65)
Opx	13	55.02(27)	33.94(51)	1.14(38)	0.08(2)	8.38(72)		-			0.19(18)		98.79(33)
Sulph	18	-	0.02(2)	0.09(4)	0.01(1)	54.55(65)		35.16(29)			11.27(85)		101.12(58)
V578a (6 GPa, 1400 °C) + 6 wt. % FeS													
Liq	5	17.90(9.57)	20.57(5.42)	14.71(7.27)	0.09(5)	13.99(1.89)		-			-	31.93	68.07(7.98)
Ol	49	40.41(28)	46.65(37)	0.24(7)	0.02(1)	14.25(42)		0.01(1)			-		101.67(24)
Cpx	29	56.54(36)	23.52(1.18)	15.99(1.62)	0.13(4)	5.73(53)		-			-		102.02(38)
Opx	10	58.35(42)	32.95(63)	2.97(62)	0.11(2)	7.44(44)		-			-		101.93(47)
S-liq	10	0.8(8)	-	0.15(4)	-	52.80(1.25)		33.51(77)			13.00(1.84)		99.60(1.04)
V576a (6 GPa, 1350 °C) + 10 wt.% P_2O_5													
Liq	8	3.25(56)	16.55(2.08)	19.90(3.49)	0.13(3)	3.80(75)	11.55(1.94)		0.83(10)		-	44.14	55.86(8.79)
Ol	10	40.61(27)	51.74(22)	0.17(4)	0.01(1)	6.84(9)	0.46(13)		0.1		0.10(8)		99.94(24)
Cpx	6	56.05(86)	21.10(37)	21.02(29)	0.07(2)	2.89(44)	0.07(4)		-		0.25(18)		101.50(1.17)
Opx	9	58.20(51)	35.68(57)	1.52(41)	0.08(2)	4.54(37)	0.12(10)		-		0.19(12)		100.34(83)
Apatite	14	0.57(19)	3.20(24)	51.19(33)	-	0.83(7)	45.56(1.32)		0.95(11)		0.17(15)		102.46(1.16)
V573a (6 GPa, 1400 °C) + 10 wt.% P_2O_5													
Liq	22	11.15(47)	22.40(85)	21.17(1.04)	0.27(3)	4.88(57)	19.78(1.81)		0.33(5)		0.22(20)	19.46	80.20(3.62)
Ol	2	39.68(59)	51.93(34)	0.22(5)	0.02(2)	5.92(19)	0.83(19)						98.70(38)
Cpx	21	54.59(59)	22.82(40)	19.22(52)	0.14(4)	2.35(14)	-				0.22(16)		99.47(66)
Opx	6	57.11(68)	36.29(46)	1.94(17)	0.14(2)	3.41(7)	0.09(4)						99.11(61)
Apatite	7	0.58(3)	4.20(5)	49.40(34)	-	0.85(7)	45.33(60)		1.06(5)		0.41(23)		101.84(85)
V585a (6 GPa, 1400 °C) + 25 wt.% NaCl													
Liq	14	3.53(89)	15.19(1.84)	23.87(1.34)		6.33(95)			1.37(71)	1.24(37)	0.56(23)	47.86	52.14(2.18)
Ol	24	39.96(37)	54.26(50)	0.17(2)	0.01(1)	4.58(48)			-	0.03(2)	0.25(12)		99.22(57)
Cpx	18	55.71(48)	27.07(1.15)	13.17(1.54)	0.32(15)	2.45(15)			-	0.45(10)	-		99.27(42)
Opx	11	57.80(53)	36.52(39)	2.66(30)	0.13(4)	2.51(8)			0.03(3)	0.18(4)	0.32(19)		100.10(61)

Table S3.3 Microprobe analyses of the IrFe alloy.

Run	No. points[+]	SiO_2	MgO	CaO	Al_2O_3	Fe	Ir	Tot.
H289a	1	0.32	0.34	0.08	n.d.	2.51	98.72	101.96
H298a	4	n.d.	n.d.	0.07(1)	n.d.	2.81(17)	100.60(54)	103.79(51)
V588a	2	0.10(6)	0.03	0.17(8)	n.d.	2.65(2)	100.04(1.49)	102.98(1.61)
V538a	8	n.d.	n.d.	0.09(8)	n.d.	2.97(12)	96.96(81)	100.11(71)
V426a	8	0.25(23)	0.16(13)	n.d.	n.d.	3.21(11)	94.62(1.04)	98.51(72)
V403a	6	0.04(3)	n.d.	n.d.	n.d.	4.40(28)	95.84(97)	100.38(1.00)
V406a	7	0.09(6)	0.06(5)	0.09(5)	n.d.	3.48(12)	94.20(65)	97.91(59)
V511a	13	0.04(3)	n.d.	0.09(5)	n.d.	3.56(13)	97.04(83)	100.74(77)
V542a	8	0.05(4)	n.d.	n.d.	n.d.	3.00(10)	98.04(51)	101.30(39)
V550a	2	0.09(1)	0.06(3)	0.13(9)	n.d.	2.68(23)	97.52(43)	100.47(77)
V512a	6	0.07(6)	n.d.	n.d.	n.d.	4.42(18)	96.25(85)	100.90(70)
V514a	13	n.d.	n.d.	0.06(4)	n.d.	4.31(14)	97.44(55)	101.85(46)
V592a	11	0.10(9)	n.d.	n.d.	n.d.	4.71(21)	97.70(65)	102.66(48)
V569a	6	n.d.	n.d.	0.04(3)	n.d.	3.17(16)	96.72(27)	100.00(10)
V587a	2	0.03(1)	0.02(1)	n.d.	n.d.	2.91(13)	96.44(91)	99.45(80)
Ca-free assemblage								
V538b	10	n.d.	0.04(3)	n.d.	n.d.	2.43(11)	98.33(44)	100.84(41)
V496b	4	n.d.	n.d.	n.d.	n.d.	2.53(19)	98.70(45)	101.27(37)
V406b	5	n.d.	0.04(3)	0.05(3)	n.d.	3.10(9)	96.58(83)	99.84(87)
V511b	5	n.d.	n.d.	n.d.	n.d.	3.26(10)	97.89(55)	101.44(40)
V514b	2	n.d.	n.d.	0.03	n.d.	3.57(14)	96.43(14)	100.03
S4135a	3	0.17(7)	0.12(8)	0.21(12)	n.d.	2.35(5)	98.51(80)	101.37(75)
V567a	3	n.d.	n.d.	0.14(5)	n.d.	2.47(1)	97.11(27)	100.71
V543a	5	n.d.	0.03(1)	0.07(5)	n.d.	2.60(3)	97.27(9)	102.21(47)
V539a	15	n.d.	n.d.	0.07(5)	n.d.	2.72(20)	97.80(77)	100.62(69)
V525a	14	n.d.	n.d.	0.05(3)	n.d.	3.20(8)	97.23(57)	100.52(52)
V457a	5	n.d.	n.d.	0.16(4)	n.d.	3.58(14)	95.78(81)	99.61(66)
V553a	4	n.d.	n.d.	0.08(5)	n.d.	2.40(17)	97.95(1.06)	100.75(39)
V606a	8	n.d.	n.d.	0.09(4)	n.d.	3.06(16)	96.97(46)	100.33(36)
V604a	2	n.d.	n.d.	n.d.	n.d.	2.86(29)	98.69(2.58)	102.19(1.54)
V605a	24	0.22(21)	n.d.	0.17(10)	n.d.	3.46(22)	93.23(1.54)	97.32(1.45)
V615a	2	n.d.	n.d.	0.12(7)	n.d.	3.42(17)	96.52(21)	100.45(29)
V617a	11	n.d.	0.06(5)	0.06(5)	n.d.	2.99(20)	96.60(71)	99.98(60)
Ca-free assemblage								
V539b	14	n.d.	n.d.	n.d.	n.d.	2.31(12)	98.01(70)	100.48(49)
V541b	17	n.d.	n.d.	n.d.	n.d.	1.91(13)	98.92(1.32)	101.06(75)
V458a	7	0.07(2)	n.d.	0.08(3)	n.d.	2.53(14)	95.64(32)	98.35(35)
V492a	3	n.d.	n.d.	n.d.	n.d.	2.96(9)	98.41(2.02)	102.03(1.55)
V517a	11	n.d.	n.d.	0.05(3)	n.d.	3.06(15)	98.51(1.05)	101.77(1.00)
V564a	5	n.d.	n.d.	0.12(5)	n.d.	2.78(7)	99.71(44)	102.63(42)
S4402a	5	0.04(1)	0.03(2)	n.d.	n.d.	2.60(6)	97.29(8)	100.65(2)
Ca-free assemblage								
H2759b	15	0.07(6)	n.d.	0.08(3)	n.d.	2.80(11)	96.11(52)	99.09(51)
V493b	8	n.d.	n.d.	n.d.	n.d.	2.52(5)	97.36(67)	99.25(30)
V524b	3	n.d.	0.08(5)	0.03(1)	n.d.	2.32(4)	95.55(1.13)	97.97(1.05)
V565a	4	n.d.	n.d.	0.08(6)	n.d.	2.74(19)	99.40(15)	
S4230a	2	0.93(11)	0.67(27)	0.14(3)	n.d.	2.77(20)	92.77(21)	97.27(76)
S4232b	2	0.15(3)	0.04(1)	n.d.	n.d.	3.22(10)	94.37(37)	97.78(24)
V576a	3	0.70(2)	0.64(7)	n.d.	0.02(1)	2.92(13)	97.24(50)	101.51(33)
V573a	1	n.d.	n.d.	n.d.	n.d.	2.86	98.14	101.69
V585a	2	0.12(4)	0.12(7)	0.07(3)	n.d.	2.77(10)	100.31(34)	103.39(24)

Notes: ([+]) number of points analysed. Errors in parentheses are 1σ of the mean, reported as least units cited; (n.d.) means not detectable.

Table S4.1 Microprobe phase analyses.

Phase	No meas.	SiO_2	MgO	CaO	Al_2O_3	FeO	NiO	IrO_2	Total
S4226 (16GPa/1500 °C)									
Wadsleyite	8	40.71(30)	49.79(31)	-	0.09(4)	9.26(9)	0.38(2)	0.34(21)	100.64(56)
Clinoenstatite	4	57.68(63)	37.88(45)	0.34(7)	0.03(1)	4.05(44)	-	0.32(11)	101.38(58)
Magnesite	13	-	47.19(65)	0.67(13)	-	3.68(61)	-	0.20(15)	51.95(55)
S4278 (16GPa/1550 °C)									
Wadsleyite	13	41.08(28)	50.59(46)	-	0.05(1)	8.91(17)	0.40(2)	0.32(16)	101.41(62)
Clinoenstatite	20	58.13(41)	37.97(63)	-	0.03(1)	3.54(21)	-	0.26(15)	99.93(49)
Magnesite	7	0.12(10)	48.03(69)	-		2.38(76)	-	0.11(7)	50.65(76)
H3102 (23GPa/1600 °C)									
Ringwoodite	19	40.75(39)	49.18(49)	0.06(2)	-	9.86(34)	0.25(3)	0.18(14)	100.30(70)
Mg-pv	2	57.15(66)	37.59(5)	-	0.71(9)	3.14(12)	-	0.04(2)	98.62(52)
Ca-pv	9	49.35(1.13)	0.70(59)	46.42(75)	0.05(3)	0.35(11)	0.03(2)	-	97.44(1.28)
Stishovite	26	99.37(80)	0.29(20)	0.09(6)	-	0.20(5)	-	-	100.11(78)
Magnesite	14	0.16(10)	49.09(94)	0.42(13)	-	1.76(51)	-	-	51.86(1.05)
H5946 (25GPa/1500 °C)									
Fe-periclase	8	0.02(1)	73.81(73)	0.03(1)	0.10(4)	27.86(60)	-	0.29(17)	102.17(57)
Magnesite	9	-	49.39(52)	0.30(11)	-	1.16(73)	-	0.20(17)	51.15(29)
H2982 (25GPa/1500 °C - 15hr)									
Fe-periclase	12	0.03(2)	76.53(76)	-	0.53(5)	23.87(67)	-	0.20(18)	101.50(76)
Magnesite	15	-	49.00(54)	0.13(11)	-	0.86(59)	-	0.28(21)	50.32(60)
H2887 (25GPa/1550 °C)									
Fe-periclase	8	-	74.00(81)	-	-	28.53(81)	-	0.26(16)	102.92(57)
Magnesite	12	-	50.12(79)	-	-	0.77(13)	-	0.22(17)	51.22(76)
S4807 (25GPa/1600 °C)									
Fe-periclase	5	-	72.11(1.24)	-	0.03(1)	27.20(56)	-	0.33(15)	99.73(1.26)
Magnesite	9	-	49.05(87)	0.25(12)	-	1.71(99)	-	0.19(13)	51.26(1.27)
H2981 (25GPa/1500 °C) Ni-bearing									
Fe-periclase	13	0.03(2)	54.20(1.04)	-	-	36.34(50)	11.19(21)	-	101.77(1.09)
Magnesite	9	-	49.94(33)	0.16(11)	-	1.07(11)	0.19(2)	-	51.37(31)
M131 (45GPa/1700 °C) Ni-bearing									
Fe-periclase-1	4	0.10(5)	63.29(1.21)	-	-	34.18(1.91)	5.64(2.18)	-	103.29(75)
Fe-periclase-2	3	0.05(1)	49.63(39)	-	-	47.52(13)	5.14(19)	-	102.39(59)
Magnesite	10	0.09(4)	50.15(98)	0.07(6)	-	1.12(41)	0.19(9)	-	51.63(96)
M140 (45GPa/1700 °C)									
Mg-Perovskite	17	54.03(90)	36.48(39)	0.08(2)	3.32(97)	6.23(90)	-	-	100.35(83)
Fe-periclase	5	0.05(2)	76.43(68)	-	0.15(1)	23.21(77)	-	-	99.88
Magnesite	5	0.15(2)	50.03(93)	0.16(8)		1.02(55)		0.17(12)	51.58(1.20)

Table S4.2 Microprobe analyses of IrFe alloy.

Run	No meas.	SiO_2	MgO	CaO	Al_2O_3	Fe	NiO	Ir	Total
S4226	1	0.38	0.15	0.03	0.02	3.04	0.18	94.81	98.60
S4278	1	0.48	0.05	-	-	3.86	-	93.09	97.48
H3102	9	-	0.10(9)	0.18(8)	-	3.14(19)	0.05(3)	96.39(46)	99.92(26)
H5946	6	-	0.16(7)	-	-	3.56(33)	-	99.56(92)	103.28(68)
H2982	4	-	0.44(15)	-	-	4.08(62)	-	95.57(61)	100.09(47)
S4807	9	-	0.22(21)	-	-	3.59(59)	0.03(2)	95.29(1.19)	99.13(1.14)
H2887	5	-	0.25(16)	0.04(2)	-	4.36(38)	-	95.64(36)	100.29(50)
M140	1	-	-	-	-	2.25	-	97.85	100.01

Table S5.1 Composition of product garnets.

Sample	V587	V621a	V621b	V606a	V604a	V605a	V615a(FSM1)	V620a(FSM1)	V458a
P(GPa)/T(°C)	3/1400	3/1250	3/1250	6/1150	6/1300	6/1400	6/1200	6/1350	7/1350
No. meas.	29	23	34	31	20	24	30	78	18
SiO_2	42.48(36)	42.98(18)	43.57(18)	42.99(26)	42.20(42)	42.95(50)	42.12(40)	42.40(37)	42.54(18)
Al_2O_3	23.64(19)	24.03(9)	24.78(23)	23.35(23)	22.63(40)	23.22(44)	21.64(40)	21.53(35)	22.88(14)
Cr_2O_3	n.m.	n.m.	n.m.	n.m.	n.m.	n.m.	1.89(15)	1.96(20)	n.m.
FeO*	5.67(43)	7.08(16)	6.47(23)	8.61(26)	6.86(26)	6.40(19)	7.21(20)	6.81(50)	8.65(18)
MgO	22.00(36)	22.61(32)	26.20(34)	21.18(36)	22.00(29)	23.17(42)	21.63(61)	22.20(33)	21.19(34)
CaO	5.50(28)	4.25(26)	-	5.36(31)	5.35(41)	5.02(36)	4.94(67)	4.80(42)	4.78(35)
Na_2O	n.m.	-	-	-	-	-	0.05(2)	0.05(3)	n.m.
NiO	-	-	n.m.	-	-	-	0.02(1)	-	n.m.
Tot.	99.49(32)	101.06(19)	101.02(65)	101.60(31)	99.24(60)	100.96(59)	99.73(53)	99.96(59)	100.11(20)
$Fe^{3+}/\sum Fe$	0.066	0.039	0.01	0.049	0.061	0.054	0.102	0.106	0.120
K_D	1.51(9)	1.41(3)	1.31(4)	2.02(4)	1.85(4)	1.49(4)	1.65(3)	1.92(9)	2.29(8)

V517a	S4402a	V492a	V564a	H2759b	V493b	V524b	V565a	S4230a	S4232b
7/1500	7/1400	7/1400	7/1600	7/1400	7/1400	7/1500	11/1400	11/1500	11/1500
37	23	16	22	74	23	23	27	29	22
42.78(32)	43.05(38)	42.94(67)	44.39(34)	42.74(21)	43.98(22)	43.42(22)	43.34(41)	42.96(61)	43.50(18)
22.71(28)	22.64(35)	22.78(49)	22.57(47)	24.03(24)	23.87(30)	23.48(41)	22.11(41)	22.20(56)	24.48(48)
n.m.	n.m.	n.m.	n.m.	n.m.	n.m.	n.m.	n.m.	n.m.	n.m.
6.44(18)	6.36(24)	6.82(37)	5.08(17)	5.31(10)	6.70(14)	4.99(9)	7.70(25)	8.04(23)	6.83(13)
22.91(52)	23.20(44)	22.49(42)	23.89(29)	26.15(15)	26.31(27)	26.95(24)	22.95(39)	21.81(46)	26.12(30)
4.78(88)	4.81(35)	4.89(37)	4.69(33)	n.m.	0.25(13)	0.22(8)	4.85(33)	5.44(20)	n.m.
-	-	n.m.	-	n.m.	n.m.	n.m.	n.m.	n.m.	n.m.
-	-	-	-	-	-	-	-	-	-
99.80(35)	100.14(38)	100.04(50)	100.78(27)	98.30(33)	101.33(42)	99.21(58)	101.07(54)	99.50(29)	101.05(40)
0.113	0.150	0.075	0.089	0.050	0.126	0.056	0.060	0.124	0.027
1.60(4)	1.75(5)	1.78(6)	1.66(4)	1.68(3)	1.51(3)	1.57(3)	2.01(4)	2.39(6)	1.48(2)

Table S5.1 continued. Composition of product olivines.

Sample	*V587*	*V621a*	*V621b*	*V606a*	*V604a*	*+V605a*	*V615a*	*+V620a*	*+V458a*
P(GPa)/T(°C)	*3/1400*	*3/1250*	*3/1250*	*6/1150*	*6/1300*	*6/1400*	*6/1200*	*6/1350*	*7/1350*
No. meas.	*5*	*22*	*30*	*20*	*15*	*39*	*1*	*8*	*10*
SiO_2	39.89(33)	40.25(9)	40.93(13)	41.02(27)	40.51(34)	40.55(22)	39.44	41.09(38)	40.64(15)
Al_2O_3	0.06(4)	-	0.14(9)	-	-	0.05(2)	-	0.02(1)	-
Cr_2O_3	n.m.	n.m.	n.m.	n.m.	n.m.	n.m.	-	-	n.m.
*FeO**	8.61(13)	10.80(20)	9.09(16)	10.08(12)	8.55(18)	9.12(17)	9.73	8.14(14)	8.95(62)
MgO	50.30(39)	48.55(48)	50.13(23)	50.18(29)	50.72(34)	49.31(33)	48.04	51.02(70)	50.23(53)
CaO	0.16(13)	0.20(6)	0.10(2)	0.12(4)	0.17(8)	0.22(15)	0.11	0.14(4)	0.08(2)
Na_2O	n.m.	n.m.	0.03(1)	-	-	-	-	-	n.m.
NiO	0.13(3)	0.11(2)	0.16(2)	0.18(2)	0.09(2)	0.16	0.38	0.26(2)	0.22(7)
Tot.	99.27(94)	100.31(27)	100.63(31)	101.73(47)	100.33(50)	99.41(46)	97.70	100.99(1.15)	100.55(50)
a_{fay}	*0.109*	*0.139*	*0.117*	*0.130*	*0.109*	*0.117*	*0.130*	*0.103*	*0.114*

V517a	*+S4402a*	*+V492a*	*+V564a*	*+H2759b*	*V493b*	*+V524b*	*+V565a*	*+S4230a*	*+S4232b*
7/1500	*7/1400*	*7/1400*	*7/1600*	*7/1400*	*7/1400*	*7/1500*	*11/1400*	*11/1500*	*11/1500*
6	*2*	*5*	*7*	*23*	*5*	*23*	*19*	*2*	*12*
40.47(13)	40.65(14)	40.68(13)	40.99(10)	41.12(31)	40.90(37)	40.23(54)	40.84(33)	40.01(44)	40.26(1.00)
0.69(65)	0.04(2)	0.03	0.08(2)	0.03(2)	0.05(1)	0.05(2)	-	0.03(1)	0.03(2)
n.m.	n.m.	n.m.	n.m.	n.m.	n.m.	n.m.	n.m.	n.m.	n.m.
8.75(19)	8.02(1)	8.57(18)	6.45(10)	6.27(16)	8.68(10)	6.18(7)	8.54(19)	8.06(2)	7.38(35)
49.73(85)	51.19(39)	50.40(25)	50.50(17)	51.97(43)	51.41(38)	52.32(43)	51.17(33)	52.23(72)	51.94(92)
0.26(14)	0.13(1)	0.11(1)	0.20(1)	0.03(1)	0.02(1)	0.02(1)	0.14(7)	0.12(1)	0.03(1)
n.m.	n.m.	n.m.	n.m.	n.m.	n.m.	n.m.	n.m.	n.m.	n.m.
0.12(1)	n.m.	0.17(2)	n.m.	n.m.	0.04(2)	n.m.	0.15(4)	n.m.	n.m.
100.19(32)	100.66(7)	99.96(50)	98.39(36)	99.66(37)	101.33(68)	99.04(59)	100.93(60)	100.80(88)	99.96(1.02)
0.110	*0.101*	*0.109*	*0.082*	*0.080*	*0.108*	*0.077*	*0.107*	*0.098*	*0.092*

Table S5.1 continued. Composition of product orthopyroxenes.

Sample	V587a	V621a	V621b	V606a	V604a	V605a	V615a	V620a	+V458a
P(GPa)/T(°C)	3/1400	3/1250	3/1250	6/1150	6/1300	6/1400	6/1200	6/1350	7/1350
No. meas.	9	21	28	13	2	10	3	26	4
SiO_2	55.80(23)	55.95(48)	56.59(34)	58.07(27)	57.07(35)	56.66(63)	57.31(25)	57.45(30)	57.68(22)
Al_2O_3	2.77(22)	2.56(59)	2.89(44)	0.65(18)	0.92(27)	1.38(51)	0.62(19)	0.93(27)	0.24(12)
Cr_2O_3	n.m.	n.m.	n.m.	n.m.	n.m.	n.m.	0.15(5)	0.18(4)	n.m.
FeO*	4.82(12)	6.34(15)	5.61(16)	5.82(28)	5.75(73)	5.54(17)	4.77(8)	4.66(11)	5.16(22)
MgO	33.65(32)	33.66(47)	34.96(34)	35.69(38)	35.18(73)	34.53(59)	36.32(25)	35.36(33)	35.08(76)
CaO	1.97(16)	1.30(15)	0.44(23)	1.00(24)	1.44(52)	2.21(47)	0.88(47)	1.61(18)	1.50(73)
Na_2O	n.m.	n.m.	n.m.	n.m.	n.m.	n.m.	-	-	n.m.
NiO	0.05(2)	0.05(2)	0.06(1)	0.05(1)	0.06(1)	0.05(1)	0.15(4)	0.08(2)	0.08(2)
Tot.	99.07(51)	100.00(25)	100.54(34)	101.28(40)	100.41(1.11)	100.36(48)	100.31(61)	100.09(34)	99.74(35)
a_{fs}	0.072	0.093	0.082	0.082	0.082	0.079	0.067	0.067	0.074

V517a	+S4402a	V492a	V564a	+H2759b	V493b	V524b	+V565a	+S4230a	+S4232b
7/1500	7/1400	7/1400	7/1600	7/1400	7/1400	7/1500	11/1400	11/1500	11/1500
8	25	8	18	28	27	10	9	9	11
57.08(63)	58.10(16)	57.56(20)	57.60(23)	58.21(42)	57.79(37)	57.11(82)	57.83(43)	58.78(1.00)	58.07(1.08)
0.64(13)	0.40(16)	0.65(8)	1.05(15)	0.36(9)	0.93(10)	0.99(26)	0.13(5)	0.11(5)	0.27(21)
n.m.	n.m.	n.m.	n.m.	n.m.	n.m.	n.m.	n.m.	n.m.	n.m.
5.18(31)	3.93(23)	5.11(16)	4.98(13)	4.29(27)	5.41(19)	3.88(15)	5.13(29)	4.83(29)	4.68(60)
35.28(81)	36.61(31)	35.18(35)	34.92(41)	36.03(41)	36.36(37)	36.51(25)	36.57(38)	36.48(67)	36.88(1.04)
1.74(52)	1.32(26)	1.31(30)	1.98(42)	0.26(8)	0.09(5)	0.07(3)	0.38(9)	0.58(31)	0.17(6)
n.m.	n.m.	n.m.	n.m.	n.m.	n.m.	n.m.	n.m.	n.m.	n.m.
0.02(1)	n.m.	0.04(2)	-	-	-	n.m.	0.09(2)	-	n.m.
100.04(34)	100.36(22)	99.85(31)	100.56(39)	99.15(63)	100.58(64)	98.56(88)	100.13(57)	100.78(91)	100.07(82)
0.075	0.055	0.074	0.071	0.062	0.077	0.056	0.072	0.068	0.066

Table S5.1 continued. Composition of product clinopyroxenes and carbonates (solid/liquid) .

Sample	V587 cpx	V621a cpx	V621a liq	V606a Cpx	V606a mst	V604a cpx	V604a mst(liq)	V605a Cpx	V605a liq
P(GPa)/T(°C)	3/1400	3/1250	3/1250	6/1150	6/1150	6/1300	6/1300	6/1400	6/1400
No. meas.	16	3	11	17	25	10	4	3	8
SiO_2	53.32(20)	52.66(1.13)	5.32(2.57)	55.06(22)	-	54.39(34)	-	54.63(43)	16.89(2.83)
Al_2O_3	2.56(19)	3.82(28)	1.74(1.16)	0.54(7)	-	0.80(8)	-	1.62(62)	0.89(43)
Cr_2O_3	n.m.	n.m.	n.m.	n.m.	n.m.	n.m.	n.m.	n.m.	n.m.
FeO*	3.07(17)	9.25(82)	4.93(1.15)	3.17(23)	4.53(53)	3.25(19)	5.85(7)	4.45(31)	5.84(1.16)
MgO	20.86(39)	25.39(58)	15.78(1.32)	19.77(25)	45.13(88)	21.17(60)	43.41(58)	24.73(62)	19.37(1.82)
CaO	18.72(67)	8.34(1.29)	31.00(2.57)	22.11(39)	1.87(30)	19.67(72)	4.36(49)	14.84(1.22)	24.80(1.87)
Na_2O	n.m.	0.07(2)	n.m.	n.m.	n.m.	n.m.	n.m.	n.m.	n.m.
NiO	-	0.03(2)	0.02(1)	0.03(2)	0.03(1)	0.03(1)	0.04(2)	0.04(1)	–
Tot.	98.64(28)	99.64(54)	58.84(2.61)	100.69(41)	51.57(56)	99.41(47)	53.66(45)	100.31(42)	

V615a cpx	V615a mst	V620a liq	V517a cpx	V492a cpx	V492a liq	V564a cpx	V564a liq	V493b mst	V565a cpx	V565a mst
6/1200	6/1200	6/1350	7/1500	7/1400	7/1400	7/1600	7/1600	7/1400	11/1400	11/1400
5	4	4	10	11	5	4	27	11	7	5
52.58(1.49)	1.19(68)	7.07(1.54)	54.52(18)	54.76(31)	6.13(2.92)	55.31(28)	27.05(1.00)	-	54.30(47)	-
2.39(1.37)	0.60(40)	0.63(46)	0.75(5)	0.65(13)	-	1.38(6)	1.63(29)	-	0.47(31)	-
0.33(8)	0.03(2)	0.07(3)	n.m.	n.m.	n.m.	–	n.m.	n.m.	n.m.	n.m.
2.46(18)	2.72(1.44)	4.20(1.03)	3.63(20)	3.53(19)	5.33(77)	4.25(12)	6.63(94)	1.07(1.05)	2.89(16)	3.59(11)
19.00(56)	44.64(2.14)	21.10(2.38)	22.55(71)	21.71(43)	20.45(2.87)	25.55(33)	23.54(1.40)	48.01(34)	20.43(26)	44.50(32)
21.66(70)	1.35(47)	27.02(2.40)	17.58(95)	18.73(69)	26.75(3.09)	13.35(8)	18.55(85)	0.12(10)	21.27(41)	1.44(9)
0.15(4)	-	0.03(1)	n.m.	n.m.	n.m.	0.09(2)	n.m.	n.m.	n.m.	n.m.
0.03(1)	-	-	0.03(1)	0.03(1)	-	-	n.m.	n.m.	0.03(2)	n.m.
98.11(98)	50.50(84)	60.32(2.74)	99.06(28)	99.41(36)	60.16(3.10)	99.95(52)	77.55(95)	49.32(84)	99.38(54)	49.53(67)

Table S5.2 Microprobe analyses of the IrFe alloy from experiments with sandwiched layers.

Run	No. points[+]	SiO_2	MgO	CaO	Al_2O_3	NiO	Cr_2O_3	Fe	Ir	Tot.
V621a	7	n.d.	n.d.	0.09(6)	n.d.	0.14(3)	-	3.92(15)	94.62(46)	98.77(34)
V621b	20	n.d.	n.d.	0.04(2)	n.d.	0.22(3)	-	3.80(28)	94.02(79)	98.08(63)
V587a	9	0.09(8)	0.07(5)	n.d.	n.d.	n.d.	-	2.49(12)	96.63(23)	99.27(4)
V606a	7	0.13(11)	0.18(5)	0.12(4)	n.d.	0.11(2)	-	3.60(17)	95.55(83)	99.69(62)
V604a	5	0.05(4)	0.04(3)	0.08(3)	n.d.	0.13(3)	-	3.80(29)	95.54(25)	99.64(43)
V605a	6	n.d.	n.d.	0.06(2)	n.d.	0.12(3)	-	3.09(14)	96.97(42)	100.23(39)
V615a	2	0.41(13)		0.20(7)	n.d.	0.23	0.05(3)	3.42(10)	93.47(2.41)	97.77(2.13)
V620a	8	0.14(13)	0.13(11)	0.14(7)	n.d.	0.19(3)	0.12(6)	3.16(11)	95.55(60)	99.46(71)
V492a	4	n.d.	n.d.	0.16(6)	n.d.	0.14(4)	-	3.74(23)	94.65(64)	98.70(50)
V517a	1	0.20	0.12	0.20	0.11	0.13	-	4.91	97.25	102.92
V564a	5	n.d.	n.d.	0.12(5)	n.d.	n.d.	-	2.78(7)	99.71(44)	102.61(43)
V493b	6	0.07(2)	n.d.	n.d.	n.d.	0.08(4)	-	3.38(19)	95.85(96)	99.37(1.02)
V524b	2	n.d.	0.05(4)	n.d.	0.19(6)	n.d.	-	2.24(2)	96.58(86)	99.07(87)
V565a	1	0.03	0.04	0.05	n.d.	0.04	-	3.54	95.53	99.23

Notes: ([+]) number of points analysed. (*) Total Fe is given as FeO. Errors in parentheses are 1σ of the mean, reported as least units cited; (n.d.) means not detectable.

Table S6.1 Composition of run product for eclogite experiments.

Phase	*No meas*	*SiO_2*	*MgO*	*CaO*	*Al_2O_3*	*FeO*	*TiO_2*	*Na_2O*	*IrO_2*	*CO_2*	*Tot.*
V636a (3 GPa, 950 °C) + kyanite											
Co	3	97.82(63)	0.13(9)	0.29(16)	0.43(29)	0.41(5)		0.15(7)	0.17(12)		99.41(51)
Ky	23	37.45(39)	-	0.08(7)	62.75(50)	0.47(8)		-	0.25(15)		101.10(52)
Omph	41	55.73(52)	6.90(39)	11.90(74)	15.00(62)	3.86(91)		6.67(50)	0.30(17)		100.39(71)
Gnt	28	40.23(58)	8.57(85)	10.45(1.10)	22.18(46)	19.85(1.87)		0.16(15)	0.31(18)		101.77(49)
Liq	2	8.48(70)	8.40(2.54)	37.38(1.01)	1.60(1.41)	4.78(1.65)		-	0.46(37)	38.50	61.50(16)
V637a (3 GPa, 950 °C) + kyanite											
Co	4	100.57(68)	0.05(3)	0.06(1)	0.24(13)	0.31(5)		-	-		101.34(75)
Ky	9	37.81(43)	0.03(2)	0.07(3)	63.25(13)	0.48(7)		-	0.28(19)		101.98(42)
Omph	18	56.83(52)	6.74(50)	11.72(68)	15.35(63)	3.32(46)		7.17(34)	0.24(21)		101.38(64)
Gnt	17	41.01(58)	8.98(86)	10.21(65)	22.20(69)	19.99(82)		-	0.31(22)		102.86(60)
Liq	4	6.60(5.38)	10.32(48)	35.44(2.39)	2.18(1.18)	4.63(1.39)		-	0.44(20)	39.53	60.47(4.20)
V624a (3 GPa, 1000 °C) + kyanite											
Co	6	94.83(2.55)	0.47(23)	0.80(46)	2.54(2.30)	0.68(34)		0.23(16)			100.01(83)
Ky	28	37.31(20)	-	0.07(4)	63.09(26)	0.42(9)		-	0.24(20)		101.18(41)
Omph	28	54.02(44)	8.12(42)	14.43(45)	14.51(69)	3.86(41)		5.75(31)	0.21(17)		100.93(54)
Gnt	30	40.03(58)	10.07(1.49)	10.50(99)	22.53(36)	17.95(3.40)		-	0.37(31)		101.58(1.09)
Liq	n.m.										
V636b (3 GPa, 950 °C) + TiO_2											
Co	18	98.93(71)	-	0.06(2)	0.04(3)	0.38(7)	0.32(22)	0.02(1)	-		99.86(72)
Rut	21	0.06(2)	0.04(3)	0.25(7)	0.59(2)	2.46(14)	98.85(60)	-	0.31(20)		102.59(40)
Omph	23	54.75(90)	8.29(38)	13.32(50)	9.80(96)	8.24(58)	0.52(11)	5.73(33)	-		100.86(1.04)
Gnt	12	40.19(92)	6.90(43)	10.38(61)	20.20(78)	21.71(82)	1.13(17)	0.55(28)	0.32(23)		101.40(76)
Sid	5	-	3.38(1.62)	0.68(25)	-	56.05(2.53)	0.66(30)	-	-		61.41(35)
Cc	1	0.23	22.51	12.79	0.04	18.24	0.37	0.05	0.30		54.53
V636b (3 GPa, 950 °C) + TiO_2											
Co	7	100.38(60)		0.05(3)	0.05(4)	0.42(11)	0.25(19)	0.01			101.40(69)
Rut	17	0.07(4)	0.04(2)	0.30(9)	0.59(2)	2.52(15)	97.50(62)	-	-		101.36(48)
Omph	30	55.36(51)	7.91(23)	12.86(32)	10.23(78)	8.05(50)	0.64(15)	6.21(21)	0.35(27)		101.62(58)
Gnt	18	39.94(75)	6.69(79)	9.95(72)	20.60(85)	23.05(97)	1.28(42)	0.36(19)	0.35(22)		102.23(58)
Sid	2	-	28.27(72)	4.68(18)	-	24.09(19)	0.38(26)	0.06(4)	0.46(24)		58.41(14)
V624b (3 GPa, 1000 °C) TiO_2											
Co	n.m.										
Rut	21	0.07(4)	0.03(2)	0.27(8)	1.23(2)	1.04(7)	99.09(36)	-	0.30(21)		102.08(34)
Omph	23	53.81(44)	8.52(25)	14.72(24)	13.22(39)	4.58(60)	0.60(16)	5.48(24)	0.24(15)		101.19(61)
Gnt	17	39.75(61)	8.50(57)	9.86(29)	21.26(44)	21.05(69)	1.00(15)	0.21(11)	0.28(21)		101.93(36)
Liq	n.m.										

Table S6.2 Composition ofFeIr alloy for eclogite experiments.

Phase	*No meas*	*SiO_2*	*MgO*	*CaO*	*Al_2O_3*	*Fe*	*TiO_2*	*Na_2O*	*Ir*	*Tot.*
V637a	6	0.65(48)	0.15(11)	0.22(6)	n.d.	2.99(20)	-	n.d.	97.05(1.43)	101.06(81)
V624a	1	0.35	0.08	0.32	0.14	3.03	-	n.d.	95.66	99.58
V636b	3	0.60(12)	0.12(7)	0.21(4)	n.d.	2.67(1)	0.41(15)	n.d.	93.71(56)	97.72(28)
V636b	8	n.d.	0.14(4)	0.13(7)	n.d.	2.10(43)	0.25(19)	n.d.	98.53(57)	101.18(81)
V624b	2	n.d.	n.d.	0.12(8)	n.d.	1.80(16)	0.29(19)	n.d.	96.96(44)	99.70(17)

Notes: a and b indicate respectively the kyanite- and the rutile-bearing assemblages used in the experiments. (n.d.) means not detectable.

Hiermit erkläre ich, daß ich die vorliegende Arbeit selbständig verfaßt und keine anderen als die von mir angegebenen Quellen und Hilfsmittel benutzt habe.
Ferner erkläre ich, daß ich nicht anderweitig mit oder ohne Erfolg versucht habe, eine Dissertation einzureichen und keine gleichartige Doktorprüfung an einer anderen Hochschule endgültig nicht bestanden habe.

Bayreuth, Februar 2011

Vincenzo Stagno